Annabelle Chuinard

Department of Physics, McGill University, Montreal

Single Diffraction Studies with the ATLAS detector at the Large Hadron Collider

A thesis submitted to

McGill University

in partial fullfilment of the requirements of the degree of

Doctor of Philosophy

With the support of

the **National Sciences and Engineering Research Council (NSERC)**

and the **Swiss National Science Foundation (SNSF)**

June, 2018

Abstract

The work presented in this thesis covers two studies performed between 2013 and 2018.

The main analysis is an inclusive measurement of the differential cross sections of single diffractive events recorded in 2012 from proton-proton collisions in ATLAS. This measurement is the first of its kind at $\sqrt{s} = 8$ TeV *making use of the forward ALFA spectrometers to tag the scattered proton. Cross sections are measured for three observables: the size of the rapidity gap, the proton momentum transfer,* t*, and its fractional energy loss reconstructed from the kinematics of the proton and of the diffractive system. Events are selected such as to maximize the signal significance. The remaining background contribution is assessed using a partially data-driven technique. Distributions are "unfolded" to correct for detector smearing. A* t*-slope* $B_{SD} = 7.55 \pm 0.18$ GeV^{-2} *is obtained from fitting the cross section differential in* t*. The Pomeron intercept at the mean value of* t *for this measurement is found to be* $\alpha_{\mathbb{P}}(0) = 1.071 \pm 0.028$ *and* $\alpha_{\mathbb{P}}(0) = 1.059 \pm 0.012$ *from fitting the proton and diffractive system distributions respectively.*

The second study explores the regime of hard diffraction and the possibility of using the W *boson as a probe to infer on the quarkonic content of the colourless singlet exchanged in diffractive hard interactions. The hardness of the process is such that the recently installed AFP detector is needed to tag the scattered proton. A simulation of diffractive interactions is used to assess the statistical needs for such study to be performed within acceptance constraints. The study suggests that* 300 pb^{-1} *of data are sufficient to probe the Pomeron flavour in the* $W \to \mu\nu_{\mu}$ *channel.*

Résumé

Cette thèse présente deux études portant sur la diffraction simple réalisées entre 2013 et 2018.

L'analyse principale est une mesure des sections efficaces différentielles inclusives d'événements diffractifs simples à partir de données de collision proton-proton collectées par le détecteur ATLAS. Il s'agit de la première mesure non-élastique à $\sqrt{s} = 8$ TeV *à faire usage des spectromètres frontaux d'ALFA pour tracer les protons défléchis. Les sections efficaces sont déterminées pour plusieurs observables: la largeur du gap de rapidité, la variable de Mandelstam* t *et la fraction de quantité de mouvement perdue par le proton, reconstruite à partir des cinématiques du proton et du système diffractif. Les événements sont sélectionnés de façon à maximiser la significance du signal vis-à-vis du bruit. Le bruit restant est quantifié à l'aide d'une méthode basée en partie sur les données. Un algorithme de déconvolution est utilisé pour corriger les effets des détecteurs. La section efficace différentielle en* t *est extraite par régression linéaire: une pente* $B_{SD} = 7.55 \pm 0.18$ GeV^{-2} *est obtenue. L'ordonnée à l'origine de la trajectoire du Pomeron est déterminée pour la valeur moyenne de* t *de la mesure en "fittant" la cinématique du proton et du système diffractif. Les valeurs* $\alpha_{\mathbb{P}}(0) = 1.071 \pm 0.028$ *et* $\alpha_{\mathbb{P}}(0) = 1.059 \pm 0.012$ sont obtenues respectivement.

La seconde étude s'intéresse à la diffraction dans un régime d'énergie différent. Il s'agit d'une étude de faisabilité qui explore la possibilité d'analyser l'asymétrie de charge des bosons électro-faibles W *produits diffractivement. Cette observable est sensible au contenu en quarks de valence du singulet de couleur échangé durant l'interaction diffractive. La production du* W *nécessitant un niveau d'énergie suffisamment élevé, cela implique d'utiliser le détecteur AFP récemment installé pour mesurer la cinématique du proton défléchi. La quantité de*

données nécessaires pour effectuer une telle étude est évaluée grâce à une simulation prenant en compte les contraintes en terme d'acceptance. Il ressort que 300 pb^{-1} *de données devraient suffir à tester le contenu en saveur du Pomeron en ne considérant que le canal de désintégration muonique du* W*.*

Contents

Aknowledgement

Many people contributed to the work presented in this thesis in one way or another but I would like to express all my gratitude to those who believed in me, those who made our collaborative work be more about benevolence and less about competition, and to all the frustrated idealists who keep working to make the world a better place.

I would like to thank Andrew Foster, my Birmingham-based partner in crime, for having been such an incredible driving force. Andy, without your determination, your skepticism, your creativity (especially in implementing rather original debugging messages) and your relentless efforts in realizing good ideas, I would not be able to present this work. A special thank goes to Grzegorz Gach from AGH Cracow, for mastering the implementation of our analysis backbone. Grzegorz, I learned a lot from your incredible coding skills. Thank you for having been such an humble C++ teacher. Thank you as well for inviting me to join the analysis group and for making our interactions always soft.

I would also like to thank my direct supervisor, Prof. François Corriveau, for giving me the chance to work at McGill, in the vibrant city of Montreal. I am also grateful for the opportunities given to attend different conferences and schools to discuss my research, learn more, and meet interesting people, some of them now good friends. François, thank you for

the time spent in your office for the research-related or beyond-the-standard-weather talks.

Thank you to the the McGill high energy physics team for sharing their thoughts and insights over the years. My thanks go to Sébastien Prince for welcoming me at McGill as only a Prince would, and for being the one who asks questions in meetings when nobody else does. Thank you to Benoit Lefebvre my solid, and oftentimes vocal, friend who helped me during the ups and downs of being a grad student, and endured my complains about the unreliable computing infrastructure. Many thanks to the well-named Benjamin Freund, to Robert Keyes my particular particle friend, and to Charlotte Qin, my twin of soul. A great thank you as well to the members of my supervisory committee: Prof. Brigitte Vachon and Prof. Nikolaos Provatas for their guidance over the years. Many thanks as well to all who helped me in one way or another for the grant applications, in particular, my supervisor, Prof. Corriveau, Prof. Sangyong Jeon, Prof. Andreas Warburton and the swiss state councilors Gérard Ramseyer and Carlo Lamprecht.

I would also like to thank Prof. Paul Newman, Andrew's supervisor, for having been our oracle theory-wise during these past three years. Thank you Paul as well for sharing your rich experience on collaborative working. A special mention also goes to Prof. Christophe Royon, who introduced me to the community of diffraction and welcomed me with open arms in this small field. Thank you as well to Dr. Rafal Staszewski who taught me everything about diffractive physics and publication writing. Thank you Rafal for having been so patient and for having addressed the insane amount of questions I e-mailed you. Special thanks as well to the ALFA community, particularly to Leszek Adamczyk, Hasko Stenzel and Tomas Sykora, for the precious feedback they gave on the analysis.

Many thanks as well to the McGill Outreach group for giving me the opportunity to export my passion for physics. I will always remember the special light in the eyes of the kids we visited and that heartwarming feeling when seeing them understand the principle of scattering with our crafted shape colliders modules. Thank you as well to all the members of the teaching assistant committee for helping me fulfill my teaching and learning coordination appointments.

Finally, I would like to thank my friends Hélène Seiler and Pierre-François Duc, who welcomed us at their place and helped us get back on our feet after we lost our apartment in a fire. I would like to thank my mom and dad, Claire and Jac, who, despite being mildly interested in fundamental physics, have always been strongly supportive in each and every steps I took in life. I am grateful to my sister Elsa, for being so open-minded and for the uplifting Skype chats we had in troubled times. My biggest thanks go to my life companion Gabriel Kocher for enduring my temper, forgiving my mistakes and helping me become a better person.

I dedicate this thesis to my grand-father, Jacques Chuinard, who used to work at CERN in the early ages and would certainly have been amazed to see what it became.

"...the sea's only gifts are harsh blows and, occasionally, the chance to feel strong. Now, I don't know much about the sea, but I do know that that's the way it is here. And I also know how important it is in life not necessarily to be strong but to feel strong, to measure yourself at least once, to find yourself at least once in the most ancient of human conditions, facing blind, deaf stone alone, with nothing to help you but your own hands and your own head..."

- Primo Levi

Introduction

General Motives

As the world's largest and most powerful particle collider ever built, the Large Hadron Collider (LHC), is poised to answer some of the most fundamental questions in physics: what are the mechanisms giving masses to the elementary particles? is the Standard Model of particles and interactions a complete description of nature? what is the dark matter made of? are the electroweak force and the strong nuclear force manifestations of one universal unified force, as predicted by various Grand Unification Theories?

The work in this thesis addresses some of the fundamental steps towards the answering of such questions. It aims for an understanding of a category of events termed *diffractive* by analogy to their final state topology similar to a light scattering pattern. Shading light on the nature of such interactions is necessary as they represent an important component of the inelastic cross section which needs to be well understood in order to evaluate the effects of multiple collisions per proton bunch crossing referred as *pile-up*. That most of the parameterizations predicting the total proton-proton (pp) cross section depend on the diffractive representation is another incentive to constrain the models used, as most inelastic processes are scaled according to predictions on the total cross section.

An event is termed diffractive when a colourless exchange happens during the interaction [1, 2]. The typical signature of such exchange is a space devoid of particles between the final state systems: scattered proton(s) and diffractive system(s) of particles, called rapidity gap. The underlying theory for such exchange was initially developed by Tullio Regge. As diffractive scattering is dominated by soft interactions, Quantum Chromodynamics (QCD), the theory of strong interactions, cannot describe it since the cross sections for such phenomena are not calculable with perturbative techniques. Hence, diffractive processes are commonly discussed in terms of phenomenology-derived colour singlet exchange. Regge envisioned soft interactions as driven by the exchange of resonances corresponding to poles of the scattering amplitude in the spin plane. It was later extended to the complex plane allowing to describe diffractive interactions at higher energies. The pole trajectory, often termed *Pomeron*, corresponds to hadron-like objects with net vacuum quantum numbers. By nature, a Pomeron does not radiate in the rapidity space, which explains the rapidity gap observed in the final state.

In the case of single diffraction, one of the two protons dissociates and forms a system of particles which will be detected by ATLAS central detectors. This system is often referred to as the diffractive system. The other proton looses only a small amount of its energy through the emission of the colour singlet. It slightly deviates from its initial trajectory and may be tagged by specialized detectors like A Luminosity For ATLAS (ALFA) or ATLAS Forward Proton (AFP) in the very forward or backward regions. A single-side proton together with a gap in rapidity between that proton and the diffractive system is a typical signature of diffractive events. The fraction of energy lost by the proton, which is linked to the size of the rapidity gap, and the typical momentum transferred in the interaction are quantities

that are sensitive to the nature of the exchanged Pomeron. Hence, the universality of such theory, which directly impacts the current parameterization of the total cross section, can be probed by analyzing single diffraction at the LHC.

During the last few years, the focus at the LHC has naturally been on hard processes that can test the Standard Model. The discovery of the Higgs boson [3, 4] in 2012 crowned this chapter. Most of the research done at the LHC now focuses on the search for anomalies to test the Standard Model to its limits or any deviation therefrom. In parallel, efforts also went towards a precise measurement of the total inelastic pp cross section, which includes a diffractive component (up to 30%). Measuring the single-dissociative cross section as a function of the size of the rapidity gap has been the primary focus to all single diffractive studies performed at the LHC and its predecessors, at SPS [5, 6], Tevatron [7] and HERA through photo-production [8, 9] and through deep inelastic scattering [10, 11]. In these experiments, the size of the rapidity gap was defined as being the smallest rapidity span between the most external particle from the diffractive system and the detector axis along the beam pipe on the side of the scattered proton.

Thesis Plan

In Chapter 2, the theories of interactions are discussed, with an emphasis on the Regge-Pomeranchuck model. The QCD-inspired attempt to factorize the Pomeron as a resolvable object up to a certain scale is described. Several alternatives to integrate the diffractive models into event generators are presented.

Chapter 3 presents the main features of the ATLAS experiment at the LHC. The emphasis

is placed upon the LHC beam conditioning and the ATLAS, ALFA and AFP detectors used in the work presented.

Chapters 4 and 5 present the two studies performed by the author:

- Chapter 4 is dedicated to the measurement of the single dissociative cross section with respect to the squared momentum transfer t and proton fractional energy loss ξ. The work presented uses low pile-up data collected with the ATLAS experiment at the LHC at a center-of-mass energy of 8 TeV in 2012. The diffractive system tracks were recorded using the inner detector and used to derive ξ. The ALFA detector was optimized to measure the proton scattering angle by reconstructing proton tracks and the proton transverse momentum.

- The work presented in Chapter 5 investigates one possibility of probing the Pomeron partonic content. The study suggests to measure the single diffractive $W^{\pm}$ production asymmetry using the AFP timing detectors to tag the outcoming proton. Simulation results are presented to evaluate statistical needs and constraints for such a measurement to be possible at 13 TeV.

A general conclusion about the material covered is given in Chapter 6.

Diffractive Interactions and How They Are Modelled

2.1 Reggean Interpretation of Diffraction

2.1.1 Historical Context

In the 1930s, once the quantum electrodynamics introduced the picture of the electromagnetic force as a process involving photon exchange, the question of whether or not the other forces were also mediated by some particle became a natural one. Hideki Yukawa reasoned that the electromagnetic force was infinite in range because the exchange particle was massless. In 1935, he proposed that the short range strong force came about from the exchange of a massive particle which he called a meson [12]. By observing that the effective range of the nuclear force was on the order of a fermi, he predicted from the uncertainty principle that the mass of this mediator should be of the order of 100 MeV. In 1937 a particle of mass close to Yukawa's prediction was discovered in two independent cosmic-ray experiments [13, 14]. This particle, the muon, turned out not to interact via the strong force, but the Yukawa predictions stimulated a major advance in the understanding of the strong interaction. In the subsequent years, a myriad of mesons and baryons were discovered, but the simple picture of exchange of such particles was still unable to explain the hadronic cross section measured

in experiments.

In 1959, Tullio Regge solved the non-relativistic equation for hadron scattering [15]. He *analytically continued* (see Sect. 2.1.2) the partial wave amplitudes of its solutions, allowing the angular momentum to take complex values [1]. In this case, the real poles correspond to physical bound states with different angular momenta: the mesons and the baryons. Including the imaginary solutions formed an ensemble called Regge trajectory which could be used to describe the hadronic cross section as a function of the center-of-mass energy s, by means of the optical theorem (see Sect. 2.1.2). It was concluded that, since the poles were bound states, none of the strongly interacting particle were elementary.

From the fundamental observation that hadrons are composite, there grew two points of view. Some advocated that strongly interacting particles were elementary particles composing of a quantum field theory in which the hadrons were bound states. They would nowadays be called quarks and gluons representing the symmetry of flavour SU(3) according to the theory developed by Gell-Mann and Zweig in the 1970s [16, 17]. Others supported the idea that it was possible to formulate a model, the *S-matrix theory*, without elementary particles, and in which all the hadrons were bound states lying on Regge trajectories. In the early stages of colliding physics, the empirical S-matrix theory was a reliable tool for understanding scattering. It has now been superseded by quantum chromodynamics which is better at describing strong interaction in the high energy regime. The Regge approach is however still indispensable for event simulation. The model has been extended to higher energies by introducing the Pomeron trajectory. Various flavours of this model may be used in the current Monte Carlo generators to picture diffractive interactions, all to be constrained by

experiments.

2.1.2 Model for pp Scattering at Low p_T

The S-matrix Framework

The S-matrix elements describe the probability of transitioning from an initial quantum state $|i\rangle$ to a final quantum state $|f\rangle$ through a strong interaction. The probability for a such a transition to happen is given by:

$$P_{i\to f} \equiv |\langle f| S |i\rangle|^2 \tag{2.1}$$

S is usually decomposed into the identity matrix and a transition matrix $S = \mathbb{1} + iT$, with T expressed as a function of the relativistic scattering amplitude $\mathcal{A}(i \to f)$:

$$S_{if} \equiv \langle f| S |i\rangle = \delta_{if} + iT_{if} \tag{2.2}$$

$$= \delta_{if} + i(2\pi)^4\delta^4(p_f - p_i)\mathcal{A}(i \to f). \tag{2.3}$$

For a 2-hadrons interaction process producing n particles ($1 + 2 \to n$), the amplitudes are related to the differential cross section by:

$$d\sigma = \frac{1}{\Phi}|\mathcal{A}(i \to f_n)|^2 d\Phi_n \tag{2.4}$$

Φ being the incident flux of particles and $d\Phi_n$ the Lorentz-invariant phase-space (LIPS) measure for n particles to be obtained in the final-state. By summing over all possible final state particles and final state multiplicities, the total cross section of the two incoming particles is derived. The total cross section is what sets the scale of diffractive processes. In high rate colliding machines, a precise knowledge of the total cross section is required as it enters in the calculation of the number of extra-collisions happening at the same time as the interaction of interest (pile-up).

Optical Theorem

The total proton-proton scattering cross section splits in two parts. A contribution comes from the elastic collisions and the other one from the inelastic processes:

$$\sigma_{\text{tot}} = \sigma_{\text{elastic}} + \sigma_{\text{inelastic}} \tag{2.5}$$

Measuring the elastic scattering is relevant because it can be easily related to the total cross section assuming unitarity of the S-matrices. This property follows from the fact that the sum of all probabilities to transition from one state $|i\rangle$ to any final state $|k\rangle$ should be 1.

$$\sum_k p_{i\to k} = \sum_k |\langle k|\, S\, |i\rangle|^2 = \sum_k \langle i|\, S^\dagger\, |k\rangle\, \langle k|\, S\, |i\rangle = \langle i|\, S^\dagger S\, |i\rangle = 1 \tag{2.6}$$

which means:

$$\begin{aligned} & S^\dagger S = (\mathbb{1} - iT^\dagger)(\mathbb{1} + iT) = \mathbb{1} \\ \Rightarrow\ & T^\dagger T = i(T^\dagger - T) \end{aligned} \tag{2.7}$$

Applying $\langle f|$ and $|i\rangle$ on both sides of Eq. 2.7:

$$\begin{aligned} & i\,\langle f|\, T^\dagger - T\, |i\rangle = \langle f|\, T^\dagger T\, |i\rangle \\ \Rightarrow\ & \sum_j \langle f|\, T^\dagger\, |j\rangle\, \langle j|\, T\, |i\rangle = i\,\langle f|\, T^\dagger - T\, |i\rangle \\ \Rightarrow\ & \sum_j T^*_{fj} T_{ij} = 2\Im T_{if} \end{aligned} \tag{2.8}$$

Using Eq. 2.8 when $|i\rangle = |f\rangle$ (elastic case), we can derive the following relation, which links the total pp cross section to the forward elastic nuclear scattering amplitude A_{el}:

$$\sigma_{\text{tot}} \sim \frac{1}{s}\Im A_{\text{el}}(t=0,s), \qquad s\to\infty, \tag{2.9}$$

Using this result, called the *elastic theorem*, one can express the differential elastic cross section as a function of the integrated total cross section (see full development in [18]). As

the normalization of the diffractive cross sections and the pile-up modeling depends on our knowledge of the total pp cross section, it is crucial to measure the elastic cross section with precision at various energies. Such measurement was and still is the main focus of the ATLAS forward physics program.

Mandelstam variables

One of the conditions on the S-matrices is that they must be relativistically invariant, and thus they are often expressed in terms of Lorentz invariant observables, in this case, the Mandelstam variables s, t and u.

Let us consider a process involving two bodies colliding. Entities are labelled with 1 and 2 for the initial states and 3 and 4 for the final states and their associate 4-momenta $\boldsymbol{p_i}$, $i = 1, 2, 3, 4$, as depicted on Fig. 2.1. A set of convenient variables are used to describe the momentum exchange between bodies. Named after physicist Stanley Mandelstam, they are

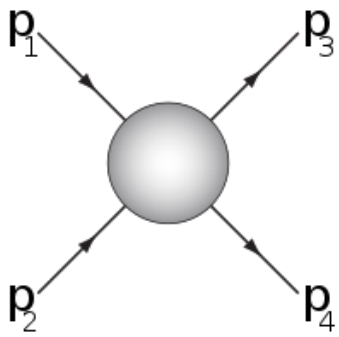

Figure 2.1: Feynman diagram of a two-body process. The blob represents any possible interaction.

defined as:

$$s = (\boldsymbol{p_1} + \boldsymbol{p_2})^2 = (\boldsymbol{p_3} + \boldsymbol{p_4})^2 \tag{2.10}$$

$$t = (\boldsymbol{p_1} - \boldsymbol{p_3})^2 = (\boldsymbol{p_2} - \boldsymbol{p_4})^2 \tag{2.11}$$

$$u = (\boldsymbol{p_1} - \boldsymbol{p_4})^2 = (\boldsymbol{p_2} - \boldsymbol{p_3})^2 \tag{2.12}$$

The Mandelstam variables represent the squared four-momentum transferred for the three different type of interactions shown on Fig. 2.2.

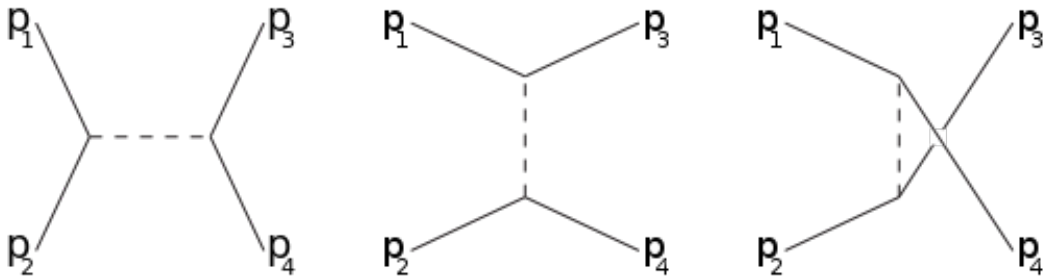

(a) s-channel. (b) t-channel (c) u-channel

Figure 2.2: Feynman diagram showing the three different types of interactions referred as the s-, t- and u- interaction channels.

s and t are the only two variables needed to define the type of process considered. In the work presented in this thesis, s corresponds to the energy level at which the collision takes place. t quantifies the "softness" of the interaction. The smaller t, the more elastic the interaction. Hence, elastic scattering corresponds to the limit where states 1 and 2 are the same as states 3 and 4, with no energy transfer (i.e. $t = 0$ in the s-channel).

From definitions [2.10 - 2.12] and energy-momentum conservation, the following formula, linking the masses, m_i, of the interacting particles to the Mandelstam variables, is derived:

$$s + t + u = \sum_{i=1}^{4} m_i^2 \tag{2.13}$$

The scattering amplitude are analytic function of s, t and u, which means they can be continued to complex values. If we consider a proton-proton interaction in the s-channel, the amplitude observed $\mathcal{A}(t,s)$ will then be obtained by taking the limit of the amplitude when s and t take real values, under the condition that there is enough center-of-mass energy to create the protons $s \geq 4m_p^2$ and that $t, u < 0$ from Eq. 2.13.

In addition, scattering amplitude are cross-symmetric, which means that the same function $\mathcal{A}(t,s)$ describes the s, t and u scattering channels in different physical domains. If the amplitude is known for the s channel when $s \geq 4m_p^2$ and $t, u < 0$, then it should be possible to extend it to the t channel whilst making sure that $t \geq 4m_p^2$ and $s, u < 0$.

The Reggeon Trajectory

The kinematics of a two-body process is totally defined by s and t. Likewise, the scattering amplitude $\mathcal{A}(t,s)$ describing the probability to go from one set of states to another, should also be a function of these two variables. One can use the Legendre polynomials P_l to express the scattering amplitude in the t-channel:

$$\mathcal{A}(t, s(t, z_t)) = 16\pi \sum_{l=0}^{\infty} (2l+1)\mathcal{A}_l(t) P_l(z_t), \qquad \text{where } z_t = 1 + \frac{2s}{t - 4m^2} \tag{2.14}$$

where $\mathcal{A}_l(t)$ are partial wave functions for angular momentum $l = 0, 1, 2, ...$ and $\mathcal{A}_l(t)$ are singular for given values of t. Eq. 2.14 is valid in the t-channel where $t \geq 4m^2$ and $s < 0$ but cannot be extended to the s-channel, where $s \geq 4m^2$ and $t < 0$ as this corresponds to $|z_t| > 1$ for which the series of Legendre polynomials does not converge.

The convergence of $\mathcal{A}(t,s)$ can be restored by allowing the angular momentum to take non-real values. This is done by continuing the partial wave function $\mathcal{A}_l(t)$ with some

interpolating function $\mathcal{A}_i(l,t)$ such that:

$$\mathcal{A}_i(l,t) = \mathcal{A}_l(t) \qquad l = 0, 1, 2, ... \tag{2.15}$$

Assuming that all the singularities of $\mathcal{A}_i(l,t)$ are poles in the complex plane for integer values of l, the methods of complex contour integration [19] may be used to recast the scattering amplitude in the Watson-Sommerfeld representation [20], which allows to get rid of the poles. Within this representation the scattering amplitude can then be continued to any channel. The amplitude in the s-channel comes down to a rather simple expression in the high energy limit. For the leading pole and when $s \to \infty$, this yields:

$$\mathcal{A}(t,s) \to -\beta(t)\frac{s^{\alpha_{\mathbb{R}}(t)}}{\sin \pi\alpha_{\mathbb{R}}(t)} \tag{2.16}$$

where $\alpha_{\mathbb{R}}(t)$ corresponds to the location of the leading pole (pole with the highest real part) with residue $\beta(t)$. A similar expression in the $s \to \infty$ limit may be derived to account for relativistic effects in scattering and will not be detailed in this thesis.

From Eq. 2.14, around the pole, the partial wave amplitude is expected to behave like:

$$\mathcal{A}_i(l,t) \approx \frac{\beta(t)}{l - \alpha_{\mathbb{R}}(t)} \tag{2.17}$$

For a given momentum exchange t', the location of the pole can be expressed as the angular momentum to which a small imaginary variation is added: $\alpha_{\mathbb{R}}(t') = l + i\epsilon$. One can then expand $\alpha_{\mathbb{R}}(t)$ around t' to the first order in ϵ which gives:

$$\mathcal{A}_i(l,t) \propto \frac{\beta(t)}{t - t' + i\Gamma}, \qquad \text{with } \Gamma = \frac{\epsilon}{\alpha'_{\mathbb{R}}(t')} \tag{2.18}$$

One recognizes the Breit-Wigner distribution centered around $\sqrt{t'}$. For real $t > 0$, each pole of $\mathcal{A}_i(l,t)$ corresponds to the resonance mass $M = \sqrt{t'}$ for a given momentum l. This derivation means that the scattering amplitude in the s-channel depends on the resonances

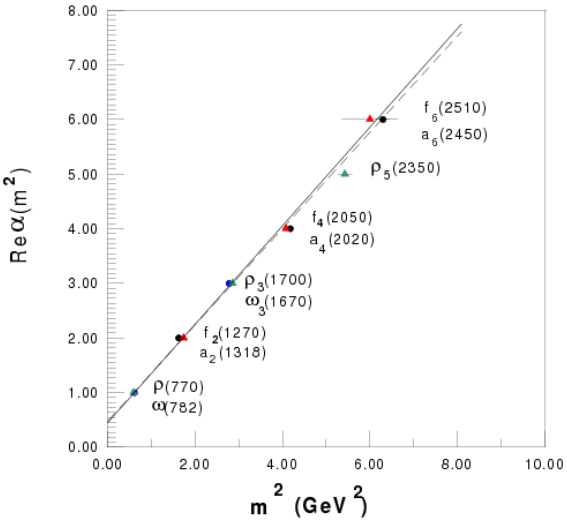

Figure 2.3: A Chew-Frautschi plot showing the Regge trajectory interpolated as a straight line between the poles of the scattering amplitude in the t-channel (from [21])

exchanged in the t-channel. These resonances are associated to existing particles as shown on the Chew-Frautschi plot presented on Fig. 2.3. A set of resonances with the same quantum numbers define a straight line called Regge trajectory, or Reggeon. This trajectory is universal for any type of process and any energy, and may be approximated as:

$$\alpha_{\mathbb{R}}(t) = \alpha_{\mathbb{R}}(0) + \alpha'_{\mathbb{R}} \cdot t, \tag{2.19}$$

where $\alpha_{\mathbb{R}}(0)$ is a Regge trajectory intercept and $\alpha'_{\mathbb{R}}$ is the slope. The total cross section can be constructed by adding up all the contributions from the Regge trajectories and using the optical theorem from Eq. 2.9. The energy behaviour of the total cross section σ_{tot}, when $s \to \infty$, is then determined by the intercept of the Regge trajectory:

- if $\alpha_{\mathbb{R}}(0) > 1$, σ_{tot} increases,
- if $\alpha_{\mathbb{R}}(0) = 1$, σ_{tot} stays constant,
- if $\alpha_{\mathbb{R}}(0) < 1$, σ_{tot} decreases.

Looking at Fig. 2.3, we see the intercept is approximately 0.5, which indicates the resulting cross section coming from the exchange of mesons should fall off as $s^{-0.5}$. This picture is valid up to energies $\sqrt{s} < 10$ GeV but is no longer reliable for higher energies for which a Pomeron model is used.

2.1.3 Model for pp Scattering at higher energies

Extending Regge theory

While the Regge trajectory can reproduce the dependence of the hadronic cross-section rather well in the low energy regime, it is not able to explain the cross-section rise for higher energy scattering displayed in Fig. 2.4. Isaak Pomeranchuk developed a theory stating that, at sufficiently high $\sqrt{s}$, the pp interaction cross section would become asymptotically equal to the $p\bar{p}$ cross section. This affirmation is only valid if the cross sections are proved to be asymptotically constant and if the ratio of the real to the imaginary parts of the scattering amplitude does not increase more rapidly than $\ln(s)$. Vladimir Gribov proposed a trajectory satisfying these conditions, which was later dubbed Pomeron [22]. In this configuration, the poles carry the quantum numbers of the vacuum and are not associated with any known particles for integer values of the angular momentum. Assuming the existence of the Pomeron, the total cross-section data can be fitted with a sum of trajectories accounting for both low and high energy regime contributions:

$$\sigma_{\text{tot}} = As^{\alpha_{\mathbb{R}}(0)-1} + Bs^{\alpha_{\mathbb{P}}(0)-1} \tag{2.20}$$

where $\alpha_{\mathbb{R}}(0)$ and $\alpha_{\mathbb{P}}(0)$ corresponds to the Reggeon and Pomeron trajectory intercepts respectively. A and B are parameters depending on the type of hadronic scattering. In this case, $\alpha_{\mathbb{R}}(0)$ is smaller than unity, which explains why the total cross section is decreasing in the low energy regime. The rise of the cross section at larger energies is then explained by

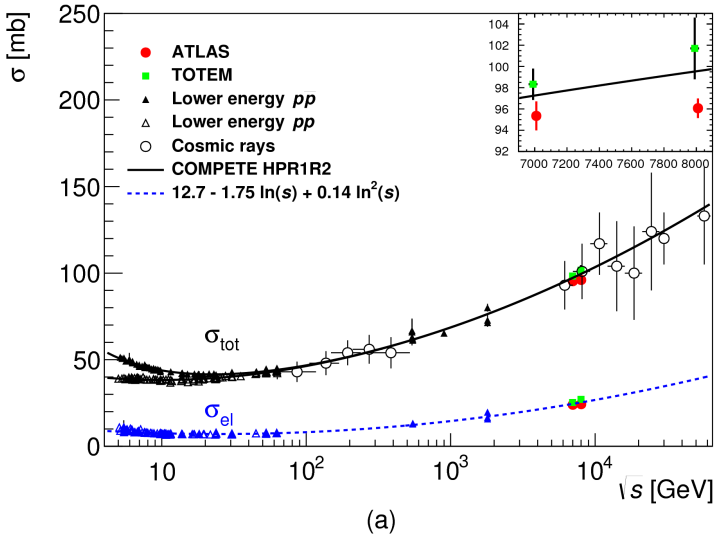

Figure 2.4: Comparison of total and elastic cross-section measurements presented here with other published measurements and model predictions (lines) as a function of the center-of-mass energy (from [25]).

$\alpha_{\mathbb{P}}(0)$ being greater than unity. Since there is no way to calculate the sum of all interactions from first principles, the Regge parameterization of the total cross section is fundamental nowadays to model its behaviour at increasing energies.

Similarly to the Regge trajectory for mesons, one can expand the Pomeron trajectory around 0 values of t at first order:

$$\alpha_{\mathbb{P}}(t) = 1 + \epsilon + \alpha'_{\mathbb{P}} t \tag{2.21}$$

where $\epsilon = \alpha_{\mathbb{P}}(0) - 1$ is a common variable used in Monte Carlo tuning and is not considered constant over the energy range. $\alpha'_{\mathbb{P}}$ is extracted from fits to small t elastic pp (ISR) and $p\bar{p}$ (Tevatron) scattering data [23, 24]. The other variables are determined from global fits to existing cross-section data.

The contribution of type s^{λ}, with $\lambda > 0$ in Eq. 2.20 should violate one of the analytical

constraints on hadron-hadron interactions: the Froissart-Martin bound [26, 27]. It states that the interaction cross section of two particles will become negligible beyond a certain impact parameter due to the time-energy uncertainty principle. Marcel Froissart showed that the impact parameter in a collision is a function of the natural logarithm of the center-of-mass energy. Hence, the scattering cross section cannot rise faster than the size of the impact parameter squared and therefore it is bounded by $\ln^2(s)$. The Froissart-Martin condition can be derived using general constraints on unitarity and analyticity and is often expressed as:

$$\sigma_{\text{tot}}(s) \leq \ln^2\left(\frac{s}{s_0}\right), \qquad \text{when } s \to \infty, \tag{2.22}$$

where s_0 is a scale parameter known to be very small, and $\ln^2\left(\frac{s}{s_0}\right)$ is de facto much larger than the cross section expected at the energies considered for this work.

Accommodating the Froissart-Martin bound

Even if the Froissart-Martin limits is not constraining the fit on the total cross section, some efforts have been made to generalize the theory and accommodate this condition by renormalizing the Pomeron flux to unity or by considering multiple Pomeron interactions. The different models with normalized fluxes or not and including or not the possibility of multiple Pomeron exchange are discussed in Sect. 2.5.

2.2 QCD-oriented Interpretation of Hard Diffraction

2.2.1 Development of QCD

We present here a brief overview of the historical development of quantum chromodynamics, with emphasis on its key features. A detailed description of the complete Standard Model theory can be found in [28].

Flavour-SU(3) Group

While Regge theory was successful at describing low energy hadronic scattering, its extension to higher energies with the Pomeron remained quite difficult to interpret, since the Pomeron poles are not real particles. A new theory pioneered by Murray Gell-Mann and Yuval Ne'eman [16, 29] was presented that organized all the recently discovered hadrons as members of specific representations of the SU(3) symmetry scheme, a group of unitary 3 x 3 matrices with determinant 1 derived from the SU(2) isospin symmetry. In 1964, Gell-Mann and George Zweig proposed that the baryons and mesons are bound states of an hypothetical triplet, which they called quarks [30]. The quarks: u, d and s form a fundamental representation of what we now call the flavour-SU(3) group. The proton was then understood to be a bound state of two u quarks and one d quark (uud), the neutron of two d quarks and one u quark (ddu), the Λ-hyperon uds, etc.

Quantum Chromodynamics and the Parton Model

The model of quarks was challenged by the discovery of spin-$\frac{3}{2}$ Δ^{++} baryon with quark content uuu. Since this is the ground state, the space wave-function should be symmetrical and the three spins of the quarks aligned to give the spin of the Δ^{++}. Hence, the wave function of the baryon does not change if two quarks are interchanged. This is not compatible with

the Pauli exclusion principle which states that the fermion wave function must be antisymmetric.

This problem was solved by Han, Nambu and Greenberg [31, 32] suggesting that the quarks had an additional SU(3) degree of freedom, which Gell-Mann and Harald Fritzsch introduced as the charge of colour. The hadrons were composed of combinations of coloured quarks which made them colour singlets. The colour symmetry SU(3) was an exact symmetry and a good representation of the quantum field theory of strong interaction: the quantum chromodynamics.

During the same period, Feynman worked on a representation in which hadrons were composed of quasi-free point-like entities he called partons [33]. His theory was inspired from observations from the Stanford Linear Accelerator (SLAC) in which 20 GeV electrons were scattered off liquid hydrogen and liquid deuterium. Through this Deep Inelatic Scattering (DIS) process, a photon was emitted from the electron, which interacted with a parton carrying a fraction of the energy of the target proton x_p. Of his model came out that measuring the outgoing electron momentum would give direct information on the distribution of charge inside the proton (the structure functions) and that the higher order corrections would be related to a another type of partons: the gluons.

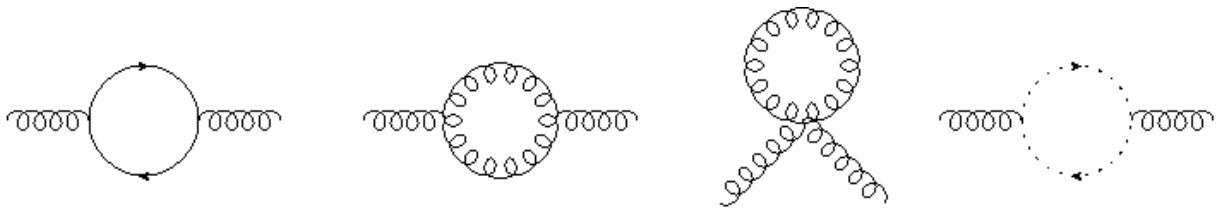

Figure 2.5: Diagrams contributing to the renormalization of the gluon propagator in QCD.

About Feynman diagrams...

To interpret the contributions to the transition amplitude, Feynman used diagrams. Each diagram topology is representing a possible interaction channel. The amplitudes which are called the matrix elements ($\mathcal{M}$) are calculated by evaluating the relevant diagrams using a set of rules appropriate to the interaction considered. In a Feynman diagram, an interaction is represented as a point-like vertex, with partons going in or out as lines in space and time. Each vertex has an associate coupling which characterizes the probability of a given interaction to happen. The probability of a given final state is then obtained by summing all the possible final diagrams. The main contribution arises from the Born diagram, to which one should add all possible corrections caused by real and virtual gluon emissions as depicted below.

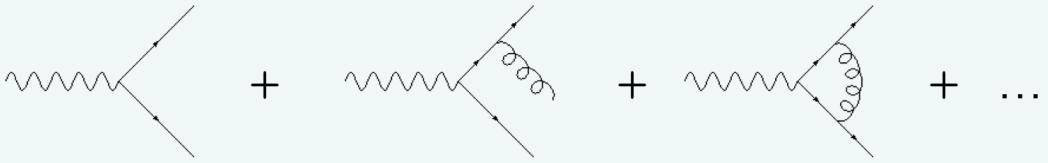

Born level Real emission Virtual correction

The naive application of such calculations often implies to add correction diagrams whose amplitudes are infinite. In order to calculate the amplitude for pp scattering in QCD, these singularities must be treated. The treatments are complex and require to introduce two parameters: the renormalization scale μ_R and the factorization scale μ_F.

Inspired from Quantum Electrodynamics (QED), one started to interpret the colour group

as a gauge group. Such a theory allows the gluons to interact not only with the quarks but also with themselves. It was found that these direct gluon-gluon interactions may manifest themselves as infinite contributions in the calculation of the scattering amplitude for a set of partons, which is an example of ultraviolet divergence. Typical self-interaction effects leading to UV divergences in the gluon propagator are shown in Fig. 2.5. UV divergences are tamed using regularization techniques. Such techniques imply to choose a scale μ_R at which the subtraction removing the ultraviolet divergences is performed. Hence, the calculated amplitude becomes dependent on the choice of scale.

Renormalization scale and asymptotic freedom

It is convenient to interpret this renormalization scale dependence as a renormalization of the coupling itself. The renormalized coupling is then said to be running. This running, i.e. the fact that partons behave as free particles at very high energy, is what is called asymptotic freedom [34, 35]. The renormalized coupling α_s, decreases logarithmically depending on a parameter Λ_{QCD} which is the scale at which QCD becomes non-perturbative. Λ_{QCD} is usually extracted from fits to measurements of α_s. For a given momentum Q^2 transferred in the interaction, the coupling can be expressed at leading order in perturbation:

$$\alpha_s(Q^2) \approx \frac{12\pi}{(33 - 2\ n_f) \ln\left(\frac{Q^2}{\Lambda^2_{\text{QCD}}}\right)} \tag{2.23}$$

where n_f is the number of quark flavours with masses less than Q^2.

In parallel to the development of the gauge theory, James Björken discovered that the functions describing the structure of the proton are scalable: they are determined not by the

center-of-mass energy of the interaction but, instead, by a dimensionless kinematic quantity, which for ep interaction is nothing else than the ratio of the four-momentum transfer q of the virtual photon squared over the electron energy loss [36]. This property, the Bjorken scaling, could be used to resolve the content of hadrons at any energy scale. The measurements at SLAC were the firsts to provide the Parton Distribution Function (PDF)s, the distributions of partons within the proton.

Factorization scale and the parton distribution functions

In the special case of pp scattering, gluons may be emitted from the initial partons. The Feynman diagrams corresponding to these Initial State Radiation (ISR) are divergent when the radiated gluon is soft or when it is emitted collinearly with respect to the initial state parton. The soft emission divergences are not problematic since they cancel out with the corrections coming from virtual emissions in the final state. However, the collinear singularities remain in the computation of the amplitude.

The problem of collinear singularities is masked by absorbing the divergences into a redefinition of the PDFs. The diverging integrals are regulated by using a cut-off parameter $\Lambda_{\mathrm{QCD}} > 0$ as the lowest integration limit, and picking a scale μ_F such that the hadronic cross section can be considered as the convolution of a soft term depending on Λ_{QCD} and μ_F and a hard term, independent of Λ_{QCD}, which is perturbatively-computable. The soft term may be absorbed in a redefinition of the PDF, which then become dependent of μ_F. This way, all the dependence on non-perturbative dynamics encoded in Λ_{QCD} has been absorbed into the PDF, which needs to be extracted from data in any case.

From the discoveries of Bjorken on PDFs and the factorization theorem [37], emerged the first formulation of a semi-perturbative cross section for hadron-hadron scattering. A consequence of the ISR divergences masking and the factorization method was that the scattering of protons could now be considered as bipartite. The first part encompasses all the partons dynamics below a certain energy scale using probability distributions. The second part accounts for the hard interaction of partons, which may be calculated from perturbation theory exploiting the principle of asymptotic freedom in QCD. Both functions depends on the scale at which one chooses the factorization to happen. The hard cross section also depends on the scale μ_R since it is a function of the coupling. If we choose, $\mu_R^2 = \mu_F^2 = Q^2$, we get:

$$\sigma_{p_A p_B \to X} = \sum_{i,j} \int dx_A \; dx_B \; f_i(x_A, Q^2) \; f_j(x_B, Q^2) \; \hat{\sigma}_{ij \to X}(x_A p_A, x_B p_B, Q^2) \tag{2.24}$$

where f_i and f_j are the PDFs for partons i and j, x_A and x_B are the momentum fractions of parton i and j in the two protons, $\hat{\sigma}$ is the hard partonic cross section for a final state X to be produced and Q^2 is the momentum scale of the hard partonic interaction.

2.2.2 Extending the concept of Pomeron

The Ingelman and Schlein Model

QCD factorization (2.24) was extended by Ingelman and Schlein to the case of Diffractive Deep Inelatic Scattering (DDIS)[38] for which it has been proven to be valid [39]. Yet, high-energy DIS experiments, H1 and ZEUS at HERA [40–42] used this principle to extract the Pomeron PDFs by analyzing single diffractive events ($p + e \to e + X + p$) from ep collisions. In the Ingelman and Schlein (IS) model, the diffractive processes are described in terms of the probability for a Pomeron to be initially preformed, such that a subsequent interaction can happen between one of the partons inside this Pomeron and the virtual photon emitted

by the electron (see Fig. 2.6a). If we assume a large enough momentum transfer between the interacting partons from the Pomeron and from the dissociating proton, which is reasonable considering the two initial state protons colliding with very high momenta, we can choose the factorization scale to be $\mu_F^2 = Q^2$ and apply the factorization theorem to separate the long-distance from the short-distance physics contribution to the diffractive cross section. We shall assume that the Pomeron has a universally defined partonic structure and we may define its contribution in the Feynman diagram as the convolution of a probability of emission, called the Pomeron flux $\phi_{\mathbb{P}}$, and its parton density function $f_{\mathbb{P}/p}$ (see Fig. 2.6b). This contribution is usually dubbed Diffractive PDF (DPDF):

$$\mathcal{F}_{\mathbb{P}/p}(\xi, \beta, Q^2) = f_{\mathbb{P}/p}(\beta, Q^2) \cdot \phi_{\mathbb{P}}(\xi) \tag{2.25}$$

where ξ is the fraction of the scattered proton transferred in the interaction. Similar to the proton PDFs, the Pomeron PDFs shall be extracted from fit to diffractive data.

Extending this vision to the inclusive production of a single diffractive system in pp collisions $pp \to Xp$, let x_p and β denote the respective fraction of the dissociating proton and Pomeron momenta involved in the interaction. By means of the factorization theorem, we decompose the cross section into the product of the diffractive PDFs and the proton PDFs convoluted with a term $d\hat{\sigma}$ describing the hard cross section of the two extracted partons:

$$\frac{d\sigma(pp \to p + X)}{d\xi dx_p d\beta dt} = \phi_{\mathbb{P}}(\xi, t) \frac{d\sigma(p\mathbb{P} \to X)}{dx_p d\beta dt} \tag{2.26}$$

where:

$$\frac{d\sigma(p\mathbb{P} \to X)}{dx_p d\beta dt} = f_p(x_p, Q^2) f_{\mathbb{P}}(\beta, Q^2) \cdot d\hat{\sigma} \tag{2.27}$$

It should be noted that the Pomeron PDF $f_{\mathbb{P}}$ may have a dependence in t, just like the photon has a PDF depending on its virtuality. For lack of a model for such a dependence we

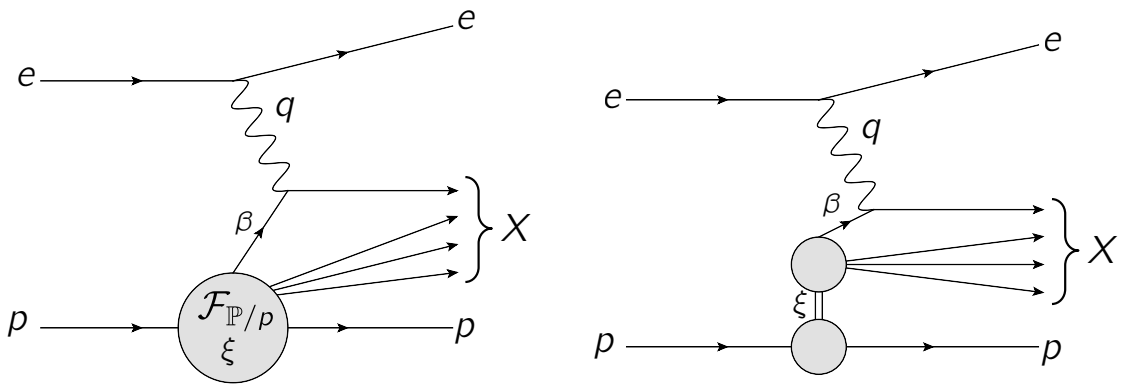

(a) Simple factorization: separating the non-diffractive from the diffractive part in the interaction. $\mathcal{F}_{\mathbb{P}/p}$ accounts for the probability to emit a Pomeron and depends on ξ.

(b) Double factorization for small ξ: decomposing the diffractive part further into the emission (flux) and the Pomeron PDF. Only the flux depends on ξ.

Figure 2.6: The $p+e \to e+X+p$ interaction diagrams using different factorizations schemes. (b) allows to extract scalable definitions for the Pomeron PDFs.

assume it to be averaged over the t range probed. The dependence in t of the flux is treated similarly: $\phi_{\mathbb{P}}(\xi) = \int_{t_{\min}}^{t_{\max}} \phi_{\mathbb{P}}(\xi, t)dt$, where $\phi_{\mathbb{P}}$ is usually modeled using an exponential whose parameters are tuned to data. It is normalized or not, depending on the models.

The reader should keep in mind that, although not stated explicitly, the hard cross section depends on the choice of renormalization scale. The parton density functions and the hard cross section also depend on the choice of factorization scale. Since the final cross section should be independent of this choice, changing μ_F will simply reshuffle the PDFs and the hard cross section in such a way that the convolution of the two stays invariant.

Assuming the decompositions from Eqs. 2.25 and 2.27 stand, we should be able to predict the single diffractive cross section using the Pomeron PDFs and Pomeron fluxes extracted from H1 [40, 41]. It turns out not to be the case: prediction of the number of QCD jets is

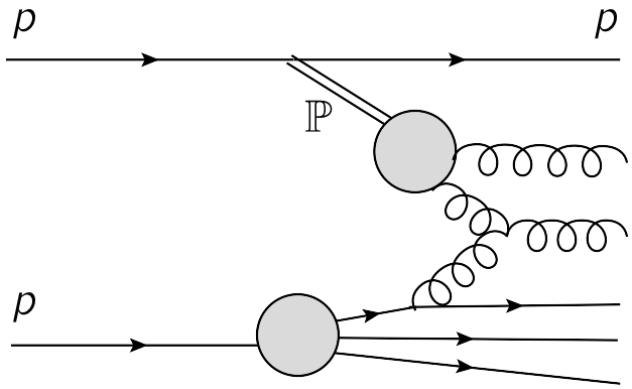

Figure 2.7: A model of hard diffraction for SD interaction using a resolved proton à la Ingelman and Schlein. In this picture, the gluonic content of the Pomeron interacts at a hard scale with the proton remnants to form the diffractive system.

about an order of magnitude higher than the observed rate at the Tevatron [43]. Soft rescattering between spectator partons of the colliding partons can produce additional final-state particles. These radiations may fill the would-be rapidity gap, making diffractive events appear as non-diffractive. This issue is dealt with by estimating the probability of such spoiling emissions to not occur.

The most common approach is to assume that the hard process occurs on a short enough timescale, such that the physics responsible for the additional emissions can be factorized and accounted for by an overall factor, called the gap survival probability and often denoted S^2. Whilst being widely used in many studies, there is still no consensus on the way the gap survival factor should be modeled, on its typical magnitude and its dependence with s.

Another more recent approach treats the soft rescattering using the artillery developed to model multiple parton interactions. In this case, the rapidity gap survival correction is calculated on an event by event basis, based on the kinematics of the hard process [44].

More details are given in Sect. 2.5.

Probing the Pomeron Content

For single diffractive scattering, the assumption of a possible factorization of long distance/short distance effects (IS model) implies that the interacting parton coming from the dissociating proton can be used as a hard probe to resolve the Pomeron content. Studies have been conducted using the observed production of electroweak bosons, as well as dijet and diphoton events at the Tevatron [45–47]. Opportunities to use these clean signatures to probe the Pomeron quarkonic structure were investigated. Some kinematic comparison between data and predictions extracted from conventional and non-conventional IS-derived models were made [48], but no conclusion was drawn that would irrefutably favor one model. Several studies showed the benefits of using the LHC forward spectrometers to identify diffractive events. In particular, the recently installed AFP detector, would allow to measure the charge production asymmetry of the W boson in single diffractive events, as this quantity should be sensitive to the Pomeron quarkonic structure function ratios. The feasibility study performed by the author on this topic is covered in Chapter 5.

In parallel, the absence of colour of the IS Pomeron and the fact that it cannot be a real particle or state, since it has a negative invariant mass, strongly suggests it to be made of virtual gluons. The most favored hypothesis [49] considers that the first contributing Feynman diagram of higher energy proton scattering would feature the exchange of two gluons. Corrections then arise as a ladder of gluon exchange, called "glueball". In the glueball model, the Pomeron intercept is supercritical ($\alpha_{\mathbb{P}}(0) = 1.5$) which means its contribution would give a dependence in t of the total pp cross section larger than from experimental observations.

Detecting and understanding glueballs is part of the program of several ongoing experiments like COMPASS [50] but none of them has been able to shed light on the substructure yet.

2.3 Models using Color Reconnection

The two studies presented in Chapters 4 and 5 rely on the Ingelman and Schlein description of a Pomeron entity, with a resolvable partonic content. An alternative to this model exists which does not consider any Pomeron dynamics. The theory is based on the assumption that soft interactions may take place with the proton not only before but also after the hard scattering, changing the hadronization in such a way that a rapidity gap occur in the final state.

The soft color interactions are represented using colour-string fields of the Lund string model [51] for hadronization typically used in Monte Carlo generators. For such soft interactions, the momentum exchange does not significantly change the momenta of emerging partons, but the exchange of colour changes the colour structure of the emerging parton system, resulting in a modified string-field topology and affecting the resulting distribution of final state hadrons. The default Lund model, described in Sect. 2.5, assumes that the colour structure, i.e. the string topology, strictly follows the colour ordering from the perturbative phase. The idea behind the *colour reconnection* model is to allow non-perturbative Soft Color Interaction (SCI) with small momentum transfers between the parton from the hard interaction and the remnants of the dissociating proton. As these interactions happen below the scale of perturbative QCD, they are modeled using a phenomenological parameter: the probability for a colour octet, like a multi-gluon object, to be exchanged between a pair of partons [52]. As an example, a comparison of the diffractive production of the W using

the Regge model and the color reconnection model is shown on Fig. 2.8. This model and its extensions [53] gave similar predictions to those using the Regge description, with some improvements when the exchange probability is calculated dynamically.

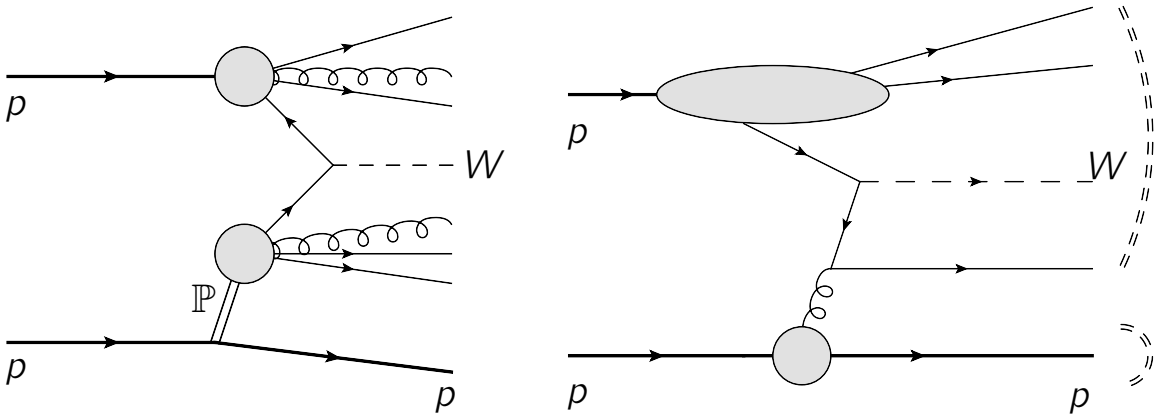

(a) Assuming a reggean interaction. The rapidity gap emerges from the exchange of Pomerons which are not radiating in the rapidity space.

(b) Assuming soft color interactions. The dashed double line shows the non-conventional string configuration which give rise to the rapidity gap in the finals state.

Figure 2.8: Feynman representations of single diffractive production of the W boson.

2.4 Kinematics of Diffraction

2.4.1 Diffractive Topologies

The characteristic feature of diffraction is that the hadronic final states - the scattered proton and the diffractive system in the case of Single Diffraction (SD) and Central Diffraction (CD) or the two diffractive systems in the case of Double Diffraction (DD) - are separated by a large gap in rapidity devoid of hadronic energy. The gap is due to the colourless nature of the diffractive exchange (by definition, colorless objects do not radiate gluons).

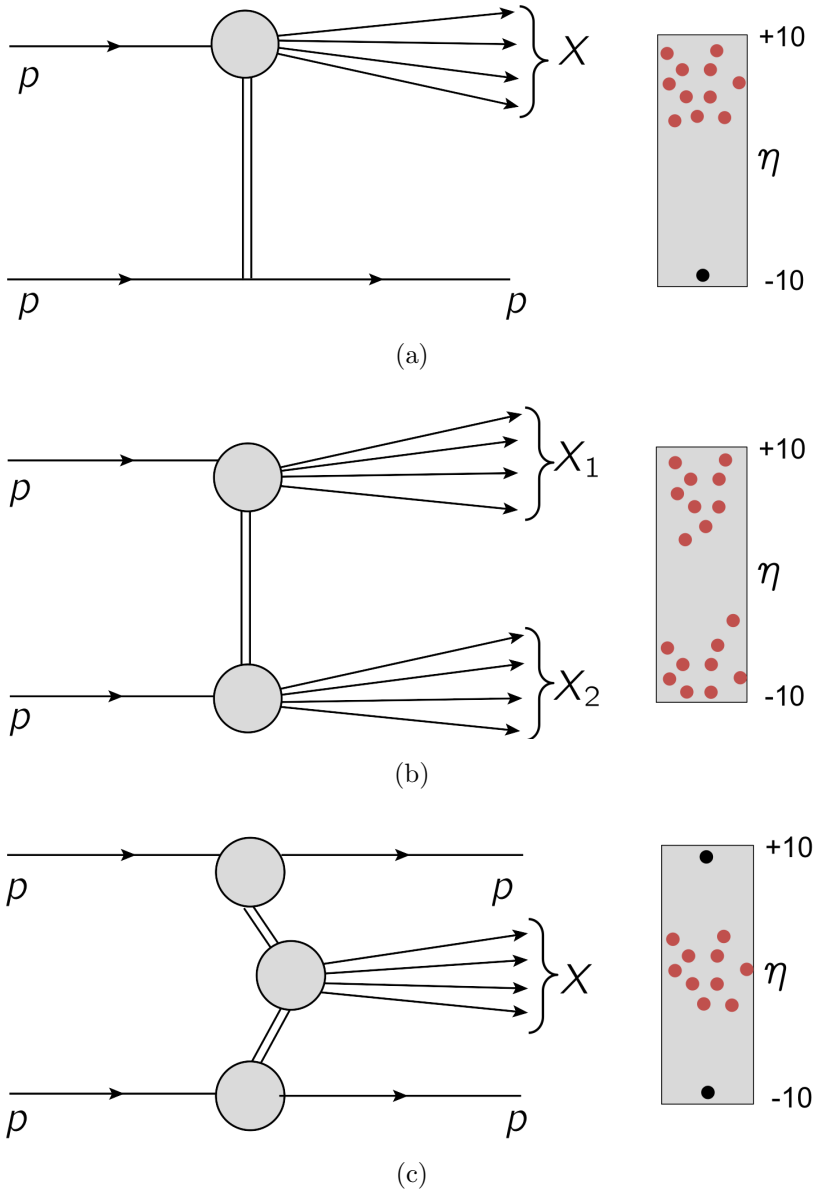

Figure 2.9: Feynman representations of single diffraction (a), double diffraction (b) and central diffraction (c) and their typical topologies along the ϕ coordinate in the detector. Black dots correspond to proton tags. Red dots represent particle hits from a diffractive system.

- In the SD case, one of the incident proton is slightly scattered and exchanges the color singlet which then interacts with a parton from the dissociating proton to form

a diffractive system X with the same quantum numbers as the the proton. A gap is observed between the out-coming proton and X. The interaction and the typical topology of this kind of interaction is depicted on Fig. 2.9a.

- In the DD case, both proton dissociate to form the diffractive systems X_1 and X_2, each with the same quantum numbers as their associate incoming proton. A rapidity gap is observed between X_1 and X_2. The interaction is depicted on Fig. 2.9b.

- In the less probable CD case, both proton are slightly scattered and both exchange Pomerons, whose interaction produces a central diffractive system X. Two rapidity gaps are observed between X and the scattered protons, as depicted on Fig. 2.9c.

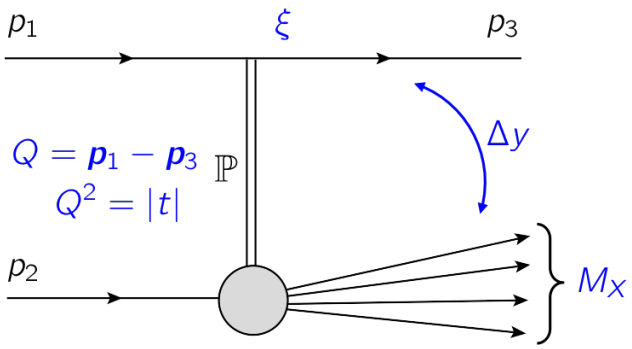

Figure 2.10: Typical kinematic variables used in this thesis to evaluate diffractive events showing the diffractive system of mass M_X and the rapidity gap $\Delta\mathcal{Y}$. Variables are defined in Sect. 2.4.2.

2.4.2 Kinematics of Diffraction

The fractional energy loss ξ, the squared momentum transfer t and the rapidity gap $\Delta\eta$, depicted on Fig. 2.10, are three kinematic variables commonly used in diffraction. Their derivation and interest are presented in the following section.

Fractional proton energy loss

We consider the two-body process $1 + 2 \to 3 + X$, where X denotes a system of particles of invariant mass m_4 and total 4-momentum $\boldsymbol{p_4}$. Using the definition of the Mandelstam variables Eqs. 2.10–2.12, we define $\boldsymbol{p_1}$ and $\boldsymbol{p_2}$ as being the 4-momenta of the two colliding protons. In the center-of-mass frame, we have:

$$\boldsymbol{p_1} = (E_1, \vec{p}) = (E_1, 0, 0, p_z) \tag{2.28}$$

$$\boldsymbol{p_2} = (E_2, -\vec{p}) = (E_2, 0, 0, -p_z) \tag{2.29}$$

$$\boldsymbol{p_3} = (E_3, \vec{p'}) = (E_3, \vec{p'_T}, p'_z) \tag{2.30}$$

$$\boldsymbol{p_4} = (E_4, -\vec{p'}) = (E_4, -\vec{p'_T}, -p'_z) \tag{2.31}$$

where the coordinate system was chosen such that particles 1 and 2 travel along the z axis. The energies E_i with $i = 1, 2, 3, 4$, initial momentum $\vec{p} = (0, 0, p_z)$ and final momentum $\vec{p'} = (\vec{p'_T}, -p'_z)$ -where $\vec{p'_T}$ is a 2D-vector representing the transverse momentum-, are extracted using the definition of Mandelstam s and the fact that particles 1, 2 and 3 are on their mass-shell:

$$E_{1,2,3,4} = \frac{1}{2\sqrt{s}}\left(s + m^2_{1,2,3,4} - m^2_{2,1,4,3}\right) \tag{2.32}$$

$$\begin{aligned} \vec{p}^2 = p_z^2 &= E_1^2 - m_1^2 \\ &= \frac{1}{4s}[s - (m_1 + m_2)^2][s - (m_1 - m_2)^2] \end{aligned} \tag{2.33}$$

$$\begin{aligned} \vec{p'}^2 = \vec{p'_T}^{\,2} + p'^2_z &= E_3^2 - m_3^2 \\ &= \frac{1}{4s}[s - (m_3 + m_4)^2][s - (m_3 - m_4)^2] \end{aligned} \tag{2.34}$$

In the case of proton-proton single diffractive interaction, $m_1 = m_2 = m_3 = m_p \ll \sqrt{s}$ and

$m_4 = M_X \gg m_p$ (see Fig. 2.10). Eqs. 2.32–2.34 simplify:

$$E_{1,2} = \frac{\sqrt{s}}{2}, \tag{2.35}$$

$$|\vec{p}| = \frac{\sqrt{s}}{2} \tag{2.36}$$

$$E_3 = \frac{1}{2\sqrt{s}}(s + m_p^2 - M_X^2) \xrightarrow[M_X \gg m_p]{} \frac{s - M_X^2}{2\sqrt{s}}, \qquad E_4 \xrightarrow[M_X \gg m_p]{} \frac{M_X^2}{2\sqrt{s}} \tag{2.37}$$

$$|\vec{p'}| = \frac{1}{2\sqrt{s}}\sqrt{[s - (m_p + M_X)^2][s - (m_p - M_X)^2]} \xrightarrow[M_X \gg m_p]{} \frac{s - M_X^2}{2\sqrt{s}} \tag{2.38}$$

We then derive the fractional energy loss of the scattered proton:

$$\xi = \frac{E_1 - E_3}{E_1} \xrightarrow[M_X \gg m_p]{} \frac{\frac{\sqrt{s}}{2} - \frac{s - M_X^2}{2\sqrt{s}}}{\frac{\sqrt{s}}{2}} = \frac{M_X^2}{s} \tag{2.39}$$

For high energy proton-proton collisions, the limit $\xi \to 0$ corresponds to the elastic case where there is no diffractive system, and two scattered protons of mass m_p. According to the definition of Good and Walker [54], a diffractive interaction should happen if the following condition between the outgoing and incoming forward momentum of the scattered proton is satisfied:

$$|\Delta p_z| = |p_z - p'_z| < \frac{1}{R} \tag{2.40}$$

where $R = 1$ fm corresponds to the size of the proton. In the limit of a very forwardly scattered proton, we get the following variation:

$$|\Delta p_z| = \frac{s - M_X^2}{2\sqrt{s}} - \frac{\sqrt{s}}{2} = \frac{M_X^2}{2\sqrt{s}} = \frac{\sqrt{s}}{2}\xi < \frac{1}{R} \tag{2.41}$$

which means that $\xi < \frac{2}{R\sqrt{s}} \ll 1$. Thus, diffractive processes correspond to very small values of ξ.

Squared Momentum Transfer

For a single diffractive interaction, t corresponds to the variable Q^2 representing the momentum exchanged by the scattered proton. The squared momentum transfer may be extracted using Eq. 2.11 knowing the initial and final energy and momentum of the scattered proton and its scattering angle θ :

$$\begin{aligned} t &= (\boldsymbol{p_1} - \boldsymbol{p_3})^2 \\ &= \boldsymbol{p_1}^2 + \boldsymbol{p_3}^2 - 2\boldsymbol{p_1}\boldsymbol{p_3} \\ &= m_1^2 + m_3^2 - 2E_1E_3 + 2\vec{p_1}\vec{p_3} \\ &= 2m_p^2 - 2E_1E_3 + 2|p_1||p_3|\cos\theta \end{aligned} \tag{2.42}$$

with θ such that: $p'_T = |\vec{p'}| \cdot \sin\theta$ and $p'_z = |\vec{p'}| \cdot \cos\theta$ with $|\vec{p'}|^2 = |\vec{p'_T}|^2 + p'^2_z$.

In the $M_X \gg m_p$ limit and for a small scattering angle, Eq. 2.42 simplifies into:

$$t = -\frac{s - M_X^2}{2}[1-\cos\theta] \approx -\frac{s - M_X^2}{2}\left[1 - \frac{\theta^2}{2}\right] = -s\frac{[1-\xi]}{2}[1-\frac{p'^2_T}{2p'^2}] = \frac{[1-\xi]}{2}\left[\frac{2p'^2_T}{[1-\xi]^2} - s\right] \tag{2.43}$$

The transverse momentum of the scattered proton in a forward detector is therefore linked to the 4-momentum transfer of the interaction. This formula also shows that ξ can easily be extracted if t was reconstructed and the scattered proton p'_T is known.

Rapidity Gap

We define the rapidity of particle i in the approximation of a very forward particle, $E_i \approx p_z^i$ and $0 < p_z^i \to \infty$:

$$\mathcal{Y}_i = \frac{1}{2}\ln\frac{E_i + P_z^i}{E_i - p_z^i} = \ln\frac{(E_i + p_z^i)^2}{E_i^2 - {p_z^i}^2} = \ln\frac{E_i + p_z^i}{\sqrt{m_i^2 + {p_T^i}^2}} \approx \ln\frac{2p_z^i}{\sqrt{m_i^2 + {p_T^i}^2}} \tag{2.44}$$

For the scattered proton, the maximum rapidity is reached when p'_z takes all the available momentum: $p'_z = |\vec{p'}|$, which means $|\vec{p'_T}| = 0$. In this case:

$$\mathcal{Y}_3^{\max} = \ln \frac{\sqrt{s}}{m_p} \tag{2.45}$$

Similarly, the upper bound in rapidity for the diffractive system is reached in the extreme case where only one particle is produced and carries all the momentum (elastic case):

$$\mathcal{Y}_X^{\max} = \ln \frac{\sqrt{s}}{m_p} \tag{2.46}$$

On the other hand, the minimum rapidity value of a particle in the diffractive system corresponds to the case where all the particles produced in the diffractive system share the momentum equally. Assuming that these particles have a typical mass m, they will have a transverse momentum proportional to the ratio of their mass to the invariant mass of the system: $p_z = (m/M_X)\sqrt{s}$. In such a way, the total momentum along z is minimal but Eq. 2.44 is still valid. The lowest rapidity is achieved when the transverse momentum is maximal i.e. $p_T^2 + m^2 \approx M_X^2$. In this case:

$$\mathcal{Y}_X^{\min} \approx \ln \frac{m\sqrt{s}}{M_X^2} \tag{2.47}$$

The rapidity gap corresponds to the span in rapidity between the scattered proton and the particle from the diffractive system the closest to it. It can be expressed by comparing Eq. 2.47 with Eq. 2.45:

$$\Delta\mathcal{Y} = \mathcal{Y}_3^{\max} - \mathcal{Y}_X^{\min} \approx \ln \frac{s}{M_X^2} \approx -\ln \xi \tag{2.48}$$

Therefore, since diffractive processes are associated with small values of ξ, they will exhibit large rapidity gaps.

2.5 Modelling Diffraction

In Sects. 2.1–2.3 were presented several approaches used to model diffraction and explain the energy variation of the total pp cross section, would it be a resolvable Pomeron with renormalized Pomeron fluxes or not, assuming a constant or a dynamical rapidity gap survival probability or even considering only soft color interaction reshuffling without introducing any Pomeron dynamics. These alternatives should not be mutually exclusive as they can represent different aspects of the correct underlying physics, which is still not understood from first principles.

By simulating interaction processes and the detection of the associate final states, Monte Carlo generators are extremely useful to assess the quality of a given model. In this section, we discuss the steps leading to the generation of final state particles with a diffractive signature for various kinematic configurations. We focus on the features available in Pythia8 [55, 56], the general purpose generator used for the analysis of single diffractive events (see Chapter 4), as well as the ones available in the Forward Physics Monte Carlo (FPMC) [57], the Herwig [58]-based forward-physics dedicated generator used for the study of single diffractive W production (see Chapter 5). Details about how the detector response is simulated and how this information is interpreted are given in Chapter 3.

Typically, somebody willing to generate a set of diffractive events would have to consider the following points, which are addressed in detail in the next sections:

- If the sample to generate is fully inclusive, which means it contains all the diffractive contributions, the total, elastic and diffractive cross sections should be set according

to a given parameterization,

- To model the physics at low mass where perturbative-QCD is not an option, an empirical model should be picked,

- In the regime of semi-hard to hard diffraction, one must choose a theory for parton-parton interactions, and decide how the physics of multi-parton is handled.

Other crucial but more general aspects of Monte Carlo generation such as parton showers and their matching to the matrix elements as well as hadronization techniques are briefly discussed in Sect. 2.5.5.

2.5.1 Parameterizing the Cross Sections

When generating an inclusive sample, the fraction of each component to the total cross section should be specified. General purpose generators such as PYTHIA8 typically takes the expected cross sections for elastic, diffractive and total pp interactions from which it deduces the non-diffractive component.

Cross sections are parameterized from fits to various data using effective models. Ideally, such models should respect the s and t channel unitarity constraints and be valid up to the limit of infinite energies. However, to avoid dealing with a highly complex formalism, most parameterizations are valid only in a certain kinematic range.

The total cross section typically takes the form of a sum of powers of center-of-mass s (see Sect. 2.1.3) including a high and a low energy contributions derived from Regge theory. The elastic cross section is derived from the total cross section by invoking the optical

theorem [18]. Knowing the total and elastic cross section from the fits, the inelastic cross section is deduced by a simple subtraction:

$$\sigma_{\text{inel}}(s) = \sigma_{\text{tot}}(s) - \sigma_{\text{el}}(s) \tag{2.49}$$

There is no definitive description that would freeze the breakdown of the diffractive contributions inside the inelastic cross section however. The predictions are not well constrained since they are very sensitive to the way diffractive interactions are treated in the theory, and the limited amount of diffractive data does not allow to favour one models over the others. We discuss two alternative treatments of the diffractive interactions: the default Schuler and Sjöstrand (SaS) parameterization and the Minimum Bias Rockefeller (MBR). Disregarding the diffractive model used, the non diffractive contribution is always calculated as:

$$\sigma_{\text{ND}}(s) = \sigma_{\text{inel}}(s) - (\sigma_{\text{SD}} + \sigma_{\text{DD}} + \sigma_{\text{CD}}) \tag{2.50}$$

The Schuler and Sjöstrand model

This model [59] is what defines the cross sections by default in Pythia8. We use the predictions from this model to perform the analysis of Chapter 4. It assumes the total cross section follows the 1992 Donnachie-Landshoff description [60] which includes a Pomeron and a Reggeon contribution determined by fitting $p^{\pm}p$ data:

$$\sigma_{\text{tot}}(s) = (21.70 s^{0.0808} + 56.08 s^{-0.4545}) \text{ mb}, \tag{2.51}$$

with s expressed in GeV^2. In this model, the elastic cross section in Pythia8 is described by an exponential falloff valid in the small t range and related to the total cross section via the optical theorem:

$$\frac{d\sigma_{\text{el}}}{dt} = \frac{(\sigma_{\text{tot}})^2}{16\pi} e^{B_{\text{el}}(s)t}, \tag{2.52}$$

giving the following expression after integration: $\sigma_{\text{el}} = \frac{(\sigma_{\text{tot}})^2}{16\pi B_{\text{el}}(s)}$ where

$B_{\mathrm{el}}(s) = 5 + 4s^{0.0808}$ is the pp elastic slope in GeV^{-2}.

This model assumes the following expression for the single and double diffractive pp cross sections:

$$\frac{d^2\sigma_{\mathrm{SD}}(s)}{dtd\xi} = \frac{g_{3\mathbb{P}}}{16\pi}\frac{\beta^3_{p\mathbb{P}}(0)}{\xi}F_{\mathrm{SD}}(\xi)e^{B_{\mathrm{SD}}t} \tag{2.53}$$

$$\frac{d^3\sigma_{\mathrm{DD}}(s)}{dtd\xi_1 d\xi_2} = \frac{g_{3\mathbb{P}}}{16\pi}\frac{\beta^3_{p\mathbb{P}}(0)}{\xi_1\xi_2}F_{\mathrm{DD}}(\xi_1,\xi_2)e^{B_{\mathrm{DD}}t} \tag{2.54}$$

where the ξ's are the fractionnal momentum losses of the scattered protons, $g_{3\mathbb{P}}$ represents the triple Pomeron coupling shown on Fig. 2.7 and $\beta_{p\mathbb{P}}(0)$ is the Pomeron-proton coupling, which can be obtained from the analysis of the total cross section. B_{SD} and B_{DD} are mass- and energy-dependent slopes, and F_{SD} and F_{DD} are fudge factors allowing to extend the formula to the full phase-space. These fudge factors are defined with respect to arbitrary mass scales as detailed in [61].

The total diffractive cross sections are obtained by integrating Eqs. 2.53–2.54 over the full phase space. The results have been parameterized for pp interactions as a function of the center-of-mass energy [59]. The typical behaviour observed is:

$$\sigma_{\mathrm{SD}} \propto \ln(\ln(s)) \tag{2.55}$$

$$\sigma_{\mathrm{DD}} \propto \ln(s)\cdot\ln(\ln(s)) \tag{2.56}$$

The central-diffractive component was added later [55] on and is parameterized according to the following scaling assumption:

$$\sigma_{\mathrm{CD}}(s) = \sigma_{\mathrm{CD}}(s_{\mathrm{ref}})\left(\frac{\ln(0.06\ s/s_0)}{\ln(0.06\ s_{\mathrm{ref}}/s_0)}\right)^{3/2} \tag{2.57}$$

where $\sqrt{s_0} = 1$ TeV and $\sigma_{\mathrm{CD}}(s_{\mathrm{ref}})$ is the cross section at the reference energy $\sqrt{s_{\mathrm{ref}}} = 2$ TeV. Since the Pomeron exchange occurs on both proton sides, the spectrum in terms of $t_{1,2}$ and

$\xi_{1,2}$, the transferred momenta squared and proton fractional energy losses, can be described using a convolution of two single diffractive functions:

$$\frac{d\sigma_{\mathrm{CD}}(s)}{dt_1 dt_2 d\xi_1 d\xi_2} \propto \frac{1}{\xi_1 \xi_2} e^{B_{\mathrm{SD}} t_1} e^{B_{\mathrm{SD}} t_2} \tag{2.58}$$

with a central diffractive mass $M_X = \sqrt{\xi_1 \xi_2 s}$.

All cross sections exhibit an exponential dependance in t and an explicit inverse diffractive mass squared dependance counterbalanced in some regions of phase space by the mass dependance of the diffractive slopes and the fudge factors.

This model is not unitary which means that it could violate the Froissart-Martin bound even if this happens in an energy regime not reached by current scattering experiments.

The Minimum Bias Rockefeller model (MBR)

In this model, also available as an option in PYTHIA8, $\sigma_{\mathrm{tot}}(s)$ takes a different form depending on the energy regime:

$$\sigma_{\mathrm{tot}}(s) = \begin{cases} 16.79 s^{0.104} + 60.81 s^{-0.32} - 31.68 s^{-0.54}, & \text{for } \sqrt{s} < 1.8 \text{ TeV} \\ \sigma_{\mathrm{tot}}^{\mathrm{CDF}} + \frac{\pi}{s_0} \left[\left(\ln \frac{s}{s_F} \right)^2 - \left(\ln \frac{s^{\mathrm{CDF}}}{s_F} \right)^2 \right], & \text{for } \sqrt{s} \geq 1.8 \text{ TeV} \end{cases} \tag{2.59}$$

where $\sigma_{\mathrm{tot}}^{\mathrm{CDF}}$ is the total cross section measured by the CDF experiment and s^{CDF} the associate center-of-mass energy squared. The term for $\sqrt{s} < 1.8$ TeV is obtained from a global Regge-theory fit to pre-LHC data using $p^{\pm}p$, $K^{\pm}p$ and $\pi^{\pm}p$ cross sections [62]. For $\sqrt{s} \geq 1.8$ TeV, it uses a prediction of a unitarized model based on a saturated Froissard bound [63]. This model depends on two parameters: a scale parameter s_0, and a saturation s-values, s_F, above which the Froissart bound is reached. The interested reader may find more details about the MBR unitarization procedure in the literature, e.g. [63].

The elastic cross section for $\sqrt{s} \geq 1.8$ TeV is extracted by scaling σ_{tot} to the ratio of the elastic to total cross section obtained from the global fit performed at lower energy.

The diffractive differential cross sections are calculated using the renormalized model discussed in [64] assuming a supercritical Pomeron ($\epsilon > 0$). They are based on renormalized versions of Eqs. 2.53–2.57. For readability, the cross sections are usually expressed in terms of the kinematics of the rapidity gaps(s) using the fact that $\xi \approx e^{-\Delta\eta}$, $\xi_{\text{SD}} = M_X^2/s$, $\xi_{\text{DD}} = (M_1^2 M_2)(s \cdot s_0)$ and $\xi_{\text{CD}} = \xi_1\xi_2 = M_X^2/s$:

$$\frac{d^2\sigma_{\text{SD}}}{dtd\Delta\eta} = \frac{1}{N_{\text{norm}}(s)} \left[\frac{\beta_{p\mathbb{P}}^2(t)}{16\pi} e^{2[\alpha(t)-1]\Delta\eta}\right] \cdot \left\{\kappa\beta_{p\mathbb{P}}^2(0) \left(\frac{s'}{s_0}\right)^{\epsilon}\right\}, \tag{2.60}$$

$$\frac{d^2\sigma_{\text{DD}}}{dtd\Delta\eta d\eta_0} = \frac{1}{N_{\text{norm}}(s)} \left[\kappa\frac{\beta_{p\mathbb{P}}^2(0)}{16\pi} e^{2[\alpha(t)-1]\Delta\eta}\right] \cdot \left\{\kappa\beta_{p\mathbb{P}}^2(0) \left(\frac{s'}{s_0}\right)^{\epsilon}\right\}, \tag{2.61}$$

$$\frac{d^2\sigma_{\text{CD}}}{dt_1dt_2d\Delta\ \eta d\eta_c} = \frac{1}{N_{\text{norm}}(s)} \left[\Pi_i \left(\frac{\beta_{p\mathbb{P}}^2(t_i)}{16\pi} e^{2[\alpha(t_i)-1]\Delta\eta_i}\right)\right] \cdot \kappa \left\{\kappa\beta_{p\mathbb{P}}^2(0) \left(\frac{s'}{s_0}\right)^{\epsilon}\right\}, \tag{2.62}$$

where t is the square of the four-momentum-transfer, $\Delta\eta$ is the rapidity gap, $\beta_{p\mathbb{P}}$ is describing the Pomeron-proton coupling and κ is the ratio of the triple-Pomeron to the proton-Pomeron coupling. For central diffraction, the subscript $i = 1, 2$ enumerates the Pomerons since it involves a double Pomeron exchange, and the rapidity gap is defined as the sum of both gaps $\Delta\eta = \Delta\eta_1 + \Delta\eta_2$. η_c is the center in η of the centrally-produced hadronic system. For double diffraction, the variable y_0 is the center of the rapidity gap.

Practically, the term in squared brackets in Eq. 2.60 is the analogue to the Pomeron flux. It is renormalized with the parameter $N_{\text{norm}}(s)$. With this renormalization procedure, the Pomeron flux can be interpreted as the probability for a diffractive gap to form. On the other hand, the part in curly brackets corresponds to the effective total cross section of the Pomeron-proton system at a reduced energy s'. More details, in particular on how the

parameter s_0 and κ are determined, are given in [65].

2.5.2 Modeling Soft Diffraction

Soft diffraction corresponds to the case where there is no hard scale. For such events with a low transverse momentum and low mass diffractive system, it is not possible to resolve the Pomeron by means of the factorization theorem and all descriptions are based on effective interpretations. The collision is understood by means of string theory. A Pomeron kicks out either a valence quark or a gluon from the diffractively excited proton which will form a string from the diquark remnant. The probability for the Pomeron to interact with either a quark or a gluon depends on the mass of the diffractive system, such that larger mass systems are mostly produced through Pomeron-gluon interaction. PYTHIA8 does not implement further Multi-Parton Interactions (MPI) in this low-p_T regime. The strings are simply hadronised using the Lund fragmentation model [66].

2.5.3 Modelling Semi-Hard Diffraction

In the high-mass regime, $M_X > 10$ GeV, energies are high enough to make use of perturbation theory. In this regime PYTHIA8 considers the Pomeron as a hadronic state, and the diffractive system can be described as a hadron-hadron collision at a reduced energy. In most models, the Reggeon contribution is neglected and only the PDFs and the flux of the Pomeron have to be defined (see Sect. 2.2.2). This section presents the set of flux and PDFs available in the two Monte-Carlo generators used in this thesis.

Choice of Pomeron Flux

The Pomeron flux parameterization is what will define the mass of the diffractive system(s) and the typical t of the exchanged Pomeron.

Schuler and Sjöstrand Parameterization (SaS flux) This model is the default Pomeron flux available in PYTHIA8. It is based on a critical Pomeron with $\epsilon = 0$ and $\alpha' = 0.25$ GeV^{-2} in Eq. 2.21:

$$\phi_{\mathbb{P}}(\xi, t) = \frac{1}{\xi}\beta^2_{p\mathbb{P}}(0)e^{2t\left[2.3+0.25\ln(\frac{1}{\xi})\right]} \tag{2.63}$$

This gives a typical dM_X^2/M_X^2 mass spectrum and a mass-dependent exponential t-slope.

Donnachie-Landshoff Parameterization (DL flux) This model is based on a super-critical Pomeron with $\epsilon > 0$ with default value in PYTHIA8: $\epsilon = 0.085$ and $\alpha'_{\mathbb{P}} = 0.25$. It assumes a power law in ξ:

$$\phi_{\mathbb{P}}(\xi, t) = \frac{9\beta^2_{p\mathbb{P}}(0)}{4\pi^2}\xi^{1-2\alpha_{\mathbb{P}}(t)}\left[F_1(t)\right]^2 \tag{2.64}$$

where $F_1(t)$ is the elastic from factor that takes account of the proton wave function. $F_1(t)$ is well parameterized as:

$$F_1(t) = \frac{4m_p^2 - 2.8t}{4m_p^2 - t}\frac{1}{(1 - \frac{t}{0.7})^2} \tag{2.65}$$

This model gives a stronger peaking towards low-mass diffractive states.

Minimum Bias Rockefeller Renormalized Model (MBR flux) This model follows the prescriptions to have a flux renormalized to unity to cope with the Martin-Froissart bound. The Pomeron parameterization is very similar to the one from Donnachie-Landshoff but the Pomeron intercept is larger with $\epsilon = 0.104$ and $\alpha'_{\mathbb{P}} = 0.25$:

$$\phi_{\mathbb{P}}(\xi, t) = \frac{1}{N_{\text{norm}}(s)}\frac{\beta^2_{p\mathbb{P}}(0)}{16\pi^2}\xi^{1-2\alpha_{\mathbb{P}}(t)}[F_1(t)]^2$$

N_{norm} is defined such that $\int\int \phi(\xi, t)d\xi dt = 1$ with integration limits defined in [64]. For the form factor, Eq. 2.65 is used.

Pomeron fluxes from HERA Fits A and B (H1 Fit A/B) These models use fits to the DDIS data from the H1 experiment [40, 41]. The typical DPDF takes the following form:

$$\mathcal{F}_{\mathbb{P}+\mathbb{R}/p}(\xi, Q^2) = f_{\mathbb{P}/p}(Q^2) \cdot \phi_{\mathbb{P}}(\xi) + n_{\mathbb{R}} \cdot f_{\mathbb{R}/p}(Q^2) \cdot \phi_{\mathbb{R}}(\xi) \tag{2.66}$$

The Pomeron and Reggeon fluxes have a typical Donnaschie-Landshoff behaviour:

$$\phi_{\mathbb{P}/\mathbb{R}}(\xi, t) = \mathcal{A}_{\mathbb{P}/\mathbb{R}} \cdot \xi^{1-2\alpha_{\mathbb{P}/\mathbb{R}}(t)} e^{B_{\mathbb{P}/\mathbb{R}} t} \tag{2.67}$$

The terms $\mathcal{A}_{\mathbb{P}/\mathbb{R}}$ are chosen such that $\xi \int \phi_{\mathbb{P}/\mathbb{R}}(t)dt = 1$ at $\xi = 0.003$ over the full kinematic t range available. The PDF of the Reggeon is taken to be the PDF of a pion by default as being one of the pole of the Regge trajectory. $n_{\mathbb{R}}$, the Pomeron intercept and the parameters defining the Pomeron PDF, are free parameters of the fit. The Reggeon trajectory and slope are fixed.

Fit A and B differ by the parameterization assumed for the Pomeron PDFs [10] discussed in the next subsection. Each parameterization yields slightly different Pomeron intercepts since the DPDFs are convolutions of the PDFs with the flux : $\alpha_{\mathbb{P}}^{\text{Fit A}}(0) = 1.118 \pm 0.008$ and $\alpha_{\mathbb{P}}^{\text{Fit B}}(0) = 1.111 \pm 0.007$.

The SaS and Donnachie-Landshoff (DL) models were used in the analysis of inclusive single-diffractive events in ATLAS presented in Chapter 4. The HERA fit fluxes were used to model the Pomeron in FPMC for the diffractive W study discussed in Chapter 5. The other fluxes available are not detailed since they were not used for the work presented in this thesis. We show on Fig. 2.11 the typical ξ distributions from the available models. We note the large sensitivity to the choice of Pomeron flux, especially in the low and large ξ region. The low

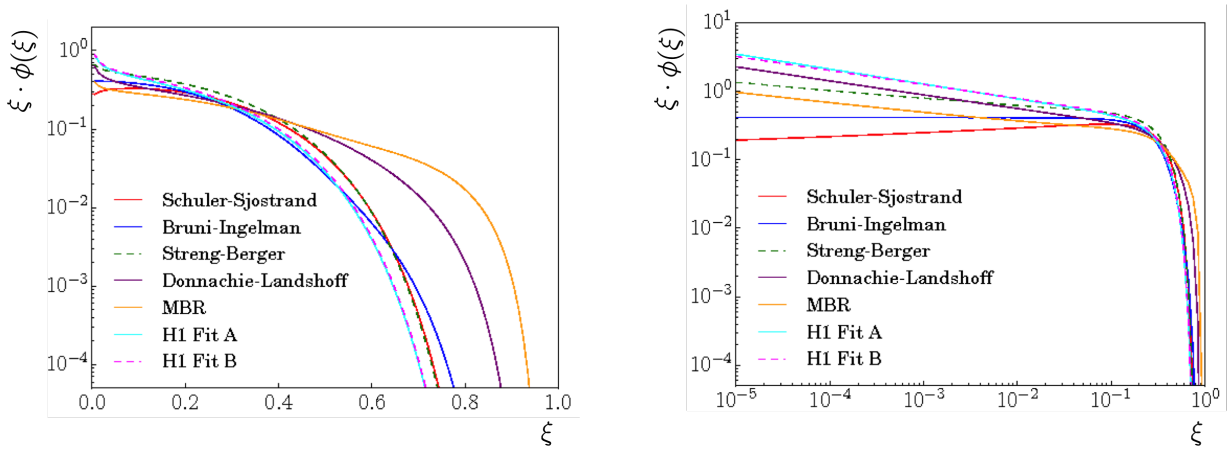

Figure 2.11: Typical kinematics of seven different Pomeron fluxes on linear (a) and log scale (b). The MBR flux has not been renormalized to allow a sensible comparison.

ξ regions directly ties up to the value of the Pomeron intercept. However, the differences observed at large ξ should be considered carefully since this kinematic region should mostly be populated by non-diffractive events.

Choice of Pomeron PDFs

Several parameterizations exist for the Pomeron PDFs. We focus on the one used in this thesis: the H1 2006 Fit B LO. This set is the default implemented in PYTHIA8 and FPMC. We discuss other alternatives and justify our choice afterwards.

Fit constraints For the two studies presented in this thesis, the H1 2006 Fit B LO DPDFs were used. They were extracted from data from the H1 experiment at HERA. For a given energy Q_0^2, the Pomeron quark and gluon PDFs should have the following form, z being the

longitudinal momentum fraction of the parton entering the hard sub-process:

$$z f_g(z, Q_0^2) = A_g z^{B_g} \tag{2.68}$$

$$z f_q(z, Q_0^2) = A_q z^{B_q} (1 - z)^{C_q} \tag{2.69}$$

where g and q indices stand for gluon and quark respectively, and A_g, B_g, A_q, B_q and C_q are the free parameters from the fit above-mentioned. The PDFs are evolved to the energy of interest by means of the Dokchizer, Gribov, Lipatov, Altarelli, Parisi (DGLAP) equations [28]. In this case, the DGLAP evolution is performed at Leading Order (LO) only, but Next-to-Leading Order (NLO) calculations exist [67].

About the DGLAP evolution equations...

The PDFs depend on the factorization scale μ_F being chosen by the groups performing the fit to the data (e.g. NNPDF, MSTW, CTEQ collaborations). In analogy with the renormalization of the strong coupling, one can vary the factorization scale and get a normalization group equation for parton distributions. The equations (DGLAP) driving this evolution were formulated in 1970.

The evolution of a quark density with respect to the energy scale is described by evaluating the probabilities of real or virtual gluon emissions within a change of scale ($\mu^2 \to \mu^2 + \delta\mu^2$). At leading order, only the simple emissions are considered. To go to higher orders, further corrections should be added, which require complex calculations. The emission probabilities, the splitting functions, are the backbone of the renormalization group equations. The precision at which they are calculated is what defines the evolution of the PDFs with the energy scale, up to leading order, next-to-leading order or even next-to-next-to-leading order.

The choice of a set of LO PDFs was justified by the fact that PYTHIA8 only contains LO matrix elements for QCD processes, so there is no point in having such a high precision for the PDFs. Furthermore, for the type of physics regime considered, small x_p and rather small Q^2, the gluon PDF of the proton is known to be smaller when calculated at NLO than at LO. This is to compensate the fact that the NLO corrections to the LO matrix elements are positive in this region. However, it is not obvious how such a compensation should be handled in the context of a Pomeron-proton interaction. For these two reasons, it was chosen to use LO PDFs only for both Pomeron and proton.

Other PDFs Many other alternatives exist to the model we just presented. Most of them are NLO which make them less well suited for the purpose of simulating diffraction.

- **H1 2006 Fit B NLO** [10]: Based on a tune to HERA H1 data. Same PDF parameterization as H1 2006 Fit B LO, but the splitting functions includes NLO corrections
- **H1 2006 Fit A LO/NLO** [10]: Based on a tune to HERA H1 data. The PDF parameterization is different from Fit B. LO and NLO calculations available.
- **ACTW B/D/SG NLO 0.14** [68]: Based on a tune to H1 and ZEUS data. Three different PDF parameterizations (B, D and SG) with $\alpha_{\mathbb{P}} = 1.14$. NLO only.
- **ACTW D NLO 0.19** [68]: Based on a tune to H1 and ZEUS data. With $\alpha_{\mathbb{P}} = 1.19$. NLO only.

Studies using PYTHIA8 showed that the diffractive cross sections seemed to be less sensitive to the choice of PDF than it is to the Pomeron flux. However, the PDF sets currently available all include the same data and correlated assumptions for the definition of diffractive events. In the end, a more relevant quantity is the convolution of the Pomeron PDFs with the flux.

Fig. 2.12 shows the typical behaviour of such quantity for a few specific combinations of flux and PDF.

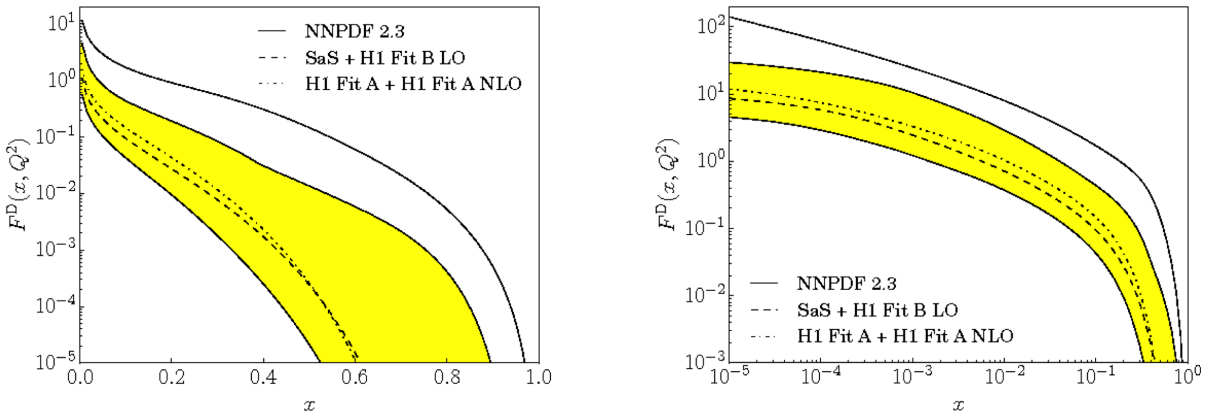

(a) (b)

Figure 2.12: Constructed structure function in linear scale (a) and log scale (b) for different combinations of Pomeron flux and PDFs, compared to the proton PDF from NNPDF 2.3. The yellow band shows the spread between the extreme combination cases.

2.5.4 Effects of Soft Parton Rescattering

Rapidity gaps are typical signatures expected from diffractive interactions and the cross section for such events should agree with theoretical predictions, provided that the factorization theorem stands for semi-hard interactions. However, as mentioned in Sect. 2.2.2, a strong disagreement was observed for high energy collisions, the cross section for such gaps being highly suppressed.

This can be explained by the fact that, in pp collisions, such a gap would often be spoiled by particles from spectator parton interactions. If some colour connexion is created between the scattered proton and the rest of the system, the rapidity gap would then be filled by emissions (see Fig. 2.13a). If this happens between the partons of the diffractive system, then

it will only change its internal properties without affecting the rapidity gap (see Fig. 2.13b). In any case, MPI would affect mostly high Q^2 collisions where their probability to happen is increased.

In the following section, we detail the procedures developed to model colour flows between the diffractive system and the scattered proton and inside the diffractive system itself.

MPI Screening in the Rapidity Gap Space

Phenomenological Approach One may consider that the hard process occurs on a short enough timescale, such that the physics responsible for the additional interactions can be factorized into a single term regrouping all soft to semi-soft effects. This approach is implemented in FPMC where the diffractive cross sections are normalized by a factor (`SURV`) manually set by the user. By default, the value for this gap survival probability is set to 0.03 [69]. It should encompass all the physics of soft colour connexions and its value should be adjusted depending on the energy considered.

MPI-based Categorization The survival probability may also be calculated dynamically. This approach is now available as an addition to the standard Pythia8 treatment of diffraction and is particularly suited for the generation of diffractively-produced hard states. In this case, one first fully applies the MPI artillery to the whole system. Then, only the events that did not undergo any MPI between the two incoming protons are kept as being truly diffractive. For those events, the $p\mathbb{P}$ system is set and the hard parton-parton interaction is allowed to take place. The bare hard process can then be dressed with radiations and internal MPI may occur, just like for non-diffractive systems.

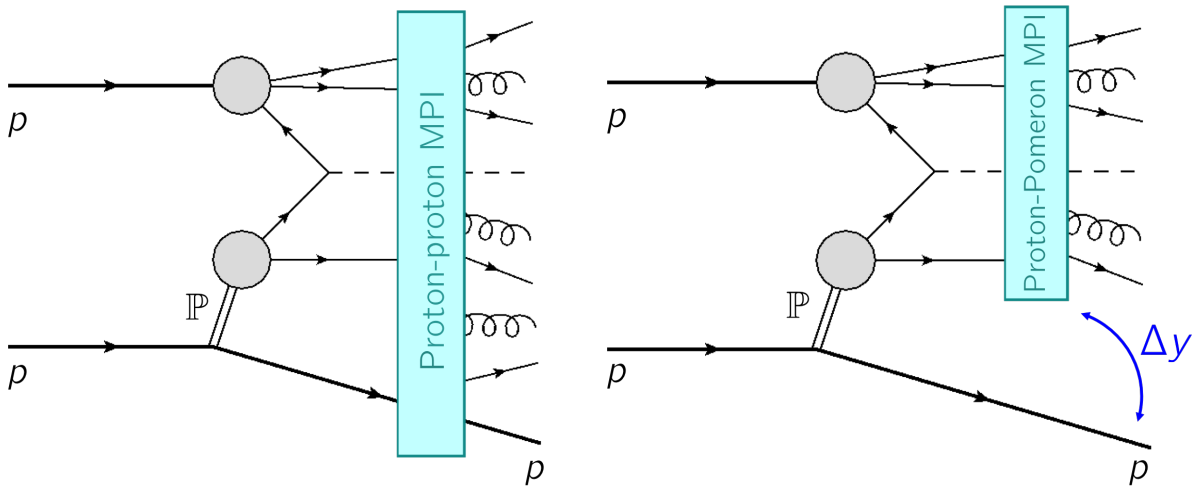

Figure 2.13: The effect of MPI when applied over the full Feynman diagram for hard diffraction (a) or only within the diffractive system (b). In case (a), colour connexions with the scattered proton fill the gap. In case (b), the gap is maintained.

MPI inside the Diffractive System

In Pythia8, the IS model is assumed, which makes the bold assumption that only one Pomeron is exchanged per hadron-hadron collision, not the multiple ones expected in Regge theory. However, since hadrons are composite objects, and provided that the Pomeron is a hadronic state, the possibility for several other partons interactions to happen in addition to the semi-hard parton-parton scattering itself is not to be neglected.

Once a hard enough subprocess is defined as being diffractive, should it be using an MPI-based categorization or not, the hard process can occur. The system is set in the same way as a for a non diffractive process, but the energy at which the hard interaction takes place is reduced since one of the incoming partons comes from the Pomeron. The hard process can be dressed with initial and final state gluon emission using the techniques described in [56]

and in Sect. 2.5.5. The way MPI are handled is a bit different however. In particular it requires to provide an ansatz on the total $p\mathbb{P}$ cross section, which is poorly constrained at the moment. More details may be found in [55].

2.5.5 Monte Carlo Methods

Just like for non-diffractive event generation, models should be picked to define the steps to go from the hard parton-parton interaction to the final state hadrons observed in the detectors. The procedure is usually split in three main steps, illustrated in Fig. 2.14, which are sometimes performed by separate generators:

1. **Hard subprocess setup:** The PDFs and DPDFs are evolved up to the scale of the hard process by means of the DGLAP equations. The matrix elements give the differential cross section of that hard parton-parton interaction (dark red blob on Fig. 2.14). The convolution of the matrix elements with the PDFs and DPDFs gives the total cross section of the hard process once integrated over phase-space. The Monte Carlo method [70] is used to sample the convolution of these variables. This sampling is what will define which final state partons will be produced at the first generation level.

2. **Parton Shower:** Any incoming or outgoing object of the hard subprocess will be eligible for parton showering. Accelerated coloured partons emit QCD radiations in the forms of gluons. When emitted by an incoming parton, those are referred to as the already mentioned ISR. Gluon emission in the final state are termed Final-State Radiation (FSR). The FSR process corresponds to the red branchings on Fig. 2.14. The emitted gluons carry colour charges and can therefore emit further radiations, leading to parton showers. In theory, the probability of such emissions corresponds to correction to the hard subprocess matrix elements, but these corrections are not computable.

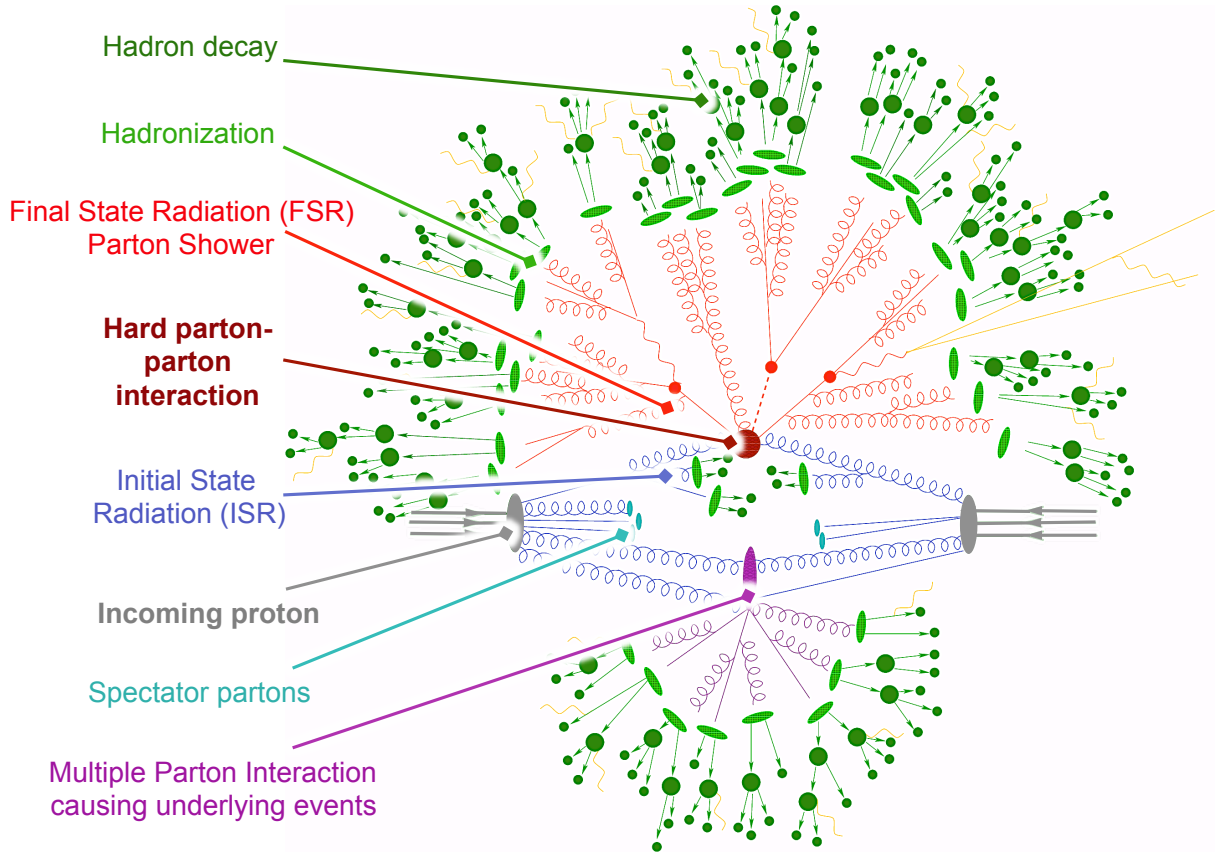

Figure 2.14: Sketch of a hadron-hadron collision as simulated by a Monte Carlo event generator.

One way to treat this problem is to consider only the dominant contributions. These contributions are calculated using *splitting functions*. For each successive emission, the splitting function is sampled using the Monte Carlo method to pick the kinematics of the emission products until the emitted partons reach their mass shell or until the emission angle becomes too small. This approximation is typically used in HERWIG assuming angular ordered emissions. Another approximation, used in PYTHIA8, is based on the concept of dipole showering. In this approach, gluon emission is generated not by splitting a parton but according to the dipole radiation pattern of a pair of partons. When the dipole split, it emits a gluon and two dipoles are formed, which

split again, and so on until some minimum scale of dipole mass or relative transverse momentum is reached. Before getting hadronized, spectator partons are allowed to interact: this corresponds to the MPI effect discussed in Sect. 2.5.4. An example of MPI is represented by the purple blob on Fig. 2.14.

3. **Hadronization:** Due to confinement, when increasing the distance between to coloured objects, the colour field energy, often described as a *string tension*, increases rapidly. When this energy becomes greater than the rest mass of a quark-antiquark pair, this pair is created and the string breaks in two. The process goes on and on until the final state hadrons are created (light green blobs on Fig. 2.14). Those hadrons are then allowed to decay. Different assumptions on the evolution of the colour structure are made, which lead to hadronization models. The most common ones are the Lund string model used by PYTHIA8 and the clustering model used in HERWIG. These models are detailed in [28].

2.5.6 Monte Carlo Tuning

Hadronization and multiple parton interactions involve non-perturbative QCD physics and are therefore driven by empirical parameters which may be correlated to each others. Hence the need to tune the simulation for a given set of parameters. Several ATLAS tunes are available in PYTHIA8, obtained with different PDFs and with different emphasis on minimum-bias and underlying-event data [55].

Experimental Setup

As highlighted in the previous chapters, there is a strong interest in using high energy accelerators as a probe for the physics of diffractive interactions. Both studies presented in this thesis make use or foresee the usage of the LHC to accelerate proton bunches at extremely high energies. The two beams meet to collide at the so called *Point 1* (P1) Interaction Point (IP) where the ATLAS detector is housed. The products of the collisions propagate through space to reach the dedicated sub-detectors. Scattered hadrons may travel along the beam pipe to be detected by forward installations.

In this chapter, the LHC design and the typical features required to accelerate, maintain and collide proton bunches in the conditions required for diffraction (Sect. 3.1) are discussed. An overview of the ATLAS detector and the way it collects signals and process them is given. The focus is on the sub-detectors used to measure the particles from the diffractive system (Sect. 3.2.1), and to detect forward protons, specifically the ALFA and AFP detectors (Sect. 3.2.2). The second part of the chapter details the data acquisition principles giving details on the specific triggers used for diffraction studies. Finally, the process through which datasets are distributed to analysis teams is presented. The design of the LHC experiments, from detectors to datasets treatment, is not set in stone. Since 2008, many upgrades were implemented to improve the overall quality of data, its acquisition and distribution. A sub-

stantial part of this chapter is based on [71] and [72] which are snapshots of the installations at the time they were put in place.

3.1 The Large Hadron Collider

The *Conseil Européen pour la Recherche Nucléaire* (CERN), established in 1954, is the world's largest organization for particle physics research. Its institutions are based in the vicinity of Geneva, Switzerland, across the border between France and Switzerland. CERN currently comprised 22 full member states and maintains varying levels of relations with numerous other nations. Its primary focus is the development, construction and operation of particle colliders, of which, the LHC is the current leading representative.

The LHC is a two-ring superconducting hadron accelerator and collider. It is installed in the 26.7 km circumference tunnel originally constructed for the Large Electron-Position collider (LEP), which operated between 1989 and 2000. The LHC was designed to accelerate two counter-rotating beams of protons up to an energy of 7 TeV per proton which represents a center-of-mass energy at collision of $\sqrt{s} = 14$ TeV. The LHC is also used for proton-lead, lead-lead and xenon-xenon ion collisions. The LHC supports four independent experimental collaborations: ALICE, ATLAS, CMS and LHCb. The ring is broken up into octants, numbered in clockwise order (see Fig. 3.1). Beams meet in P1, the hosting site of the ATLAS experiment. Other interactions points are set in three of the remaining octants where A Large Ions Collider Experiment (ALICE) - octant 2 -, the Compact Muon Solenoid (CMS) - octant 5 - and LHCb - octant 8 - experiments are located. The last four octants are used for LHC-related functionalities [72] like beam cleaning (octant 3 and 7) dedicated to the removal of particles with large transverse or longitudinal oscillation amplitude, accelerating

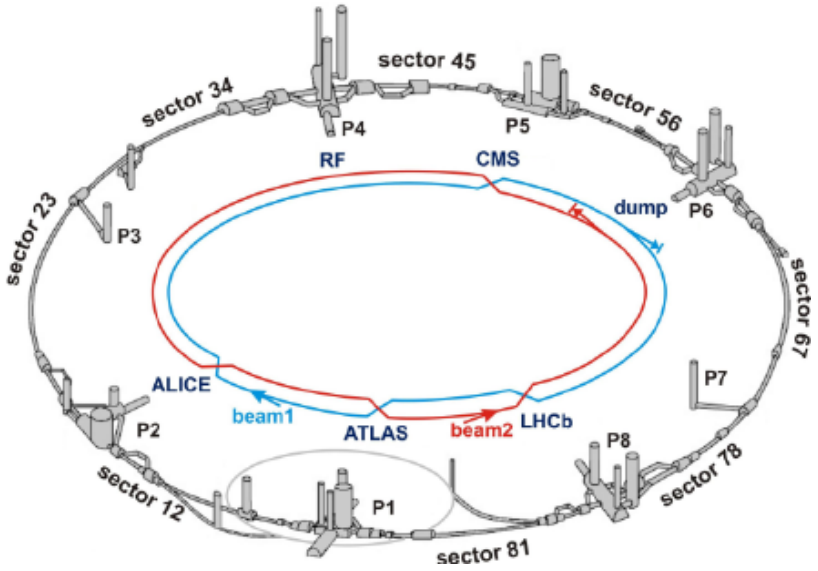

Figure 3.1: Layout of LHC showing the function of the 8 octants (P_i), the direction of each beam, and the 4 interaction points (IPs) where the beams cross to collide.

Radio Frequency (RF) cavities (octant 4) or beam dumping (octant 6) used to extract the beam from the LHC without damaging detectors.

The intensity of the beam is defined in terms of a measurable observable called *luminosity*. Whilst ATLAS and CMS are mostly designed for high-luminosity operation (up to 10^{34} cm^{-2} s^{-1}), ALICE and LHCb operate at a rather low luminosity (around 10^{32} cm^{-2} s^{-1}). The physics programs of ATLAS and CMS are quite similar with a focus on measurements testing the Standard Model, and searching for new Physics beyond it. With its single arm and asymmetrical beam boost, LHCb is more oriented towards the physics of long-lived particles, while ALICE is specialized in the study of heavy ion collisions.

3.1.1 Accelerating Particles

In this thesis, we cover the steps towards accelerating protons. Lead and xenon nuclei are accelerated following a very similar procedure.

In order to isolate protons, hydrogen molecules are passed through a strong electric field to strip off their electrons. The remaining protons are then injected into a linear accelerator (LINAC 2) [73] that brings their energy to 50 MeV. From the LINAC 2, protons get to fill a succession of synchrotron rings: they first enter the Proton Synchrotron Booster (PSB) where they get focused into bunches and accelerated to around 1.4 GeV, then the bunches are sent to the Proton Synchrotron (PS) [74] where they are arranged into trains to be accelerated to an energy of 26 GeV. They overcome a final pre-injection acceleration in the Super Proton Synchrotron (SPS) [73] from which they come out with an energy of 450 GeV. The beams are then ready to fill the LHC pipes.

The LHC beam pipes are about 3 cm in diameter and are put under a ultrahigh vacuum (10^{-10} to 10^{-11} mbar) to limit possible interactions of the beams with gas molecules inside the accelerator. Protons are guided in the pipe thanks to more than 9000 magnets. Among them, 1232 are cooled superconducting dipoles used to bent the beam in a circular orbit. The segments around the IPs all have a similar optical setup, composed of 13 main quadrupole magnets on both sides of the IP, among which 6 are situated in the common beam line and are used for the final beam focusing. The process of focusing the beam for collision using the P1 magnet lattice is discussed in Sect. 3.1.2.

To achieve the designed luminosity, which quantifies the beam intensity, the LHC should be filled with 2808 bunches containing around 10^{11} protons at a rate of one bunch every 25 ns, providing a collision rate of 40 MHz. It should be noted that, before June 2016, the 50 ns spacing was preferred, with a number of bunches around 1380, hence a smaller instantaneous

beam luminosity.

Each proton bunch can reach an energy of 7 TeV (and potentially higher) by being accelerated in RF cavities [75]. Once the target energy is reached, the proton beams circulating in the two counter-rotating beam pipes are steered into a common pipe to collide at one of the IPs. The products of the collision are recorded by means of detectors carefully timed to the LHC bunch crossing clock. Fig. 3.2 shows the LHC multistage injection systems and their location in the CERN accelerator complex.

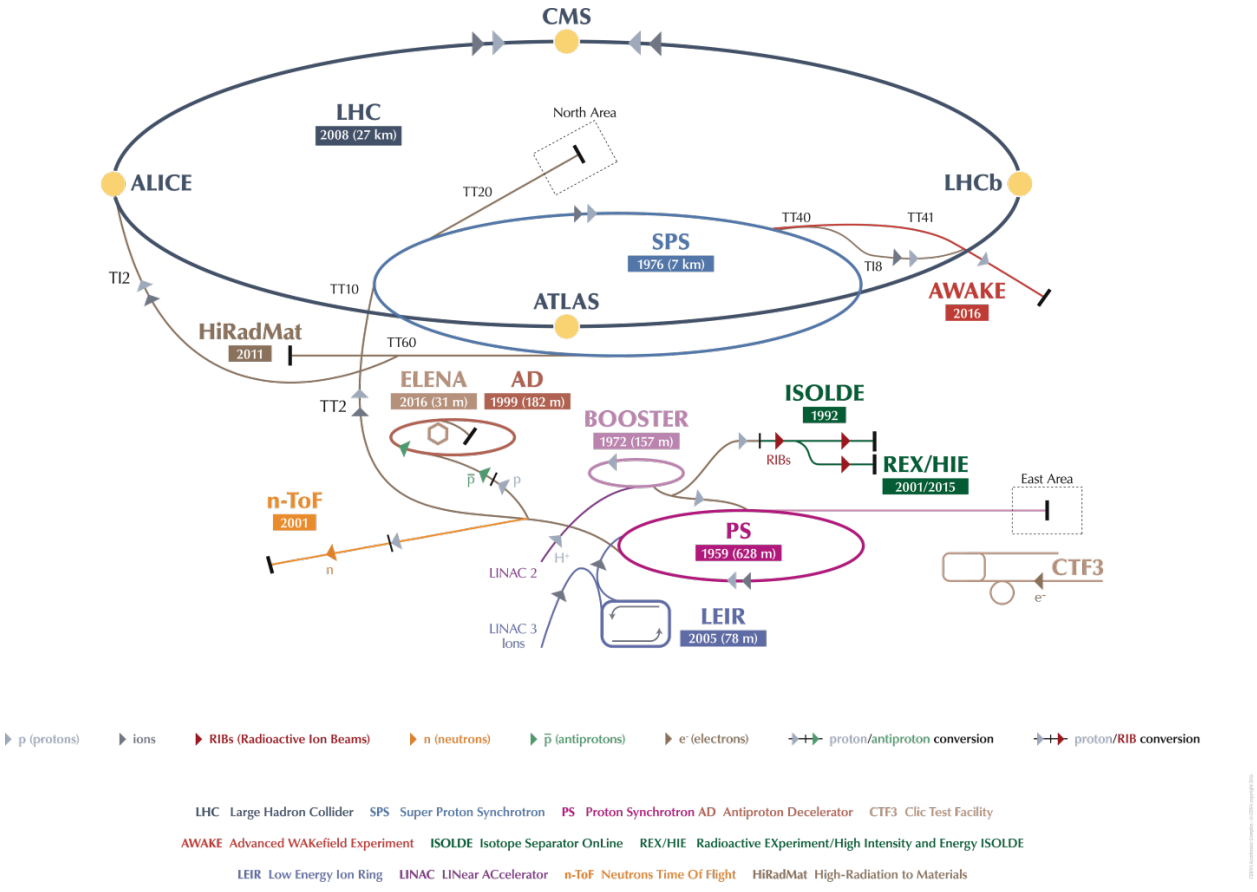

Figure 3.2: The CERN accelerator installations with their date of commissioning, featuring the Linear Accelerator 2 (LINAC 2), the Booster, the Proton Synchrotron (PS) and the Super Proton Synchrotron (SPS) used for accelerating the protons before filling into the LHC. Picture taken from [76].

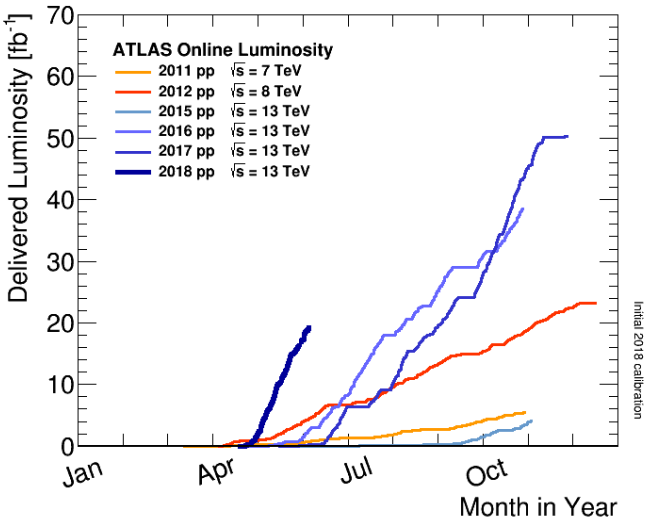

Figure 3.3: Integrated luminosity versus day delivered to ATLAS during stable beams and for high energy pp collisions between 2011 and 2018 [77].

3.1.2 Conditioning the Beams

The proton beams consist of bunch trains. The bunch size and frequency are directly relevant to the number of interactions happening per bunch crossing. The intensity of the relativistic beam is defined in terms of its instantaneous luminosity, L:

$$L = \frac{f_{\mathrm{BC}} N_1 N_2}{4\pi\epsilon\beta^*} \tag{3.1}$$

where f_{BC} is the frequency at which bunches interact, $N_{1,2}$ corresponds to the number of protons per bunches in beam 1 and 2 respectively, β^* is the distance form the IP such that the beam cross-sectional size doubles, and ϵ is the beam emittance. A correction factor may be applied if the two bunches are colliding at a non-zero angle.

Once integrated over a full period of time, the instantaneous luminosity corresponds to the total luminosity delivered by the machine. Fig. 3.3 shows the integrated luminosity as measured in ATLAS for five data taking campaigns between 2011 and 2018. The system of

magnets at the LHC can be set to different configurations or *optics* to achieve the desired beam configuration.

By design, the beam is propagating along z, spreading out in the (x-y) plane. The trajectories of all beam particles are described around a reference orbit, which is defined as the trajectory of a particle with the beam nominal energy. The trajectories are described in a curved coordinate system with the origin at a longitudinal position $s = 0$. Protons perform small oscillations in the transverse plane, around the reference orbit and their motion is described by a vector $(u, \dot{u})$ where $u = \{x, y\}$ defines the transverse coordinate of the proton with respect to the reference orbit along z which has position $(x, y, z) = (0, 0, s)$, and $\dot{u} = du/dz$ is the local angle of the proton path relative to the beam axis. The transverse motion of a given proton is described at first order by the following equation [78] where the x and y oscillations are decoupled:

$$\ddot{u} + M(s)u = 0 \tag{3.2}$$

where M is calculated from the transfer matrices representing the total action of all the magnets along the ring. Since the proton orbit is closed, M obeys the following periodicity condition: $M(s) = M(s + L_{\text{LHC}})$ where L_{LHC} is the circumference of the LHC beam pipe. If one assumes all protons to have the same energy, the M term does not have to account for the momentum dispersion and a stable solution to Eq. 3.2 may be found that depends on $\beta(s)$, called the *amplitude betatron function*:

$$u(s) = \sqrt{\epsilon\beta(s)}\cos\left(\phi(s) - \delta\right), \tag{3.3}$$

$$\dot{u}(s) = -\sqrt{\frac{\epsilon}{\beta(s)}}\left[\sin(\phi(s) - \delta) + \alpha(s)\cos(\phi(s) - \delta\right], \tag{3.4}$$

where $\phi(s) = \int_0^s 1/\beta(t)\ dt$ is the phase function, δ is an arbitrary constant phase shift,

$\alpha(s) = -\frac{1}{1}\frac{d\beta(s)}{ds}$ and ϵ is the transverse emittance of the beam. The betatron function depends on the beam focusing properties of the magnetic lattice and is a measure of the beam cross section at a given position s. $\alpha(s)$, $\beta(s)$ and $\gamma(s) = (1 + \alpha^2(s))/\beta(s)$ are functions describing the beam often referred as the *Twiss parameters*.

Transverse Emittance of a Beam

The transverse emittance ϵ measures the average spread of particle coordinates in the position-momentum phase space. It is defined in Eqs. 3.3 and 3.4 and depends only on the initial filling conditions of the beam. It is inversely proportional to the momentum of the proton and therefore a normalized invariant-under-boost emittance ϵ_N, is often quoted:

$$\epsilon_N = \beta_r \gamma_r \epsilon, \qquad \text{with } \beta_r = \frac{v}{c} \text{ and } \gamma_r = \frac{1}{\sqrt{1-\beta_r^2}} \tag{3.5}$$

The emittance is determined by moving a thin wire through the beam in the transverse direction and measuring the secondary particles produced by the interaction of the beam with the wire at each step of the wire sweeping. This method, called *wire scan*, is detailed in [79].

The solutions for the proton trajectory (Eqs. 3.3 and 3.4) map out an ellipse (Fig. 3.4) centered in zero in the $(u, \dot{u})$ plane whose dimensions will change with z. The shape of the ellipse depends on $\beta(z)$, but its area is constant and equals $\pi\epsilon$. The $\beta(z)$ and $\sqrt{1/\beta(z)}$ dependences in Eqs. 3.3 and 3.4 imply that the beam cannot be extremely narrow and extremely focused at the same time.

The size of the beam in s is then:

$$\sigma(s) = \sqrt{\epsilon\beta(s)} \tag{3.6}$$

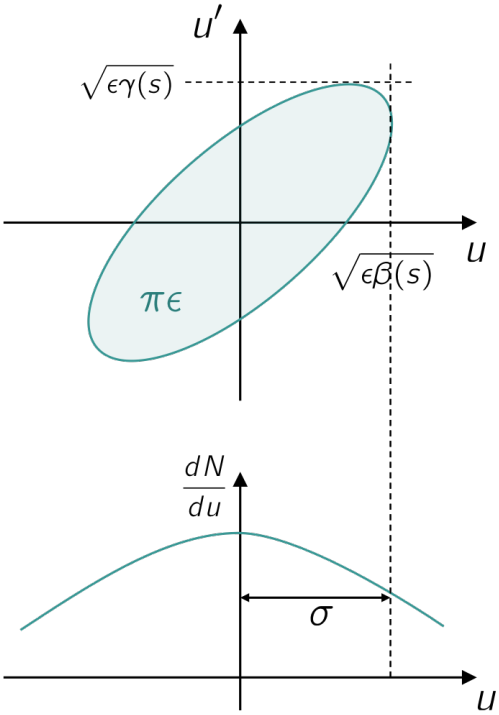

Figure 3.4: The transverse phase space ellipse for a proton at position z along the beam and how it relates to the beam profile. 68% of protons should be contained in the envelope

Standard β^* Optics

Many of the interesting physics processes studied at LHC (Higgs physics, physics beyond the SM etc), have or are expected to have, very low cross sections. A large integrated luminosity is then required to reach the significance of a discovery or observation. Therefore, in most standard LHC runs, the value of $\beta(s)$ at the IP, β^*, is chosen to be very low (0.55 m for 8 TeV protons) in order to get as narrow beams as possible to maximize the luminosity. A consequence is that the focus of such beams is poor and strong quadrupoles must be located close to the IP to refocus each beam after collision. For such high luminosity runs, a crossing angle between the beams is introduced to avoid one bunch of the first beam to collide with several bunches of the second beam, a phenomenon being part of the so-called *out-of-time pile-up*.

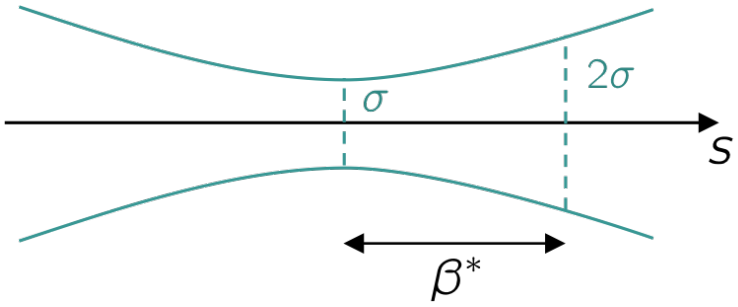

Figure 3.5: Schematic of the β^* optics showing the doubling of the beam width σ at $s = \beta^*$.

High β^* Optics

Runs dedicated to elastic and soft to semi-hard diffraction studies usually use a high β^* magnet configuration. This gives larger beams of almost collinear protons. The optics used for the analysis in Chapter 4 was set such that $\beta^* = 90$ m, which means one has to go 90 m away from the IP to see the beam double in size (see Fig. 3.5). This setup is particularly suited for elastic and soft diffraction as it allows to place the forward proton detectors as close as possible from the beam to detect the smallest proton deflection angle, but far enough from the IP to separate scattered protons from the beam. As discussed in Sect. 2.4.2, the scattering angle is the observable from which the t variable is extracted, and the ability to measure small angles is directly linked to the fiducial acceptance of small t values, thanks to a special magnet configuration: the *parallel-to-point* optics.

For low β^* beams, the luminosity is smaller which reduces the amount of pile-up. In the absence of proton timing techniques, which would allow to associate a forward proton to its primary vertex, low pile-up conditions are required to avoid recording multiple proton tracks in the forward detectors.

Usually high β^* runs require a limited number of filled bunches and consequently no crossing

angle is needed.

More details about how protons are transported through the magnet lattice to the forward detectors stations and how the optics affects the acceptance coverage of the ALFA and AFP detectors are given in Sect. 3.2.2.

About Pile-up...

Pile-up is defined as being the number of proton-proton interactions happening in addition to the interaction of interest in a given time window. Two type of pile-up should be considered:

- **In-time pile-up:** Additional proton-proton collisions occurring in the same bunch crossing. The average number of such collision $\langle\mu\rangle$, is what is often quoted to quantify the amount of in-time pile-up. If the luminosity increases, the probability for such interaction to happen also increases. In high β^* runs, the amount of in-time pile-up is typically very low ($\langle\mu\rangle < 0.1$). For low β^* runs, the pile-up average amount can be as high as $\langle\mu\rangle = 40$.

- **Out-of-time pile-up:** Additional proton-proton collisions occurring in bunch-crossings just before and after the collision of interest. When detectors are sensitive to several bunch-crossings or their electronics integrate over more than frequency of at which bunches cross, these collisions can affect the signal in the collision of interest. This type of pile-up is therefore very dependent on the detectors themselves.

3.2 Detecting Particles

3.2.1 The ATLAS Detector

A Toroidal LHC ApparatuS (ATLAS) is a multilayer general purpose installation sitting in a large cavern at 93 m underground, designed to study hadron collisions at the TeV scale. In order to fulfill its role, the ATLAS detector must excel in several fields:

- It must be able to detect and identify a wide spectrum of particles, including charged leptons, hadrons and photons.
- It must be able to measure the kinematic properties of these particles, such as their energies and directions, with a high resolution.
- It must maintain its resolution over a large range of energies: from 1 GeV up to the TeV scale.
- It must be able to perform these measurements at an extremely high rate, millions of times a second, and over the entire lifetime of the experiment.
- It must be able to record and store data, and successfully distribute it for offline usage.

In the following subsections, the general layout of the ATLAS apparatus is presented. The emphasis is placed on the inner detector as this is the one used to perform the measurement of the diffractive system in Chapter 4. The calorimeters and muon spectrometers description is given in Appendix A.

General Layout

ATLAS has an overall cylindrical geometry with a revolution symmetry along the beam pipe. The detector has a diameter of 25 m, is 46 m long, and weighs 7000 tonnes. It is

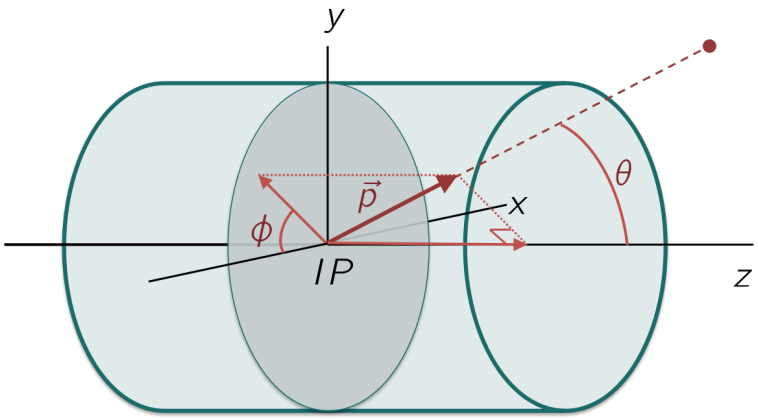

Figure 3.6: Illustration of the ATLAS coordinate system. The cylindrical shape represent the ATLAS detector, and the bold arrow corresponds to the momentum $\vec{p}$ of a particle.

described using a right-handed coordinate system with its origin at the nominal IP. The z-axis corresponds to the revolution axis of the beam pipe. The x-axis points from the IP to the center of the LHC ring, and the y-axis points upward. In addition, cylindrical coordinates (r, ϕ) may be used in the transverse plane, $\phi = \tan^{-1}(\frac{y}{x})$ being the azimuthal angle around the beam pipe measured anti-clockwise around the positive z-axis, and $r = \sqrt{x^2 + y^2}$. Objects location may be given in terms of their pseudo-rapidity, defined as:

$$\eta = -\ln\left(\tan\frac{\theta}{2}\right) \tag{3.7}$$

where θ is the angle the object position makes with the z-axis with respect to the interaction point. The region $-\infty < \eta < 0$ is referred as the A side and the region $0 < \eta < +\infty$ is called the C side.

ATLAS is composed of a cylindrical barrel part and two symmetric wheel-shaped endcaps on the $+z$ and $-z$ sides, which all together provide almost hermetic coverage enabling reconstruction and identification of nearly every energetic particle produced in a collision at the IP. A massive particle traveling at a relativistic speed through the detectors is usually

defined in term of its rapidity $\mathcal{Y}$:

$$\mathcal{Y} = \frac{1}{2} \ln \left(\frac{E + p_z}{E - p_z} \right) \tag{3.8}$$

where $= \sqrt{|\vec{p}|^2 + M^2}$ is the energy of the particle of mass M and momentum $\vec{p}$ with z-component p_z. For massless or highly relativistic particle, the energy of the particle is equivalent to its momentum and the longitudinal angle of emission θ of the particle is then usually defined using the pseudo-rapidity variable from Eq. 3.7 expressed in terms of the total and longitudinal momentum of the particle:

$$\eta = \frac{1}{2} \ln \left(\frac{|\vec{p}| + p_z}{|\vec{p}| - p_z} \right) = - \ln \left(\tan \frac{\theta}{2} \right) \tag{3.9}$$

The barrel and endcaps, are combinations of several layers whose functions are to identify and characterize the different types of particles emerging from the collision. The innermost layers are an ensemble of three precision tracking detectors offering a coverage up to $|\eta| = 2.5$. This system is surrounded by a central solenoid magnet (CS) that produces a 2 T magnetic field. The middle layers correspond to calorimeters. They are segmented into three main regions covering rapidities up to 4.9. The calorimetry layer is surrounded by a toroidal magnet system: a barrel (BT) and two endcaps (ECT); which provide bending power in the outermost layer. The latter is a muon spectrometer covering the $|\eta| < 2.7$ region. Each different level is presented in the following. Fig. 3.7 shows the different sub-detectors and their layout around the beam line.

The Inner Detector

The inner detector is comprised of three light radiation-resistant layers immersed within the 2T magnetic field generated by the superconducting solenoid magnet. The ensemble is 6.2 m long with a diameter of 2.1 m and provides excellent track and vertex reconstruction, and

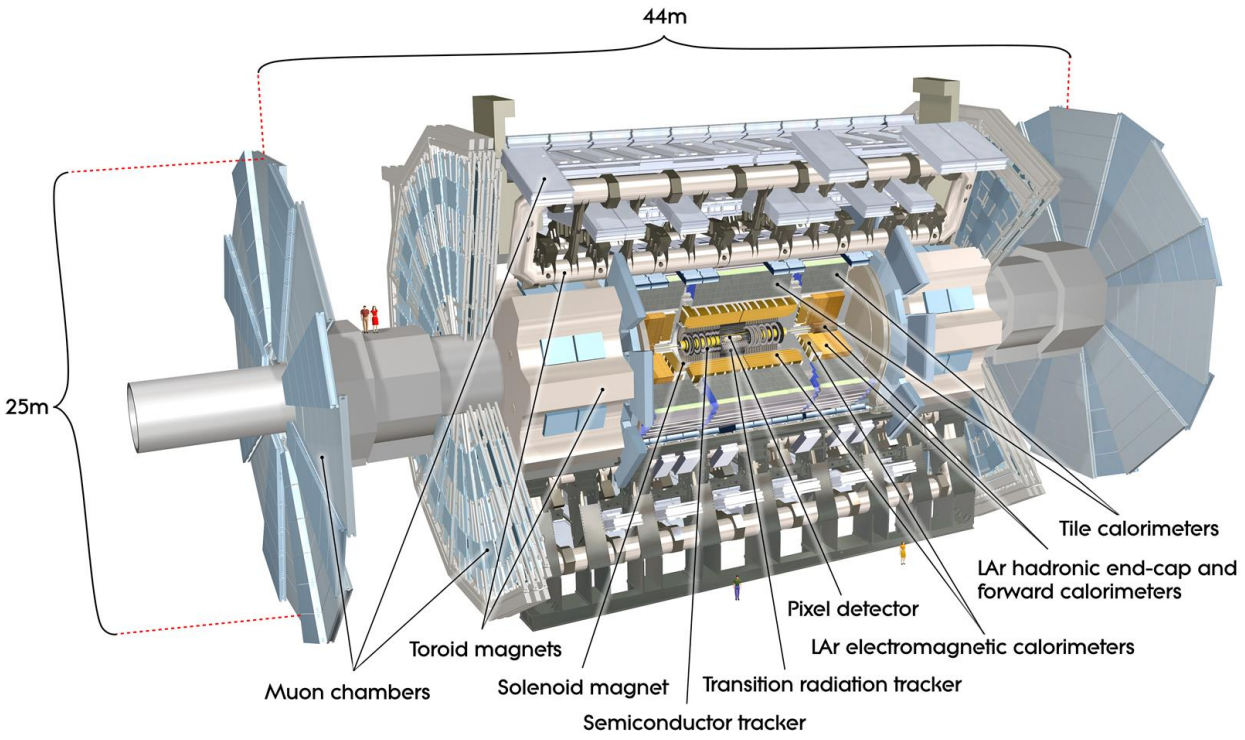

Figure 3.7: Infographics of the ATLAS apparatus.

momentum resolution for particles with $|\eta| < 2.5$ (see Figs. 3.8 and 3.9). A particle traveling through the detectors will deposit some amount of energy, which will be recorded by sensors as a succession of signal hits. Once combined, those hits form a track which describes the trajectory of the particle. By reconstructing its trajectory, the *impact parameter* of the particle, its closest transverse position with respect to the beam-line, can be extrapolated, which helps localizing the position of its production vertex.

The inner detector also provides particle characterization based on track curvature. Trajectories of charged particles propagating through the axial magnetic field are bent in the plane transverse to the beam direction. The strength of the bending is directly linked to the momentum of the particle, and the direction of it gives the charge of the particles. This

dependence is made explicit by the formula describing the Lorentz force applied on a particle of charge q and mass m with momentum $\vec{p}$, bathed in a magnetic field $\vec{B}$:

$$\vec{F} = \frac{q}{m}\vec{p} \times \vec{B} \tag{3.10}$$

The inner detector comprised three subsystems: the Pixel detector, the Semi-Conductor Tracker (SCT) and the Transition Radiation Tracker (TRT). Those systems are described in the following sub-sections and their relative size and layout are shown in Figs. 3.8 and 3.9.

The Pixel Detector The silicon Pixel detector is the innermost part of the inner detector (see green parts on Figs. 3.8 and 3.9). Until Spring 2014, it contained three layers of high precision and high granularity semi-conducting modules. Since May 2014, an extra layer, the Insertable B-layer (IBL), was added to compensate for aging- and pile-up-induced tracking and readout inefficiencies and improve tracking precision, in particular for b-hadrons [80]. The work presented in Chapter 4, makes use of the 2012 version of the inner detector, without the IBL, whose design will therefore not be discussed. The pre-2014 detector contained 1744 sensors, each made up of 47232 pixels. The minimum size for a pixel is 50 μm in the (r,ϕ) plane and 400 μm in the z direction. The silicon pixels are doped with a material such that a depletion zone is created, which is enlarged by applying a voltage over the cell. A charged particle going through the sensor loses energy due to ionization and creates multiple electron-hole pairs, which drift towards the electrodes, giving a current which signals a hit when exceeding an adjustable threshold [81]. Each pixel module contains 16 radiation-hard front-end chips, which provide read out. The pixel layers ensures space point measurements with a precision in the (r,ϕ) plane of 10 μm and in the axial (z, barrel) and radial (r, endcaps) planes of 115 μm.

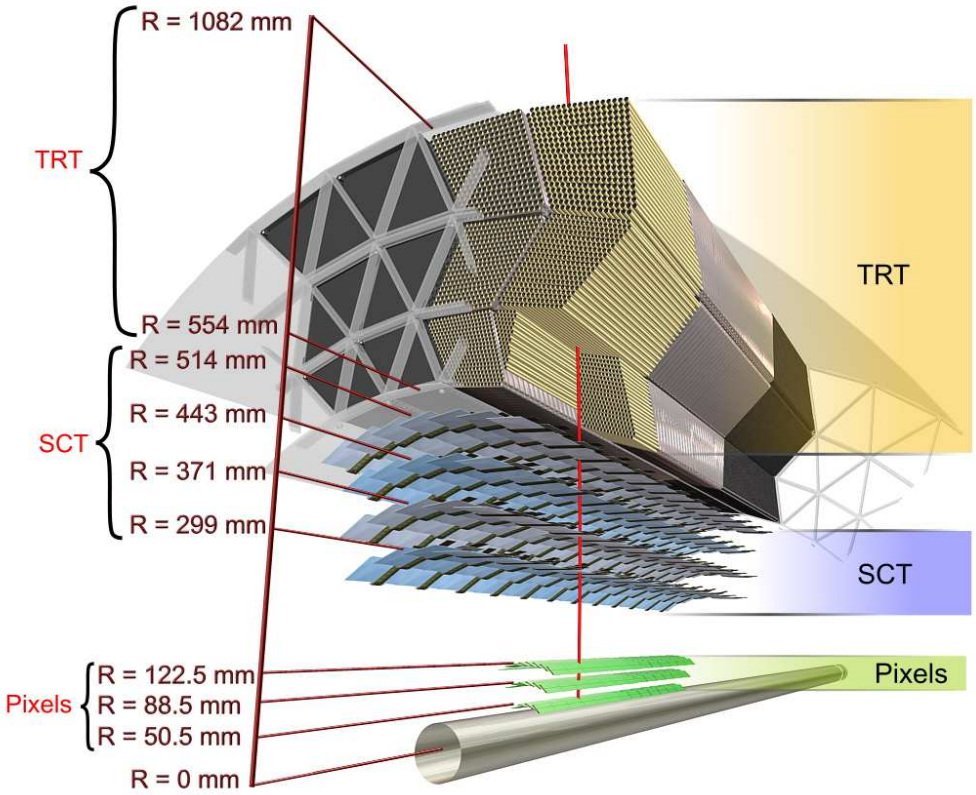

Figure 3.8: Graphics of the inner detector showing the different layers in the barrel. Taken from [82].

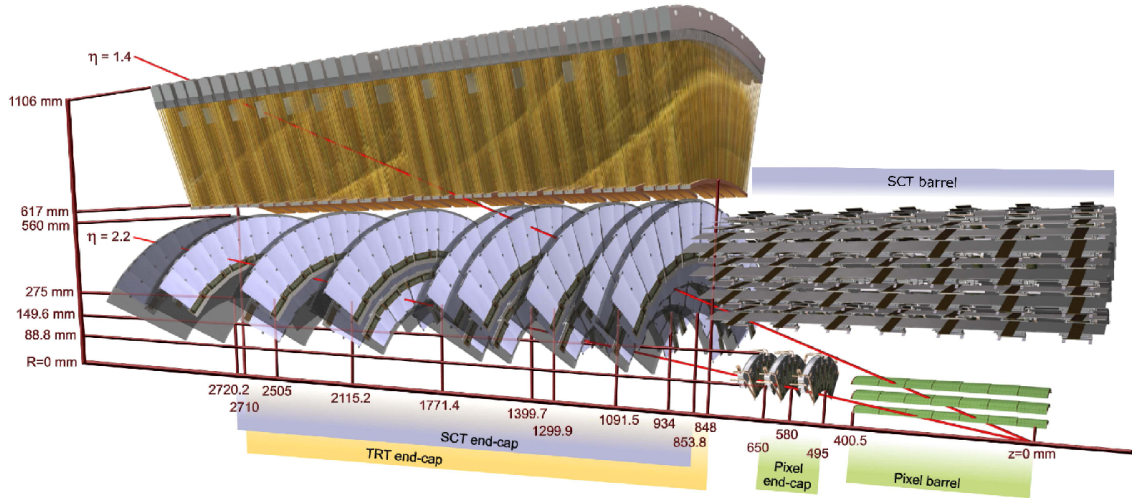

Figure 3.9: Graphics showing part of the barrel and all the endcap layers of the inner detector with pseudo-rapidity labeled tracks for reference. Taken from [83].

The Semi-Conductor Tracker The second layer of the inner detector is a SCT made of 4,088 micro-strip silicon wafers. The strip modules are arranged in a central barrel containing four concentric layers extending to $|\eta| = 1.5$, and two endcaps each containing nine disks perpendicular to the beam axis (see blue parts on Figs. 3.8 and 3.9). Most modules contain four strip sensors. Two daisy-chained sensors are positioned on either side of each module that provide 768 strips of length 12.8 cm all together. The strips on either side of the module are oriented with a stereo angle of 40 mrad between them to provide a single space point measurement. The precision of the SCT is of 17 μm in the (r, ϕ) plane and 580 μm in the z direction.

The Transition Radiation Tracker The TRT is the component of the inner detector installed the furthest from the IP. It consists in a collection of 298,304 thin drift tubes. Each tube is 4 mm in diameter and is filled with a gas mixture of Xe, CO_2 and O_2 [71]. A voltage can be applied between the outer wall of the tube and a central anode wire. The TRT has a barrel and two endcaps. The drift tubes in the barrel section are 144 cm long and arranged in three concentric layers, split in sectors. The drift tubes in the endcaps are 37 cm long and arranged radially in stacked wheels (see yellow parts on Figs. 3.8 and 3.9). A charged particle passing through the tubes ionizes the gas, thus producing ionization electrons. An electrical field is applied forcing the electrons to the central anode. The time that the signal is received at the cathode compared to the anode gives a drift time measurement, which allows to infer the position with a precision of 130 μm in the (r, ϕ) plane. The gas tubes are interleaved with polypropylene fibres or foils to provide electron identification through transition radiation [81]. Signals from ionization electrons and transition radiation photons are detected by separate low and high threshold discriminators in the front-end

electronics [84].

3.2.2 The Forward Detectors

ATLAS is equipped with several forward detectors. One of which, the AFP detector [85], was installed very recently to study diffractive interactions at high t. It was not in place at the time the data used in Chapter 4 was taken.

The other detectors were developed primarily to monitor the conditions required for collision. The LUminosity measurement using Čerenkov Integrating Detector (LUCID) gives information about the relative luminosity by measuring the inelastic low-p_T proton-proton scattering. The Zero Degree Calorimeter (ZDC) provides a trigger for the whole ATLAS detector by recording forward neutral particles. ZDC is not always set active for data taking and it was typically not operating when the data used in Chapter 4 was taken. ALFA [86] complements LUCID by measuring the elastic proton-proton scattering down to the Coulomb-nuclei interference region ($|t| \sim 0.00065$ GeV^2) where it is proportional to the absolute luminosity of the beams.

Since ALFA is able to measure a sensible range of scattering angles, the measurement of protons coming from soft to semi-hard diffractive interactions is also possible. ξ and t are then reconstructed from analyzing the diffractive tracks up to the acceptance limits. The AFP detector which can operate in a higher luminosity environment, complements ALFA by offering a large angular coverage, and some background exclusion possibilities and pile-up removal by comparing protons time-of-flights.

The relative positions of LUCID, ZDC, ALFA and AFP along the beam line are shown Fig. 3.10. In the following sections, the ALFA and AFP detectors are described. LUCID and ZDC are detailed in [71].

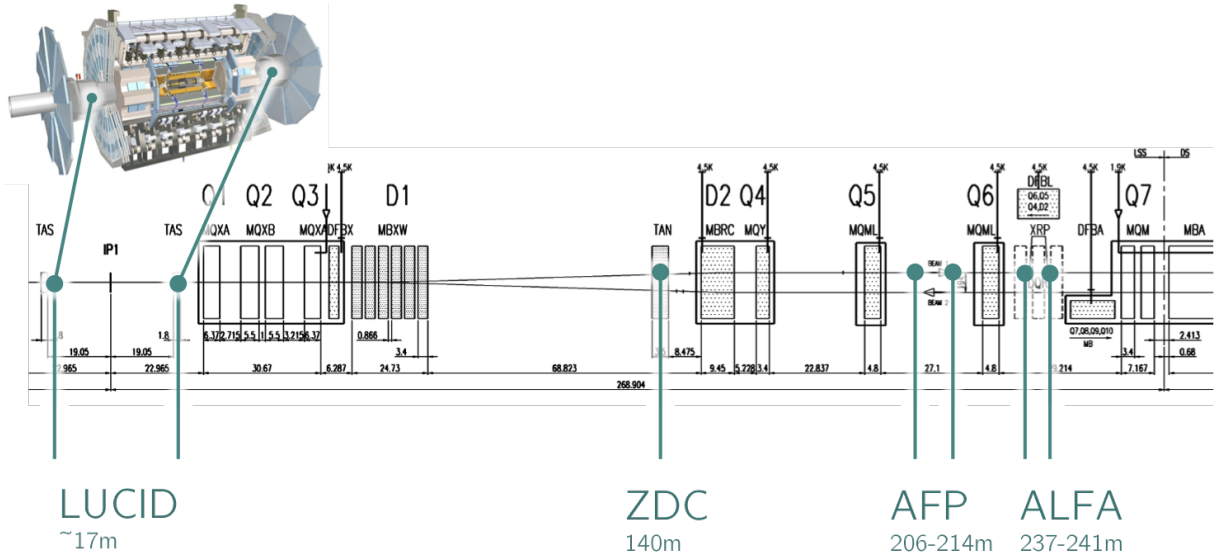

Figure 3.10: Schematic showing the location of the ATLAS forward installations on one side with respect to the beam lines and their distance to the interaction point P1). The Q_i's, $i = 1, \ldots, 7$ show the location of the quadrupole magnets of the optic lattice. D_i's, $i = 1, 2$ correspond to the dipole magnets.

The ALFA Detector

The ALFA detector is a forward proton tracker sensitive to the physics of the low momentum exchanges. For such kinematic range, the protons are scattered at very small angles, typically a few micro-radians. It was discussed in Sect. 3.1.2 that ALFA needs to operate at a high β^*, first to ensure a low enough luminosity and limit the probability of coincidental ALFA tracks coming from pile-up protons, and second, to be able to approach the beam as closely as possible to measure these very small angles. By trigonometry, a better resolution is achieved when placing the ALFA stations far away from the IP. Hence, those are situated at 237.4 and 241.5 m respectively on each side of P1 as depicted on Fig. 3.11. Some additional beam

conditions (parallel-to-point optics) are also required to make the vertical track position in ALFA independent of the point of collision. This allows to calibrate ALFA detectors.

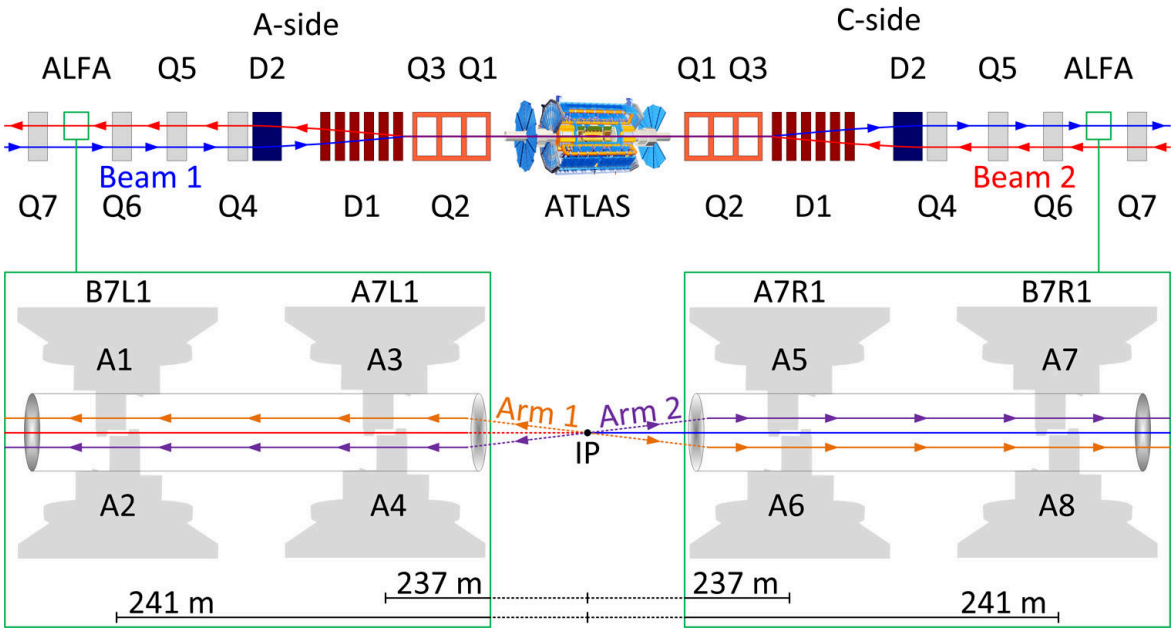

Figure 3.11: Sketch of the experimental setup (not to scale) showing a side view of the position of the ALFA Roman Pots (green circled zoomed in region) with respect to the interaction point (IP) shown on top (top view). The quadrupole magnets are labeled with Q_i, $i = 1, \ldots, 7$ and the dipole collimators with D_i, $i = 1, 2$. The red and blue arrowed lines indicate the incoming beams. The orange and purple arrowed lines show the trajectory of the scattered protons.

General Layout On the ATLAS C-side, the A7R1 station with its two pots situated above and below the beam pipe: A7R1U (sometimes referred as A5) and A7R1L (A6) is the closest to the interaction point. The B7R1 station, composed of B7R1U (A7) and B7R1L (A8), is the furthest. Similarly, there are two stations on the A-side, one closer to the IP, A7L1 , and one further, B7L1, each composed of up and down pots (also referred as A1, A2, A3 and A4 as depicted on Fig. 3.11). The pots contain charged particle detectors made of scintillating fibres. A traversing proton excites some of the electrons in the material of the

fiber, and a light pulse is emitted when the electrons return to the ground state. In the Main ALFA Detector (MD) of each ALFA Roman Pot (RP), 64 aluminium-coated fibres of 0.5 mm diameter, each spaced by 70 μm, are carefully aligned and glued on the back and front side of a titanium support. Fibers in the front and the back are oriented perpendicularly to each other, in directions called u and v, to allow for 2-dimensional position determination.

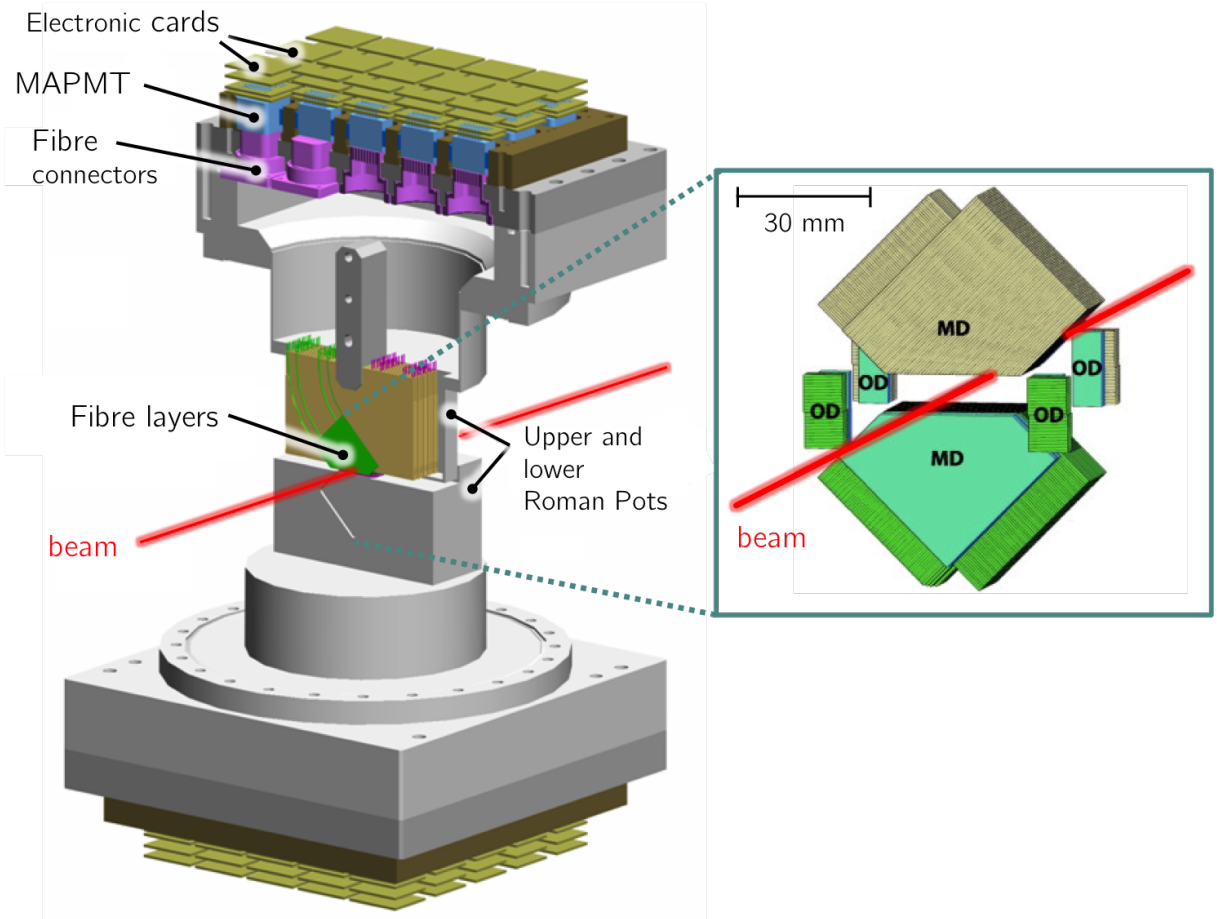

Figure 3.12: Technical drawing of two ALFA Roman Pots moving above and below the beam line. The box on the right shows the diamond-shaped detection areas of the up and down plates magnified. In this zoomed area, MD labels the main detectors above and below the beam while OD stands for the overlap detectors. The lines across MDs and ODs indicate the orientation of the scintillating fibres forming two plates referred as U and V. The teal areas with a flat texture correspond to the trigger tiles located in front of the ODs and the MD on one side.

On the side closest to the beam line, in order to measure protons with very small deflection angles, the fibers are cut at 45 degree with respect to the horizontal plane. This forms a diamond-shaped detection area (see zoomed region on Fig. 3.12). The resolution obtained with this configuration is 30 μm (see Appendix B.1 for computation).

In addition, 3 layers of 30 fibres situated on either side of the MD constitute each of the overlap detectors (ODs). They are used to find the distance d_y between the upper and lower MDs. The ALFA Overlap Detector (OD)s use particles from the halo of the beam for such alignment. When a halo proton traverses both ODs from the lower and the upper detector, its position is recorded and the difference in positions indicates by how much the upper and lower stations are misaligned.

The arrangement of the MDs and ODs with respect to the beam on a given side is illustrated in Fig. 3.12. All the fibres are read out by an array Multi-Anode PhotoMultiplier Tubes (MAPMT). A compact front-end electronics is attached to the back side of each MAPMT to treat the signal before transmission to the central ATLAS data acquisition system.
In addition, each MD is instrumented with two optically separated fast response plastic scintillator tiles. These tiles are used as triggers and cover the entire area of the MD. They are positioned on both sides of the detector in order to make coincidences. The ODs have scintillating trigger tiles too. Only one tile per OD is needed however, since the coincidence is obtained from simultaneous signal in the overlapping ODs from the upper and lower pots.

Because of the ultra high vacuum in the LHC, only equipment that does not pollute the vacuum can be used. As the glue in the ALFA detectors might evaporate, the detectors are

installed in RPs [87, 88] mounted on isolated bellows which allow them to move towards the beam in an independent way. These pots are designed to host the diamond-shaped plates, the MAPMTs and all the electronics. To reduce the probability of interaction of the protons with the pot material, the wall in front of the MD is thinned down to 500 μm.

For standard physics data taking and beam calibration procedures, the pots are removed from the vicinity of the beam to avoid radiation damages. When running in low luminosity conditions, each RP is brought closer to the beam at a step size of 5 μm until a sudden increase in the LHC Beam Loss Monitor (BLM) located right after the ALFA stations shows that it scraps the beam edge. The detector is then moved away from the beam to a now known position. This position depends on the beam stability and corresponds to several standard deviations of the beam size. A depiction of a station with a cross-sectional view of one of the RPs is shown on the left part of Fig. 3.12.

Track Reconstruction The best estimate of the track position is given by the overlap region of the hit areas of all fibres from the 10 plates. This requires the deflection angle of the proton to be negligible while traveling though the 10 fiber layers. This is a valid assumption for protons reaching the ALFA acceptance. As illustrated in Fig. 3.13, the shifted staggering of the fibres narrows the overlap region and thereby improves the resolution. The center of the overlap region gives the u or v coordinates, while the width determines the resolution. More details on the track reconstruction efficiency are given in Sect. 4.4.2. Pairs of u and v coordinates are then transformed to spatial positions with respect to the RPs which then can be expressed in terms of the beam defined coordinate system. The reconstruction of 2 positions in the (x, y) plane in two consecutive pots from the same armlet allows to deduce

the proton trajectory and deflection angle.

The scenario of multiple tracks in ALFA is treated offline. If two charged particles enter a station, they will both leave tracks in the U and V plates. The information about which U-track corresponds to which V-track is inferred by analyzing the 4 tracks collected, looking for the largest location overlap. This association procedure may fail when two or more particles cross the detection area, meaning a fake track will be reconstructed. This typically happens when a charged particle showered ahead of the first station or in between the two stations of an arm. The amount of fakes can be mitigated by requiring two tracks of good quality in both the close and far stations of an arm (see Sect. 4.2.2).

Geometrical Acceptance and Kinematic Constrains The energy and transverse momentum ranges of the protons that can be recorded by the ALFA detectors depend on the geometrical acceptance of the whole system. A proton that would be too close to the beam or scattered with a too large angle will never reach the ALFA detection volume.

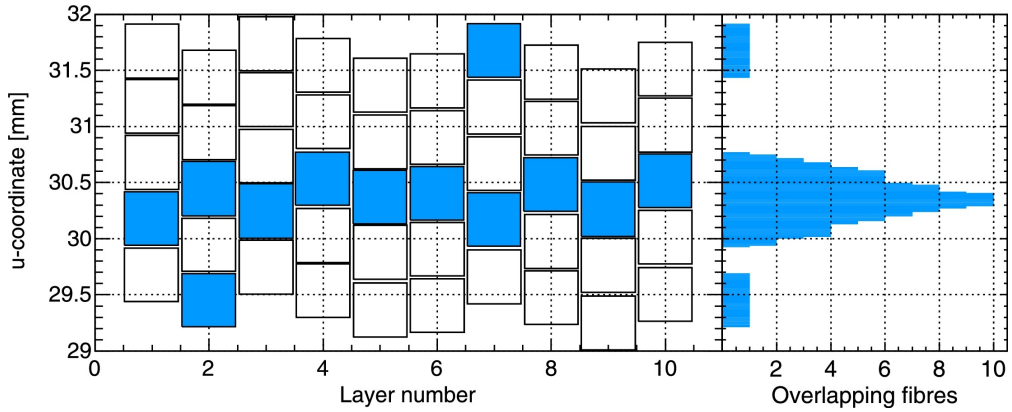

Figure 3.13: Illustration of the reconstruction of the track u position in one pot for 10 layers from [89]. Only 5 fibers per plate are shown. The histogram on the right is a stack of all hits accumulated over the plates. The bin with the maximum entries gives the averaged track position.

Fig. 3.14 shows simulated trajectories of elastic protons, when a $\beta^* = 90$ m optics is used, for different fractional energy losses ξ, and for protons with same nominal energy but varying the proton initial p_x and p_y. From these plots it appears that the less energetic the proton is, the more it will be deflected. It also shows that protons exhibiting a small transverse momentum component after collision will end up being massively deflected when reaching the ALFA stations. The p_y component of the transverse momentum has more impact on the deviation than p_x does. In this high β^* configuration, the crossing angle between the proton beams is set to zero. Hence, the observed elastic proton hit positions in x and y due to p_x and p_y components are centered around (0,0) in the (x, y) plane.

For protons coming from diffractive interactions, the typical diffractive hit pattern will be displaced along the x-axis compared to the elastic hits centered in (0,0). Due to the absence of crossing angle, the hits are still centered around $y = 0$. As for elastics, the optics will amplify the effect of the p_y component at IP much more than that of the p_x component producing an ellipsoidal hit map spread out in the y-direction. Fig. 3.15 shows the typical hit pattern obtained from simulation for single diffractive events compared to elastics, where a clear shift in x with respect to 0 is observed for diffractive protons.

As the deflection angle of the proton, and by extension, its position in the ALFA detector, is tied to the momentum exchanged during the interaction, the geometrical constrains translate into limits in the kinematic range that can be explored with such detectors.

The proton kinematics at the IP are usually described with three variables: the fractional

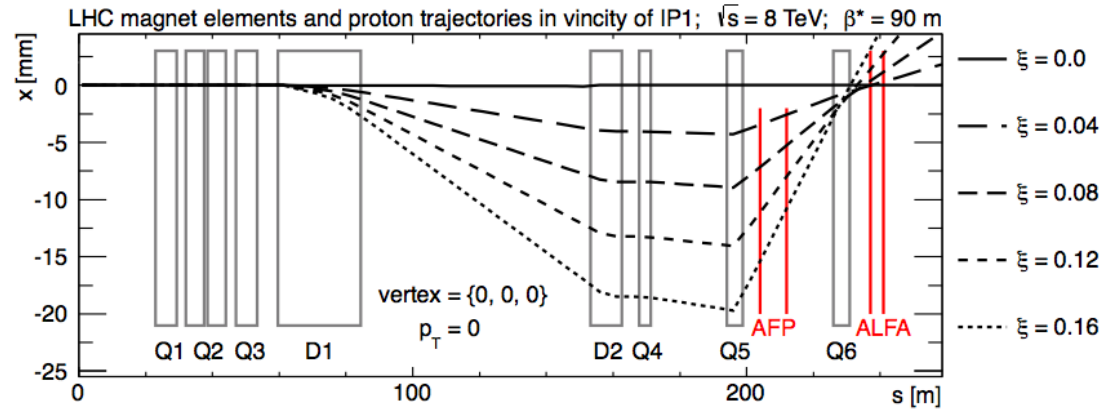

(a)

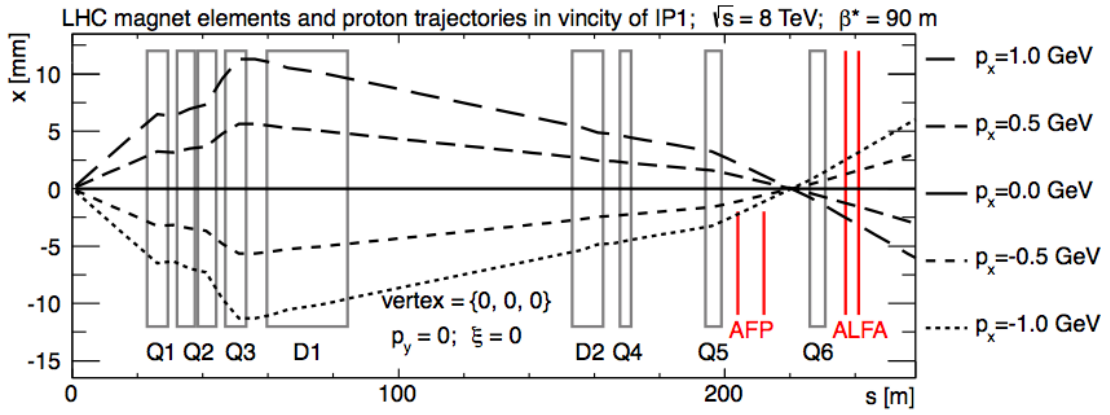

(b)

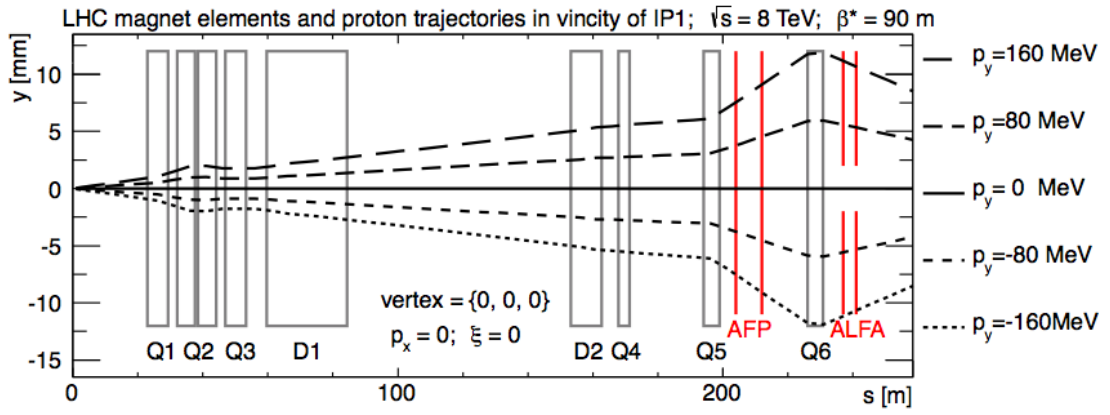

(c)

Figure 3.14: Optical path of protons with varying (a) fractional energy loss ξ, (b) transverse momentum x-component (c) transverse momentum y-component, assuming $\beta^* = 90$ m and no crossing-angle, from [90].

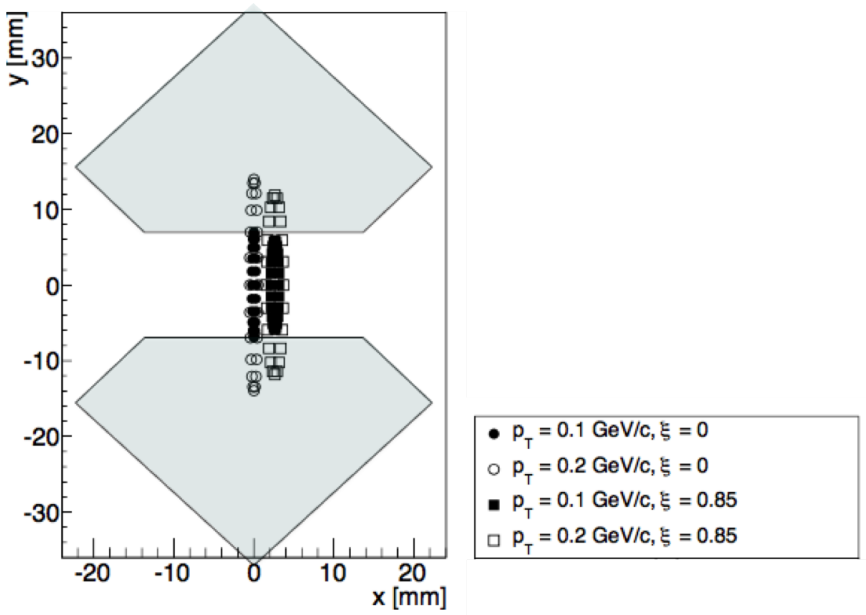

Figure 3.15: Hit map for elastic ($\xi = 0$) and a set of diffractive events ($\xi = 0.85$) in the ALFA first station ($z = 237$ m) obtained from Monte Carlo simulation using a $\beta^* = 90$ m optics. The solid lines mark the ALFA detector active area. The figure is taken from [91].

energy loss ξ, the proton transverse momentum p_T and its azimuthal angle ϕ. Fig. 3.16 shows the acceptance plots for diffractively scattered protons at $z = 237$ m. These plots were obtained through Monte Carlo simulations using a package that use a set of classes called `ForwardTracker` [92] to propagate the proton from the IP to the ALFA station. More details about the proton transport software are given in Sect. 3.5. Figs. 3.16(a)–3.16(c) show the effect of the LHC magnet on the amount of protons reaching the first ALFA station. Figs. 3.16(d)–3.16(f) show the ALFA acceptance by taking into account not only the LHC magnet effects, but also the effective detection surface covered by the ALFA tracker.

By analyzing Figs. 3.16(a)/(b) and 3.16(d)/(e), one can see that, for $\xi < 0.17$, most protons make it to the ALFA station and the actual detection surface is the acceptance limiting factor. Protons with $p_T < 0.1$ will not make it to ALFA since they are simply too close

to the beam. Figs. 3.16(b)/(c) and 3.16(e)/(f) show that protons with an azimuthal angle approaching 0 or $\pm\pi$ will not be detected due to the inherent gap between the upper and lower MDs.

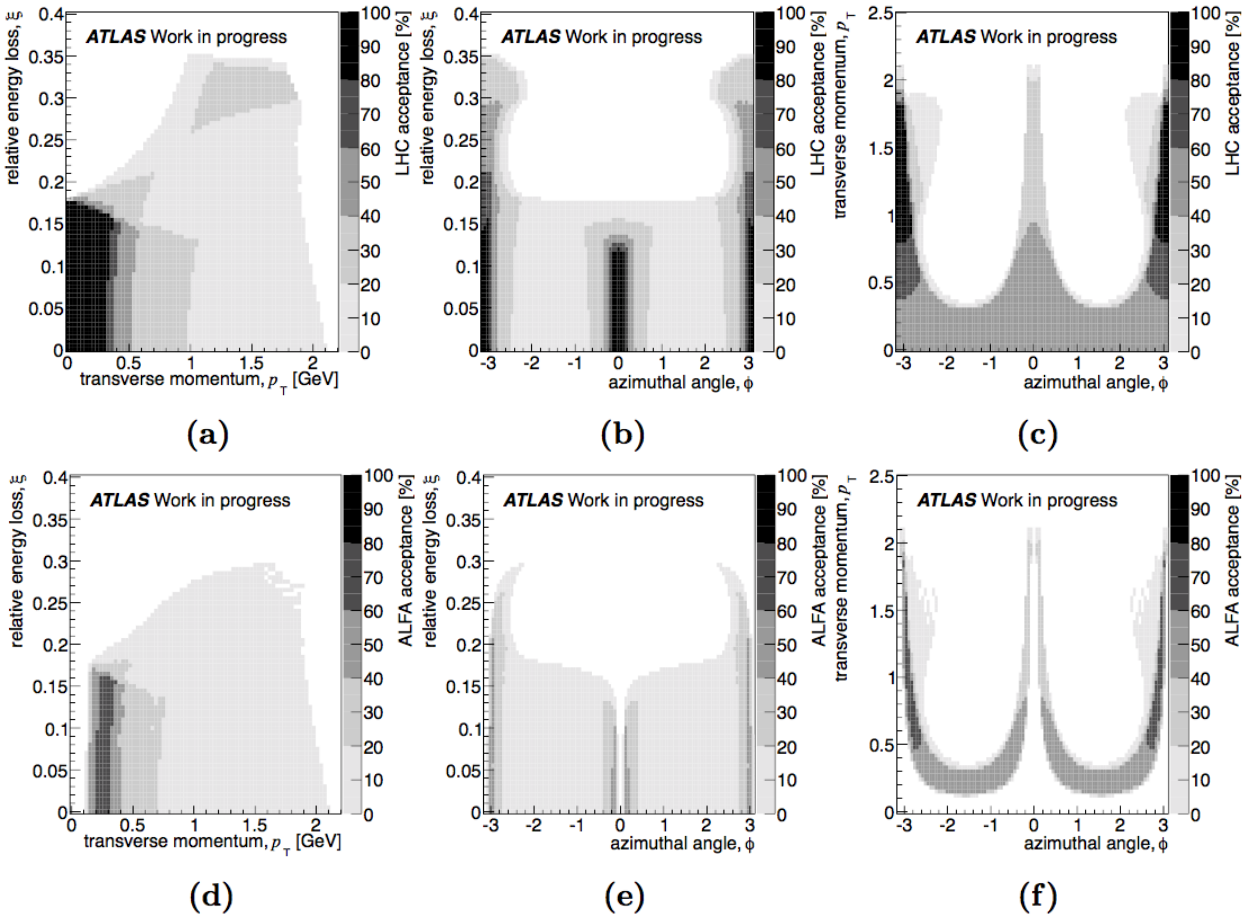

Figure 3.16: The LHC (a), (b) and (c) and ALFA (d), (e) and (f) geometrical acceptances obtained from Monte Carlo simulation using a $\beta^* = 90$ m optic [90], where ϕ is the azimuthal angle of the ALFA track with respect to the vertical plan. The LHC acceptance shows the effect of the optics on the protons. The ALFA acceptance takes into account the effect of the LHC combined with the actual detection area of the ALFA tracking plates, for each combination of these three variables.

Proton Reconstruction In order to reconstruct the proton energy, p_T and ϕ from the signal obtained in ALFA, the two following steps are performed:

- First, a parameterization is found investigating correlations between the hit profile in ALFA and the proton kinematics for the run of interest,
- Then, this parameterization is used to minimize a χ^2 fit to the data of the proton kinematics parameters on a event-by-event basis

The parameterization is performed by analyzing Monte Carlo proton produced at IP and transported through the optics lattice using a package for beam transport. The proton x and y hit positions in the two consecutive ALFA detectors may be parametrized as a function of the energy E, the horizontal momentum p_x, the vertical momentum p_y knowing the (x, y) coordinates of the IP, v_x and v_y. In Chapter 4, the standard `ALFAReco` package (described in [93]) was used to extract the kinematics, which makes use of the `ForwardTracker` base classes to transport the protons. The parameterization used in this package is:

$$x(E, p_x, v_x) = C_x(E) + \Delta C_x(E) \cdot v_x + p_x \cdot a(E) \tag{3.11}$$

$$y(E, p_y, v_y) = C_y(E) + \Delta C_y(E) \cdot v_y + p_y \cdot b(E) \tag{3.12}$$

where C_x, C_y, ΔC_x, ΔC_y, a and b are functions of the proton energy detailed in
A χ^2 fit is then performed to find the best set of parameters matching the data. Beforehand, the data hit positions which are defined with respect to the beam line, must be expressed in the LHC/ATLAS coordinate system. The χ^2 minimization is performed using Minuit. When two minima are found, the lowest energy is chosen as the best estimate to avoid reconstructing protons with energies above the kinematic limit.

Alignment A precise knowledge of the positions of the tracking detectors with respect to the circulating beams is required for the reconstruction of the proton kinematics with ALFA. For physics analysis, the detector positions are determined from the elastic-scattering data.

The alignment procedure is based on the distribution of track positions in the stations in the full elastic-scattering event sample. The elastic proton hits distribution in ALFA is expected to form a narrow ellipse with its major axis in the vertical direction. This typical pattern can be used as a reference to deduce the alignment constants. Diffractive data taking happening in the same fill as an elastic measurement campaign may use the same alignment constants. The independent position of each station is defined using three parameters: the horizontal and vertical offsets with respect to the beam position, Δx and Δy, and the rotation angle, θ, around the beam axis, whose values relevant to the analysis presented at Chapter 4, are listed in Table 3.1. The horizontal offset is the center of the projection in x of the symmetrical hit distribution. The rotation angle is obtained from a linear fit to a profile histogram of the $x - y$ correlation [89]. The vertical offset is determined with respect to the center of the beam by comparing the density of tracks in the upper and lower detectors using a sliding window technique [89]. As already mentioned, the relative distance d_y between the up and down detectors in a given station is calculated by looking at overlap region between the upper and lower ODs. A detailed description of the alignment procedure is presented in [94].

The tracks in ALFA are measured in the RP reference frame, x_{det} and y_{det}. The alignment provides information about the horizontal and vertical offsets as well as the rotation of each Roman Pot. Combination of this information allows calculation of tracks positions in the beam reference frame, x_{beam} and y_{beam}, using the following formulas

$$x_{\text{beam}} = [x_{\text{det}} - \Delta x]\cos(\theta) - \left[y_{\text{det}} + y_{\text{edge}}^{\text{beam}}\right]\sin(\theta) \tag{3.13}$$

$$y_{\text{beam}} = [x_{\text{det}} - \Delta x]\sin(\theta) + \left[y_{\text{det}} + y_{\text{edge}}^{\text{beam}}\right]\cos(\theta) \pm d_y/2 - \Delta y - y_{\text{edge}}^{\text{beam}} + d_y^{\text{edge}} \tag{3.14}$$

where d_y^{edge} is the distance between the Roman Pot edge and the sensitive part of the detector

Station	ALFA detector	Δy[µm]	θ [mrad]	Δx[mm]	d_y [mm]
0	B7L1U	40.45	4.753	0.442857	16.04354
	B7L1L		1.015	-0.308812	
1	A7L1U	26.51	3.702	0.749871	16.76960
	A7L1L		2.27	0.485853	
2	A7R1U	-36.047	0.0	-0.128387	16.629955
	A7R1L		0.0	-0.010984	
3	B7R1U	8.8	1.366	0.013385	16.0205
	B7R1L		0.744	0.070536	

Table 3.1: Alignment constants defining the positions of the ALFA detectors with respect to the beam. The offsets in y were calculated using the sliding window method. The last column lists the distance in y between the up and down detectors of the same station extracted from the analysis of tracks in the overlapping ODs.

extracted from a off-site test beam and $y_{\text{edge}}^{\text{beam}}$ is the position of the edge of the detector in the beam coordinate system.

The AFP Detector

The ALFA detector was build to be operated when the pile-up is low such that it can approach the beam as close as possible without being damaged by radiation. When using high β^* optics, the ALFA design is particularly convenient if it allows to access the coulomb region of elastic interactions. It can also be used, to a certain extent, to study diffractive interaction for various values of ξ. The AFP detector is complementary to ALFA as, in particular, it can detect protons up to way larger angles with a decent coverage in ξ when used in collision optics mode ($\beta^* = 0.55$ m). Hence, it can probe the kinematic range of harder diffractive interactions, in particular diffractive dijets, photons, photon+jet and electroweak bosons production.

The detector consists of tracking systems based on silicon pixel sensors enclosed in RPs located at 204 and 217 m on either side of the IP. The 217 m stations are complemented by Time-of-Flight (ToF) detectors that allow to reduce the background from pile-up protons during high luminosity operation. Contrary to ALFA, the AFP RP insertion is done along the x axis, from the external side of the LHC ring towards the beam line only, which means there is only one RP per station.

The installation of two extra position and timing detectors at 420 meters away from the IP was foreseen, which would have allowed to probe protons with much smaller ξ, but this project was abandoned due to installation costs and trigger-related technical constrains. At the time this thesis is written, the AFP system is in its *2+2 configuration*, meaning the 2 stations are installed on both sides. The first side (0+2 configuration) was set up in 2015, and the two remaining stations were put in place during the Winter 2016-2017 shutdown. Due to glue transparency issues in the ToF detectors, proton timing is not yet available. The installation of the ToF systems is scheduled for 2018. A schematic representation of one of the design of a single armlet is shown on Fig. 3.17. More technical details may be found in [85].

Tracking Detectors The AFP tracking detectors must be able to approach the beam closely and should be radiation hard to operate under high luminosity conditions. For this reason, the baseline tracker was chosen to be the same as the ATLAS IBL one. It uses n- and p-type column-like silicon electrodes which are more resistant to radiation than other

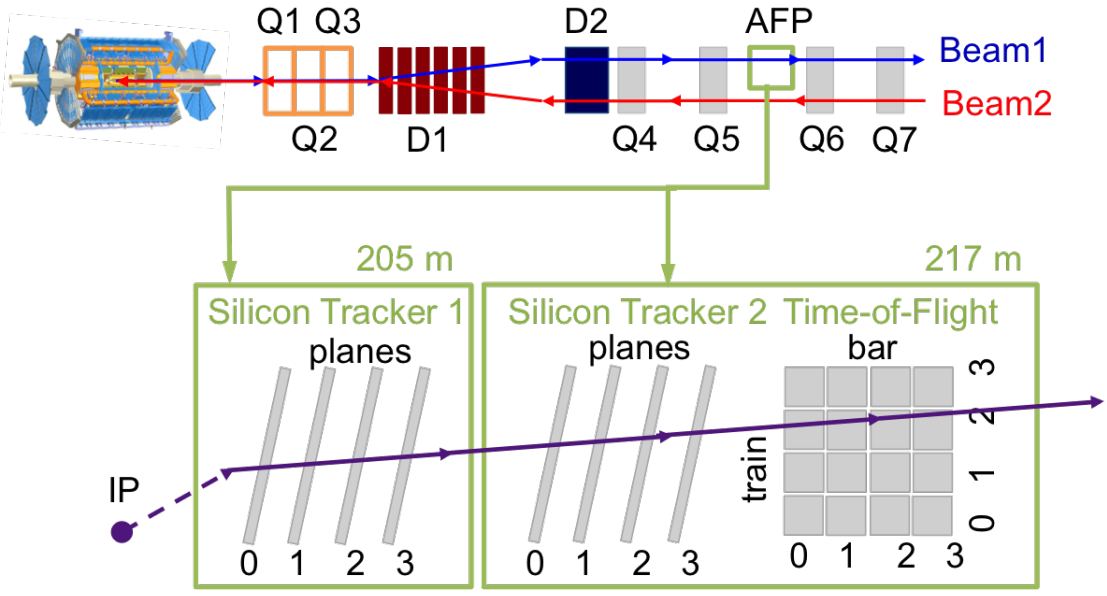

Figure 3.17: Sketch of the experimental setup (not to scale) showing the position of the AFP Roman Pots (green circled zoomed in region) with respect to the interaction point (IP). Only one arm is shown. The quadrupole magnets are labeled with Q_i, $i = 1, \ldots, 7$ and the dipole collimators with D_i, $i = 1, 2$. The purple arrowed lines show the trajectory of a scattered proton. The gray areas represent the SiT plates and ToF bars.

planar silicon technologies. Each tracking station is made of 4 layers staggered along z each comprising 26880 pixels. A complete description of the Silicon Tracker (SiT) is available in [95]. Fig. 3.18 shows the design inside the 217 m RPs which contain both SiT and ToF detectors. The staggered 3D pixel sensors are placed in front of the ToF detector. They are tilted with an angle of 14° to achieve a spatial resolution of 6 μm in the (x, y) plane.

Time-of-Flight Detectors The goal of the ToF detectors is to measure with a high precision the time difference between the arrival of a pair of protons in the forward and background AFP stations. If the two protons were from the same interaction (i.e. central diffractive protons), the position of the vertex as measured by the central tracks will be consistent with the position determined by comparing the time of flights. At high instantaneous luminosity,

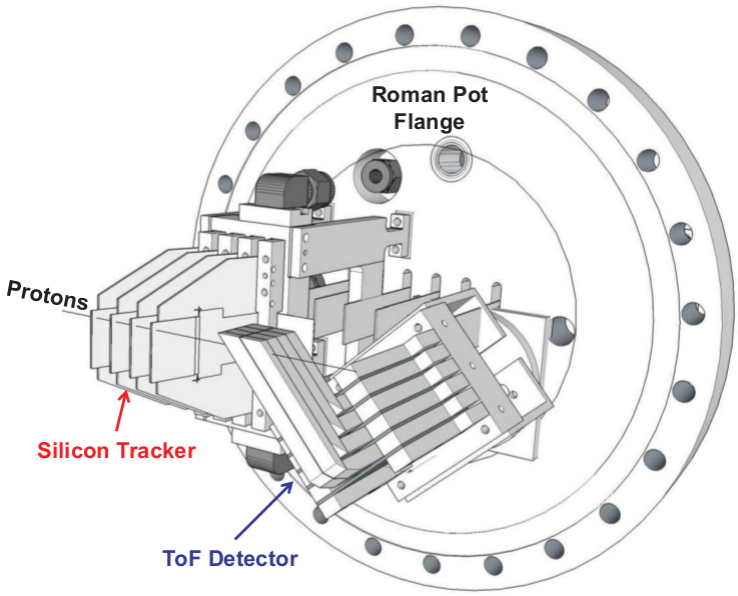

Figure 3.18: Design of the AFP detector including tracking and time of flight systems mounted on the Roman Pot flange. The diffractive protons arrive from the left.

when the number of protons coming from pile-up is high ($\mu > 50$), the timing system should have a small enough time resolution and be highly segmented in x to be able to distinguish coincidental protons.

The baseline timing system is a Quartz Timing Čerenkov detector (QUARTIC) which consists of quartz radiator bars coupled to Micro-Channel Plate PhotoMultipliers Tubes (MCP-PMT) to convert the light into a signal. The QUARTIC bars are oriented at the average Čerenkov angle with respect to the incident proton. This way, the length of the bars decreases with increasing z such that the effective path length of the Čerenkov light to the MCP-PMT is independent of where the photon is emitted along the path of the proton. The bars are functioning both as radiators, producing Čerenkov light when traversed by a relativistic proton, and as light guides that funnels the light to the phototube. The bending is done in such a way that the MCP-PMT can be installed along the x axis, i.e., as an

extension of the pot.

The ToF detector is equipped with fast timing electronics including High Precision Time to Digital Converter (HPTDC) chips that will collect signals and do the digitization. The chips are synchronized to the LHC beam crossing clock for triggering and time-of-flight difference measurement. Since the ToF detectors from both sides are widely separated, a feedback loop is implemented to correct for distortions of the clock signal through its propagation from the transmitter board to the location of the RP 210 m away.

The performance of the ToF detectors using data from 2016 is still under study, but preliminary test beams, gave a time resolution of 14 ps.

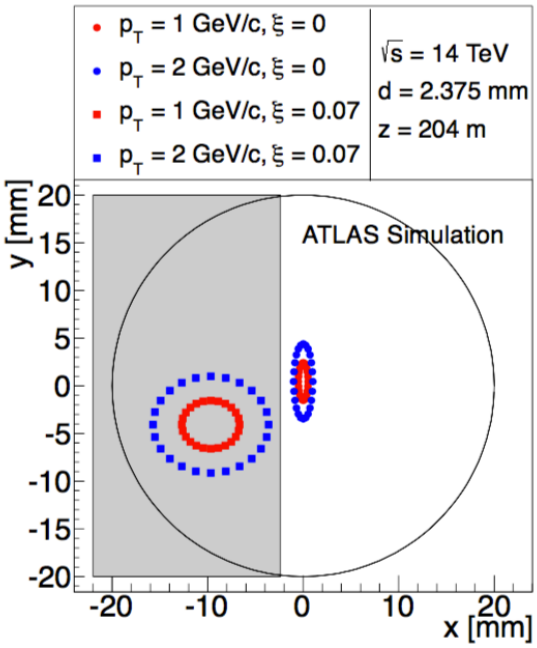

Figure 3.19: Positions of protons with different fractional energy loss (ξ) and transverse momentum (p_T) at the first AFP station for the LHC collision optics. The grey area show the AFP tracker detection area. Simulation taken from [90].

AFP Acceptance The dependence of the scattered proton track position in the AFP tracker on its energy and momentum is shown on Fig. 3.19. For that simulation, a center-of-mass energy was assumed. The most up-to-date version of the optic lattice and the collision configuration were used. The elastic hit pattern lies outside of the detection area which means that AFP typically measures only diffractive events. Fig. 3.20 shows a comparison of the acceptance of ALFA and AFP in terms of ξ and p_T. The AFP kinematic range with higher-than-80% acceptance is much larger than for ALFA when used within the design configuration.

3.3 Acquiring Data

During the 2012 data taking period, the proton bunches were set to cross every 50 ns which gave a collision frequency of 20 MHz. The time separation was later decreased to 25 ns

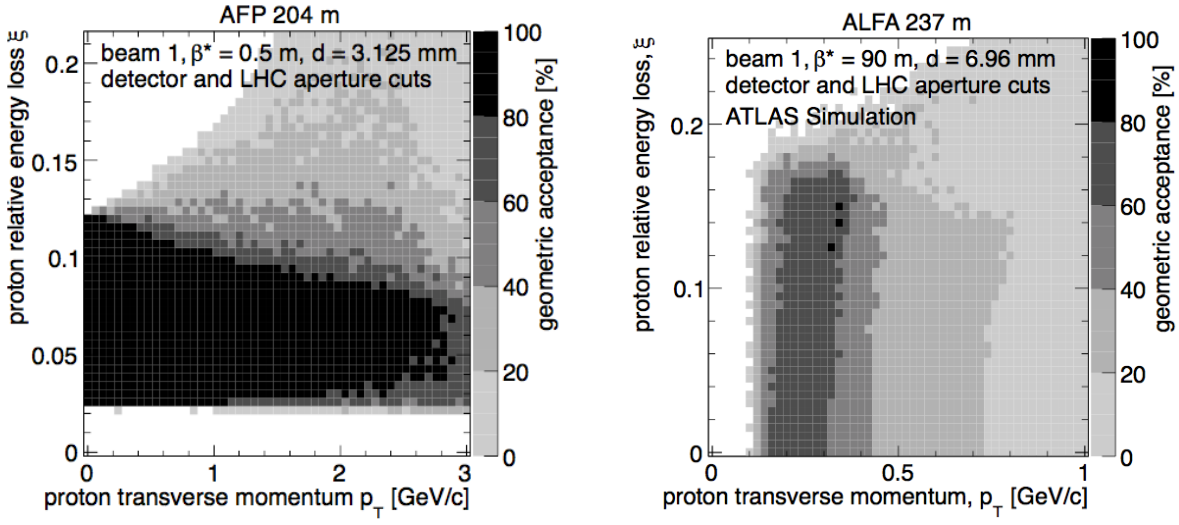

(a) AFP acceptance, for 14 TeV protons, with the LHC most recent optics and $\beta^* = 0.55$ m

(b) ALFA Acceptance, for 8 TeV protons, with the LHC 2012 optical setup and $\beta^* = 90$ m

Figure 3.20: Comparison of the AFP and ALFA simulated acceptances [90] in relative energy loss (ξ) and transverse momentum (p_T) used in their operational design conditions

to satisfy the design luminosity requirement, increasing the frequency by a factor 2. The detectors cannot read out and record information at those very high frequencies. A trigger system must be developed to select, on the fly, the events of interest and reduce the rate of information to be recorded.

3.3.1 Trigger Definition

Depending on the analysis, the triggers are chosen to satisfy a given topology. The event will be selected if it satisfies a set of topological criteria defined in a collection of *trigger chains*. The trigger chains give the set of observables to be measured above a certain threshold, for instance an electron with a transverse energy above a given value, for the event to be selected.

The frequency at which a given process is expected to occur defines the rate of information to be treated by the associated trigger. These rates vary a lot depending on the type of process considered. For very abundant processes like low energy scattering or dijet events, the rates may be *prescaled* by a given factor. A prescale value of 100, means that 1 out of 100 triggered events will be selected. A prescale of 1 means all interesting events are kept. Trigger thresholds and prescales are adjusted depending on the type of physics run. Events selected by a very loose trigger, i.e. with as few requirements as possible, are said to be *minimum bias events* as the bias introduced by the trigger selection is reduced. Events selected using a trigger that picks events randomly are said to be *zero bias events*. The complete set of trigger chains available in a run and their associate prescales is referred as the *trigger menu*.

3.3.2 Trigger Architecture

In this section, the trigger structure from 2012, time at which the data analyzed in Chapter 4 was taken, is presented. The state of the art trigger was made available after the Long Shut Down for the second ATLAS run campaign (Run II) in 2015. It includes in particular a new topological trigger system, a merging of the higher levels of the trigger: L2 and HLT described below, and the addition of a Fast TracKer (FTK) to provide track reconstruction at the trigger level. The interested reader is invited to see [96] for details about the trigger current architecture. In 2012, the ATLAS trigger system was comprised of three levels:

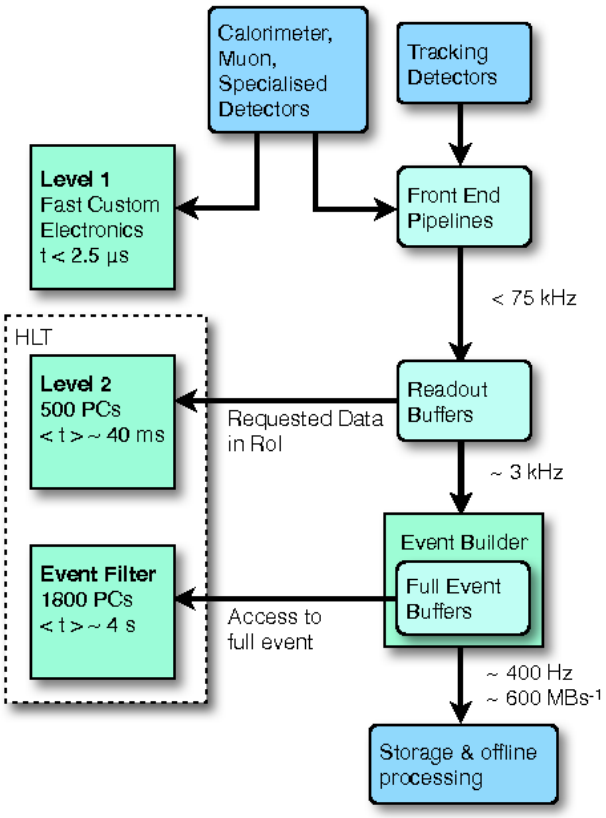

Figure 3.21: Schematic of the Run I architecture of the ATLAS trigger taken from [97].

Level 1 (L1), Level 2 (L2) and the Event Filter (EF). The action of each combined enables a reduction of the quantity of information to be recorded over time down to 200 Hz. Before

taking a decision, a trigger system must first wait for the detectors to complete their read-out and check if the signals collected satisfy a given chain criterion. Collecting the signals takes much longer than the frequency at which proton bunches collide. Hence, a performant system of storage must be available to buffer information from several collisions before they can be treated. The general architecture of the 2012 ATLAS trigger is depicted in Fig. 3.21.

Level 1 Trigger The L1 trigger reduces the event rate from 20 MHz to 75 kHz. It requires some level of activity in either the calorimeters or the muon systems, as these are the only detectors which can perform a simple reconstruction and trigger decision within 2.5 μs on an event-by-event basis. It uses the information from calorimeters towers (clusters of fired cells) to identify electrons, photons and particle jets. The muons are identified using the fast response spectrometers. In addition, several minimum bias triggers based on signals coming from the Minimum Bias Trigger Scintillators (MBTS), ZDC, LUCID or ALFA as well as zero bias triggers based on random signals are available.

The final trigger decision at L1-level is ordered by the Central Trigger Processor (CTP) which decides whether or not a prescale should be applied. The decision is then distributed to the individual sub-detector readouts, which stored signal information in their front-end electronic boards meanwhile.

Once an accept signal is received, one or several Region(s) of Interest (RoI) specifying the η and ϕ coordinates of the interesting object(s), are defined. The specific trigger requirements passed and the location of the RoIs are then sent to the L2 trigger. The rest of the information accepted is sent to some readout buffer.

Level 2 Trigger The L2 trigger reduces the event rate from 75 kHz to 3.5 kHz. It matches the inner detector information to the received RoIs and makes a decision by applying further energy thresholds and multiplicity requirements. Successfully selected events are then passed to the Event Filter.

Event Filter The final level of the trigger, the EF, is a farm of computers in charge of making decisions based on fully-reconstructed events. It allows to reduce the trigger rate to 200 Hz. It runs the standard ATLAS event reconstruction and analysis software and select the final set of events to be stored for offline analysis. The raw information is moved to a more permanent storage, Tier 0, where it gets converted into an object-oriented data format. The raw files are then distributed around the world to be converted into different formats for later analyses.

3.3.3 Trigger Chains and Streams

A trigger is named by a specific chain of items which specifies the level (`L1`, `L2`, or `EF`) at which the trigger selection is applied, and the type of signature it contains (e.g. jet: `J`, muon: `MU`, ALFA hit: `ALFA`, MBTS hit: `MBTS`. For instance `L1_J15` corresponds to the L1 trigger chain selecting jets with a transverse energy greater than 15 GeV, while `L1_ALFA_ANY` will trigger when at least one hit in one of the ALFA stations occurs. Different set of trigger chains are organized in *streams*. In the analysis presented in Chapter 4, the main triggers are taken from the `ALFA` stream. The `ALFA_Calib` and `minbias` streams were also used for background estimations (see Sect. 4.2.1).

3.3.4 The Minimum Bias Trigger Scintillator System

The MBTS system is the only detector in ATLAS whose primary purpose is to trigger on specific events. It was designed to form the trigger signals corresponding to minimum bias events during low-luminosity data taking. As it is known to be fully efficient in selecting low energy jets, it is also used as a reference to calculate the lowest threshold jet selection efficiency of calorimeter triggers. The MBTS plays a crucial role in selecting diffractive events and is therefore detailed in this section.

Since the 2012 data taking campaign, the MBTS went under some upgrade of its readout system and the replacement of some scintillators suffering from radiation. The design stays more or less the same, so the description given here is based on the initial technical report. The MBTS consists of two sets of 16 scintillating counters covering a pseudo-rapidity region of $2.09 < |\eta| < 3.84$. Each of the sets is composed of one inner and one outer ring made of 2 cm thick plates of polystyrene scintillator. Each counter comprises two pieces of scintillator glued together. Wavelength shifting fibres are embedded in grooves at the edges of the counters and down the center between the two pieces of scintillator (see Fig. 3.22). These optical fibres guide the emitted light to PMTs which are read out by the Tile calorimeter electronics. The signals are shaped so that the pulse amplitude is proportional to the amount of energy deposited in the counter. The total charge collected as well as the arrival time of the signal are recorded. This allows to use the MBTS not only as an online trigger for minimum bias events, but also as a particle counter recording information for offline analysis.

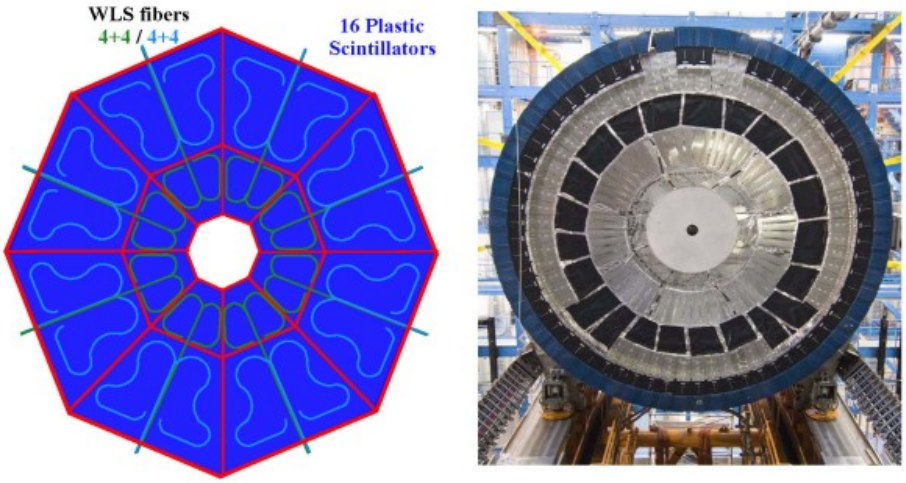

Figure 3.22: Schematic and picture of one of the MBTS wheels from [98].

3.4 Distributing Data

3.4.1 The LHC Computing Grid

The enormous amount of data produced from LHC collisions requires a high performance distributed computing system. This requirement is met through the deployment of a vast computing grid. The Worldwide LHC Computing Grid (WLCG) is composed of several levels of nodes, the *Tiers*. The events are initially recorded and reconstructed at the CERN-based Tier 0 (T0) data centre which represents approximately 20% of the total computing power of the WLCG. They are then either taped for long term storage or sent to the Tier 1 (T1) facilities. There are currently 11 Tier 1 centres dispatched all around the world which together account for 5% of the total computing power. They serve for data storage as well as sample reprocessing and analysis. The datasets can then be requested by Tier 2 (T2) centres, which are typically hosted by universities, and which provide additional computing resources for specific analysis. Individual scientists can access the Grid through local (Tier 3) computing resources, which can consist of local clusters in a university department or even an individual PC.

3.4.2 Data Formats

Datasets are available in a few main formats. Some of them are only accessible at the T0 and T1 level and they will not be detailed in this thesis. Among those available for direct analysis, the most detailed ones are the Event Summary Data (ESD), which contain all of the reconstructed information and are therefore very large in size. The ESDs are typically not stored except in certain cases where the specificity of the analysis requires them to be used. During Run I, the most broadly used format in ATLAS was the Derived Physics Data (D3PD). D3PDs are skimmed to keep only the relevant events and slimmed to keep only the relevant information on the remaining objects. The skimming and slimming procedures are defined by the working groups or analysis teams, and therefore final D3PDs contain only the events satisfying specific criteria (e.g. selection cuts, triggers). Run II analysis are now performed using the extended Analysis Object Data (xAOD) format which is discussed in [99]. For each step, datasets are given a named based on conventions [100] which explicits the type of events contained and when they were recorded, the reconstruction steps undergone, and the data format.

3.5 Modelling the Detectors

The stable particles produced by Monte Carlo generators after hadronization are often referred as *truth particles* as they are representations of the best knowledge we have of hadron interactions. The level giving the particle states before they get detected or lost due to detectors limitations is referred as the *particle level*. To provide the complete picture, particles must be transported from their production vertex to detectors. The interaction they may overcome on their way to the detector and the response of such detectors should also be simulated.

3.5.1 Geant4

GEANT4 [101] is the state of the art software used for this purpose. It typically simulates the hadronic and electromagnetic cascades starting from truth hadrons, then models the energy deposits (hits) caused by the cascade products and other non-showering particles and emulates the signal collection and digitization processes of the detectors. This level of information corresponds to what is called the *detector level*. A minimum bias event sample can also be overlaid to the initial truth sample. The response of the detectors due to this additional set of particles would thereby represent the effect of pile-up. The collected information can then be reconstructed in the same way as for real data. A full description of GEANT4 is available in the literature. The analysis presented in in Chapter 4 makes use of GEANT4 for the simulation of the particle interaction from the diffractive system and the production of showers with the ALFA station. Simulated protons are transported up to the ALFA station using a package, developed independently from GEANT4 and designed to emulate the optics over long distances, and which is discussed in the following section.

3.5.2 Forward Transport Packages

Protons coming from elastic scattering and diffractive events may be transported from the IP to the forward detectors using the full GEANT4 transport simulation through the optics. Since this full simulation is very time consuming, faster solutions have been developed to simulate the propagation of forward particles beyond 20 m [102]. The package `ForwardTransportSvc` was embedded in GEANT4 while `ForwardTransportFast` was designed to be used standalone. Both packages are based on a collection of classes already mentioned in Sect. 3.2.2, called `ForwardTracker` [92]. These packages are based on the following working principles:

- they will only transport GEANT4 stable particles entering the most forward beam pipe section that are identified as protons with a chosen minimum energy and pseudorapidity, and kill all other particles that do not satisfy these criteria,
- they will change the status code of the selected particle such that they are ignored by GEANT4 during the transport to the ALFA stations location,
- the selected particles will be tracked down the beam line by iterating over the beam line elements until they either go out of aperture or traverse an end tracking plane.

ForwardTransportFast The `ForwardTransportFast` package was developed for fast optics calculations and reconstruction studies. It was used by the ALFA group at the University of Copenhagen in order evaluate the impact of the optics on the parameterization of the proton kinematics from the ALFA hitmaps. The Copenhagen parameterization is used in the analysis presented in this thesis for the reconstruction of the proton kinematics in ALFA (see Sect. 3.2.2).

ForwardTransportSvc The `ForwardTransportSvc` package is embedded in GEANT4 and was used for the generation of all the simulated samples used in Chapter 5. Since only protons reaching the most forward region of the beam pipe are transported, this technique of transport is much faster than running GEANT4 over the full phase-space. One drawback however is that material-initiated showers can only take place after the protons reach their final transport position. Any shower happening upstream the ALFA station will not be simulated. The effects of unsimulated showers are discussed in Sect. 4.3.2.

Measurement of the Inclusive Single Dissociative Cross Section at 8 TeV with ATLAS

This chapter presents the most recent work of the student. It was performed in collaboration with Ph.D. candidate A. Foster (University of Birmingham, UK), and Dr. G. Gach, (Cracow Institute of Technology - AGH, Poland), with guidance from Prof. P. Newman, (University of Birmingham, UK). Contributions from the author started in March 2016, and include Monte Carlo custom configuration of private and public generation, event selection optimization, detector and background studies. The author also took part to the development of the background subtraction and unfolding techniques. The evaluation of uncertainties and their contributions to systematics is still evolving and is currently performed by another student. The contributions from all analyzers are presented according to the supporting note recently submitted to the analysis group conveners. Following the ATLAS publication guidelines, an editorial board was requested in January which will lead to a journal publication by the end of 2018.

In this chapter, the full analysis of single-diffractive events selected from a 24.11 nb^{-1} sample collected by the ATLAS experiment during $\sqrt{s} = 8$ TeV pp collisions at LHC in 2012 is presented. The inclusive cross section for such events was measured differentially in ξ, $|t|$

and $\Delta\eta$ and corrected to get back to the particle level of data for comparison with theoretical predictions. These observables are defined hereafter.

Momentum Transferred Squared This analysis makes use of the information of the track hitmaps in ALFA to reconstruct the $|t|$ observable using principles discussed in Sect. 3.2.2.

Fractional Energy Loss The fraction energy loss of the intact proton is measured with two ways:

- either it is reconstructed from the proton kinematics in ALFA using Eq. 2.43, and in this case it is referred to as ξ^p,
- or, it is reconstructed from the kinematics of the particles composing the diffractive system (see Eq. 2.4.2) using the following approximation:

$$\xi_{Ep_z} = \frac{\sum_i (E^i \mp p_z^i)}{\sqrt{s}} \tag{4.1}$$

  where i runs over all particles measured in the inner detector, with energy E_i and longitudinal momentum p_z^i and the $\mp$ sign depends on the direction of the scattered proton. However, neutral particles are not visible in the inner detector. In addition some charged particles of the diffractive system may escape the inner detector acceptance and remain undetected due to the intrinsic detection threshold of the detector. The reconstructed value of ξ using this technique will therefore underestimate the true value.

Fig. 4.1 shows the distributions of the reconstructed values of ξ_{Ep_z} and ξp compared with the truth for single diffractive simulated events. The complementary coverages of the two measurements appears clearly. The underestimation of ξ when using the inner detector information is also visible.

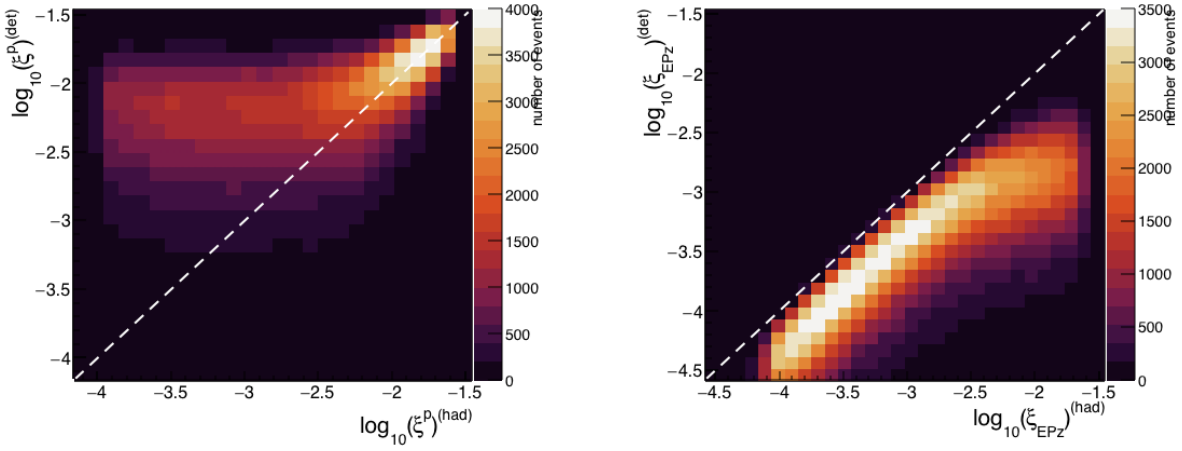

(a) (b)

Figure 4.1: Distribution of the reconstructed and truth ξ using the information from the reconstructed proton in ALFA (a) and using the information from the reconstructed diffractive system in the inner detector (b).

Rapidity Gap Instead of measuring the gap from the proton directly, it was chosen to measure it with respect to the inner edge of the inner detector on the side of the proton tag. Rapidity gaps measured using this definition are denoted $\Delta\eta^F$. This allows comparison with a previous rapidity gap study [103] where this variable was used. Since there are five units of rapidity from the positive-z edge to negative-z edge, the maximum measurable $\Delta\eta^F$ is 5. This can clearly be seen on Fig. 4.2 showing the rapidity gap measured from the edge of the inner detector on the proton side.

The effect of having a vertex displaced along z with respect to the ATLAS coordinate origin was investigated. The maximum angle spread will be for two tracks perpendicular to the z-axis originating from vertices located at a 12 cm distance from each other, corresponding to the typical size of the interaction region. In this case, the maximum difference in rapidity (neglecting the effect of the magnetic field) is calculated to be smaller than 0.5, the size of

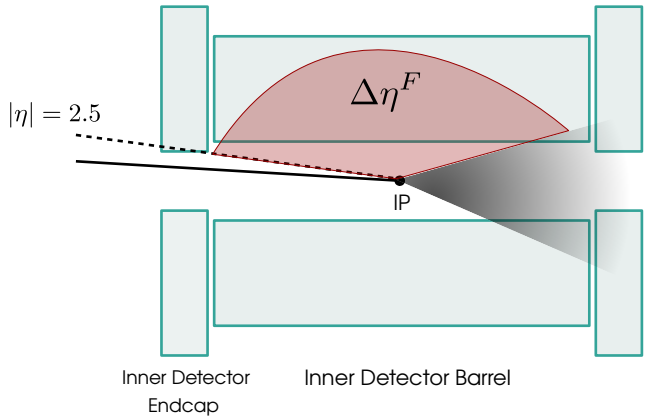

Figure 4.2: Sketch showing the span of the rapidity gap (in red) observed between the diffractive system (black spray) and the edge of the inner detector on the side of the proton forward tag.

the binning used in this analysis for the $\Delta\eta^F$ distribution. As most of the tracks used to define the diffractive system have larger rapidities, the typical shift in rapidity due to a longitudinal shift of the vertex position will be very small on average and is thereby neglected. For the x and y vertex positions, the spread is typically two orders of magnitude smaller and its effect, maximized for tracks at the most forward edge of the inner detector, is therefore also neglected.

It is the first time in ATLAS that such cross section is measured with respect to all three observables. In the absence of information from forward proton detectors, previous studies [103][104] were only able the measure the cross section with respect to the size of the rapidity gap.

The signal yield per bin in the variable of interest, $n_{\text{sig}}^{\text{reco}}$, is determined by subtracting the expected number of background events, $n_{\text{bkg}}^{\text{reco}}$, from the reconstructed number of events, corrected for the trigger inefficiency (ϵ_{trig}). Monte Carlo simulations are used to evaluate

$n_{\text{bkg}}^{\text{reco}}$. A correction factor C is applied to Monte Carlo events to compensate for mismodelling effects. Detector effects (resolutions, calibrations, geometrical acceptance constrains and limited reconstruction efficiency) are all corrected for by means of an iterative Bayesian unfolding, a transformation (U^{-1}) accounting for event migration between bins. A final division by the total integrated luminosity L of the run considered will give the cross section with respect to the variable of interest :

$$\frac{d\sigma}{dx} = \frac{1}{L} U^{-1} \left[\frac{1}{\Delta x_i} \left(\frac{n_{\text{sig}}^{\text{reco}}}{\epsilon_{\text{trig}}} - C n_{\text{bkg}}^{\text{reco}} \right) \right] \tag{4.2}$$

where U^{-1} corresponds to the correction to be applied to the bin extracted and depends on the choice of unfolding procedure.

Details about the Monte Carlo simulation performed for this analysis are given in Sect. 4.1. The way the data is collected and selected is detailed in Sect. 4.2. The sources of background are discussed in Sect. 4.3. The corrections applied to account for detector effects are discussed in Sect. 4.4. The systematic uncertainty contributions are presented in Sect. 4.5. In Sect. 4.6, preliminary distributions at particle level are compared with theoretical predictions and discussed.

4.1 Monte Carlo Simulations

The main control samples used in the analysis were produced by the ATLAS grid production team after approval of the ATLAS Standard Model group conveners. Several iterations were necessary, that required the author to test the generation of the matrix elements, the simulation of the detector response and the reconstruction of events, and to help with the configuration of the grid jobs by experts. The full generation process took a full year, from

the first test ran by the analysis team to the last sample to be made available on the grid.

Monte Carlo samples are used at different levels in this analysis:

- Simulated distributions of the observables of interest at the reconstruction level are used to subtract the background components coming from double-, central- and non-diffractive events exhibiting a single-diffractive signature (see Sect. 4.3.1). The choice of model used in the simulation introduces a bias which is accounted for as a systematic uncertainty (see Sect. 4.5).

- Simulated distributions at the truth level are compared with unfolded data (see Sect. 4.6) to test the theoretical assumptions on the kinematic dependences of diffractive observables (see Sect. 2.5).

Event Generation The event generation was done using the ATLAS data derived A2 [105] and A3 [106] tunes. The A2 tune is based on the first ATLAS run campaign (Run I) minimum bias data. It takes the PDFs (Parton Distributions Functions) of the proton from the MSTW2008LO [107] fit, extracted from pre-LHC data. For this tune, diffraction is modeled assuming a SaS (Schuler and Sjöstrand) Pomeron flux. The A3 tune is based on a larger set of samples including minimum bias data from $\sqrt{s}$ = 900 GeV, 7 TeV and 13 TeV data taking campaigns. The PDFs are taken from a more inclusive fit as well, the NNPDF2.3 [108] at leading order. In addition, A3 is derived from the Monash 2013 tune [109] which uses a different model than A2 for the MPI. It assumes a DL (Donnachie-Landshoff) Pomeron flux by default, which was shown to better model the inelastic cross section and the minimum-bias observables [106].

Detector Simulation and Reconstruction The detector simulation was performed using GEANT4 for all the particles generated in the central detectors acceptance. As detailed in Sect. 3.5.2, protons were propagated to the ALFA stations with the `ForwardTransportSvc` package with constraints on the energy and pseudo-rapidity of the transported particle: $\xi < 0.8$ and $\eta > 7.5$. The interactions of successfully transported particles with the ALFA stations was modeled by GEANT4. The central detector activity was reconstructed using standard ATLAS software packages, and the reconstruction of the proton kinematics in ALFA was performed using the Copenhagen reconstruction package (`ALFAReco`).

Limitations Due to incompatibilities between the `ForwardTransportSvc` package and the tool used to simulate in-time pile-up, `PileUpTool` (see Sect. 3.1.2), it was chosen to disable pile-up emulation for all the samples generated for this analysis. In addition, protons from the halo of the beam traveling outside its defined emittance are not simulated by GEANT4. Backgrounds originating from halo protons are therefore not visible in the simulated ALFA detector response (see Sect. 4.3.2).

The general usage of the samples generated is summarized in Table 4.1. Also listed are the cross sections for each diffractive and non-diffractive components based on the Schuler and Sjöstrand prescription. These cross sections are used by default for all the control plots shown in the thesis.

DSID	Tune	Type	Model	σ [mb]	Stat.	Usage
207324	A3	SD	DL (default)	12.48	8 M	Unfolding
207330	A3	DD	DL (default)	8.254	1.0 M	Background subtraction
207331	A3	CD	DL (default)	1.211	0.5 M	Background subtraction
207332	A3	ND	DL (default)	50.91	0.5 M	Background subtraction
Private	A2	SD	SaS (default)	12.48	1M	Model dependence
Private	A3	Elastic	DL (default)	19.89	1M	ALFA reco. efficiency

Table 4.1: Summary of the Monte Carlo PYTHIA8 simulation datasets and their usage in the analysis. The DSIDs are serial numbers used in the sample production.

4.2 Data Collection and Selection

This analysis makes use of a single run, run 206881, which took place in July 2012 during the Run I data taking campaign. For this low luminosity run (with an average pile-up $\langle\mu\rangle = 8.16 \cdot 10^{-2}$), the $\beta^* = 90$ m optics (see Sect. 3.1.2) was used. For this special run, there was no crossing angle between the beams. A beam-based alignment of the RPs (Roman Pots) with respect to the beam (beam scrapping discussed in Sect. 3.2.2) was performed before data taking. The ALFA detector positions inside the RPs were determined afterwards by selecting elastic events and evaluating their hit profiles. The alignment procedure and final values were already given at Sect. 3.2.2. The luminosity block range [398-630] was used, corresponding to data taken during stable beams, and amounts to an integrated luminosity of $(16.748 \pm 0.34)\,\text{nb}^{-1}$. Only the events leaving signals in the central detectors in coincidence with a single proton tag were recorded. The scattered proton is required to leave a good quality track on one side of the detector, while several hits are present in the ATLAS detectors on the opposite side as shown on Fig. 4.3. For this reason, the ALFA, MBTS and tracking detectors must be fully operational. The calorimeter information was recorded but not used due to latency issues.

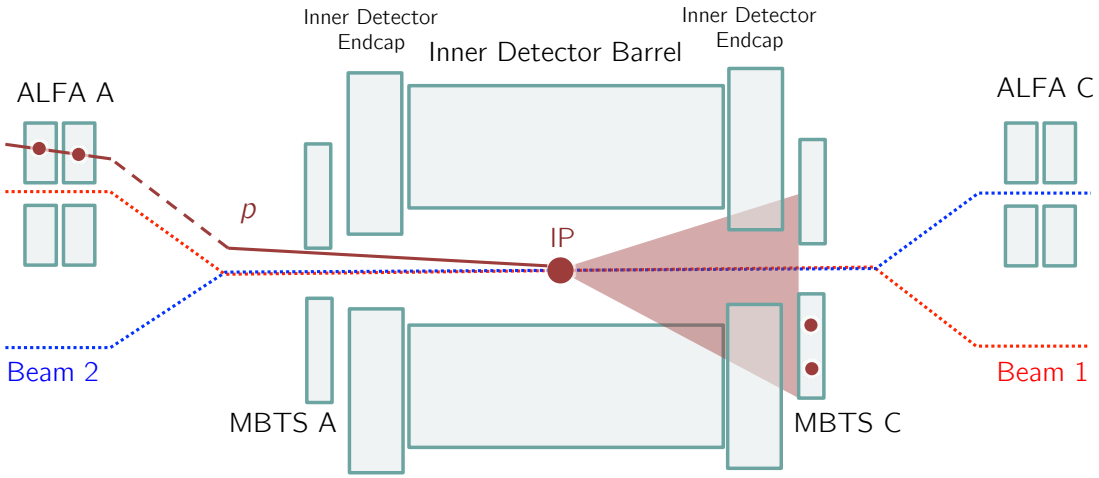

Figure 4.3: Sketch of the typical selection of single-diffractive events. In this case, the scattered proton is tagged in the ALFA stations on side A and the diffractive system (shaded area) hits the MBTS system on side C and is partially recorded by the inner detector.

4.2.1 Online Selection

Events are selected on the fly using the `L1_MBTS_2_A(c)_ALFA_C(A)` unprescaled triggers (see Sect. 3.3.3), which require at least two MBTS counters to have a signal above threshold on side A (side C) in coincidence with a hit in the ALFA trigger tiles on side C (side A). The prescale and the limited efficiency of these combined triggers are accounted for in the calculation of the cross section (see Sect. 4.4.1). The list of all trigger chains, their associate stream and usage is given in Table 4.2 as a reference. Further details are given in the next sections. In this chapter, the term *central detectors* is used to designate the MBTS and Inner Detector systems.

4.2.2 Offline Selection

Trigger chains	Streams	Usage
L1_MBTS_2_A(c)_ALFA_C(A)	ALFA	Event selection
L1_RD0_FILLED	minimum bias	MBTS threshold determination
ALFA_UNPAIRED_ISO	ALFA	Beam halo background estimation
EF_mbSpTrk	ALFA	Trigger efficiency calculation
L1_MBTS_2	minimum bias	Beam-gas background estimation
L1_LUCID	ALFA calibration	Trigger efficiency systematics
L1_ALFA_ELAST15(18)	ALFA	ALFA reconstruction efficiency calculation

Table 4.2: Summary of the trigger chains used in the analysis showing the stream they are taken from and their typical usage.

Diffractive System Selection

MBTS Offline Selection The trigger used in this analysis requires at least two MBTS counters firing with a charge above the trigger threshold on the side opposite to the ALFA tag. The charge collected per event per counter is recorded for offline treatment. Among events passing the combined trigger requirements, only those cumulating at least five counter hits are kept. Such selection was chosen to minimize the impact of the trigger efficiency (see Sect. 4.4.1). A hit is defined when the charge in the counter is above a threshold determined a posteriori for both Monte Carlo and randomly-triggered data.

Disagreements were observed in the number of MBTS hits for the Monte Carlo and the data. Those were partially mitigated by requiring a minimum of five hits for the diffractive system selection. Strategies to account for such mismodelling, including a "reweighting" of the Monte Carlo, are being discussed with the editorial board at the time this thesis is written. The background contributions yielding activity in the MBTS are beam-halo, beam-gas interactions and afterglow. None of them are modeled in the simulation, but their contributions are discussed hereafter and estimates are given in Sect. 4.3.

Non-Collision Backgrounds

Three phenomena may affect the measurement: *beam-gas* background, generated by particles created when the beam interacts with some particle gas inside ATLAS, *halo* background, arising from scattered particles circulating with the beam, and cavern radiations, or *afterglow*, which is correlated to the physics activity happening during a given bunch crossing (in-time afterglow), or in the preceding crossings (out-of-time afterglow). Beam-gas and beam-halo backgrounds are quantified using isolated unpaired bunches where no activity other than in-time beam background is expected in the central systems. The afterglow contributions are more difficult to estimate as they depend on the type of activity happening in ATLAS before and during the bunch crossing of interest. Their effect are expected to be non-significant for such a low luminosity run. They were therefore not investigated over the time allocated for the thesis.

Offline charge thresholds are set based on the analysis of the noise distribution in each MBTS segment. The noise signal in the MBTS is generated by dark current in the PhotoMultipliers Tubes (PMTs) and by the read-out electronics. It is typically well described by a double Gaussian. However, the amplitude of the second Gaussian was proven to be small [110] and a single Gaussian can be used for simplicity. Fig. 4.4 shows the charge profile for MBTS counter-0 for data triggered randomly using the `L1_RD0_FILLED` trigger, and for minimum bias Monte Carlo scaled to the data luminosity. The symmetrical peak centered on zero corresponds to the noise profile from which the threshold is defined. The region above the noise peak corresponds to charges coming from true particle energy deposits. In this region,

the event multiplicity is lower for data, since the sample was randomly triggered and thus contains a larger fraction of events with no physics activity. Monte Carlo and random data also exhibit different shapes. In the simulation, the response of the segments was tuned to earlier data and does not account for the most recent effects of aging of the scintillating plates nor the possible electronic alterations.

The offline threshold is extracted by fitting a Gaussian function to the noise in the charge profile of each MBTS counters and taking the right value 4 standard deviations away from the mean of the Gaussian. The probability to trigger on two fake hits or one true hit and one fake, was proven from simulation to be negligible.

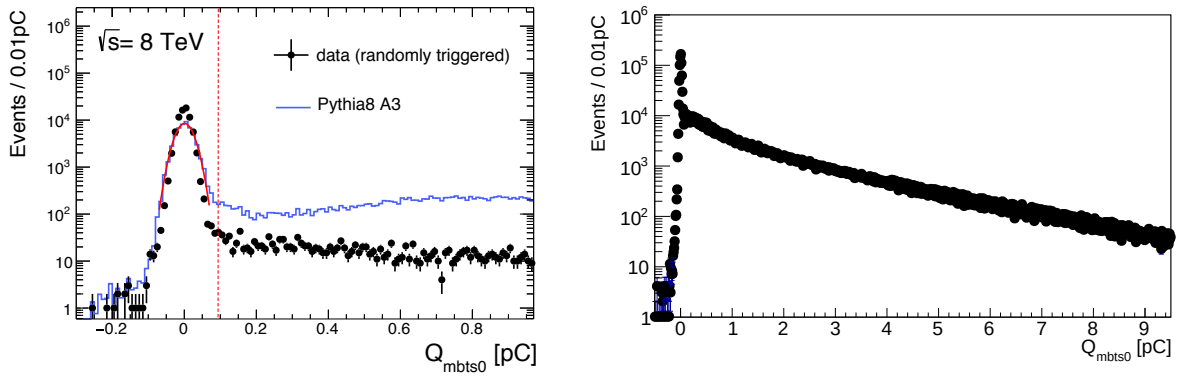

Figure 4.4: Left: Distribution of charges collected in counter-0 of the MBTS C system. The data, in black, is randomly triggered which favors the electronic background over physics signal. The Monte Carlo simulation, in blue, contains minimum bias events and is normalized to the data over the full charge range. The red line corresponds to the Gaussian fit to the Monte Carlo and the dashed line shows the location of the cut for the Monte Carlo. For readability, only charges below 1 pC are presented but the distribution is extending to 100 pC. Right: Charge collected in counter-0 for the data selected by the standard analysis trigger showing part of the tail of the distribution.

Inner Detector Selection Events passing the `L1_MBTS_2_A(c)_ALFA_C(A)` triggers are required to have at least one track with a transverse momentum $p_T > 200$ MeV, to match the reference trigger used in the trigger efficiency calculations (see Sect. 4.4.2). The following track selection cuts, recommended for minimum bias events in ATLAS, are applied to tighten the quality of all tracks:

- inner detector acceptance cut: $|\eta| < 2.5$
- 1 hit in the Pixel B-Layer if the extrapolated track passes through a sensitive region of an operational module therein,
- ≥ 1 hit in the Pixel detector,
- ≥ 2, 4 or 6 hits in the SCT for tracks within 100$< p_T <$200 MeV, 200$< p_T <$300 MeV or $p_T >$300 MeV, respectively,
- a track-fit with a χ^2 probability >0.01[1] for tracks with $p_T >$10 GeV to remove mis-measured tracks with very high reconstructed transverse momentum due to issues with the detector alignment or high occupancy,
- a transverse and longitudinal impact parameter of $|d_0^{\mathrm{PV}}| < 1.5$ mm and $|z_0^{\mathrm{PV}} \sin\theta| <$ 1.5 mm[2] respectively, measured with respect to the reconstructed primary vertex, to remove non-primary tracks.

As the proton and the dissociative system travel in opposite directions in the detector reference frame, the proton tagging on either sides of the detector is what imposes the directionality of the event. Details about the tagging are given in the next section.

[1] This probability is computed as $1 - P(n_{\mathrm{dof}}/2, \chi^2/2)$, where $P(n_{\mathrm{dof}}/2, \chi^2/2)$ is the incomplete gamma function and n_{dof} is the number of degrees of freedom of the fit. It represents the probability that an observed χ^2 exceeds the observed value for a correct model.

[2] θ is measured with respect to the beam line.

Proton Selection

In order to reduce the amount of background, it is required that exactly one proton is reconstructed in one of the four arms of ALFA. A proton is reconstructed by pairing a single qualifying track in the near ALFA station with a single qualifying track in the far station of that same arm. Qualifying tracks are the ones satisfying the criteria listed hereafter.
In this thesis, we define:

- an **armlet**, as a pair of aligned far and near stations, for instance B7L1U + A7L1U (see Fig. 3.11),
- an **arm**, as two diagonally opposite pairs of aligned far and near stations. ALFA has two arms B7L1U+A7L1U+B7R1L+A7R1L and B7L1L+A7L1L+B7R1U+A7R1U (see Fig. 3.11) ,
- a **track segment**, as a track reconstructed in a given station,
- a **track**, as a track reconstructed from two track segments, one in each station of an armlet.

Tracks Reconstruction To limit the amount of mis-reconstructed tracks, tracks in a station are required to have at least six overlapping hit fibers in both the U and V planes. Where more than one track is reconstructed in an individual station, the track with the most overlapping fibers is selected and is referred in the thesis as the *primary track*. With the requirement of at least 6 U and 6 V plane fiber hits, only 1% of events after full selection have more than one track per detector. The efficiency of the track reconstruction in ALFA is studied in Sect. 4.4.2.

Tracks Fiducial Cuts The proton track formed by the two stations hits has to be contained in the fiducial volume of ALFA. This is achieved by imposing two cuts on the vertical coordinate of the track:

- Tracks are required to be at least 90 μm away from the physical detector edge close to the beam to ensure a maximal efficiency of the fiber. The position of the edge is determined from elastic data taken with the same beam configuration.

- Protons hitting the beam screen, a protection element of the quadrupoles, will generate hadronic showers whose fragments may reach the ALFA acceptance and be misinterpreted as protons. Therefore, collected tracks are required to be at least 1 mm away from the *shadow* of the beam screen, i.e. its projection surface on the ALFA detection area. The beam screen shadow was determined by looking at hit patterns from a sample from the same physics run where no beam screen cut is applied [111].

The position of the vertical edge cuts for each detector are given in Table 4.3 and the edge and beam screen cuts are shown on Fig. 4.5a for station B7L1U. Fig. 4.5b shows the hitmap after the full selection is applied including the correlations cuts detailed hereafter.

Correlation Cuts Further geometrical constraints are derived from the analysis of the correlation pattern between the average x-position of the track between the near and far stations in the LHC coordinate system, $\bar{x} = (x_{\text{near}} + x_{\text{far}})/2$ and the local angle the track makes in the (x, z) plane, $\theta_x \approx (x_{\text{near}} - x_{\text{far}})/(z_{\text{near}} - z_{\text{far}})$.

Fig. 4.6 displays the $(\bar{x}, \theta_x)$ profiles in the upper forward armlet for the SD (Fig. 4.6a), CD (Fig. 4.6b), DD (Fig. 4.6c) and Non Diffractive (ND) (Fig. 4.6d) Monte Carlo A3 samples, for all ALFA primary tracks satisfying the far and near selection criteria and passing the

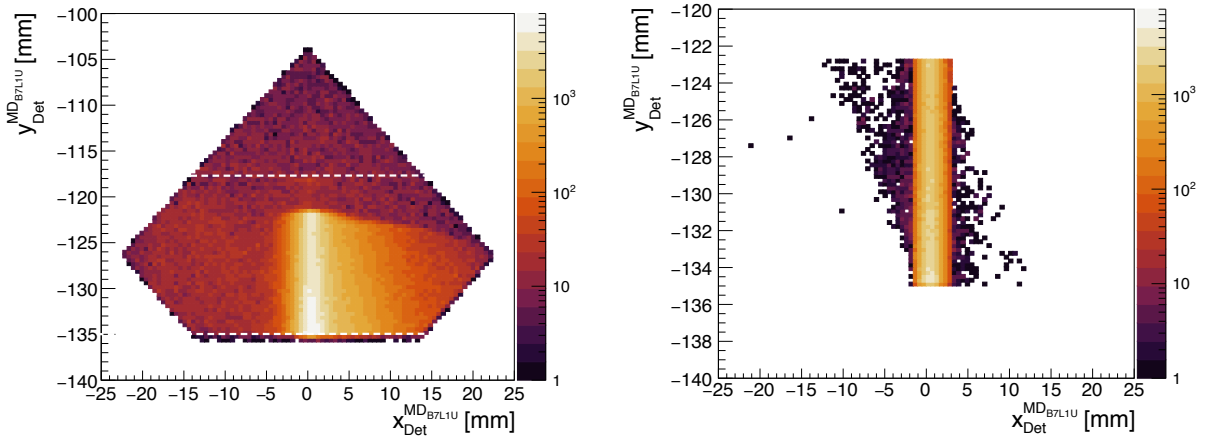

(a) (b)

Figure 4.5: Hit maps for the reconstructed primary tracks in station B7L1U obtained for data events satisfying the analysis standard selection criteria without any requirement on the track position in the stations (a) and when applying the bivariate Gaussian track selection (see paragraph "Correlation Cuts") and the track fiducial cuts (b). The upper dashed lines indicates the beam screen cuts. The lower dashed line corresponds to the edge cut. Coordinates are given in the detector reference frame. The color scale indicates the number of primary tracks reconstructed.

Roman Pot	Detector edge cut [mm]	Beam screen shadow cut [mm]
0	8.071	20.2569
1	-8.152	-18.8136
2	8.472	21.3361
3	-8.477	-19.7859
4	8.441	20.3758
5	-8.369	-20.6309
6	8.091	19.3522
7	-8.109	-19.6288

Table 4.3: Detector edge and beam screen shadow vertical selection in LHC coordinates for the Roman Pot of each ALFA station.

fiducial cuts, from events passing the central detector selection criteria. Similar profiles are obtained for the other arms. Fig. 4.6a shows that diffractive protons are concentrated about the (0,0) center of the ($\bar{x}$, θ_x) distribution. The CD, DD and ND Monte Carlos show that tracks are distributed inside a region stretching in the positive $\bar{x}$ and θ_x directions which overlaps with the signal region. The tails of the distributions correspond to tracks with a bigger local angle. These tracks deviate quite a lot from the $\bar{x} = 0$ position, and are therefore assumed to be mostly populated with tracks from real forward protons created though QCD fluctuations. A steep-slope low multiplicity trail spreading over a large range in θ_x is visible. Such tracks are typically reconstructed when a real proton track segment in the close station is paired with a background track in the far station. Most background tracks recorded in the far station are expected to come from showering and will therefore spread over non-zero θ_x's, while most proton tracks are coming from real SD protons, which concentrate inside a 2-dimensional Gaussian region, with small θ_x. The combination of a signal-initiated track segment in the close station with a background-initiated track segment in the far station, will result in the typical low-multiplicity correlation patterns clearly visible on Fig. 4.6a and Fig. 4.6b.

Inspired from previous elastic studies [25, 94], a signal-enhanced region was defined by fitting the SD Monte Carlo correlation pattern with a bivariate Gaussian for each station (see Fig. 4.7) and using the 3σ contour as the selected region in both data and simulation. The 3σ contour was favoured as it maximized the signal significance by removing 63.1% of the tracks from the CD, DD and ND contributions while keeping 67.8% of the SD events. The SD and CD+DD+ND acceptances and their ratios, obtained from selecting the 2σ and 4σ contours instead of 3σ, are given in Table 4.4 for comparison. It was also proven to

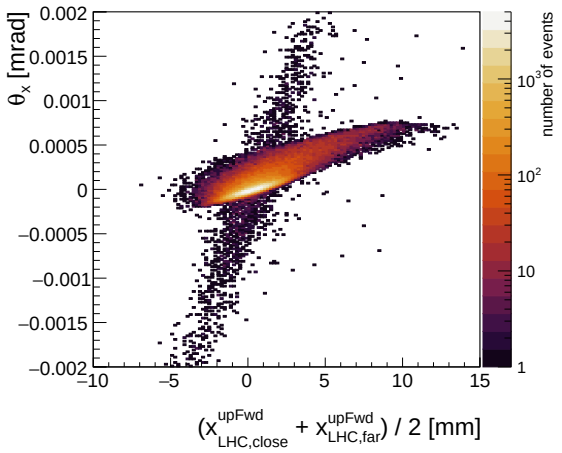

(a) SD Monte Carlo before $\bar{x}$ and θ_x selection

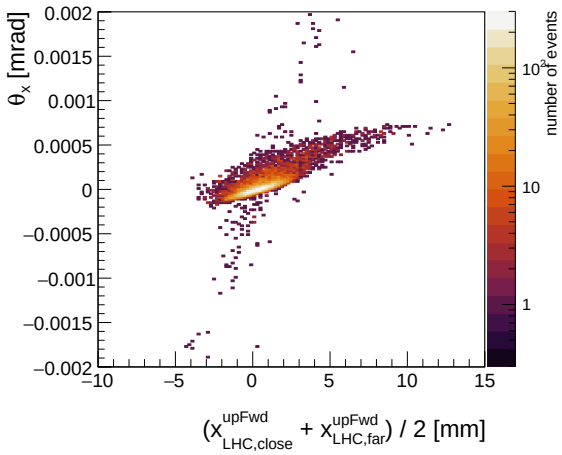

(b) CD Monte Carlo before $\bar{x}$ and θ_x selection

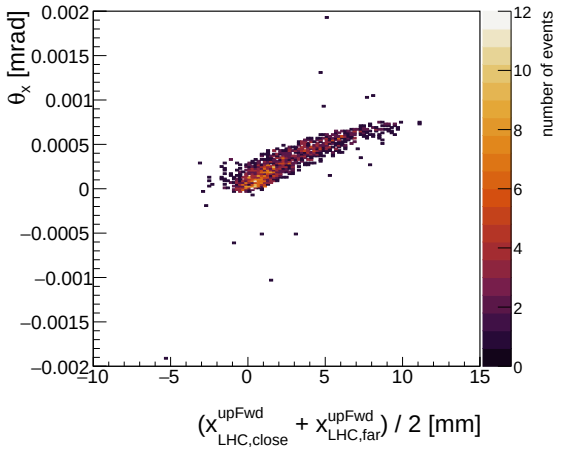

(c) DD Monte Carlo before $\bar{x}$ and θ_x selection

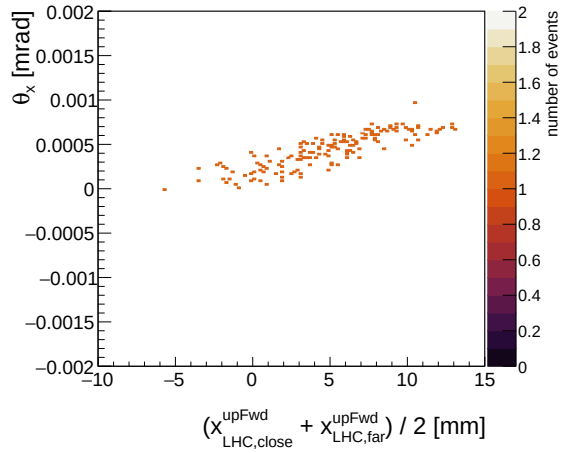

(d) ND Monte Carlo before $\bar{x}$ and θ_x selection

Figure 4.6: $\bar{x}$ vs θ_x correlation patterns for SD(a), CD(b), DD(c) and ND(d) Monte Carlo simulations. The high multiplicity correlation trail is populated by tracks coming from real SD protons and protons from QCD fluctuations. The low multiplicity trail, exhibiting a steep slope, corresponds to fake tracks generated when a shower track in the far station is paired with a signal track in the close station. Color scales along the z-axis were adjusted for each sample depending on the multiplicity of tracks. No cross-section scaling is applied.

$(\bar{x}, \theta_x)$ selection	SD acceptance, A_S	CD+DD+ND acceptance, A_B	$\frac{A_S}{A_B}$
None	1.000	1.000	1.000
2σ ellipse	0.530	0.293	1.811
3σ ellipse	0.678	0.369	1.835
4σ ellipse	0.747	0.408	1.830

Table 4.4: Signal and simulated background acceptance, and their ratio, for events passing the bivariate Gaussian track selection in ($\bar{x}$,θ_x), using multiples of the width as the selection contours. Values come from [112].

improve the measurement of ξ extracted from the proton kinematics by cutting away most of the showers.

The same correlation plot generated from data tracks, displayed on Fig. 4.8, shows the contribution of non-simulated backgrounds overlapping with the signal selection region. The quantitative approach designed to assess their background contributions in the signal region is detailed in Sect. 4.3.2.

Fiducial Region of the Analysis

In this analysis, observable distributions and cross sections are shown for a defined fiducial range. The *fiducial region* is defined as the nominal coverage of these observables that would be accessible given the event selection imposed in the analysis, if there were no detector effects. A cross section measured in the fiducial range of an observable and corrected for detector effects can later be extrapolated to the full phase space for comparison with theoretical predictions.

The fiducial range for the ξ and t observables is estimated from simulation calculating the selection acceptance by counting the number of events passing the selection over the total number of events in each bin of the observable of interest. Fig. 4.9 shows that there is very

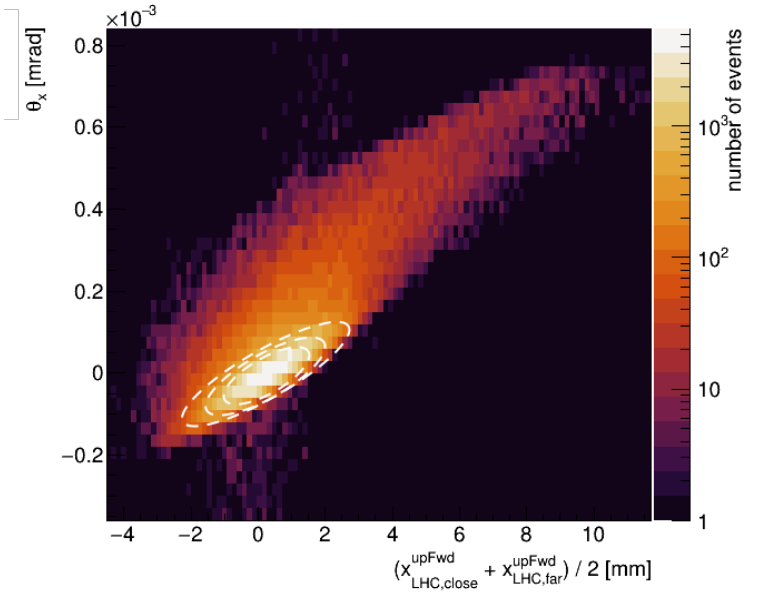

Figure 4.7: Simulated correlation map for the SD Monte Carlo proton tracks coming from events passing the central detector selection. The dashed ellipses indicate the 2σ, 3σ and 4σ contours of the bivariate Gaussian fit.

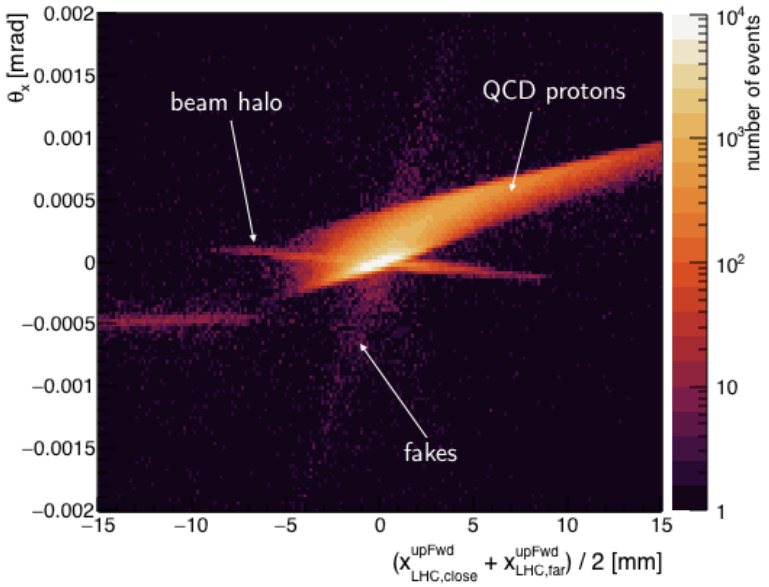

Figure 4.8: Correlation map for proton tracks from the data coming from events passing the standard selection without the requirement on the track position. The origin of the bottom left band around $\theta_x = -0.005$ is unknown but this background does not overlap with the selected region.

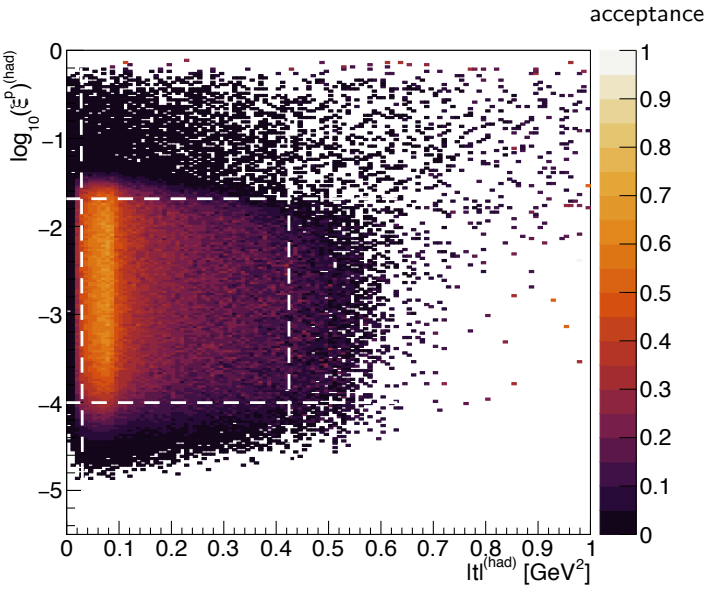

Figure 4.9: Selection acceptance for ξ^p and $|t|$. The dashed lines show the fiducial region contour cuts.

little correlation between the ξ and $|t|$ acceptances, and therefore a square fiducial area is chosen. The boundaries of the fiducial region are defined as the value at half maximum of the ξ^p acceptance plateau and, since the acceptance in $|t|$ is not flat, the fiducial range in $|t|$ is taken to be that where the acceptance is greater than 10%. Since the size of the rapidity gap is completely correlated to ξ and $|t|$, it is not considered in the definition of the fiducial region. The fiducial region of this analysis is:

- $-4.0 < \log_{10}(\xi) < -1.6$,
- $0.016 < |t| < 0.43$ GeV^2.

4.3 Background Sources

Coincidental Contribution The source of physics background in the analysis may come from the combination of two occurrences, when at least one of the signals measured is

background:

1. a proton-like signal is recorded in ALFA on only one side of ATLAS,

2. a diffractive-like activity is recorded in the inner detector on the side opposite to the ALFA signal side.

These backgrounds are accounted for by means of the Monte Carlo simulations and using data-driven techniques for contributions that are not simulated.

Contributions due to Fake Tracks or Absence of Signal in ALFA When two or more particles traverse the ALFA detection area at the same time, the ALFA tracking algorithm may reconstruct a fake track or fail. Most fake tracks should lie at a 45 degree angle in the detector coordinates, which corresponds to the mean position obtained from averaging the signal hits and the beam halo hits positions [93]. Such pattern is however not observed (see Fig. 4.5a) and fakes are therefore considered to be negligible in this study. The probability of a failure of the reconstruction algorithm, i.e. no track reconstructed, is calculated for both data and simulation using a *tag and probe* technique detailed in Sect. 4.4.2. The Monte Carlo simulation is scaled to match the reconstruction efficiency of the data before unfolding. When happening in the case of a central-diffractive or elastic event, a failure on one side may cause the event to be promoted as signal-like, if it simultaneously satisfies the central detector requirements.

4.3.1 Simulated Background Sources

Background proton signatures modeled by the Monte Carlo arise from :

- high energy forward protons produced via QCD fluctuations,

- real diffractive protons from CD interactions,
- showering happening inside an RP or in between the two RPs (upstream showers are not simulated and should be accounted for by other means).

When coincidental to a diffractive-like signal in the inner-detector, these fake single-side protons would mimic a single diffractive signature.

The fractions of simulated background events passing the selection are given in Table 4.5. The uncertainty coming from the theoretical assumptions in the simulation are accounted for when subtracting such backgrounds to the reconstructed data (see Sect. 4.5.1).

Contribution	Fraction Passing Offline Selection in %
CD	8.55
DD	0.06
ND	<0.01

Table 4.5: Fraction of events passing the full offline selection for each Monte Carlo-modeled contribution.

Other contributions are constrained using data-driven techniques as explained in the next section.

4.3.2 Non-simulated Background Sources

The background contributions that are not accounted for by simulations come from any single-side proton-like signal collected in coincidence with a single-diffractive like signal in the inner detector, that would not come from a DD, a CD or a ND interaction. A single-side proton like signature can have different causes: beam halo, elastic collision, beam gas

Number of tracks in	unpaired bunches sample	std sel. sample
the sideband region	1406	11063
the signal region	508	1756498

Table 4.6: Numbers used in the scaling of the beam halo background in the signal region.

interaction, showering and even pile-up. Among those, the background contribution from the halo protons can be estimated using a data driven technique based on the analysis of the tracks correlation map. Other less-easy-to-constrain backgrounds are accounted for by means of an inclusive technique referred as the *proton overlay method*.

Beam Halo Particles in ALFA

The track correlation pattern for beam halo protons is obtained from analyzing events passing the `ALFA_UNPAIRED_ISO` trigger, which fires for isolated unpaired bunches. The ($\bar{x}$, θ_x) correlation pattern for such events on Fig. 4.10a shows that most of the control sample is composed of beam halo protons concentrated in the region around $\theta_x = 0$ along the x-axis. The fraction of tracks lying outside this high multiplicity band is calculated to be $< 1\%$, thereby being neglected. A 2D-sideband method is used to scale the beam halo contribution in the signal region. The sideband regions are chosen for each armlet such that they contain only beam halo background and exclude the signal (see Fig. 4.10b). The sideband region contour line closest to the signal region is defined at the 6σ contour of the double Gaussian signal region (defined in Sect. 4.2.2, in particular Fig. 4.7), hence insuring minimum signal leakage. The ratio of the number of tracks in all sideband regions in the data to the unpaired bunches sample is then used to scale the background in the four signal regions of the standard data (see Table 4.6). The contribution was found to amount to $1.24 \pm 0.07\%$ of the total number of tracks selected in the four armlets.

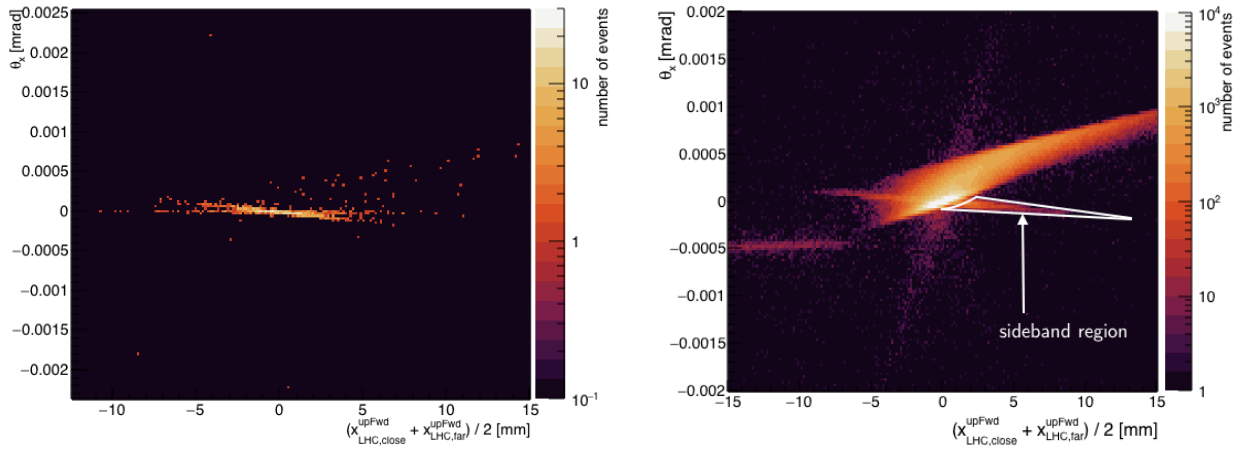

(a) Data from unpaired bunches before $\bar{x}$ and θ_x selection

(b) Standard data before $\bar{x}$ and θ_x selection

Figure 4.10: (a) $\bar{x}$ vs θ_x correlation pattern for data tracks satisfying the unpaired bunches trigger. Beam halo background tracks are concentrated along the x-axis at very small θ_x. (b) $\bar{x}$ vs θ_x correlation pattern for data tracks satisfying the close and far requirement, the reconstruction requirement and satisfying the fiducial criteria for events passing the central detector selection. The white triangle contour corresponds to the control region used to scale the beam halo background contribution. Color scales show the multiplicity of tracks.

Constraints using the "Proton Overlay" Method

An inclusive estimation of all the background contributions combined is performed using a partially data-driven method called *proton overlay*. The latter is based on the idea of adding extra-protons to the simulated background contributions with a certain probability calculated from a control data sample where no ALFA activity from diffraction is expected.

Control Sample Events in the control sample are required to have passed an inclusive trigger `EF_mbSpTrk`, which is as little biased as possible. The offline selection applied on such sample is designed to favor ND events over all contributions:

- 32 MBTS segment hits are required,
- at least one particle track satisfying the minimum bias criteria from Sect. 4.2.2 has to be reconstructed in the inner detector,
- only small rapidity gaps, $\Delta\eta^F < 0.5$ are tolerated.

Applying the selection to the Monte Carlo samples showed that ND events have 99.48% chance of satisfying those criteria while the remaining 0.52% are mostly due to leaking SD events, with very little contribution from DD and CD events. The activity observed in ALFA for the data events selected under these criteria was therefore considered to have no correlation with the inner detector activity.

Overlay proton probabilities The number of protons passing the ALFA proton track selection of the analysis (see Sect. 4.2.2) was calculated for this control sample. Table 4.7 shows the derived probabilities of getting 1, 2, 3 or 4 protons passing the ALFA selection. The probabilities were corrected for the possible leakage of SD, CD and DD signal observed

in the simulation.

Being uncorrelated to the inner detector activity, the probabilities are used to quantify the addition of an extra-proton to any kind of events. This is done by artificially adding in the Monte Carlo 1, 2, 3 or 4 to the selected proton multiplicity on either side of ALFA $p_{1p}^{\text{data}}\%$, $p_{2p}^{\text{data}}\%$, $p_{3p}^{\text{data}}\%$ and $p_{4p}^{\text{data}}\%$ of the time respectively, where p_{ip}, $i = 1, 2, 3, 4$ are the probabilities to have i overlaying proton(s) according to the control sample study.

Proton(s) passing ALFA selection	Probability of overlay in %
1	$p_{1p}^{\text{data}} = 0.7678$
2	$p_{2p}^{\text{data}} = 0.7295$
3	$p_{3p}^{\text{data}} = 0.0023$
4	$p_{4p}^{\text{data}} = 0.0009$

Table 4.7: Probability of having extra protons coming from elastics, beam halo, beam-gas interaction or pile-up extracted from the control sample analysis.

Background Shapes The name of the technique suggests that protons are added to the simulation. In practice only the proton multiplicity is altered on an event-by-event basis, depending on the overlay probabilities. The distribution shape of the proton kinematics for the proton overlay background contribution should therefore be taken from the control sample and be scaled to the number of extra events that would pass the analysis selection with one or several extra protons. Fig. 4.11 gives the breakdown of each contributions compared with the data corrected for the trigger inefficiencies detailed in Sect. 4.4. A good agreement in shape is observed for the variable of interest. In the region where the SD contribution dominates, a factor of about 1.5 in the normalization is observed between the

SD+backgrounds and the data distribution (see ratio plots on Fig. 4.11). This suggests an overestimation of the SD cross section in PYTHIA8. A similar comparison was performed using an SD sample whose cross section was tuned to a value of 7.7 mb (with respect to the default value of 12.48 mb used in PYTHIA8), to give the best agreement with the data. The related plots are given in Appendix C for information.

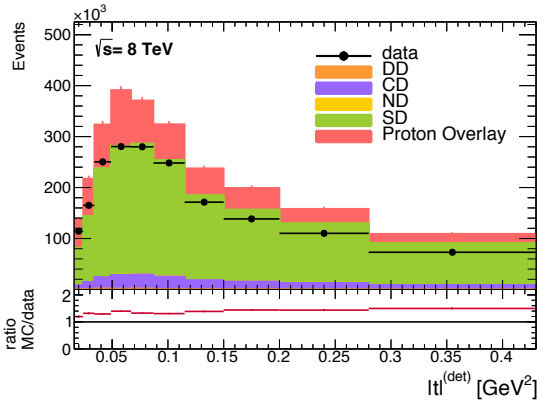

(a) Absolute value of the momentum transferred squared

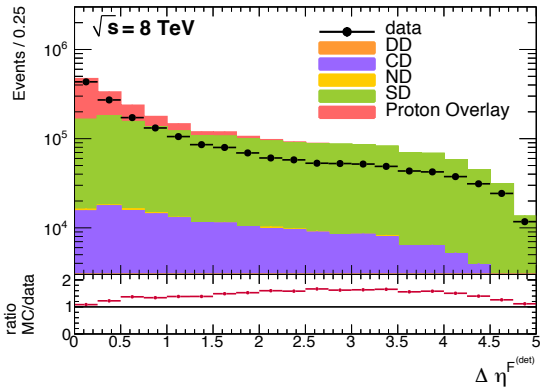

(b) Rapidity gap measured from the inner detector tracker edge on the side of the proton tag

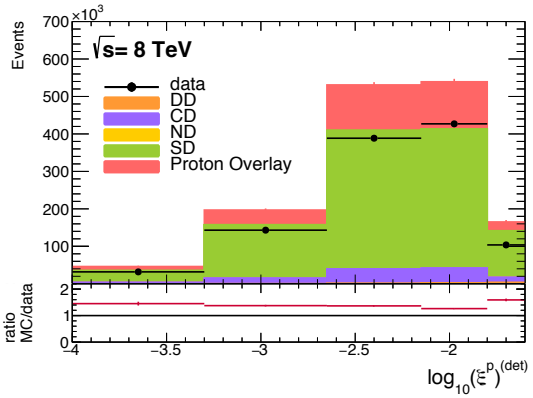

(c) Scattered proton fractional energy loss reconstructed from ALFA

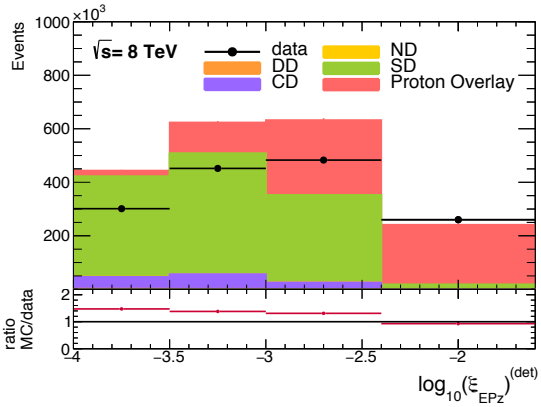

(d) Scattered proton fractional energy loss reconstructed from the diffractive system

Figure 4.11: Control distributions showing the comparison of the sum of each Monte Carlo contributions and the proton overlay contribution stacked, with the data corrected for the trigger and ALFA reconstruction algorithm inefficiencies. For each variable presented, the binning was chosen to match the resolution determined from simulation.

Crosschecks The proton overlay normalization was checked to be valid in the fiducial range of the analysis and in a control region defined from the analysis selection criteria but requiring two proton tags on each side instead of one on one side. Fig. 4.12 shows the distributions of the number of hits in the MBTS system for events passing the standard selection criteria (Fig. 4.12a) and for events passing control region selection, i.e., two protons reconstructed in two different armlets (Fig. 4.12b). For both selections, a good agreement is observed for large hit multiplicity. The high multiplicity range is likely to be populated by non-diffractive events, for which a high level of activity is expected in the MBTS system, in coincidence with an elastic or a beam halo proton. A fair agreement is observed for average multiplicities. For events with a number of MBTS hits below 10, the agreement between the simulation and the data is degraded due to the incomplete modeling of the MBTS response. Being mostly composed of non-diffractive initiated backgrounds, the 2-protons control region is less affected by the MBTS modeling.

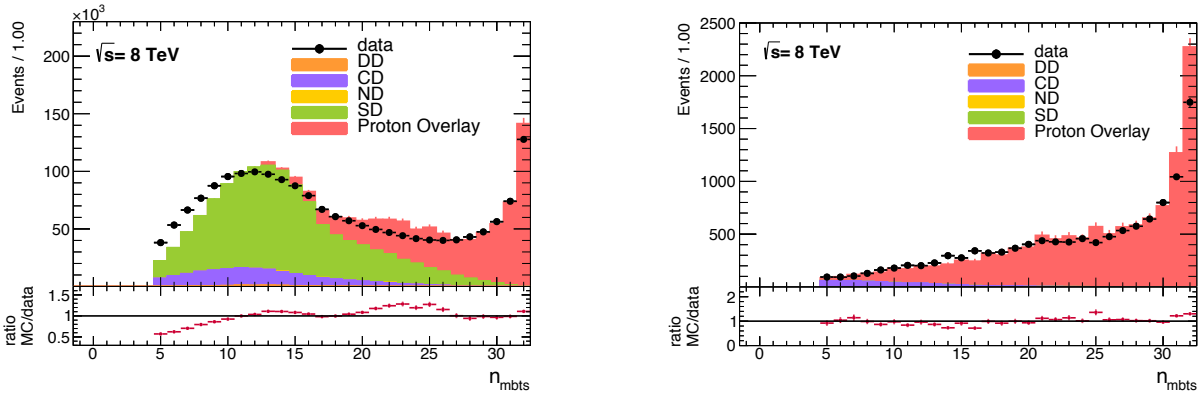

Figure 4.12: Distribution of the number of hits in the MBTS for events passing the standard analysis selection (a) and the elastic-favoring 2-protons selection (b). The SD contribution was scaled to the tuned cross section. The proton overlay background populates the high multiplicity tail..

Uncertainty The uncertainty on the proton overlay background is underpinned by the knowledge on the diffractive cross-sections breakdown. For the cross section differential in $\log(\xi_{Ep_z})$ and $\Delta\eta^F$, this background distribution is filled by Monte Carlo events with proton overlay, which pass the selection, thereby depending on how each simulated contribution is normalized with respect to the others. As most Monte Carlo events with an overlaid proton that pass the 2-protons selection turn out being mostly non-diffractive (other components $< 1\%$), the uncertainty from the cross sections is mostly driven by that of the ND contribution. Besides this aspect, one should account for the possibility of forward hadrons leaking in the ND-enriched sample. This may affect the probability calculation but most importantly the shape of the ALFA-derived distributions.

The overall uncertainty is evaluated by comparing the observable spectrum of the proton overlay contribution with the data spectrum in the two-protons control region where it is known that all other background contributions are suppressed. As can be seen on Fig. 4.13, the uncertainty is maximal for large ξ^p (around 75%) where forward hadrons are expected to contribute the most. This feature is not visible in the same range of ξ_{Ep_z} whose shape was extracted from Monte Carlo distributions with no possible contamination of forward hadrons. The uncertainty is rather large ($> 30\%$) in the high $|t|$ region, for the same reason. The systematic impact of this uncertainty is discussed in Sect. 4.5.1.

Background in the Central Detectors

Beam-Gas and Beam-Halo Backgrounds In the run considered and for the luminosity blocks of interest, four unpaired isolated bunches per beam were setup at the end of the train. Such a beam configuration allows to study the background contribution coming from the beam that may result in diffractive-like activity in central detectors. Those special

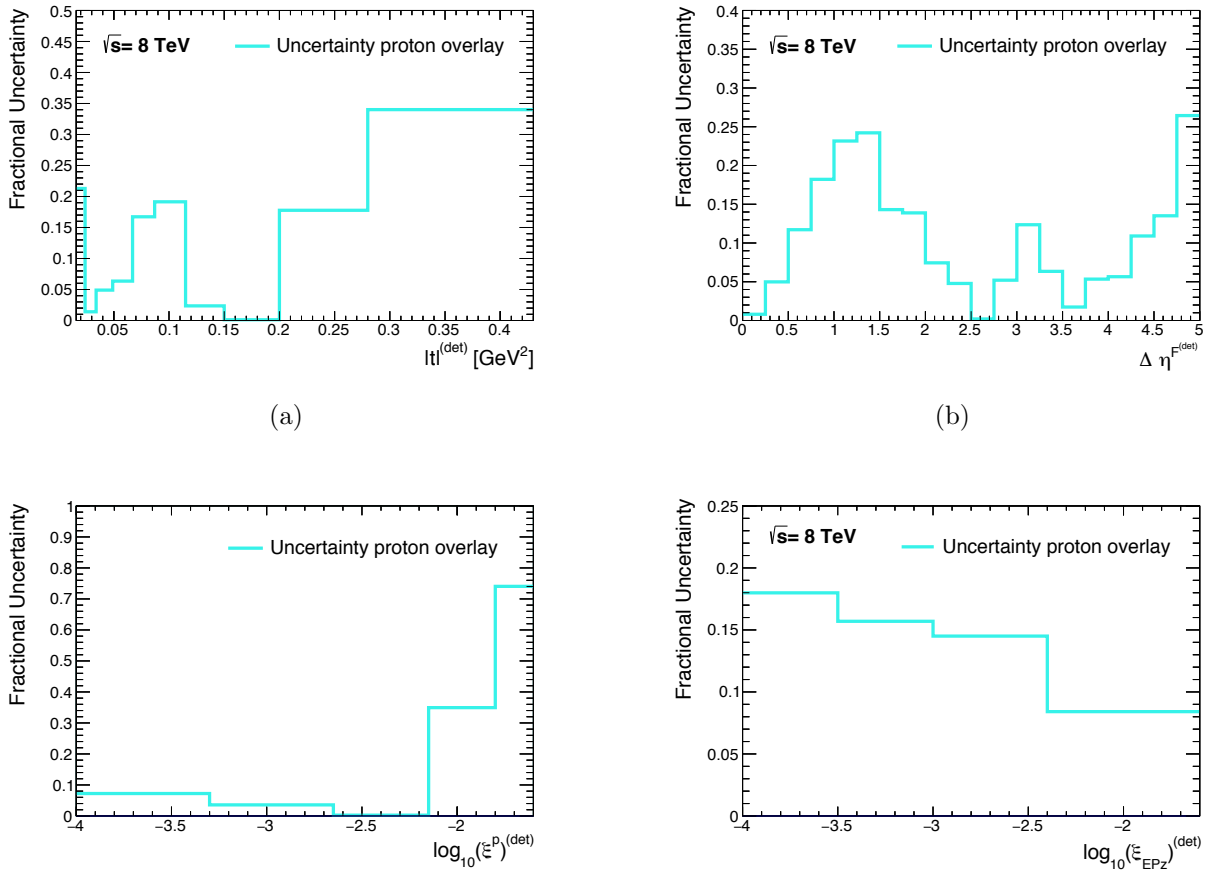

Figure 4.13: Uncertainty on the proton overlay background measured for $|t|$ (a), $\Delta\eta^F$ (b), $\log_{10}(\xi^p)$(c) and $\log_{10}(\xi_{Ep_z})$ (d), by comparing the data and proton-overlaid distributions passing the 2-protons control region selection.

bunches are isolated enough from the rest of the bunches in the train to limit out-of-time afterglow effects and no collision between bunches happen. The bunch filling scheme used for the luminosity blocks setup is shown on Fig. 4.14. The average number of protons in these bunches is typically the same as for the paired bunches. The contribution from beam background in the central system can therefore be estimated by calculating the number of events originating from those isolated unpaired bunches, $n_{\mathrm{BB}}^{\mathrm{unp}}$, which pass the central detector selection of the analysis, where BB stands for beam backgrounds. This amount should then

be doubled to account for the effect of both beams and scaled to the effective number of paired bunch crossings.

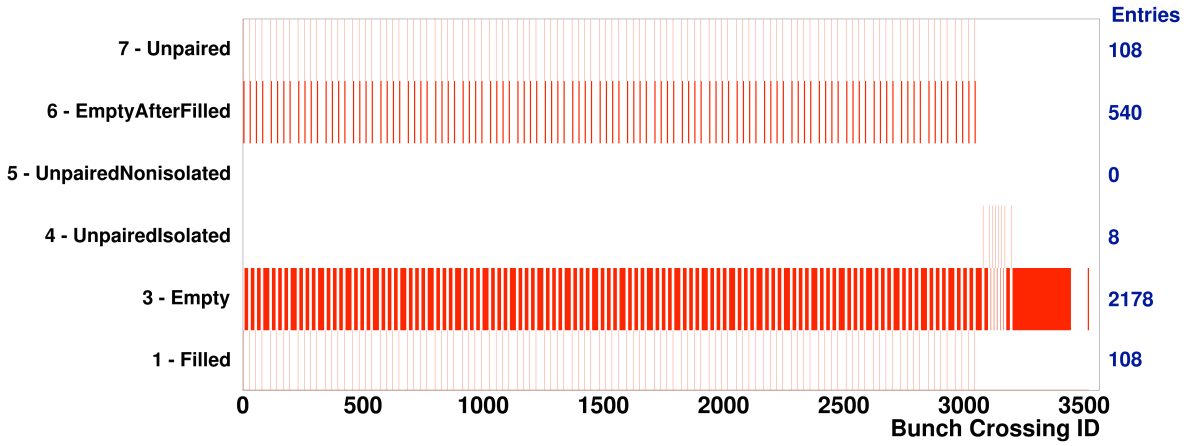

Figure 4.14: Diagram showing the filling scheme of the bunch train for the set of luminosity blocks used in the analysis. The horizontal axis shows the label of bunch (BCID). The fourth line (labeled 4) indicates the position of the 8 unpaired isolated bunches used for background measurement. The sixth line (labeled 1) corresponds to the 108 bunches to be paired for collision. This plot was generated from selected information available for the run of interest through *runquery*, the ATLAS run database [113].

The fraction $f_{\mathrm{BB}}^{\mathrm{pair}}$ of background signatures in the central detectors ($n_{\mathrm{BB}}^{\mathrm{pair}}$) to be observed in the paired bunches among all the events selected n_{sel}, is calculated as follows:

$$\begin{aligned} f_{\mathrm{BB}}^{\mathrm{pair}} &= \frac{n_{\mathrm{BB}}^{\mathrm{pair}}}{n_{\mathrm{sel}}} \\ &= \frac{n_{\mathrm{BB}}^{\mathrm{unp}} \cdot 2^{\frac{n_{\mathrm{pair}}}{n_{\mathrm{unp}}}}}{n_{\mathrm{sel}}} \\ &= \frac{3393 \cdot 2^{\frac{108}{8}}}{n_{\mathrm{sel}}} = 5.2\% \end{aligned}$$

A background event with a signal-like topology in the central detector will be selected if it happens to have a proton tag on the opposite side. The probability to get a proton on any side with no diffractive signal in the central detector can be extracted from the simulation. The number of events passing the ALFA standard selection and featuring no more than 1

hit in the MBTS system (i.e not passing the trigger chain L1_MBTS_2), n_{1p}^{MC}, is extracted and divided by the total number of events selected in the simulation $n_{\mathrm{sel}}^{\mathrm{MC}}$:

$$p_{1p}^{\mathrm{MC}} = \frac{n_{1p}^{\mathrm{MC}}}{n_{\mathrm{sel}}^{\mathrm{MC}}} = 1.1\% \tag{4.3}$$

Other single-diffractive like protons come from elastic scattering and beam halo, and so the probability for the coincidence is calculated from weighting $f_{\mathrm{BB}}^{\mathrm{pair}}$ by the sum of p_{1p}^{MC} and p_{1p}^{data}, and halving the result to account for the two sides:

$$p_{BB} \approx \frac{f_{\mathrm{BB}}^{\mathrm{pair}} \cdot \left[p_{1p}^{\mathrm{data}} + p_{1p}^{\mathrm{MC}}\right]}{2} = \frac{5.2\% \cdot [0.7678\% + 1.1\%]}{2} = 0.05\% \tag{4.4}$$

Hence, the impact of beam backgrounds in the central detectors is very small, thereby neglected.

4.4 Acceptance Efficiency

4.4.1 Trigger Efficiency and prescales

The combined efficiency of the L1_MBTS_2_A_ALFA_C and L1_MBTS_2_C_ALFA_A, i.e. the probability for a reference event to pass the trigger requirements of the analysis, is calculated per bin for the variable of interest for a subset of data events passing a reference trigger. A reference event is an event passing a reference trigger, i.e. a trigger which has as least bias as possible with respect to the trigger one wants to probe the efficiency of.

The reference trigger is therefore chosen to limit calculation bias arising if the reference selection is not completely random. The random track trigger EF_mbSpTrk which is derived from the L2_mbSpTrk track trigger, which itself is seeded by the the L1_RD0_FILLED random trigger, is a good compromise. Its only bias is to impose events to have at least one track with $p_{\mathrm{T}} > 200\,\mathrm{MeV}$ which is rather inclusive, while having a rather low total prescale of 72,

which limits the statistical uncertainties on the efficiency calculation. The following formula was used to compute the trigger efficiency in each bin x_i of x where x can be any variable of interest:

$$\epsilon_{\text{trig}}(x_i) = \frac{n_{\text{events}}(x_i)\ [\texttt{L1\_MBTS\_2\_A\_ALFA\_C} \cup \texttt{L1\_MBTS\_2\_C\_ALFA\_A}] \cap [\texttt{EF\_mbSpTrk}]}{n_{\text{events}}(x_i)\ [\texttt{EF\_mbSpTrk}]}. \quad (4.5)$$

The distributions will then be 'reweighted' bin-by-bin to correct for the inefficiency of the trigger. Fig. 4.15 shows an example of the trigger efficiency as a function of the number of tracks in the inner detector (Fig. 4.15a) and as function of the number of segments hit in the MBTS on the side opposite to the ALFA proton tag (Fig. 4.15b). With a five segments hit requirement on the side opposite to the proton tag, the analysis is set in the region of best performance of the trigger, with $\epsilon_{\text{trig}} > 65\%$.

The unbiased `L1_LUCID` trigger of the LUCID detector was used to assess possible bias caused by the nominal reference trigger (`EF_mbSpTrk`). As shown on Fig. 4.15, no difference was observed in the trigger efficiency outside of the statistical fluctuations in the LUCID-triggered sample owing to its large prescale. The difference in efficiency observed was used as a systematic variation (see Sect. 4.5).

4.4.2 ALFA Track Reconstruction Efficiency

As the fibers in ALFA are fully efficient, all inefficiencies on the proton track measurement derive entirely from the ability to reconstruct tracks from the fiber hits. A failure of the algorithm may happen when several tracks are recorded in a station at the same time. In this case, it is not always possible to find a single candidate for the best-fiber hits overlap (see Sect. 3.2.2). The computation presented in this section assumes that single-diffractive protons tracks are similar to elastic proton tracks such that one can safely use elastics tracks

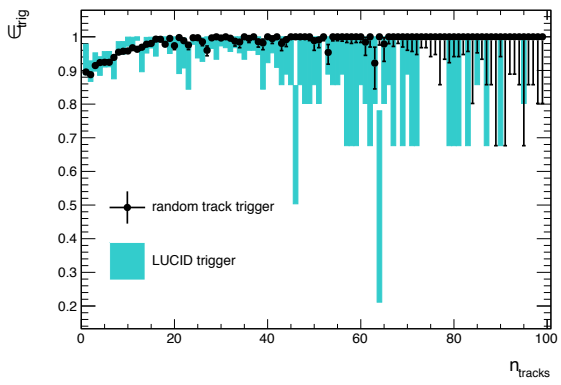

(a) n_{MBTS}

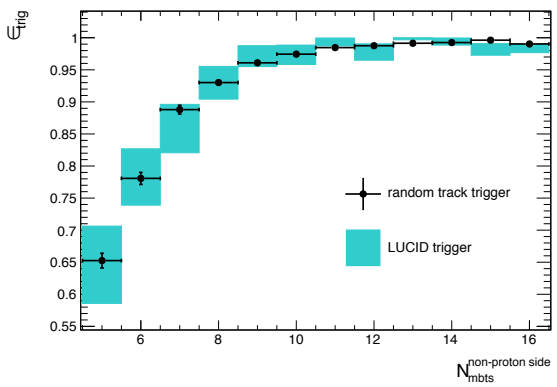

(b) $N_{\mathrm{MBTS}}^{\text{non-proton side}}$

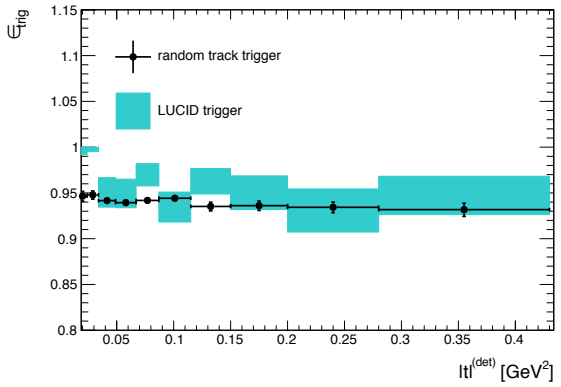

(c) $|t|$

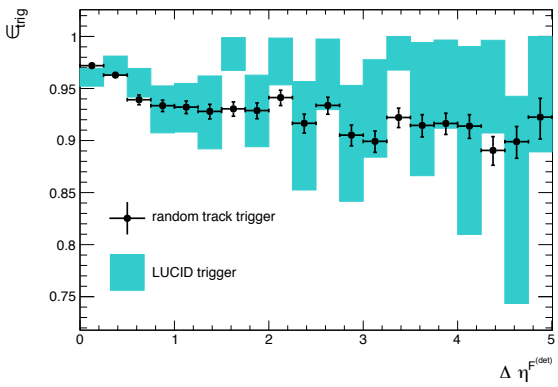

(d) $\Delta\eta^F$

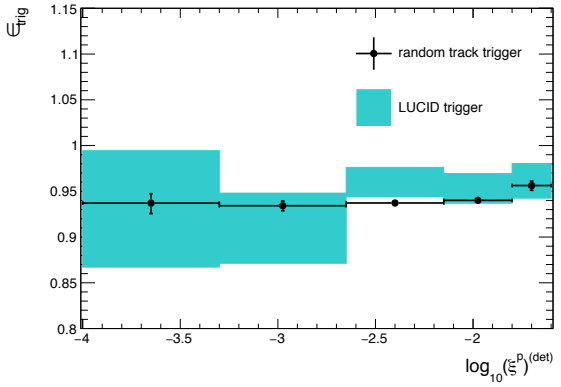

(e) ξ^p

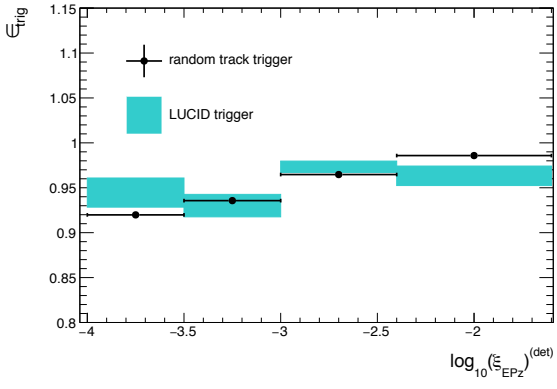

(f) ξ_{Ep_z}

Figure 4.15: Trigger efficiency as a function of (a) the number of tracks selected in the inner detector, (b) the number of MBTS counter hits on the opposite side of the detector to the ALFA-tagged proton and (c), (d), (e) and (f) the four observables of interest in the analysis, for events passing the `EF_mbSpTrk` reference trigger (black dots) and the `L1_LUCID` reference trigger (blue uncertainty band). Statistical error bars are calculated using a Bayesian credible interval obtained when using a Jeffreys prior [114].

in place of diffractive ones to probe the efficiency by means of a *tag and probe* technique. A sample enriched in elastic events is selected using the `L1_ALFA_ELAST15` and `L1_ALFA_ELAST18` trigger chains. The elastics purity is improved by vetoing any activity in the MBTS system and in the LUCID and ZDC main triggers, which should fire only in the case of a non-elastic collision.

Method The selected subset is mostly composed of events featuring two protons with opposite momenta on the ALFA A and C sides. Each armlet is therefore used to tag one proton using the standard track selection detailed in Sect. 4.2. The bias introduced by such selection will be evaluated in Sect. 4.5. The armlet opposite to it is then probed for the presence of another proton (see Fig. 4.16).

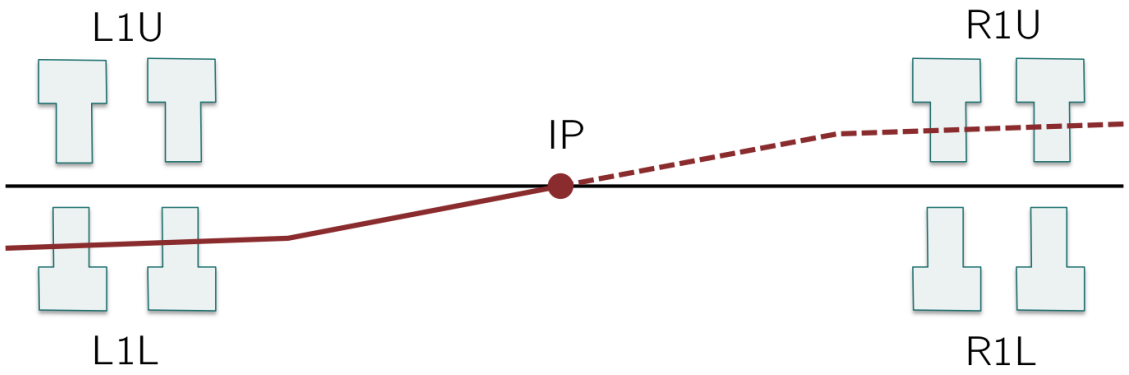

Figure 4.16: Schematic showing the principle of the tag and probe technique. A proton is tagged in the L1L armlet and the R1U armlet is probed for the presence of a tracks.

The algorithm is considered to have failed when 1 or 2 of the stations fired of the armlet did not reconstruct a track. By fired, it is meant that the triggers associated to the stations in question fired. Therefore, for a given fired armlet i = L1U, L1L, R1U or R1L, the number of

events which fail to be reconstructed while a tag was present on the opposite armlet, N^i_{fail}, corresponds to the sum of the cases where zero track out of two possible segment, $N^i_{0/2}$, and only one track out of two possible segments, $N^i_{1/2}$, was reconstructed. Denoting N^i_{pass} the number of events where two tracks are properly reconstructed in armlet i, the efficiency is derived:

$$\epsilon^i_{\text{reco}} = \frac{N^i_{\text{pass}}}{N^i_{\text{pass}} + N^i_{\text{fail}}} = \frac{N^i_{\text{pass}}}{N^i_{\text{pass}} + N^i_{0/2} + N^i_{1/2}} \tag{4.6}$$

Correction due to Scattering and Showering Effects It is possible that an elastic protons fails being reconstructed on the probed armlet, not because of inefficiencies of the reconstruction algorithm itself but because the proton scattered outside the selection area. This would mimic a failure of the algorithm while actually being a physical effect and should therefore be corrected for. If in addition, the scattered proton showers, it can alter the reconstruction of other tracks. The correction due to scattering is estimated by counting the number of events where a track was reconstructed in the two armlets but which were categorized as $N_{0/2}$ or $N_{1/2}$ in the end. Those events are removed from the $N_{0/2} + N_{1/2}$ category as, by definition, they do not derive from algorithm inefficiencies. The effect of showering of scattered proton is accounted for by removing some more events to the $N_{0/2} + N_{1/2}$ category, assuming that scattered protons will shower and cause a failure for an estimated 10% of the time.

Non-Elastic Leakage N^i_{pass} and N^i_{fail} should be corrected for the amount of non-elastic events leaking in the sample. This is estimated by analyzing the activity in the two remaining armlets when a two-proton event is identified. Therein, the *tag* is defined for events which register tracks in 2 diagonally opposite armlets. Under these conditions, the number of tracks reconstructed in the two remaining armlets is probed. For each probed armlet, it is

asked that the track on the opposite side has no more than 12 fiber hits, to suppress the contribution from elastic pile-up. The number of events where two tracks out of two are reconstructed, $N^i_{\text{bkg, 2/2}}$ is extracted, and the number of events where at least one station did not manage to reconstruct a track out of the 12 hits, $N^i_{\text{bkg, 0/2+1/2}} = N^i_{\text{bkg, 0/2}} + N^i_{\text{bkg, 1/2}}$, is extracted.

Probability of Failure Table 4.8 shows the number of events N^i_{pass} satisfying the elastic probe and the number of non-elastic background events, $N^i_{\text{bkg, 2/2}}$ and $N^i_{\text{bkg, 0/2+1/2}}$, extracted from the background leakage estimate with their corresponding probabilities.

Armlet i	N^i_{pass}	$N^i_{\text{bkg, 2/2}}$	$p^i_{\text{leak, 2/2}}$ [%]	$N^i_{\text{bkg, 0/2+1/2}}$	$p^i_{\text{leak,0/2+1/2}}$ [%]
L1U	65272	69	0.101	8	0.012
L1L	67929	61	0.090	17	0.025
R1U	67929	63	0.093	17	0.025
R1L	65284	67	0.103	12	0.018

Table 4.8: Number of events passing the elastic probe selection and the number of events passing the background leakage probe 0/2+1/2 and 2/2 selections with their associate probabilities.

When probing armlet i, with j denoting the armlet opposite to i, the probability for the background to have the same configuration as an algorithm "pass" event is calculated to be:

$$p^i_{\text{bkg, pass}} = p^i_{\text{leak, 2/2}} \cdot p^j_{\text{leak, 2/2}} \tag{4.7}$$

Similarly, the probability to have the same configuration as an algorithm "fail" events is:

$$p^i_{\text{bkg, fail}} = p^i_{\text{leak, 0/2+1/2}} \cdot p^j_{\text{leak, 2/2}} \tag{4.8}$$

These probabilities are used to correct Eq. 4.6 as follows:

$$\epsilon^i_{\text{reco}} = \frac{N^i_{\text{pass}}(1 - p^i_{\text{bkg, pass}})}{N^i_{\text{pass}}(1 - p^i_{\text{bkg, pass}}) + N^i_{\text{fail}}(1 - p^i_{\text{bkg, fail}})} \tag{4.9}$$

As $p^i_{\text{bkg, pass}} \sim 0.01\%$ and $p^i_{\text{bkg, fail}} < 0.003\%$, the effect of the corrections on the efficiency is relatively small.

Efficiencies Table 4.9 summarizes the efficiencies obtained from Eq. 4.9 for each armlet. The study was reproduced when using a Monte Carlo generated elastic sample using the same magnet configuration as the analysis run. The efficiencies which do not account for background leakage (as it is not modeled), were, as expected, higher by a few percents but consistent with the data-driven results. The ratio of the data/MC efficiencies were used

Armlet i	$\epsilon^i_{\text{reco, data}}[\%]$	$\epsilon^i_{\text{reco, MC}}[\%]$	$C = \epsilon^i_{\text{reco, data}}/\epsilon^i_{\text{reco, MC}}$
L1U	94.2	94.9	99.33
L1L	91.2	91.8	99.41
R1U	92.4	94.1	98.26
R1L	91.7	93.9	97.74

Table 4.9: ALFA track reconstruction efficiencies for each armlet calculated from data and elastic Monte Carlo, and the ratio C of efficiencies used to correct the Monte Carlo distributions.

to correct the Monte Carlo samples where the elastic and beam halo backgrounds are not present. This allows to compare uncorrected distributions using the same inefficiency and both samples can be reweighted using the reconstruction efficiency of the data ϵ_{reco}.

Uncertainty The uncertainty on the track reconstruction efficiency measurement is assessed by varying the selection criteria for elastic events and measuring the maximum positive and negative variation with respect to the nominal efficiency. Each criterion was varied independently:

- the beam screen and detector edge cuts were removed or doubled,

- the number of fibers required in the probed armlet was increased to 16 or decreased to 8,
- the size of the (x, θ_x) signal region was reduced to 2σ or extended to 4σ of the bivariate Gaussian.

In addition the background leakage and showering probability were either removed or doubled. The quadratic sum of all systematic variations for the data and the elastic Monte Carlo is given in Table 4.10 for each armlet. The thesis gives results for the set of criteria considered above. A more complete version including more variations and the breakdown of each error contributions is given in [112].

Uncertainty	L1U	L1L	R1U	R1L
Data	+0.0062 -0.0070	+0.0089 -0.0114	+0.0064 -0091	+0.0082 -0.0124
Elastic MC	+0.008 -0.0102	+0.0180 -0.164	-0.0074 -0.0081	+0.0126 -0.0214

Table 4.10: Uncertainty on the ALFA reconstruction efficiency calculated by loosening or tightening the track selection criteria in the probed armlet.

4.4.3 Unfolding Procedure

Event distributions are deconvoluted back to truth level in ξ, $|t|$ and $\Delta\eta^F$ by means of a Bayesian iterative algorithm [115]. This procedure accounts for the migration of events across bins due to limited detector reconstruction efficiencies and resolutions. Instead of dealing with response matrix inversion, a procedure that can introduce large unphysical fluctuations, the algorithm used in this thesis makes use of Bayesian statistics and proceeds by iterations.

Unfolding Principle

The distributions of quantities shown in the last sections are noisy and distorted by the instruments they have been measured with. The combined effect of the inefficiencies, the

limited resolution and the imperfect calibration of the detectors and that of the presence of physical noise should therefore be inferred, in order to compensate for it. The purpose of unfolding is to find a description for the "unsmeared" distributions given the observed distributions and assuming some knowledge about the smearing.

Bayesian Iterative Method

The Bayesian method uses probability theory to learn about physical quantities and their relationships, from experimental data. Given a set of causes $\{C_1, ...C_n\}$ and their effects $\{O_1, ...O_n\}$, the number of events in a distribution that are assignable to a cause C_i, N_{C_i}, is estimated from the number of observed events displaying the effect O_j, N_{O_j}, as follows:

$$\hat{N}_{C_i} = \frac{1}{\epsilon_i} \sum_j N_{O_j} P(C_i|O_j, I), \tag{4.10}$$

where $P(C_i|O_j, I)$ is a probability that needs to be extracted from the unfolding and I stands for the state of information under which the analysis is performed and with which the probability is constrained. The term ϵ_i is there to account for the fact that a given cause C_i may not produce any effect. This is equivalent to a reconstruction efficiency and can therefore be expressed as:

$$\epsilon_i = \sum_j P(O_j|C_i, I) \tag{4.11}$$

Using Bayes theorem, the probability term in Eq. 4.10 can be decomposed as follows:

$$P(C_i|O_j, I) = \frac{P(O_j|C_i, I) \cdot P(C_i|I)}{\sum_i P(O_j|C_i, I) \cdot P(C_i|I)} = \frac{\lambda_{ji} \cdot P(C_i|I)}{\sum_i \lambda_{ji} \cdot P(C_i|I)} \tag{4.12}$$

The term $\lambda_{ji} = P(O_j|C_i, I)$ is called the *likelihood* and corresponds to the response of the apparatus in the measurement. $P(C_i|I)$ is the *prior* which represents our prior knowledge about the probability distribution of the cause C_i.

In the `RooUnfold` Bayesian algorithm used in this analysis, the λ_{ji} terms are derived from

the Monte Carlo information, using the elements of the Monte Carlo response matrix. ϵ_i is estimated by summing over all Monte Carlo derived λ_{ji}. The statistical uncertainty on the λ_{ji}'s is taken into account by calculating an error propagation matrix [116].

Knowing the λ_{ij} terms, one can determine $P(C_i|O_j, I)$. This requires to assume a shape for $P(C_i|I)$. From $P(C_i|O_j, I)$, N_{C_i} is estimated using Eq. 4.10 which gives $\hat{N}_C$ when summing over all possible causes.

The unfolding algorithm implemented in the `RooUnfold` package [116] proceeds by iterations to limit the dependence on the prior used:

1. At first, the Monte Carlo SD simulation is used to extract the λ_{ij} terms and the first prior (usually taken to be flat) from which $P(C_i|O_j, I)$ is derived. On estimation of N_{C_i} is then calculated and, from this information, an estimation of N_C is extracted.

2. The second iteration uses $P_{\text{new}}(C_i|I) = \hat{N}_{C_i}/\hat{N}_C$, as the new prior. And all calculations are done again, until a new estimation of N_C is found.

3. Steps 1. and 2. are performed iteratively until reaching a minimum on the systematics introduced by the unfolding. The uncertainty minimization is detailed in the next section.

Application to the Distributions of Interest

Response Matrices The uncertainty coming form the unfolding of a distribution is linked to the likelihood which describes the typical response of the detector. Fig. 4.17 shows that the response matrices obtained from the Monte Carlo simulation of SD events are quite different in shape. For each observable, bins are filled depending on the truth and reconstructed values of the observable of each event passing the detector and fiducial selection cuts. Bins

are then normalized by the total number of events in the given truth bin. The diagonal values thereby indicates the purity. The $\Delta\eta^F$ and $|t|$ matrices are fairly diagonal, meaning that no important migration of events between the bins of these variables is present. By contrast, the ξ distributions are far from being diagonal and the diagonal bins have rather low purity. Since the detector response affects the ξ observable a lot, it was decided to optimize the number of iterations for each observable independently.

Regularization The number of iterations was chosen such that it minimizes the mean uncertainty coming from the unfolding procedure itself, i.e. when the reconstructed distribution is the least biased by the prior. The uncertainty was calculated by means of a closure test commonly used in ATLAS. This test is based on the idea of mimicking the data by a clever reweighting of the Monte Carlo simulation, and measuring the effect of unfolding by comparing the distribution before and after it has been unfolded. The following steps were performed for each unfolded observable:

1. The Monte Carlo truth distribution of the observable is reweighted by a function (typically a polynomial) such that, at reconstructed level, the resulting distribution fairly agrees with the reconstructed data distribution. The reweighting polynomials are given in Appendix D.

2. The reweighted truth is used as an input to the unfolding algorithm and the result is compared with the truth.

3. The difference in each bin is taken as the systematic uncertainty.

Table 4.11 shows the mean uncertainty, i.e. integrated over the fiducial range of each observable, for various iterations. A maximum of one iteration was chosen for the unfolding of $\log_{10}(\xi_{Ep_z})$ and $|t|$. For the unfolding of $\Delta\eta^F$ and $\log_{10}(\xi^p)$, two iterations were used.

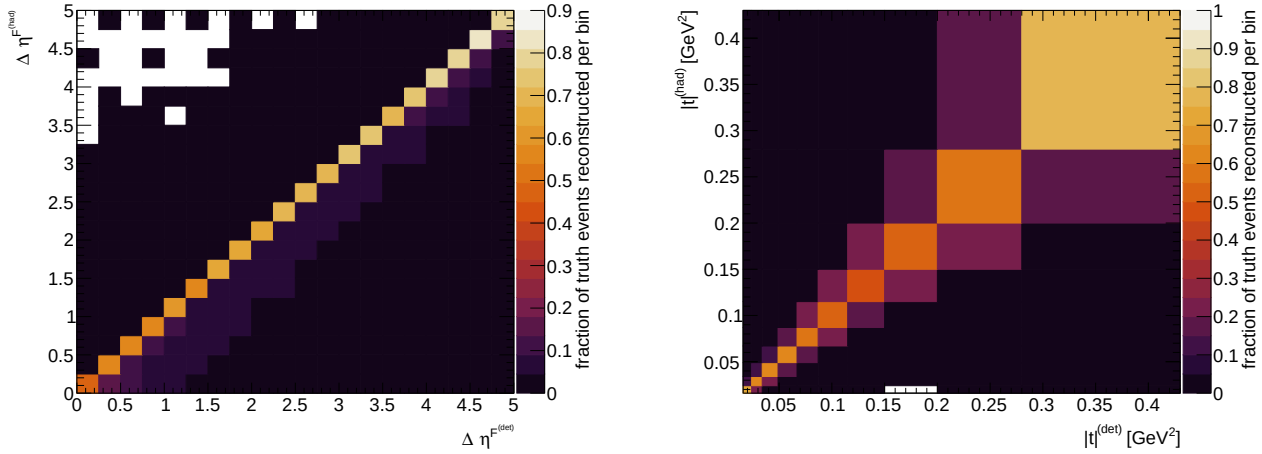

(a) $\Delta\eta^F$ (b) $|t|$

(c) ξ_{Ep_z} (d) ξ^p

Figure 4.17: Response matrices showing the correlation of the truth (y-axis) and reconstructed (x-axis) variables $\Delta\eta^F$ (a), $|t|$ (b), ξ_{Ep_z} (c) and ξ_p (d) for SD Monte Carlo events passing the standard analysis selection. Fiducial cuts are applied at the truth level. Truth events that were not reconstructed are not shown but are accounted for by an efficiency correction in the unfolding algorithm.

4.5 Systematics Uncertainties

The author participated in the discussions about the systematics but did not contribute to the implementation. For this reason, and for the sake of brevity, only the fundamentals about

Nb of iterations	$\Delta\eta^F$ [%]	$\|t\|$ [%]	$\log_{10}(\xi^p)$ [%]	$\log_{10}(\xi_{Ep_z})$ [%]
1	4.42	**1.09**	12.0	**2.82**
2	**2.43**	3.56	**11.9**	6.80
3	2.48	3.84	12.6	6.60
4	2.54	3.94	12.9	6.50

Table 4.11: Mean systematic uncertainties calculated by comparing the reweighted truth with the reweighted reconstructed Monte Carlo unfolded. The bold values indicate the minima chosen for the number of iterations.

how each contribution was calculated are presented. The final breakdown using the latest error calculation on each parameters [117] is also given for completeness. Technical details are made available to the members of the ATLAS collaboration in the supporting note [117].

Some observables are more biased than others towards a certain source of uncertainty, but overall the dominant systematic contribution comes from the uncertainty on the proton overlay distribution which is discussed in details in Sect. 4.3.2. For the proton fractional energy loss distributions, the migrations between bins is sometimes significant which results in larger uncertainties due to the unfolding. Contributions are presented approximately by order of importance. A more detailed overview of the main contributions for each spectrum is given on Fig. 4.18.

For an independent source s of uncertainty, the systematic contribution is determined following these steps:

- the analysis is performed by varying the source by the maximal positive amount within the uncertainty Δs^+ and the associate number of events $N_{\Delta s^+}$ is extracted,
- the analysis is performed by varying the source by the maximal negative amount within

the uncertainty Δs^- and the associate number of events $N_{\Delta s^-}$ is extracted,

- for each distribution of the observable x, the fractional up and down systematics in in bin Δx_i, $f^{\pm}_{\text{syst.}}(\Delta x_i)$, are obtained by calculating the deviation observed with respect to the nominal distribution N_{nom}:

$$f^{\pm}_{\text{syst.}}(\Delta x_i) = \pm \frac{|N_{\Delta s^{\pm}}(\Delta x_i) - N_{\text{nom}}(\Delta x_i)|}{N_{\text{nom}}(\Delta x_i)} \tag{4.13}$$

4.5.1 Dominant Contributions

Systematics from Proton Overlay Distribution

The uncertainties derived for each observable in Sect. 4.3.2 are used to vary the contribution from the proton overlay. The largest uncertainties (20-30%) are observed for very small $|t|$ and in the the large ξ^p region where the proton overlay is poorly constrained.

Systematics from the Unfolding Procedure

The uncertainty on the unfolding procedure was already discussed in Sect. 4.4.3. The maximum effects are observed at very large gaps (+15%) due to statistical effects and for small ξ^p (-20%) due to migrations.

4.5.2 Moderate Contributions

Systematics from the Tracking in the Inner Detector

In this study, the track reconstruction efficiency is considered to be well modeled in the Monte Carlo and its effect on the events is taken care of by the unfolding procedure. The size of the uncertainty on such efficiency is taken from a minimum bias particle multiplicity study at 8 TeV [118]. The analysis is performed again with removing (resp. adding) a number of tracks in each bin of the data (resp. Monte Carlo) track p_T and η to match the lowest (resp. highest) uncertainty bound of the efficiency determined in this bin. The largest

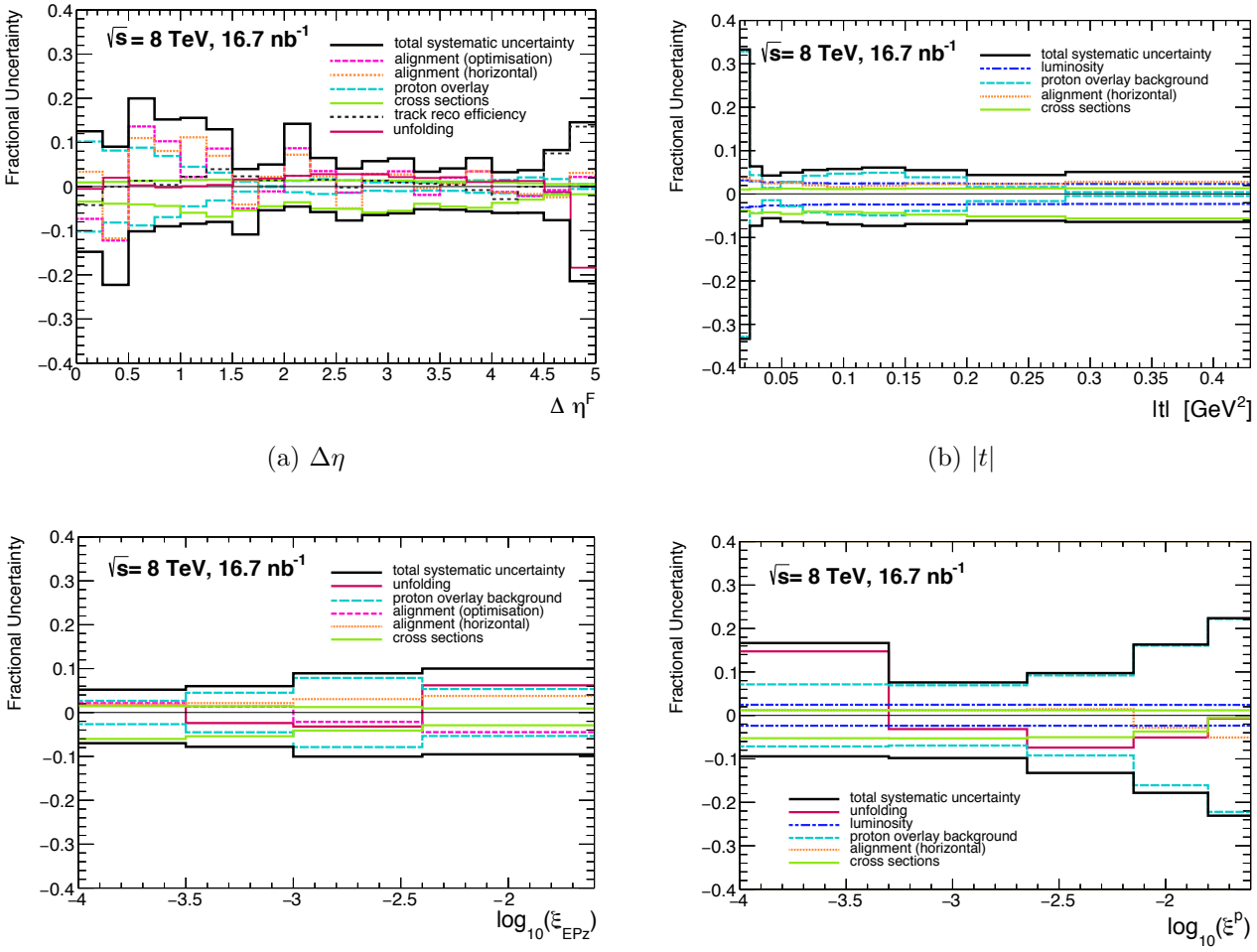

(a) $\Delta\eta$ (b) $|t|$

(c) ξ_{Ep_z} (d) ξ^p

Figure 4.18: The main systematic contributions for the four observables of interest. Only the most important contributions are drawn. The black line indicates the sum in quadrature of each contributions including those which are not drawn.

deviation observed with the standard distribution is taken as the uncertainty. The biggest impact is observed for $\Delta\eta^F$ in the large gap region, where this uncertainty reaches 14%.

Systematics from the Alignment of ALFA

The uncertainties from the alignment of the ALFA detectors are evaluated by varying the correction constants for horizontal and vertical offsets, by varying the rotation within their

uncertainties as determined from variations of the alignment procedures, and by taking the difference between different optimization configurations for the vertical alignment parameters [111]. The biggest impact is observed for the $\Delta\eta^F$ distribution, where the uncertainty due to alignment parameters is above 10% in the small to medium gap range.

Systematics from the Cross Section Breakdown

The cross section breakdown used for the generation of the Monte Carlo is poorly constrained and depends on the parameterization assumed for the diffractive contributions (see Sect. 2.5.1). Some constrains were imposed by CDF [119][120] bounding the ratio of the SD and DD cross section as follows:

$$0.29 < \frac{\sigma_{\mathrm{DD}}}{\sigma_{\mathrm{SD}}} < 0.68 \tag{4.14}$$

In addition, it was observed at the Tevatron and corroborated by generators that the CD cross section could be expressed as a fraction of the SD cross section. In this analysis, the result from Tevatron [121] is used as a constraint:

$$\sigma_{\mathrm{CD}} = 0.093\ \sigma_{\mathrm{SD}}, \tag{4.15}$$

Table 4.12 gives the values for σ_{SD}, σ_{DD} and σ_{CD} obtained at the limit set by the constraints. σ_{ND} is not varied as its effective contribution is negligible. As the proton overlay background contribution mostly or completely comes from ND events with an overlaid proton, the possible variation in the ND cross section are already underpinned by the proton overlay uncertainty (see Sect. 4.3.2).

The cross section of each background contributions are varied by the amount given in Table 4.12. The maximum impact is smaller than 6%.

	PYTHIA8 default	$\sigma_{DD} = 0.29\ \sigma_{SD}$	$\sigma_{DD} = 0.68\ \sigma_{SD}$
σ_{SD} [mb]	12.48	16.07	12.34
σ_{DD} [mb]	8.25	4.66	8.39
σ_{CD} [mb]	1.21	1.56	1.20

Table 4.12: Sets of cross sections used to calculate the systematic uncertainty on the background cross sections.

4.5.3 Minor Contributions

Systematics from the trigger efficiency

The systematics were derived by varying the efficiency upwards and downwards by its uncertainty calculated in Sect. 4.4.1. The biggest impact is observed in the $\Delta\eta^F$ distribution where the uncertainty reaches 3%.

Systematics from the MBTS Response Treatment

The MBTS charge threshold is varied between 3σ and 5σ from the mean of the Gaussian fit to the noise (see Sect. 4.2.2). The maximum effect observed is smaller than 2%.

Uncertainty on the Luminosity

The uncertainty on the luminosity is taken from the elastic scattering analysis using the same run [111] to be $\pm 1.47\%$.

Systematics from the ALFA reconstruction efficiency

As detailed in Sect. 4.4.2, the uncertainty on ϵ_{reco}^{MC} and ϵ_{reco}^{data} were estimated by varying the event selection and background assumption independently and summing each variations in quadrature to get the total upper and lower bound uncertainties.

The Monte Carlo was then reweighted by the ratio $\epsilon^{\text{data}}/\epsilon^{\text{MC}}$ obtained with the two sets of criteria respectively and the maximum variation with respect to the reference distribution was taken as the uncertainty. For all distributions, the bias caused by the uncertainty on the reconstruction efficiency is smaller than 1%.

4.6 Results and Interpretation

The results presented in this section are to be considered as preliminary as the thesis cannot wait for the ATLAS internal review process to be completed.

4.6.1 Differential Cross Sections

The cross sections are given for the observables in the fiducial ξ and $|t|$ ranges of the analysis defined in Sect. 4.2.2:

- $-4.0 < \log_{10}(\xi) < -1.6$,
- $0.016 < |t| < 0.43$ GeV^2.

Cross section differential in ξ

Fig. 4.19 shows the differential cross sections with respect to the effective fractional momentum loss of the scattered proton ξ, when it is obtained from the proton kinematics in ALFA (ξ^p) and when it is approximated based on Eq. 4.1 using the information from the inner detector (ξ_{Ep_z}). Both data and Monte Carlo distributions in the two variables show similar shapes. As expected, the ratio of the Monte Carlo and data cross sections is slightly smaller than their proton-reconstructed counterparts. This is to be correlated to the impossibility of measuring all particles of the diffractive system in the inner detector discussed in the

introduction section of this chapter. The unfolding was performed on both ξ^p and ξ_{Ep_z} using the true non-approximated value of ξ to build the Monte Carlo response matrix, thereby correcting for the limited acceptance of the inner detector. The unfolded distributions were found to agree very well within uncertainties (see Sect. 4.6.2).

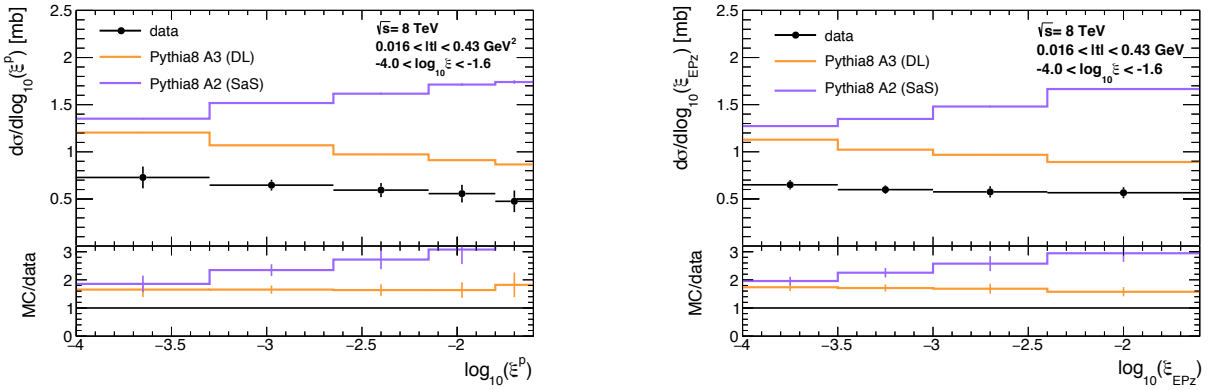

(a) ξ reconstructed from the proton kinematics

(b) ξ reconstructed from the diffractive system

Figure 4.19: Unfolded cross sections differential in ξ^p (a) and ξ_{Ep_z} (b) compared with the Pythia8 A3 model (violet) where the Donnachie Landshoff flux parameterization is assumed, with $\epsilon = 0.085$ and $\alpha'_{\mathbb{P}} = 0.25$ and the A2 model (orange) where the Schuler and Sjöstrand model is assumed, with $\epsilon = 0.0$ and $\alpha'_{\mathbb{P}} = 0.25$. The lower plots show the ratio of the predictions to the measurements. Error bars represent the combination of statistical and systematic uncertainties.

The Pythia8 A3 tune which uses the Donnachie-Landshoff model for the Pomeron flux (see Sect. 2.5.3) and a latest set of PDFs for the proton (NNPDF3.2) describes the data very well in shape but the normalization is off by a factor 1.75, which questions the validity of the single diffractive cross section used in simulations. By contrast, the Pythia8 A2 model, which uses the Schuler and Sjöstrand Pomeron model and the MSTW set of PDFs, does poorly at modeling both normalization and shape. The same distribution obtained for a control sample generated with the A2 tune but using the DL Pomeron flux instead of the

default, was found to be compatible with the A3 sample proving the shape and normalization differences to be mostly coming from the choice of Pomeron flux.

Cross section differential in $\Delta\eta^F$

Fig. 4.20 shows the differential cross sections with respect to the rapidity gap, $\Delta\eta^F$, whose definition is given in the introduction of this chapter. The cross section exhibits a plateau at around 0.3 mb for $\Delta\eta^F > 1.5$, a characteristic feature of soft diffractive interactions where a correlation in $\ln\xi$ is expected (see Eq. 2.48). The increase at smaller gaps, and decrease at larger gap sizes is due to the definition of the observable in terms of a rapidity range restricted by the inner detector acceptance. If the most extraneous particles which would normally define the rapidity gap, escapes the inner detector acceptance on side A (C), the second largest rapidity gap would be measured from the inner detector edge on side C(A), hence biasing the measurement towards smaller rapidity gap values. This implies that events with rapidity gap $\Delta\eta^F > 3.5$, will end up populating the small gap region.

Again, the normalization is better with the Pythia8 A3 model. For both models, the shape is reasonably described in the region of large enough rapidity gaps ($\Delta\eta^F > 1.8$), up to the inner detector acceptance turn-off.

Cross section differential in $|t|$

Fig. 4.21 shows the cross section differential in $|t|$. The data is well described by an exponential behaviour, as predicted by Regge theory. The best agreement in terms of normalization is again obtained with the Pythia8 A3 model. The t-slope was fitted yielding a value compatible with both models. This is detailed in Sect. 4.6.2.

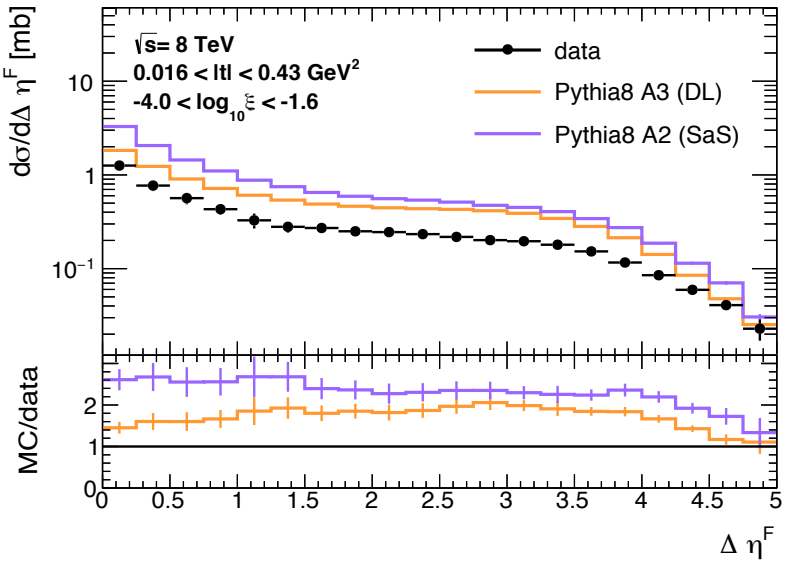

Figure 4.20: Unfolded cross section differential in $\Delta\eta^F$ compared with the PYTHIA8 A3 model (violet) where the Donnachie Landshoff flux parameterization is assumed: $\epsilon = 0.085$, $\alpha'_{\mathbb{P}} = 0.25$ and the A2 model (orange) where the Schuler and Sjöstrand model is assumed: $\epsilon = 0.0$, $\alpha'_{\mathbb{P}} = 0.25$. The lower plot shows the ratio of the predictions to the measurement. Error bars show the combination of systematic and statistical uncertainties

4.6.2 Agreement of the Models

In this section, the Pomeron intercept and t-slope are derived and compared to model predictions and other experiments results.

Derivation of the Pomeron Intercept

From Eq. 2.53, detailing $g_{3\mathbb{P}}$, one may derive the following relationship which depends on the Pomeron trajectory:

$$\frac{d^2\sigma_{\mathrm{SD}}(s)}{dtd\xi} \propto \xi^{1-2\alpha_{\mathbb{P}}(t)} e^{B_{\mathrm{SD}}t} \tag{4.16}$$

To get the differential in ξ solely, one could integrate Eq. 4.16 over the t range considered in the measurement, or simply approximate it by using the average momentum squared at the energy considered $\langle t \rangle$. The latter should lie between the value used to set the energy scale

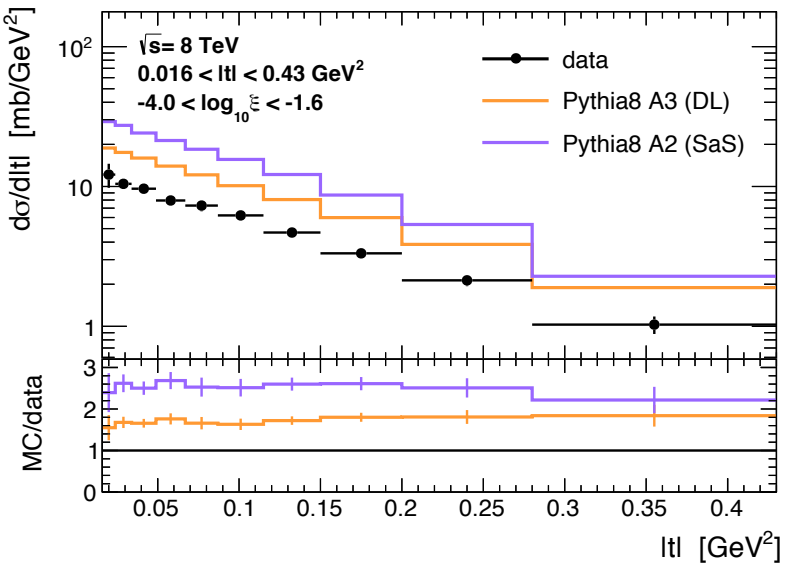

Figure 4.21: Unfolded cross section differential in $|t|$ compared with the PYTHIA8 A3 model (violet) where the Donnachie Landshoff flux parameterization is assumed, with $\epsilon = 0.085$, $\alpha'_{\mathbb{P}} = 0.25$ and the A2 model (orange) where the Schuler and Sjöstrand model is assumed, with $\epsilon = 0.0$, $\alpha'_{\mathbb{P}} = 0.25$. The lower plot shows the ratio of the predictions to the measurement. Error bars show the combination of statistical and systematic uncertainties.

of the interaction in PYTHIA8 A2, $\langle t \rangle_{\text{A2}}$, and the one used in PYTHIA8 A3, $\langle t \rangle_{\text{A3}}$. For lack of a better knowledge, the mean of the two is taken using the difference as the uncertainty bandwidth. This yields:

$$\frac{d\sigma_{\text{SD}}}{d\log_{10}(\xi)} = C\xi^{2[1-\alpha(\langle t \rangle)]} \tag{4.17}$$

$$= C10^{2\log_{10}(\xi)[1-\alpha(\langle t \rangle)]} \tag{4.18}$$

where C is a constant parameter and $\langle t \rangle = \frac{\langle t \rangle_{\text{A2}} + \langle t \rangle_{\text{A3}}}{2} = \frac{-0.136-0.129}{2} = -0.1325 \pm 0.0035$ GeV^2. By fitting the cross section differential in ξ (see Fig. 4.22), $\alpha_{\mathbb{P}}(\langle t \rangle)$ is extracted and the Pomeron intercept is derived from its trajectory evaluated in $\langle t \rangle$, using the standard value $\alpha'_{\mathbb{P}} = 0.25$:

$$\alpha_{\mathbb{P}}(0) = \alpha_{\mathbb{P}}(\langle t \rangle) - \alpha'_{\mathbb{P}} \cdot \langle t \rangle \tag{4.19}$$

Observable	$\langle t \rangle$	$\alpha_{\mathbb{P}}(\langle t \rangle)$	$\alpha_{\mathbb{P}}(0)$
ξ^p	-0.1325	1.038 ± 0.028	1.071 ± 0.028
ξ_{Ep_z}	-0.1325	1.026 ± 0.011	1.059 ± 0.012

Table 4.13: Value of $\alpha_{\mathbb{P}}(\langle t \rangle)$ obtained from the fit to the ξ^p and ξ_{Ep_z} differential cross sections and the extrapolation to the Pomeron intercept.

Table 4.13 gives the result of the fit of $\alpha_{\mathbb{P}}$ for the average momentum squared considered and the value of the intercept extrapolated for the cross section differential in ξ_{Ep_z} and the cross section differential in ξ^p. The Pomeron intercept obtained from the the extrapolation of the fit value is agreeing to 1σ with the intercept used in the PYTHIA8 A3 model : $\alpha_{\mathbb{P}}^{A3}(0) = 1.071$ [55]. However, it does not agree with the intercept from PYTHIA8 A2, $\alpha_{\mathbb{P}}^{A2}(0) = 1.003$ [55].

Derivation of the t-Slope

A fit is performed on the cross section shown in Fig. 4.21 using the following parameterization:

$$\frac{d\sigma_{SD}}{dt} = Ce^{B_{\mathrm{SD}}t} \tag{4.20}$$

The bias caused by the binning is corrected for by shifting the data point associated to each bin on the left or the right depending on the distribution of events within the bin. The shifts are determined from simulation and are given in Appendix E. The fit function is plotted on Fig. 4.23.

The systematic uncertainty on the fit is evaluated from performing the fit several times with all systematic shifts and summing all deviations from the nominal fit in quadrature.

The t-slope obtained from this procedure is: $B = 7.55 \pm 0.18$ GeV^{-2} which lies in between

the PYTHIA8 A2 and PYTHIA8 A3 derived slopes:

$$B_{\mathrm{A2}} = 7.82 \pm 0.03 \text{ GeV}^{-2} \qquad B_{\mathrm{A3}} = 7.10 \pm 0.01 \text{ GeV}^{-2} \tag{4.21}$$

This is the first measurement in ATLAS of the t-slope for single diffraction.

4.6.3 Summary

The analysis presented in this chapter is the first detailed and precise study of single diffractive processes, i.e. $pp \to p + X$, with the ATLAS and ALFA detectors. The measurement used a small dedicated sample recorded in 2012 at $\sqrt{s} = 8$ TeV. During this run the average pile-up was low and no crossing angle was set between the beams.

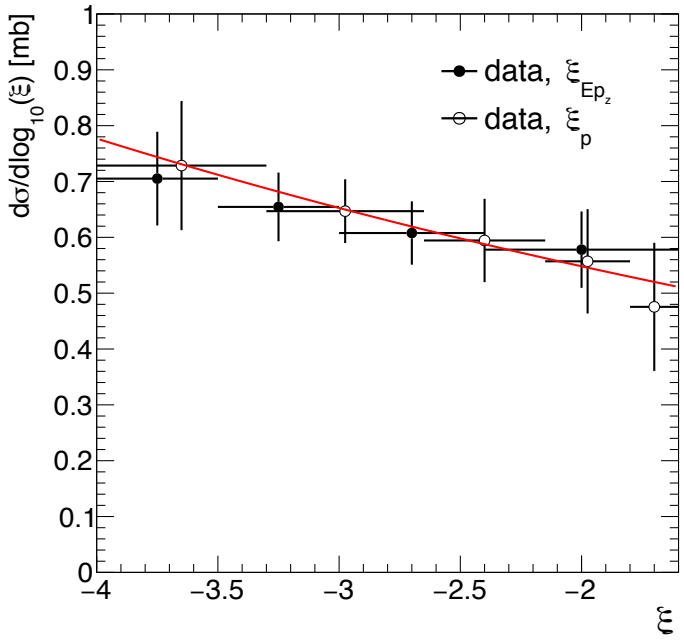

Figure 4.22: Combination of the cross section reconstructed from ξ^p (white) and ξ_{Ep_z} (black). The red line shows the fit result performed on the ξ^p cross section to extract $\alpha_{\mathbb{P}}(\langle t \rangle)$. Error bars represent the combination of statistical and systematic uncertainties.

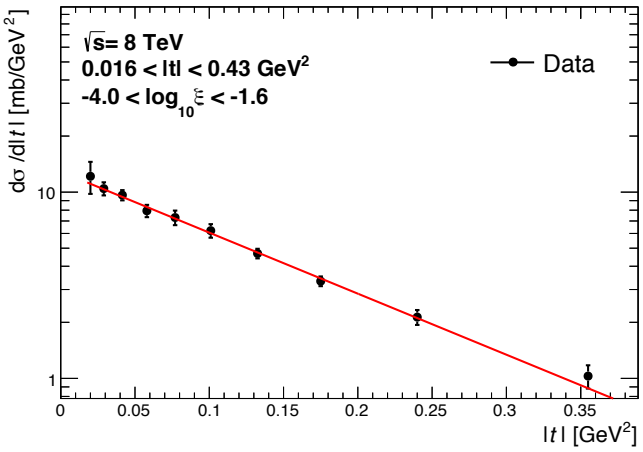

Figure 4.23: Fit on the $|t|$ data cross section with the bin centers shifted to account for the distribution of events in a bin. Error bars represent the combination of statistical and systematic uncertainties.

The event selection is based on the coincidence of signals recorded in opposite directions with respect to the interaction point: a forward proton signal is required in the ALFA spectrometers in conjunction with some activity in the central detectors (MBTS and inner detectors). The selected sample is dominated by the SD process but also contains a significant fraction of background. Backgrounds are due to uncorrelated signal in ALFA, mostly coming from elastic events, as well as inner detector activity arising mainly from non-diffractive processes.

The data is unfolded using a Bayesian algorithm which makes use of the simulated SD detector response to correct for resolution and reconstruction biases. Prior to the unfolding, the Monte Carlo samples were corrected to account for the ALFA reconstruction efficiency mismodelling, and the data was corrected for trigger inefficiencies.

Cross-section spectra are obtained with respect to the four momentum transfer squared, $|t|$,

the size of the rapidity gap measured from the edge of the inner detector on the proton tag side, $\Delta\eta^F$, and the fractional momentum loss, ξ, reconstructed from two different methods. Results are given for a fiducial range of $-4.0 < \log_{10}\xi < -1.6$ and $0.026 < |t| < 0.43$ GeV^2.

The rapidity gap cross section exhibits the typical diffractive plateau but the measurement is limited in range by acceptance effects. The cross section differential in $|t|$ can be described by an exponential with a t dependence driven by the slope: $B = 7.55 \pm 0.18$ GeV^{-2}, whose value is compatible with both the Donnachie-Landshoff and the Schuler-Sjöstrand Pomeron models. The cross sections derived from the two ξ reconstructions are in excellent agreement. The distribution shape agree well with the Pythia8 A3 model but a normalization factor is observed. The cause of such disagreement is to be investigated. It was shown recently that a different treatment of multi-parton interactions, for hard diffractive events generated with Pythia8, could impact the cross section quite a lot by suppressing the diffractive signature [122].

The fit based on Regge phenomenology, performed on the inner-detector spectrum (ξ_{Ep_z}), allows to evaluate the Pomeron trajectory at the energy scale considered, and its intercept can be extrapolated to a value of $\alpha(0) = 1.059 \pm 0.012$ when a Pomeron slope $\alpha' = 0.25$ GeV^2 is assumed. This result is in remarkable agreement with extractions from total and elastic cross-sections measurements, despite being obtained based on a very different approach.

Probing the Pomeron Content by Measuring the Charge Production Asymmetry of Electroweak Bosons

The work presented in this chapter was supported by SNSF-Doc.Mobility and NSERC. It was performed entirely by the author of the thesis with guidance from Dr. Rafal Staszewski and Prof. Christophe Royon, from CEA-Saclay, between 2013 and 2015. It led to a publication in the Journal of High Energy Physics (JHEP) in April 2016 [123]. The study was initially meant to be followed by an ATLAS/AFP analysis but this project was aborted due to AFP-driven time constraints and as Prof. Royon, left for another experiment.

The phenomenological study of electroweak bosons diffractive production interaction is presented. Prospective results are reported regarding the possibility of constraining the quark content of the Pomeron in a high energy collision scenario, making use of forward proton taggers designed for diffractive measurements such as the recently installed ATLAS Forward Proton (AFP) detector [85].

5.1 Constraints on the PDFs

The non-diffractive production of electroweak boson (Z and W) in hadronic collision is of particular interest as it allows to constrain the hadrons PDFs. At first order, the W and

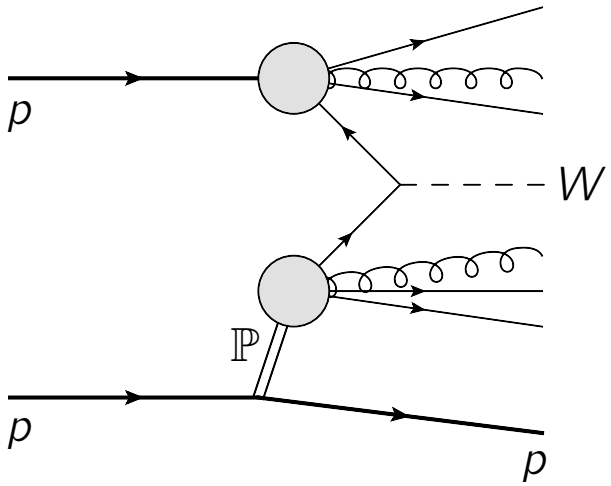

Figure 5.1: Feynman representation of a W boson produced diffractively through the interaction of two quarks. The Ingelman and Schlein (IS) model is assumed.

Z bosons are produced from annihilation of two quarks from a hard sub-process. For such processes, the factorization theorem allows to choose a scale at which one can separate the non-resolvable dynamics from the hard parton-parton interaction as detailed in Eq. 2.24 of Sect. 2.2.1. The non-resolvable part corresponds to the PDFs, the distributions functions of the partons inside the colliding objects (typically protons or anti-protons). For a given energy scale, a direct measurement of the PDFs is possible by analyzing the $W^{\pm}$ production asymmetry in rapidity. At a given rapidity, the two charged vector bosons are produced by quarks of different flavours. Hence, the measured asymmetry can be used as a constraint in the global fit of the PDFs. In particular, it directly constrains the ratio of the u- and d- quark distributions. Such constraints on the proton PDFs were derived from extensive analysis of Tevatron data collected by DØ [124] and CDF [125][126] before the LHC era.

The study presented in this chapter assumes that, by analogy to the non-diffractive case, the Pomeron DPDFs (defined in Sect2.2.2 can also be constrained by measuring the charge asymmetry of the W bosons when the latter are produced diffractively. This requires the

Pomeron to be a resolvable object and the semi-hard parton-parton interaction to be interpreted within the IS model (see Sect. 2.2.2). In the case of single diffraction, the partons involved in the (semi) hard sub-process would then come from the dissociating parton on one side and from the resolvable Pomeron on the other side (see Fig. 5.1), hence providing constraints on both the proton and Pomeron parton content. As discussed in Sect. 2.3, the IS model is now competing with the color reconnection hypothesis, so there is a strong interest in testing the Pomeron structure as it questions the universality of the Pomeron picture itself.

Invoking factorization at a scale $\mu_F^2 = Q^2$ and making explicit the dependence on the type of incoming partons in the hard sub-subprocess by labeling them with i and j, the cross section in terms of the Reggeon and Pomeron contributions is given by:

$$\frac{d\sigma}{d\xi dx_p d\beta dt} = S^2 \sum_{i,j} \left[\mathcal{F}^i_{\mathbb{R}/p}(\xi,\beta,t,Q^2) + \mathcal{F}^i_{\mathbb{P}/p}(\xi,\beta,t,Q^2)\right] f_p^j(x_p,Q^2)\, d\hat{\sigma}^{ij\to W} \tag{5.1}$$

where $d\hat{\sigma}^{ij\to W}$ corresponds to the hard parton-parton cross section of the W boson for a set of incoming quarks i and j, x_p and β denote the respective fraction of the dissociating proton and Pomeron momenta involved in the interaction and S^2 is the rapidity gap survival probability, that factorizes all the soft effects suppressing the rapidity gap at high $\sqrt{s}$ (details were given in Sect. 2.2.2). Diffractive PDFs for the Reggeon and the Pomeron are expressed in term of fluxes by analogy with Eq. 2.25:

$$\mathcal{F}^{ij}_{\mathbb{R}/p}(\xi,\beta,t,Q^2) = f_{\mathbb{R}/p}(\beta,Q^2)\cdot\phi_{\mathbb{R}}(\xi,t) \tag{5.2}$$

$$\mathcal{F}^{ij}_{\mathbb{P}/p}(\xi,\beta,t,Q^2) = f_{\mathbb{P}/p}(\beta,Q^2)\cdot\phi_{\mathbb{P}}(\xi,t). \tag{5.3}$$

Eq. 5.1 is only valid if no interference between Reggeon and Pomeron diagrams is assumed. The DPDF fits assuming either minimal or maximal interference are both in good agreement with the data collected at HERA [41] and the coupling term is thereby often neglected.

A W boson has a 32% chance to decay leptonically by emitting a neutrino ($W \to \mu\nu_\mu$). Leptonic decays involving muons have a clean signature in the detector as muons are long-lived particles that can easily e.g. be identified in the ATLAS spectrometers. Table 5.1 shows the Forward Proton Monte Carlo (FPMC) diffractive cross-section predictions when applying a kinematic cut on ξ to account for the AFP limited acceptance. The contributions coming from the Reggeon and Pomeron exchange are given separately. The sum of both contributions, corresponding to the integral of Eq. 5.1 and the fraction of the cross section coming from the Reggeon exchange, are also quoted. As predicted by the theory, the relative Reggeon contribution decreases as $\sqrt{s}$ increases.

Acceptance	$\sqrt{s}$	$\sigma_{\mathbb{P}}$ [pb]	$\sigma_{\mathbb{R}}$ [pb]	$\sigma_{\mathbb{P}} + \sigma_{\mathbb{R}}$ [pb]	$\sigma_{\mathbb{R}}/(\sigma_{\mathbb{P}} + \sigma_{\mathbb{R}})$
$0.02 < \xi < 0.12$	2 TeV	68.10	19.69	87.79	0.22
	7 TeV	493.1	91.35	584.45	0.16
	13 TeV	1213	177.8	1390.8	0.13
	14 TeV	1350	188.3	1538.3	0.12

Table 5.1: Cross sections for production of single-diffractive W bosons through the muonic channel $W \to \mu\nu_\mu$ given by the FPMC generator. Both Pomeron and Reggeon pictures are presented with the center-of-mass energy of the collision ranging from 2 to 14 TeV for the typical acceptance in ξ of the AFP detector. No rapidity gap survival factor is applied. ($S^2 = 1$).

5.2 Constraints on the Pomeron Quarkonic Structure

5.2.1 Structure Function of the Pomeron

By analogy to the structure function F_2 describing the structure of the proton, one can define a Pomeron structure function $F_2^{\mathbb{P}}$ as being the charge weighted sum of the partons DPDFs

$f_{\mathbb{P}/p}$ at a given energy scale $\mu_F^2 = Q^2$:

$$F_2^{\mathbb{P}}(\beta, Q^2) = \sum_i \beta q_i^2 f_{\mathbb{P}/p}(\beta, Q^2) \tag{5.4}$$

where q_i corresponds to the charge of parton i.

An often used quantity is the diffractive structure function $F_2^{D(4)}$ where the above sum is convoluted with the Pomeron flux $\phi_{\mathbb{P}}$:

$$F_2^{D(4)}(\xi, t, \beta, Q^2) = \phi_{\mathbb{P}}(\xi, t) \cdot F_2^{\mathbb{P}}(\beta, Q^2) \tag{5.5}$$

which gives the following dependence in terms of the Pomeron PDFs:

$$F_2^{D(4)} \propto \left(\frac{2}{3}\right)^2 u_{\mathbb{P}} + \left(\frac{1}{3}\right)^2 d_{\mathbb{P}} + \left(-\frac{1}{3}\right)^2 s_{\mathbb{P}} \tag{5.6}$$

The current Pomeron PDFs were measured from HERA DDIS data (see Sect. 2.2.2). In these measurements, the charge neutrality of the Pomeron was accounted for by imposing symmetry conditions on the PDFs : $u_{\mathbb{P}} = \bar{u}_{\mathbb{P}}$, $d_{\mathbb{P}} = \bar{d}_{\mathbb{P}}$ and $s_{\mathbb{P}} = \bar{s}_{\mathbb{P}}$. In addition, since HERA inclusive measurements were not flavour-sensitive, the PDFs were all assumed to be the same [127]:

$$u_{\mathbb{P}} = d_{\mathbb{P}} = s_{\mathbb{P}} \equiv q. \tag{5.7}$$

This will be referred in the following as the HERA hypothesis. From this assumption, Eq. 5.6 can be rewritten as a condition on the Pomeron PDFs, with no more dependence on β and $\phi_{\mathbb{P}}$:

$$4u_{\mathbb{P}} + d_{\mathbb{P}} + s_{\mathbb{P}} = 6q \tag{5.8}$$

Let us define the scaling factors R_{ud} and R_{sd} as:

$$R_{ud} = \frac{u_{\mathbb{P}}}{d_{\mathbb{P}}}, \text{ and } R_{sd} = \frac{s_{\mathbb{P}}}{d_{\mathbb{P}}},$$

and the Pomeron PDFs can then be expressed as:

$$u_{\mathbb{P}}(\beta, Q^2) = \frac{6R_{ud}}{1 + R_{sd} + 4R_{ud}} \cdot q(\beta, Q^2) \tag{5.9}$$

$$d_{\mathbb{P}}(\beta, Q^2) = \frac{6}{1 + R_{sd} + 4R_{ud}} \cdot q(\beta, Q^2) \tag{5.10}$$

$$s_{\mathbb{P}}(\beta, Q^2) = \frac{6R_{sd}}{1 + R_{sd} + 4R_{ud}} \cdot q(\beta, Q^2) \tag{5.11}$$

It should be noted that R_{ud} and R_{sd} depend on β and the choice of scale. The case $R_{ud} = R_{sd} = 1$ corresponds to the HERA default assumption.

5.2.2 PDF Scale Factors

In the case of HERA data, an electron is used to probe the content of the Pomeron and the typical cross section for any DDIS process depends on the Pomeron PDFs as follows:

$$\begin{aligned}\sigma \sim \iint \mathrm{d}\beta\, \mathrm{d}Q^2 \Big(& u_{\mathbb{P}}|V_{ud}|^2 + u_{\mathbb{P}}|V_{us}|^2 \\ & + d_{\mathbb{P}}|V_{ud}|^2 + s_{\mathbb{P}}|V_{us}|^2 \\ & + \rho(Q^2) s_{\mathbb{P}}|V_{sc}|^2 + \rho(Q^2) d_{\mathbb{P}}|V_{dc}|^2 \Big)\end{aligned} \tag{5.12}$$

where $V_{qq'}$ corresponds to the CKM matrix element coupling quark q to quark q' (only the main contributions are considered). The suppression of the contributions involving heavy quarks is accounted for by adding an energy dependent correction factor $\rho(Q^2)$ ranging from 0 (full suppression) to 1 (no suppression) to the terms that involve c-quark interaction. Replacing the PDFs by there expressions in terms of the scaling factor (Eqs. 5.9–5.11) yields:

$$\sigma = A \cdot \frac{1}{1 + R_{sd} + 4R_{ud}} \Big[R_{ud}\big(|V_{ud}|^2 + |V_{us}|^2\big) + |V_{ud}|^2 + \bar{\rho}|V_{dc}|^2 + R_{sd}\big(|V_{us}|^2 + \bar{\rho}|V_{sc}|^2\big) \Big]$$

where $\bar{\rho}$ is the average ρ over Q^2, and

$$A \sim \iint q(\beta, Q^2)\, \mathrm{d}\beta\, \mathrm{d}Q^2 \tag{5.13}$$

The cross section for the W production process when assuming Eq. 5.7 is predicted to be $\sigma_0 = \sigma|_{R_{ud}=R_{sd}=1} = 500$ fb, while the actual H1 measurement [10] gave: $\sigma = 390 \pm 120\,(\text{stat.}) \pm 70\,(\text{syst.})$ fb. These values can be used to constrain the ratio of the cross sections as:

$$0.4 = \frac{390 - 120 - 70}{500} < \sigma/\sigma_0 < \frac{390 + 120 + 70}{500} = 1.16 \tag{5.14}$$

where

$$\begin{aligned}\sigma/\sigma_0 =& \frac{1}{2|V_{ud}|^2 + 2|V_{us}|^2 + \bar{\rho}|V_{dc}|^2 + \bar{\rho}|V_{sc}|^2} \cdot \frac{6}{1 + R_{sd} + 4R_{ud}} \\ &\cdot \left[R_{ud}\Big(|V_{ud}|^2 + |V_{us}|^2\Big) + |V_{us}|^2 + \bar{\rho}|V_{sc}|^2 + R_{sd}\Big(|V_{ud}|^2 + \bar{\rho}|V_{dc}|^2\Big) \right].\end{aligned}$$

Fig. 5.2 shows the limits the H1 measurement sets on the flavour ratios for ratio values ranging between 0.1 and 10. R_{ud} must thereby satisfy $0.4 < R_{ud}$, while R_{sd} can take any value in the range considered. These constrains are defined independently of the value of β and the choice of factorization scale.

5.3 Measurement using W Boson Charge Asymmetry

5.3.1 Theoretical Motivations

Provided a large enough transverse momentum of the W boson, the hard cross section $d\hat{\sigma}^{ij\to W}$ can be approximated at first order by:

$$d\sigma^{ij\to W} = \frac{2\pi G_F}{3\sqrt{2}} M_W^2 |V_{ij}|^2 \delta(\hat{s} - M_W^2) \tag{5.15}$$

where $\hat{s} = s\xi$ is the central energy of the diffractive system, M_W is the mass of the W boson, G_F is the Fermi constant and V_{ij} is the CKM matrix element associated to quarks i and j. The ud vertices are depicted on Fig. 5.3. the W boson: Assuming that we are in a regime that allows the Reggeon vertices to be neglected ($\xi < 0.12$ and $\sqrt{s}$ high enough) and with

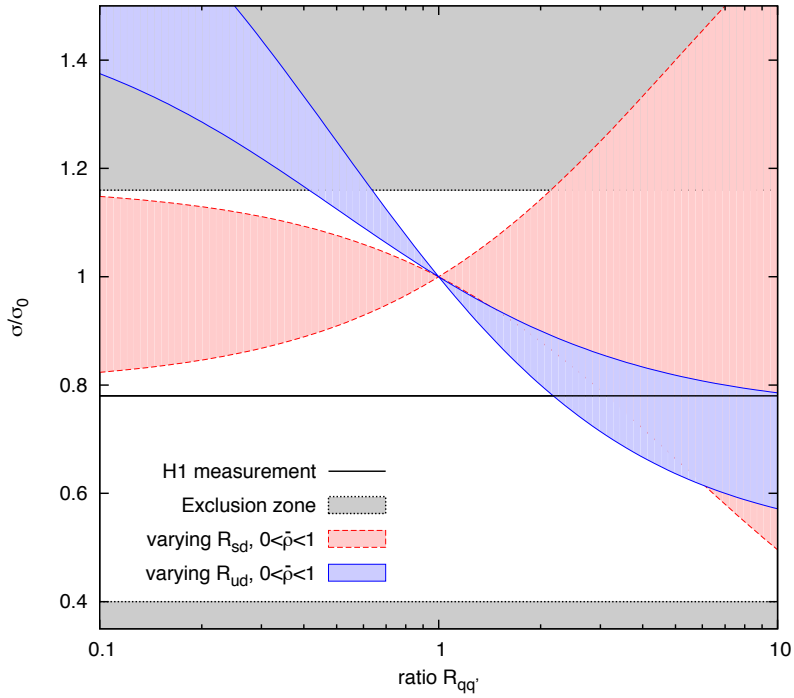

Figure 5.2: Constraints on the quark content of the Pomeron. σ_0 (σ) corresponds to the cross section with (without) the $R_{ud} = R_{sd} = 1$ hypothesis. The black solid line is the value measured by H1. The gray area with dashed contour corresponds to the excluded region defined in Eq. 5.14. The filled area delimited by blue plain (resp. red dotted) lines corresponds to the case were R_{ud} (resp. R_{sd}) is varied for $\bar{\rho}$ ranging from 0 to 1.

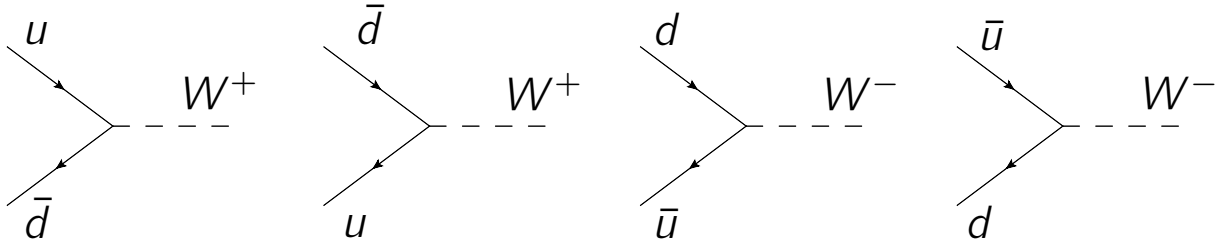

Figure 5.3: Leading-order diagrams for W boson production. The CKM suppressed [us] vertices are not shown here. For pp collisions, the two sea quarks contributions depicted on the right of the figure are suppressed.

$Q^2 = M_W^2$, we derive the following relation for the differential cross section as a function of

the rapidity $\mathcal{Y}$ of the W boson:

$$\frac{d\sigma}{d\mathcal{Y}\,d\xi} = S^2 G_0 \sum_{ij} |V_{ij}|^2\, \phi_{\mathbb{P}}(\xi, t)\, f^i_{\mathbb{P}}(\beta, M_W^2)\, f^j_p(x_p, M_W^2) \tag{5.16}$$

where $G_0 = \frac{2\pi G_F M_W^2}{3\sqrt{2}s}$.

In terms of the two charges we get:

$$\begin{aligned}\frac{d\sigma_{W^+}}{d\mathcal{Y}\,d\xi} = S^2\, G_0\, \phi_{\mathbb{P}}\Big(&|V_{ud}|^2 \left[u_{\mathbb{P}} \cdot \bar{d}_p + \bar{d}_{\mathbb{P}} \cdot u_p\right] \\ &+|V_{us}|^2 \left[\bar{s}_{\mathbb{P}} \cdot u_p + u_{\mathbb{P}} \cdot \bar{s}_p\right]\Big)\end{aligned} \tag{5.17}$$

$$\begin{aligned}\frac{d\sigma_{W^-}}{d\mathcal{Y}\,d\xi} = S^2\, G_0\, \phi_{\mathbb{P}}\Big(&|V_{ud}|^2 \left[\bar{u}_{\mathbb{P}} \cdot d_p + d_{\mathbb{P}} \cdot \bar{u}_p\right] \\ &+|V_{us}|^2 \left[s_{\mathbb{P}} \cdot \bar{u}_p + \bar{u}_{\mathbb{P}} \cdot s_p\right]\Big)\end{aligned} \tag{5.18}$$

where the PDFs with index p are the proton PDFs. The kinematics dependences on the PDFs and Pomeron flux are not displayed here for simplicity.

The charge asymmetry $\mathcal{A}$ of the W boson produced through a single diffractive mechanism is defined as the normalized difference between the cross sections of production of W^+ and W^-. It can be extracted from Monte Carlo simulation by counting the number of positive and negative W bosons produced diffractively, N^+ and N^-, for a given integrated luminosity:

$$\mathcal{A} = \frac{d\sigma_{W^+} - d\sigma_{W^-}}{d\sigma_{W^+} + d\sigma_{W^-}} = \frac{N^+ - N^-}{N^+ + N^-} = \frac{N^+ - N^-}{N} \tag{5.19}$$

where $N = N^+ + N^-$ is the sum of all event containing a W boson.

$\mathcal{A}$ is a particularly good observable since it is not sensitive to the gap survival probability which cancels out when dividing numerator and denominator. Another advantage is that the systematic contributions to the uncertainty that are common to W^+ and W^- measurements will cancel out when taking the ratio. Combining Eqs. 5.9–5.11 with Eqs. 5.16 and 5.19 the

following formula is derived:

$$\frac{1-\mathcal{A}}{1+\mathcal{A}} = \frac{|V_{ud}|^2\left[R_{ud}\cdot d_p + \bar{u}_p\right] + |V_{us}|^2 R_{sd}\left[\bar{u}_p + s_p\right]}{|V_{ud}|^2\left[R_{ud}\cdot \bar{d}_p + u_p\right] + |V_{us}|^2 R_{sd}\left[u_p + \bar{s}_p\right]} \tag{5.20}$$

displaying an explicit dependence on the R_{ud} and R_{sd} Pomeron flavour ratios. Relation 5.20 can also be written in terms of of the valence quark q^v and see quark q^s distributions:

$$\frac{|V_{ud}|^2\left[R_{ud}\cdot (d_p^v + d_p^s) + \bar{u}_p^s\right] + |V_{us}|^2 R_{sd}\left[\bar{u}_p^s + s_p^v + s_p^s\right]}{|V_{ud}|^2\left[R_{ud}\cdot \bar{d}_p^s + u_p^v + u_p^s\right] + |V_{us}|^2 R_{sd}\left[u_p^v + u_p^s + \bar{s}_p^s\right]} \tag{5.21}$$

In the energy regime considered, when x_p is large with respect to ξ, the sea quarks contribution which arises from gluons (via $g \to q^s\bar{q}^s$) whose PDF becomes small compared to that of the proton valence quarks at large x_p, can be ignored (see Appendix F). We obtain the following equation for the proton valence quarks:

$$\frac{1-\mathcal{A}}{1+\mathcal{A}} \approx \frac{|V_{ud}|^2 R_{ud}\cdot d_p^v + |V_{us}|^2 R_{sd}\cdot s_p^v}{|V_{ud}|^2 R_{ud}\cdot u_p^v + |V_{us}|^2 R_{sd}\cdot u_p^v} \tag{5.22}$$

In this section, predictions obtained from simulation of $pp \to [W^{\pm}X]p$ production at $\sqrt{s} = 14$ TeV using the FPMC generator [128] are detailed. For the Pomeron PDFs, the H1 Fit B is used (see Sect. 2.5.3), which by default assumes the Pomeron flux to follow a Donnachie-Landshoff behaviour (see Eq. 2.67). The scattered protons are required to have $\xi < 0.12$ such that the Reggeon contribution can be neglected as well as the Pomeron-Reggeon interference. A gap survival probability of $S^2 = 0.03$ [69] is assumed.

5.3.2 Monte Carlo Predictions

Fig. 5.4 shows the statistical uncertainty on the charge asymmetry of truth-level W bosons as a function of the integrated luminosity of the beams for different hypothesis on the R_{ud} ratio satisfying the constrains from Fig. 5.4. The charge asymmetry sensitivity to the R_{sd}

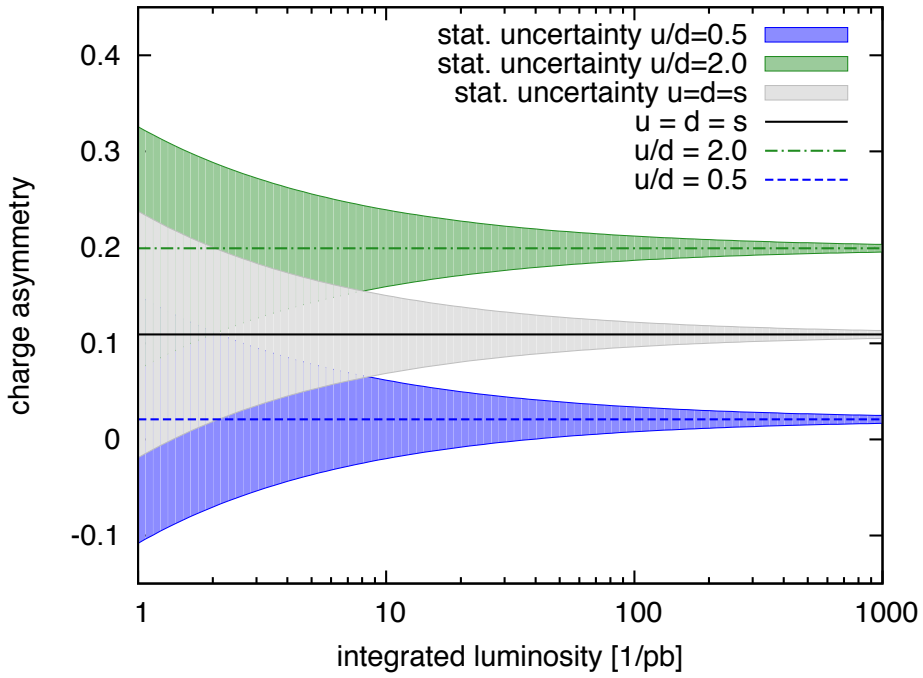

Figure 5.4: Statistical uncertainty on the charge asymmetry of the W boson integrated over the full kinematic space up to $\xi < 0.12$, for various integrated luminosity and varying the R_{ud} ratio.

ratio was found to be compatible with zero and is therefore not displayed on Fig. 5.4. Starting from 10 pb^{-1} data, it becomes statistically possible to distinguish one hypothesis from another. As derived from Monte Carlo truth information, those predictions do not account for any systematical bias.

Figs. 5.5 and 5.6 show FPMC predictions on the W boson charge asymmetry, and the muon charge asymmetry for muons coming from the $W \to \mu\nu_\mu$ decay, respectively. In the latter, the ATLAS standard set of selections is applied to the muon and neutrino transverse momenta at truth level: $p_T^\mu > 30$ GeV and $p_T^{\nu_\mu} > 35$ GeV. In addition, the reconstructed transverse mass of the W is constrained as follows:

$$M_T = \sqrt{(E_{T,\mu} + E_{T,\nu_\mu})^2 - (\vec{p}_{T,\mu} + \vec{p}_{T,\nu_\mu})^2} > 40 \text{ GeV} \tag{5.23}$$

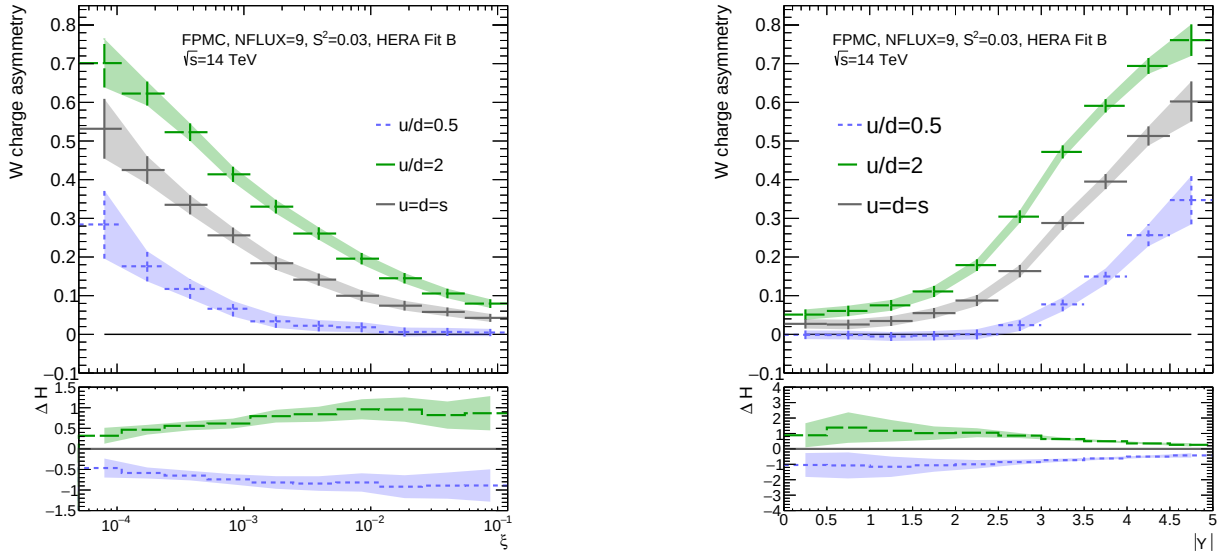

(a) (b)

Figure 5.5: Binned truth W boson charge asymmetry as a function of ξ(a) and $|\mathcal{Y}|$(b) obtained from FPMC, considering only a Pomeron exchange contribution. Various values of R_{ud} are tested. A kinematic cut $\xi < 0.12$ is applied to all samples. The bottom plots show the deviations with respect to the HERA hypothesis. The shaded areas show the statistical uncertainty obtained by scaling the Monte Carlo sample to a 100 pb^{-1} luminosity.

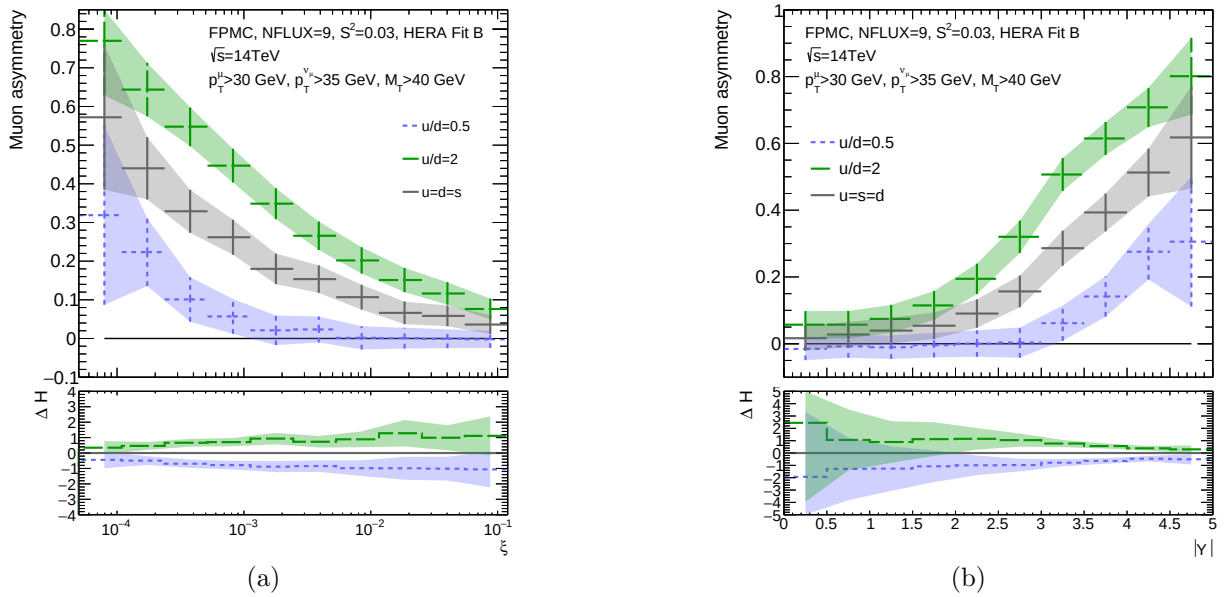

(a) (b)

Figure 5.6: Binned truth muon charge asymmetry as a function of ξ(a) and $|\mathcal{Y}|$(b) obtained from FPMC, considering only a Pomeron exchange contribution. Various values of R_{ud} are tested. Some kinematic cuts are applied. The bottom plots show the deviations with respect to the HERA hypothesis. The shaded areas show the statistical uncertainty obtained by scaling the Monte Carlo sample to a 300 pb^{-1} luminosity.

where $E_{T,\mu} = \sqrt{m_\mu^2 + \vec{p_{T,\mu}}^{\,2}}$ and $E_{T,\nu_\mu} = p_{T,\nu_\mu}$ are the transverse energies of the muons and the neutrino and $\vec{p}_{T,\mu}$ and $\vec{p}_{T,\nu_\mu}$ their transverse momenta. The sensitivity of the asymmetry to such selection was assessed by evaluating $\mathcal{A}$ (Eq. 5.19) for various sets of cut on p_T^μ, $p_T^{\nu_\mu}$ and M_T (see Appendix G). For the HERA hypothesis case, the asymmetry value varies by less than 5% when the selection on the muon transverse momentum is varied from $p_T^\mu > 10$ GeV to $p_T^\mu > 35$ GeV or when the selection on the transverse missing energy is varied from $p_T^{\nu_\mu} > 10$ GeV to $p_T^{\nu_\mu} > 35$ GeV. Also, when varying the cut on the transverse mass from $m_T > 10$ GeV to $m_T > 70$ GeV, the asymmetry varies by less than 4%. Hence, the measurement bias caused by applying the ATLAS standard set of cuts is small. The sensitivity of $\mathcal{A}$ to the selection criteria can then be considered negligible as long as the later are in the above-mentioned ranges.

The asymmetry dependence in ξ and $\mathcal{Y}$ are shown for three different scalings: $R_{ud} = 0.5$, 1, 2. The bottom plots show the relative deviation from the asymmetry imposed by the HERA hypothesis $\mathcal{A}_H$ ($u_{\mathbb{P}} = s_{\mathbb{P}} = d_{\mathbb{P}}$): $\Delta H = \frac{\mathcal{A}-\mathcal{A}_H}{\mathcal{A}_H}$. The $R_{sd} = 0.5$ and $R_{sd} = 2$ cases are not displayed because the distributions were found to be compatible with the HERA hypothesis.

The distributions of the number of charges are considered binomial. Hence, the sample proportion of W^+ is assumed to have the following variance:

$$\mathrm{var}\left(\frac{N^+}{N}\right) = \frac{1}{N^2}\mathrm{var}(N^+) = \frac{1}{N^2}\cdot\frac{N^+}{N}\cdot\frac{N-N^+}{N} = \frac{N^+(N-N^+)}{N^3} \tag{5.24}$$

and the error will be:

$$\sigma\left(\frac{N^+}{N}\right) = \sqrt{\frac{N^+(N-N^+)}{N^3}} \tag{5.25}$$

$\mathcal{A}$ can be expressed in term of N^+/N as $\mathcal{A} = 2\frac{N^+}{N} - 1$, giving the following error on $\mathcal{A}$:

$$\sigma(\mathcal{A}) = 2\,\sigma\left(\frac{N^+}{N}\right) = \sqrt{\frac{4N^+(N-N^+)}{N^3}} = \sqrt{\frac{4N^+N^-}{N^3}} \tag{5.26}$$

Statistical uncertainties are calculated by scaling the Monte Carlo to a given integrated luminosity. Statistical uncertainties shown on Fig. 5.5 correspond to a luminosity of 100 pb^{-1} while, for Fig. 5.6, an integrated luminosity $L = 300$ pb^{-1} was used.

5.4 Feasibility Discussion

It was shown that 300 pb^{-1} data would be sufficient in order to test the different Pomeron content hypothesis when analyzing the charge asymmetry differential in ξ and $\mathcal{Y}$ for the muon channel $W \to \mu\nu_\mu$. This decay channel has a clean signature and is therefore favoured. The electron channel could be investigated too, with extra challenges coming from the electron identification. The standard ATLAS W boson selection may be applied, with possibilities of a small tightening up of the cuts.

The study is conducted in a restrained kinematic range $\xi < 0.12$ where the Reggeon exchange contribution is negligible. The AFP detector was designed to have an acceptance above 80% for $0.025 < \xi < 0.12$ when used with the collision optics. It is therefore very well suited to perform high diffraction studies such as the one presented in this chapter.

For the simulation, a constant rapidity gap survival probability was assumed, and the value of $S^2 = 0.03$ was chosen, in line with other diffractive studies. There is no consensus for such a choice however and the study of the diffractive W boson production at LHC will therefore put a stringent test on the IS model and the possibility to factorize the physics phenomena responsible for the rapidity-gap filling.

Conclusion

In this thesis, two studies are presented, both covering the topic of diffractive interactions in pp collisions at high energies. Both studies are based on the assumption that diffractive interactions are driven by Pomeron exchanges, and that, at the LHC energies, the Pomeron structure is resolvable. The nature of the exchange may be probed by analyzing a set of inclusive observables and testing the models towards the measurement. This is typically what was done in Chapter 4, which combines the first precise results from the measurement of the single-diffractive cross section in ATLAS. In this case, scattered protons are tagged using the ALFA spectrometers whose acceptance was optimized for elastic scattering studies, thereby restraining the analysis to a rather small t range. The work presented in Chapter 5 adopts a more exclusive approach by analyzing the possibility of probing the Pomeron content by measuring the relatively frequent production of electroweak bosons through hard but diffractive interactions. The study suggests that such measurements can be performed with the newly installed AFP detectors which offers access to harder processes with a broader coverage in t and no elastic cross-contamination.

The inclusive analysis detailed in Chapter 4 shows the preliminary results comparing the measured differential cross sections with the Pythia8 A2 and A3 tunes. Both models assume the HERA-derived diffractive PDFs for the Pomeron but the flux models differ: the A2

tune uses the Schuler and Sjöstrand representation while A3 uses the Donnachie-Landshoff model. In addition, the A3 model is having a different set of parameters for the multi-parton interaction modeling and it makes use of a more inclusive set of proton PDFs. With this description, a relatively better agreement in shape is observed than when using the A2 tune. A 1.75 factor in the normalization is observed, which at first sight questions the validity of the cross-section breakdown assumed in the Monte Carlo models. A new treatment of the gap survival at hard scales in PYTHIA8 [122] gives encouraging results however. A dynamical model for the multi-parton interactions may be appropriate for diffractive interactions in the energy regime considered.

The t-slope extracted from fitting the t cross-section spectrum, $B = 7.55 \pm 0.18$ GeV^{-2}, lies in between and is compatible with the predicted values from the Donnachie-Landshoff and the Schuler-Sjöstrand models within 2.4σ and 1.3σ respectively. The values of the Pomeron intercept, extracted from fitting the ξ spectra measured either from the proton kinematic or based on the information from the inner detector, are both found to be compatible with that of the A3 model to less than 1σ. This supports the universality of the description of diffractive processes in a single framework via the optical theorem, within the phase space covered by this measurement.

Further investigations of the transition region from soft to hard diffraction are targeted at exclusive productions. For 2018, ALFA will continue to operate under low pile-up conditions with large bunch separation (100 ns) to cope with the ALFA trigger front-end dead time. The planning for the data-taking is still under discussion, the special beam setups requiring some coordination with the other LHC experiments. Diffractive physics at larger t and the

possible breakdown of the factorization theorem at a higher energy scale will be investigated with AFP. By being able to collect data at higher luminosities, such detector will enable the study of rarer final states with clean signatures.

The charge asymmetry analysis discussed in Chapter 5 is one example of such study probing the flavour of the Pomeron, provided it is resolvable. In this thesis, it was shown that the charge asymmetry of leptons coming from the W boson leptonic decay, where the electroweak boson comes from a single-diffractive interaction, is sensitive to the valence quark content of the Pomeron. It was demonstrated that 300 pb^{-1} of diffractive data should be statistically sufficient to discriminate between different Pomeron quarkonic PDFs scenarios in the muonic channel only, if one restrains oneself to the kinematic range where the Pomeron trajectory dominates over the Reggeon's. These predictions rely on the way diffraction (as well as parton shower and hadronization) is modeled in FPMC (Forward Physics Monte Carlo), the HERWIG-derived generator used to produce the samples. The cross sections also typically depend on which factor is used as the rapidity gap survival probability. The AFP machine is currently undergoing its second phase of commissioning and all four trackers are now installed. In 2017, more than 150 pb^{-1} of exploitable data were collected with an average pile-up of 2. The analysis of diffractive W can therefore be started. Other ongoing or foreseen studies include the production of single diffractive jet, central diffractive dijets, jet-gap-jet and photon+jet events, as well as Z boson. All make use of standard ATLAS triggers, simply adding a proton tag at Level 1 when necessary.

The time-of-flight detector (ToF), which will allow to reconstruct diffractive vertices in a very high pile-up environment, is planned to be installed this year (2018) but the schedule is

still not fixed. AFP will operate without the ToF under standard and reduced pile-up beam conditions until the next technical stop. The addition of the ToF will allow to study rarer diffractive processes, such as central exclusive production, with a low level of background, thereby providing clean ways to search for new resonances. Some photon-induced processes will have a relatively large cross sections under these conditions which is of interest for anomalous gauge coupling searches [129–131]. In this context, proton tagging will effectively allow the LHC to function as an energy-tunable gluon-gluon or photon-photon collider.

Appendices

The ATLAS Calorimetry and Muon Spectroscopy Systems

This appendix refers to Sect. 3.2.1. The ATLAS calorimetry and muon spectrometry systems were not used for the work presented in this thesis. They constitute nevertheless most of the ATLAS detector volume and are briefly described in this appendix.

A.1 Calorimeters

The ATLAS detector includes several calorimeters designed to measure the energy of electrons, photons, taus and hadron jets. Particles escaping the Inner Detector may undergo electromagnetic or hadronic interactions with the material of the calorimeter, producing showers of particles.

There are two types of cascades depending on the nature of the source: electromagnetic showers are primarily initiated by electrons or photons, while hadronic showers are coming from hadrons. Electromagnetic and hadronic showers have radically different properties and thus require separate detection techniques.

There are two levels of detectors throughout the full range of $|\eta| < 4.9$, with an inner layer of electromagnetic calorimeters and an outer layer of hadronic calorimeters (see Fig. F.1). The ATLAS calorimeters are all sampling calorimeters, meaning that alternating layers of absorbing and active material are used as illustrated in Fig. A.1. The layer design allows

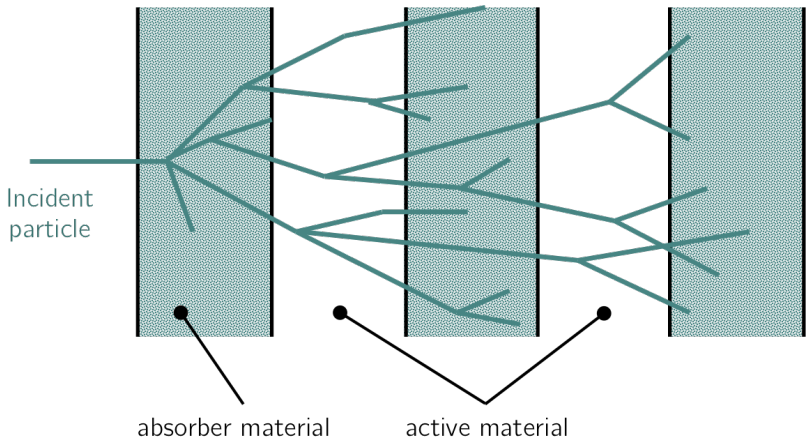

Figure A.1: Illustration of the development of a shower in a sampling calorimeter.

for creating compact calorimeters with excellent shower containment, but at the cost of energy lost in the absorption layers. By knowing the expected fraction of energy lost in the absorber, one can however rescale the energy of the shower to account for the unobserved contribution. It should be noted that the term *electromagnetic calorimeter* refers to a type of detector designed to fully contain most electromagnetic showers. Hadronic showers may very well appear in the EM calorimeters although they are more likely to start in the hadronic calorimeters. A complete description of the full set of calorimeters can be found in [71]. Since the calorimeter information was not used in the context of this thesis, the Liquid Argon and Tile calorimeters are only briefly described.

A.1.1 The Liquid Argon Calorimeters

The ATLAS Liquid Argon calorimeters (LAr) are sub-detectors designed for both electromagnetic and hadronic calorimetry [132]. The system is composed of a central barrel, two endcaps and two additional forward installations (see yellow parts on Fig. F.1). The active material for all LAr calorimeters is liquid argon. An electron (or positron) traveling through the absorber can interact with it producing photons or charged particles. A photon

traversing the absorber interacts with the material via Compton scattering, photo-electric effect or pair production. The produced particles ionize the gas. A high voltage is applied to the plates enclosing the active layers causing the electrons to drift to the electrodes. The signal arrives within a short period of time before decreasing to zero linearly. The absorber is usually made of lead, copper or cooper-tungsten depending on the expected particle flow. The EM part comprised a barrel (EMB), two endcaps (EMEC) and a forward small barrel (FCal1), all with high granularity. Put all together, the LAr EM calorimeters cover the $1.375 < |\eta| < 4.9$ pseudo-rapidity region, with a blind zone, called the *crack*, between $1.375 < |\eta| < 1.52$ at the transition between the EMB and the EMEC. The typical resolution in energy for the EMB calorimeter was determined in electron test beam measurements [133]:

$$\frac{\sigma_E}{E} = (\frac{10}{\sqrt{E}} \pm 0.2)\% \tag{A.1}$$

with E in GeV. The LAr has four additional hadronic calorimeters: the Hadronic Endcap Calorimeter (HEC) and two Forward Calorimeters (FCal2 and FCal3). The HEC is installed behind the two EMEC and uses copper absorbers. It covers the region $1.5 < |\eta| < 3.2$. FCal2 and FCal3 are located behind FCal1 in the forward regions and are using tungsten as an absorber.

The EMB, EMEC and HEC are segmented in η, ϕ and in depth to allow to measure both the energy and direction of the showers, improving the overall momentum resolution of reconstructed particles.

A.1.2 The Tile Calorimeter

The Tile and Extended Tile barrel segments are hadronic calorimeters using plastic scintillating tiles as the active medium. The absorbing layers for these calorimeters are comprised of steel. The scintillating tiles are arranged radially and perpendicularly to the beam line The

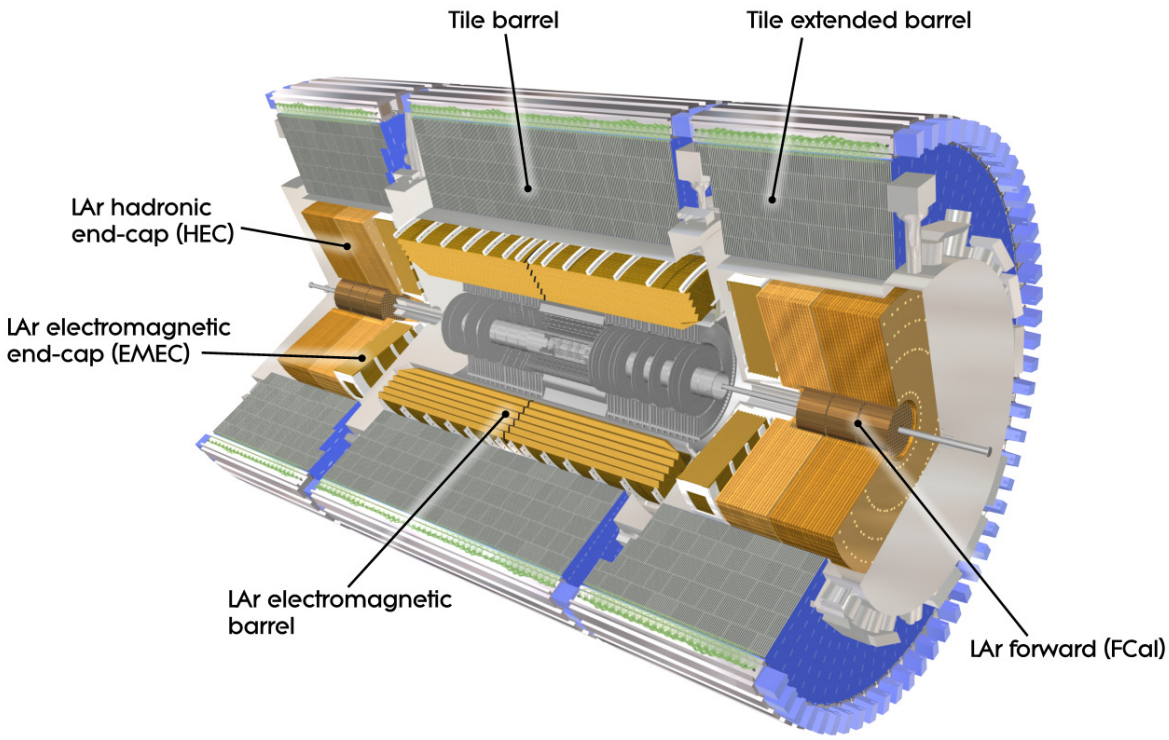

Figure A.2: Infographics of the calorimetry installation in ATLAS.

Tile barrel covers out to $|\eta| < 1.0$ and the Extended Tile barrel extends in the $0.8 < |\eta| < 1.7$ region (see blue and gray parts on Fig. A.2). At the transition region between the Tile and Extended Tile, additional modules are added to compensate for the crack in the LAr. Tile modules have a relatively coarse granularity compared to the LAr, which is suitable for hadronic shower measurement as those are much less compact than their electromagnetic counterparts. The typical resolution in energy for the Tile calorimeter was determined in test beam studies [134]:

$$\frac{\sigma_E}{E} = (\frac{52}{\sqrt{E}} \pm 5.7)\% \tag{A.2}$$

As charged particles travel through the scintillating tiles, photons are produced in proportion to the amount of energy deposited. These photons are collected with wavelength-shifting fibers within each cell. The light from a group of cells is then readout by Photo-multiplier

Tubes (PMTs).

A.2 Muons Spectrometers

For particles to make it through the full Inner Detector and calorimeter system, they must be either non-interacting or, like muons, be rarely interacting with the calorimeter material, or they must be coming from a shower which was not fully contained in the hadronic calorimeters. Non-interacting particles such as neutrinos, will escape the detector and their presence can be inferred by calculating the amount of missing energy in each event. Secondary hadrons coming from a shower are relatively rare. Most particles then reaching the outside of the calorimeter layers are muons.

The ATLAS muon spectrometer is composed of one barrel and two wheel-shaped subdetectors integrated with a series of toroidal magnets surrounding the calorimeters, which provide the magnetic field necessary to bend the particles tracks, and infer on their momenta (see yellow parts on Fig. A.3) .

Each region has two complimentary apparati: one is designed to be used as a trigger and to have a very fast response, the other one is slower but leads to a much more precise measurement of the momentum. They are briefly overviewed in the following and presented in Fig. A.3.

A.2.1 Fast Response Systems

In the barrel region ($|\eta| < 1.05$), a set Resistive Plate Chambers (RPCs) made out of two resistive plates separated by 2 mm of ionizing gas, is installed and provides a spatial resolution of 10 mm in both z and (r, ϕ). In the endcap regions ($1.05 < |\eta| < 2.4$), Thin Gap Chambers (TGCs) are used with a z axial resolution going from 2 to 6 mm, and an azimuthal resolution

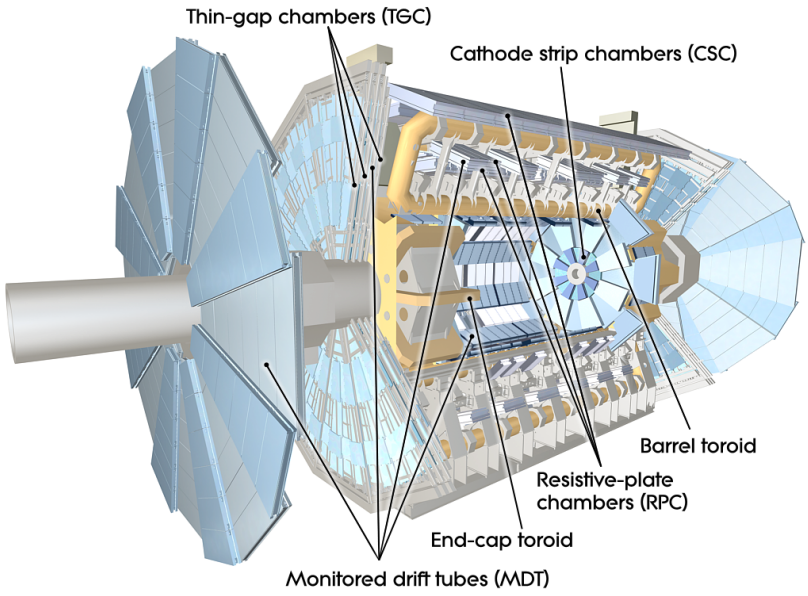

Figure A.3: Infographics of the muon spectrometers in ATLAS showing the toroid magnets used to bend the muons trajectories.

in the (r, ϕ) plane ranging from 3 to 7 mm. TGCs are multi-wire proportional chambers comprising two metal plates arranged in wheels, segmented into readout strips, with a plane of parallel metal wires in between. Both systems are able to produce a signal within 15 to 25 ns. Technical descriptions of the ATLAS RPCs and TGCs are found in [135] and [136] respectively.

A.2.2 High Resolution Systems

The slower but much more precise detectors are the Monitored Drift Tubes (MDTs) and the Cathode Strip Chambers (CSCs). The MDTs are used in both the barrel and endcap regions, covering pseudo-rapidities up to $|\eta| = 2.7$. They contain 1150 modules split into three barrel layers and four endcap layers forming a 354000-channels detection surface with z and r resolution of 35 μm. The MDT detector is built in a technology similar to the TRT, with straws filled with Ar/CO_2 gas. The typical charge collection time of such tube detectors in

700 ns, which makes it considerably slower than the RPCs and TGCs. However, its resolution is much better. CSCs have a similar resolution (40 μm) but are able to provide a faster response (typically 40 ns). They consist of multi-wire proportional chambers constructed from two parallel metal sheets with one plane of parallel wires running in between. The sheets are segmented into cathode strips in such a way that one sheet has strips aligned parallel and the other perpendicular to the direction of the wires. A reduced collection time is necessary since those detectors are located in a relatively forward region ($2.0 < |\eta| < 2.7$), where the muons flux is the most important. More details may be found in [137].

ALFA specifications

This appendix refers to Sect. 3.2.2.

B.1 Resolution of the Scintillating Fiber Plates

Each ALFA station is composed of 10 staggered supports. Each support is made of two fiber plates disposed in the front and a back side with fibers glued in the u and v directions perpendicular to each other (see Fig. B.1). This provides the two-dimensional information on the location of the track. The pixel formed by the fiber layer staggering have a width $d = 500$ μm, which corresponds to the diameter of a fiber The probability distribution for a charged particle to be detected in the plate at any (u, v) location is constant: $P(u) = P(v) = 1/d$, with d in μm. The resolution per plate is expressed from the variance of such distribution, which in the u direction gives:

$$\sigma_u^2 = \int_{-d/2}^{d/2} (u - \langle u \rangle)^2 P(u) du = \int \int_{-d/2}^{d/2} \frac{u^2}{d} = \frac{d^2}{12} \tag{B.1}$$

which corresponds to a resolution $\sigma_u = \frac{d}{\sqrt{12}} = 144$ μm. The same calculation applies to the v direction.

Since the ten support plates are staggered with a shift of the 1/10th of the fiber size, the resolution per track is improved by 10, $\sigma_{u,v}^{\text{track}} = 14.4$ μm. In practice the resolution is deteriorated by imperfect staggering, cross-talk between the imperfectly coated fibers, noise and inefficient fiber channels, and the achieved resolution is 30 μm [138].

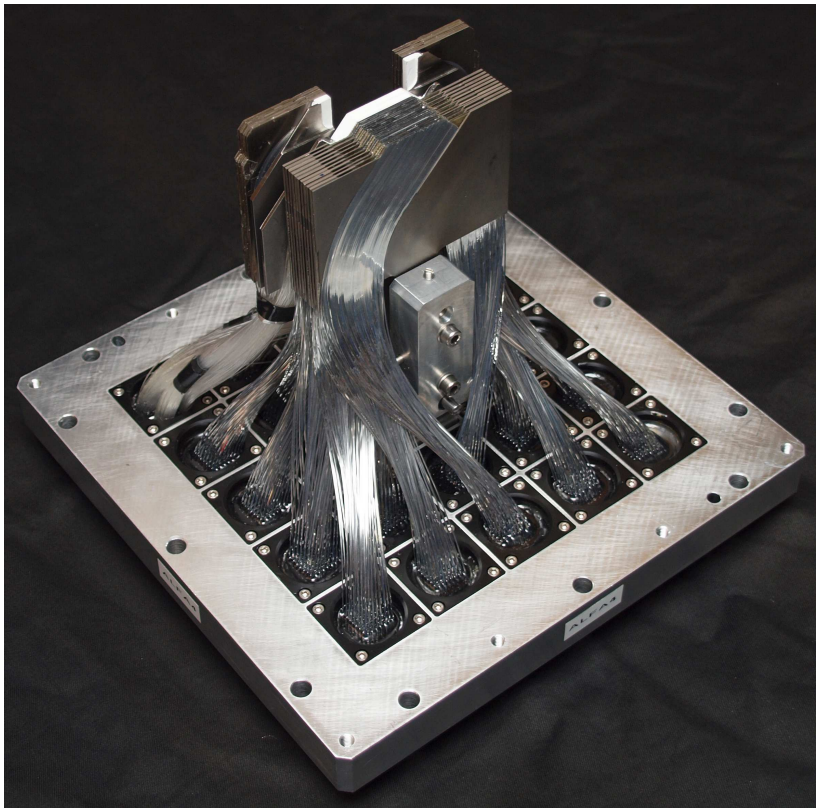

Figure B.1: Pictures showing the arrangement of the fibers in ALFA.

Tuning of the SD Cross Section

This appendix refers to Sect. 4.3.2.

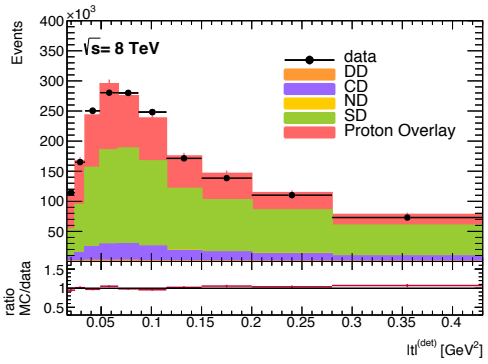

(a) Absolute value of the momentum transferred squared

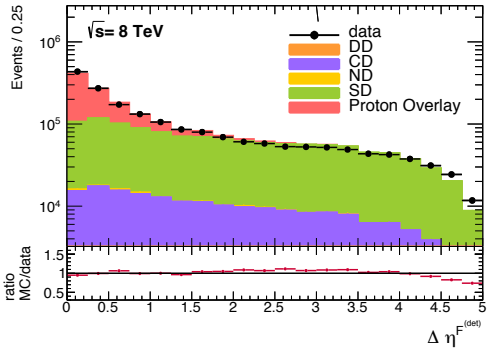

(b) Rapidity gap measured from the inner detector tracker edge on the side of the proton tag

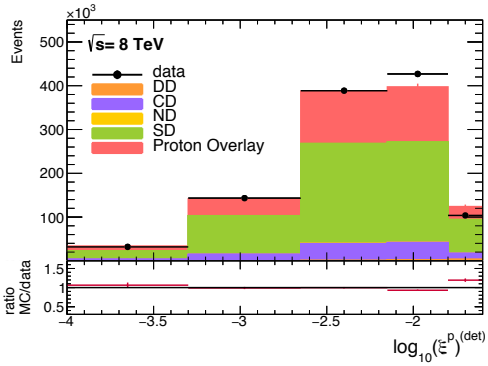

(c) Scattered proton fractional energy loss reconstructed from ALFA

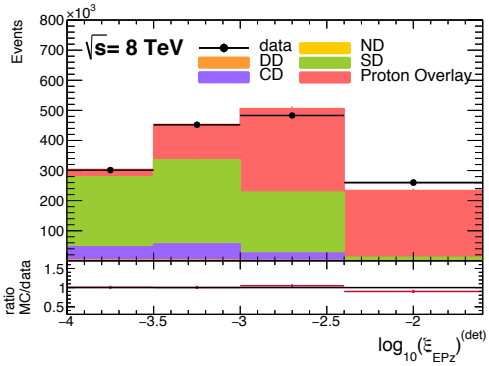

(d) Scattered proton fractional energy loss reconstructed from the diffractive system

Figure C.1: Comparison of the sum of each Monte Carlo contributions and the proton overlay contribution stacked, with the data corrected for the trigger efficiency. The SD cross section was tuned to achieve the optimal match with the data. The tuned value is $\sigma_{SD} = 7.7$ mb.

Unfolding Systematics Evaluation

This appendix refers to Sect. 4.4.3.

Table D.1 gives the functions used to reweight Monte Carlo truth distribution in order to mimic the data at reconstructed level.

Observable	Reweighting function (x = Observable)
$\log_{10}(\xi_p)$	$0.2578 - 0.3249x - 0.0697x^2$
$\log_{10}(\xi_{EPz})$	$0.0118 - 0.3723x - 0.0578x^2$
$\lvert t \rvert$	$0.63245 - 0.2750x + 0.1329x^2$
$\Delta\eta$	$0.6400 + 0.0378x - 0.0610x^2 + 0.0121x^3$

Table D.1: Polynomial used to reweight the Monte Carlo SD truth distribution for the data-driven closure test. More details may be found in [117].

Bin Point Shifts for t-Slope Fit

This appendix refers to Sect. 4.6.2.

Bin range [GeV^2]	Nominal Center [GeV^2]	Corrected Center [GeV^2]
$0.016 < \|t\| \leq 0.024$	0.0200	0.0200
$0.024 < \|t\| \leq 0.034$	0.0290	0.0289
$0.034 < \|t\| \leq 0.049$	0.0415	0.0413
$0.049 < \|t\| \leq 0.067$	0.0580	0.0578
$0.067 < \|t\| \leq 0.087$	0.0770	0.0767
$0.087 < \|t\| \leq 0.115$	0.1010	0.1005
$0.115 < \|t\| \leq 0.150$	0.1325	0.1322
$0.150 < \|t\| \leq 0.200$	0.1750	0.1740
$0.200 < \|t\| \leq 0.280$	0.2400	0.2369
$0.280 < \|t\| \leq 0.430$	0.3550	0.3437

Table E.1: List of bin centers. The nominal bin center where no shift is applied is compared to the bin center determined from the center of gravity of the bin (from [112])

Valence quarks, sea quarks and gluon PDFs

This appendix refers to Sect. 5.3.1.

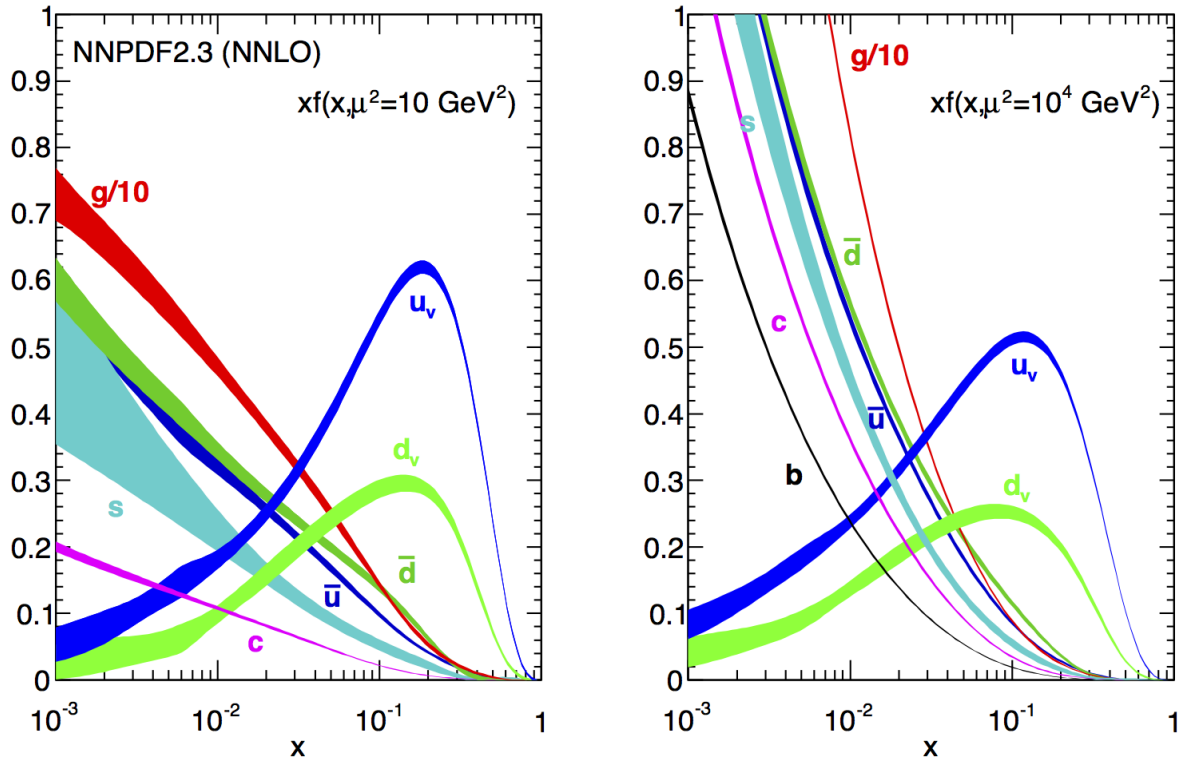

Figure F.1: Next-to-leading order parton density functions obtained by the NNPDF collaboration for $Q^2 = 10$ GeV^2 (left) and $Q^2 = 10^4$ GeV^2 (right) [139]. For large Bjorken x, the contributions from gluons, and gluon-initiated sea quarks are suppressed.

Asymmetry Sensitivity to the Selection Cuts

This appendix refers to Sect. 5.3.2.

W boson charge asymmetries extracted from samples generated with FPMC are shown for the different hypothesis on the Pomeron quark content: $R_{ud} = 0.5$, 1 and 2 when applying separately a cut on the transverse momentum of the muon $p_{T,\mu}$ (Table G.1), on the transverse momentum of the missing particle p_{T,ν_μ} (Table G.2) and on the transverse mass of the reconstructed W boson M_T (Table G.3). The shaded row corresponds to the final selection applied on the samples.

$p_{T,\mu}$ cut [GeV]	$\mathcal{A}_H$	$\mathcal{A}_{u/d=0.5}$	$\mathcal{A}_{u/d=2}$
$p_{T,\mu} > 10$	0.1132 ±0.0034	0.0136 ±0.0034	0.2169 ±0.0033
$p_{T,\mu} > 15$	0.1137 ±0.0035	0.0138 ±0.0035	0.2177 ±0.0034
$p_{T,\mu} > 20$	0.1121 ±0.0037	0.0128 ±0.0037	0.2180 ±0.0036
$p_{T,\mu} > 25$	0.1115 ±0.0040	0.0149 ±0.0040	0.2162 ±0.0039
$p_{T,\mu} > 30$	0.1108 ±0.0044	0.0153 ±0.0044	0.2158 ±0.0043
$p_{T,\mu} > 35$	0.1153 ±0.0053	0.0159 ±0.0053	0.2132 ±0.0052
$p_{T,\mu} > 40$	0.1206 ±0.0109	0.0228 ±0.0110	0.2258 ±0.0106
$p_{T,\mu} > 45$	0.0591 ±0.0358	0.0053 ±0.0365	0.2263 ±0.0346
$p_{T,\mu} > 50$	0.0559 ±0.0528	0.0722 ±0.0526	0.2708 ±0.0491

Table G.1: Extracted value of the charge asymmetry for different hypothesis: $\mathcal{A}_H$ for $R_{ud} = 1$, $\mathcal{A}_{u/d=0.5}$ for $R_{ud} = 0.5$ and $\mathcal{A}_{u/d=2}$ for $R_{ud} = 2$, as a function on the cut applied on the muon transverse momentum.

p_{T,ν_μ} cut [GeV]	$\mathcal{A}_H$	$\mathcal{A}_{u/d=0.5}$	$\mathcal{A}_{u/d=2}$
$p_{T,\nu_\mu} > 10$	0.1132 ±0.0034	0.0137 ±0.0034	0.2168 ±0.0033
$p_{T,\nu_\mu} > 15$	0.1135 ±0.0035	0.0139 ±0.0035	0.2178 ±0.0034
$p_{T,\nu_\mu} > 20$	0.1121 ±0.0037	0.0129 ±0.0037	0.2178 ±0.0036
$p_{T,\nu_\mu} > 25$	0.1112 ±0.0040	0.0149 ±0.0040	0.2160 ±0.0039
$p_{T,\nu_\mu} > 30$	0.1115 ±0.0044	0.0155 ±0.0044	0.2158 ±0.0043
$p_{T,\nu_\mu} > 35$	0.1152 ±0.0053	0.0160 ±0.0053	0.2136 ±0.0052
$p_{T,\nu_\mu} > 40$	0.1171 ±0.0109	0.0215 ±0.0110	0.2255 ±0.0106
$p_{T,\nu_\mu} > 45$	0.0593 ±0.0358	0.0067 ±0.0365	0.2242 ±0.0346
$p_{T,\nu_\mu} > 50$	0.0529 ±0.0528	0.0621 ±0.0530	0.2742 ±0.0491

Table G.2: Extracted value of the charge asymmetry for different hypothesis: $\mathcal{A}_H$ for $R_{ud} = 1$, $\mathcal{A}_{u/d=0.5}$ for $R_{ud} = 0.5$ and $\mathcal{A}_{u/d=2}$ for $R_{ud} = 2$, as a function on the cut applied on the missing particle transverse momentum.

M_T cut [GeV]	$\mathcal{A}_H$	$\mathcal{A}_{u/d=0.5}$	$\mathcal{A}_{u/d=2}$
$M_T > 10$	0.1127 ±0.0033	0.0136 ±0.0033	0.2177 ±0.0033
$M_T > 20$	0.1132 ±0.0034	0.0137 ±0.0034	0.2169 ±0.0033
$M_T > 30$	0.1134 ±0.0035	0.0138 ±0.0035	0.2178 ±0.0034
$M_T > 40$	0.1121 ±0.0037	0.0128 ±0.0037	0.2177 ±0.0036
$M_T > 50$	0.1112 ±0.0040	0.0148 ±0.0040	0.2160 ±0.0039
$M_T > 60$	0.1112 ±0.0044	0.0154 ±0.0044	0.2157 ±0.0043
$M_T > 70$	0.1151 ±0.0053	0.0165 ±0.0053	0.2131 ±0.0052
$M_T > 80$	0.1181 ±0.0109	0.0211 ±0.0110	0.2290 ±0.0106

Table G.3: Extracted value of the charge asymmetry for different hypothesis: $\mathcal{A}_H$ for $R_{ud} = 1$, $\mathcal{A}_{u/d=0.5}$ for $R_{ud} = 0.5$ and $\mathcal{A}_{u/d=2}$ for $R_{ud} = 2$, as a function on the cut applied on the W boson transverse mass.

Bibliography

[1] E. L. Feinberg and I. Pomerančuk, High energy inelastic diffraction phenomena, Il Nuovo Cimento (1955-1965) **3** (1956) p. 652, ISSN: 1827-6121, URL: http://dx.doi.org/10.1007/BF02746068.

[2] G. F. Chew and S. C. Frautschi, Principle of Equivalence for all Strongly Interacting Particles within the S-Matrix Framework, Phys. Rev. Lett. **7** (10 1961) p. 394, URL: https://link.aps.org/doi/10.1103/PhysRevLett.7.394.

[3] G. Aad et al., Observation of a new particle in the search for the Standard Model Higgs boson with the ATLAS detector at the LHC, Phys. Lett. **B716** (2012) p. 1, arXiv: 1207.7214 [hep-ex].

[4] S. Chatrchyan et al., Observation of a new boson at a mass of 125 GeV with the CMS experiment at the LHC, Phys. Lett. **B716** (2012) p. 30, arXiv: 1207.7235 [hep-ex].

[5] D. Bernard et al., The cross section of diffraction dissociation at the cern SPS collider, Physics Letters B **186** (1987) p. 227 , ISSN: 0370-2693, URL: http://www.sciencedirect.com/science/article/pii/0370269387902851.

[6] G. J. Alner et al., The UA5 High-Energy anti-p p Simulation Program, Nucl. Phys. **B291** (1987) p. 445.

[7] T. Aaltonen et al., Diffractive Dijet Production in $\bar{p}p$ Collisions at $\sqrt{s} = 1.96$ TeV, Phys. Rev. **D86** (2012) p. 032009, arXiv: 1206.3955 [hep-ex].

[8] C. Adloff et al., Diffraction dissociation in photoproduction at HERA, Z. Phys. **C74** (1997) p. 221, arXiv: hep-ex/9702003 [hep-ex].

[9] J. Breitweg et al., Study of photon dissociation in diffractive photoproduction at HERA, Z. Phys. **C75** (1997) p. 421, arXiv: hep-ex/9704008 [hep-ex].

[10] A. Aktas et al., Measurement and QCD analysis of the diffractive deep-inelastic scattering cross-section at HERA, Eur. Phys. J. **C48** (2006) p. 715, arXiv: hep-ex/0606004 [hep-ex].

[11] S. Chekanov et al., Deep inelastic scattering with leading protons or large rapidity gaps at HERA, Nucl. Phys. **B816** (2009) p. 1, arXiv: 0812.2003 [hep-ex].

[12] H. Yukawa, On the Interaction of Elementary Particles. I, Proceedings of the Physico-Mathematical Society of Japan. 3rd Series **17** (1935) p. 48.

[13] J. C. Street and E. C. Stevenson, New Evidence for the Existence of a Particle of Mass Intermediate Between the Proton and Electron, Phys. Rev. **52** (9 1937) p. 1003, URL: https://link.aps.org/doi/10.1103/PhysRev.52.1003.

[14] S. H. Neddermeyer and C. D. Anderson, Note on the Nature of Cosmic-Ray Particles, 2011.

[15] T. Regge, Introduction to complex orbital momenta, Il Nuovo Cimento (1955-1965) **14** (1959) p. 951, ISSN: 1827-6121, URL: https://doi.org/10.1007/BF02728177.

[16] M. Gell-Mann, The Eightfold Way:A Theory of strong interaction symmetry (1961).

[17] G. Zweig, An SU(3) model for strong interaction symmetry and its breaking. Version 1 (1964).

[18] V. Barone and E. Predazzi, High-Energy Particle Diffraction, Theoretical and Mathematical Physics, Springer Berlin Heidelberg, 2013, ISBN: 9783662047248, URL: https://books.google.ca/books?id=9C3qCAAAQBAJ.

[19] K. Riley, M. Hobson, and S. Bence, Mathematical Methods for Physics and Engineering: A Comprehensive Guide, Cambridge University Press, 2006, ISBN: 9781139450997, URL: https://books.google.ca/books?id=Mq1nlEKhNcsC.

[20] T. Azzarelli and P. Collas, Sommerfeld-Watson representation without poles, Lettere al Nuovo Cimento (1971-1985) **12** (1975) p. 601, ISSN: 1827-613X, URL: https://doi.org/10.1007/BF02780751.

[21] V. A. Petrov, Nonlinear Regge Trajectories in Theory and Practice, AIP Conf. Proc. **1105** (2009) p. 266, arXiv: 0812.0996 [hep-ph].

[22] V. Gribov,
The Theory of Complex Angular Momenta: Gribov Lectures on Theoretical Physics,
Cambridge Monographs on Mathematical Physics,
Cambridge University Press, 2003, ISBN: 9781139441896,
URL: https://books.google.ca/books?id=gS7we7IjvKQC.

[23] E. Nagy et al., Measurements of elastic proton-proton scattering at large momentum transfer at the CERN intersecting storage rings,
Nuclear Physics B **150** (1979) p. 221 , ISSN: 0550-3213,
URL: http://www.sciencedirect.com/science/article/pii/0550321379903018.

[24] M. Deile et al., Diffraction and total cross-section at the Tevatron and the LHC,
Springer Proc. Phys. **108** (2006) p. 40, arXiv: hep-ex/0602021 [hep-ex].

[25] G. Aad et al., Measurement of the total cross section from elastic scattering in pp collisions at $\sqrt{s} = 7$ TeV with the ATLAS detector,
Nucl. Phys. **B889** (2014) p. 486, arXiv: 1408.5778 [hep-ex].

[26] M. Froissart,
Asymptotic Behavior and Subtractions in the Mandelstam Representation,
Phys. Rev. **123** (3 1961) p. 1053,
URL: https://link.aps.org/doi/10.1103/PhysRev.123.1053.

[27] A. Martin, Extension of the axiomatic analyticity domain of scattering amplitudes by unitarity-I, Il Nuovo Cimento A (1965-1970) **42** (1966) p. 930, ISSN: 1826-9869,
URL: https://doi.org/10.1007/BF02720568.

[28] R. K. Ellis, W. J. Stirling, and B. R. Webber, QCD and Collider Physics,
Cambridge monographs on particle physics, nuclear physics, and cosmology,
Photography by S. Vascotto, Cambridge: Cambridge Univ. Press, 2003,
URL: https://cds.cern.ch/record/318585.

[29] M. Gell-Mann and Y. Ne'Eman, The Eightfold Way, Advanced book classics,
Avalon Publishing, 2000, ISBN: 9780738202990,
URL: https://books.google.ca/books?id=0vJENjZOz8UC.

[30] G. Zweig,
An SU(3) model for strong interaction symmetry and its breaking. Version 2,
Developments in the Quark theory of Hadrons. VOL. 1. 1964 - 1978,
ed. by D. Lichtenberg and S. P. Rosen, 1964 p. 22,
URL: http://inspirehep.net/record/4674/files/cern-th-412.pdf.

[31] M. Y. Han and Y. Nambu, Three-Triplet Model with Double SU(3) Symmetry, Phys. Rev. **139** (4B 1965) B1006, URL: https://link.aps.org/doi/10.1103/PhysRev.139.B1006.

[32] O. W. Greenberg, Spin and Unitary Spin Independence in a Paraquark Model of Baryons and Mesons, Phys. Rev. Lett. **13** (1964) p. 598.

[33] R. P. Feynman, Very High-Energy Collisions of Hadrons, Physical Review Letters **23** (Dec. 1969) p. 1415.

[34] D. J. Gross and F. Wilczek, Asymptotically Free Gauge Theories. 1, Phys. Rev. **D8** (1973) p. 3633.

[35] H. D. Politzer, Reliable Perturbative Results for Strong Interactions?, Phys. Rev. Lett. **30** (1973) p. 1346.

[36] J. D. Bjorken, Asymptotic Sum Rules at Infinite Momentum, Physical Review **179** (Mar. 1969) p. 1547.

[37] J. C. Collins, D. E. Soper, and G. Sterman, Factorization for one-loop corrections in the Drell-Yan process, Nuclear Physics B **223** (Aug. 1983) p. 381.

[38] G. Ingelman and P. Schlein, Jet structure in high mass diffractive scattering, Physics Letters B **152** (1985) p. 256 , ISSN: 0370-2693, URL: http://www.sciencedirect.com/science/article/pii/0370269385911815.

[39] J. C. Collins, Proof of factorization for diffractive hard scattering, Phys. Rev. **D57** (1998) p. 3051, [Erratum: Phys. Rev.D61,019902(2000)], arXiv: hep-ph/9709499 [hep-ph].

[40] T. Ahmed et al., First measurement of the deep-inelastic structure of proton diffraction, Physics Letters B **348** (1995) p. 681 , ISSN: 0370-2693, URL: http://www.sciencedirect.com/science/article/pii/037026939500279T.

[41] C. Adloff et al., Inclusive measurement of diffractive deep inelastic *ep* scattering, Z. Phys. **C76** (1997) p. 613, arXiv: hep-ex/9708016 [hep-ex].

[42] S. Chekanov et al., Measurement of the Q and energy dependence of diffractive interactions at HERA, The European Physical Journal C - Particles and Fields **25** (2002) p. 169, ISSN: 1434-6052, URL: https://doi.org/10.1007/s10052-002-1003-1.

[43] P. Newman and F.-P. Schilling,
HERA Diffractive Structure Function Data and Parton Distributions,
ArXiv High Energy Physics - Experiment e-prints (Nov. 2005),
eprint: hep-ex/0511032.

[44] C. O. Rasmussen, Hard Diffraction in Pythia 8,
EPJ Web Conf. **120** (2016) p. 02002, arXiv: 1512.05872 [hep-ph].

[45] F. Abe et al.,
Observation of Diffractive W Boson Production at the Fermilab Tevatron,
Phys. Rev. Lett. **78** (14 1997) p. 2698,
URL: https://link.aps.org/doi/10.1103/PhysRevLett.78.2698.

[46] V. M. Abazov et al.,
High mass exclusive diffractive dijet production in pp collisions at $\sqrt{s} = 1.96$ TeV,
Physics Letters B **705** (2011) p. 193 , ISSN: 0370-2693, URL:
http://www.sciencedirect.com/science/article/pii/S0370269311012457.

[47] T Aaltonen et al., Observation of Exclusive Gamma Gamma Production in p pbar Collisions at $\sqrt{s}$=1.96 TeV, **108** (Dec. 2011).

[48] R. J. M. Covolan and M. S. Soares, Analysis on the diffractive production of Ws and dijets at the DESY HERA and Fermilab Tevatron colliders,
Phys. Rev. **D60** (1999) p. 054005, [Erratum: Phys. Rev.D61,019901(2000)],
arXiv: hep-ph/9905352 [hep-ph].

[49] V. Fadin, E. Kuraev, and L. Lipatov,
On the pomeranchuk singularity in asymptotically free theories,
Physics Letters B **60** (1975) p. 50 , ISSN: 0370-2693,
URL: http://www.sciencedirect.com/science/article/pii/0370269375905249.

[50] A. Austregesilo and T Schlueter, Partial-Wave Analysis of the Centrally Produced $\pi^+\pi^-$ System in pp Reactions at COMPASS (July 2012).

[51] B. Andersson et al., Parton fragmentation and string dynamics,
Physics Reports **97** (1983) p. 31 , ISSN: 0370-1573,
URL: http://www.sciencedirect.com/science/article/pii/0370157383900807.

[52] Measurement of dijet cross sections in ep interactions with a leading neutron at HERA, The European Physical Journal C - Particles and Fields **41** (2005) p. 273,
ISSN: 1434-6052, URL: https://doi.org/10.1140/epjc/s2005-02227-8.

[53] J. Rathsman, A Generalized area law for hadronic string re-interactions,
Phys. Lett. **B452** (1999) p. 364, arXiv: hep-ph/9812423 [hep-ph].

[54] M. L. Good and W. D. Walker, Diffraction Dissociation of Beam Particles, Physical Review **120** (Dec. 1960) p. 1857.

[55] Pythia website, URL: http://home.thep.lu.se/~torbjorn/Pythia.html.

[56] T. Sjöstrand et al., An Introduction to PYTHIA 8.2, Comput. Phys. Commun. **191** (2015) p. 159, arXiv: 1410.3012 [hep-ph].

[57] FPMC website, URL: http://project-fpmc.web.cern.ch/project-fpmc/.

[58] Herwig website, URL: https://herwig.hepforge.org/.

[59] G. A. Schuler and T. Sjöstrand, Hadronic diffractive cross sections and the rise of the total cross section, Phys. Rev. D **49** (5 1994) p. 2257, URL: https://link.aps.org/doi/10.1103/PhysRevD.49.2257.

[60] A. Donnachie and P. V. Landshoff, Total cross-sections, Phys. Lett. **B296** (1992) p. 227, arXiv: hep-ph/9209205 [hep-ph].

[61] T. Sjöstrand, S. Mrenna, and P. Skands, PYTHIA 6.4 physics and manual, Journal of High Energy Physics **2006** (2006) p. 026, URL: http://stacks.iop.org/1126-6708/2006/i=05/a=026.

[62] R. Covolan, J. Montanha, and K. Goulianos, A new determination of the soft pomeron intercept, Physics Letters B **389** (1996) p. 176 , ISSN: 0370-2693, URL: http://www.sciencedirect.com/science/article/pii/S0370269396013627.

[63] K. Goulianos, Diffraction, Saturation and pp Cross Sections at the LHC (2011), arXiv: 1105.4916 [hep-ph].

[64] K. A. Goulianos, Diffraction in QCD, Proceedings, Corfu Summer Institute on Elementary Particle Physics, 2001, arXiv: hep-ph/0203141 [hep-ph].

[65] R. Ciesielski and K. Goulianos, MBR Monte Carlo Simulation in PYTHIA8, PoS **ICHEP2012** (2013) p. 301, arXiv: 1205.1446 [hep-ph].

[66] B. Andersson et al., Parton Fragmentation and String Dynamics, Phys. Rept. **97** (1983) p. 31.

[67] S. Zarrin and G. Boroun, Solution of QCDxQED coupled DGLAP equations at NLO, Nuclear Physics B **922** (2017) p. 126 , ISSN: 0550-3213, URL: http://www.sciencedirect.com/science/article/pii/S0550321317302110.

[68] L. Alvero et al.,
Diffractive production of jets and weak bosons and tests of hard-scattering factorization, Physics Review D **59**, 074022 (Apr. 1999) p. 074022, eprint: hep-ph/9805268.

[69] L. Frankfurt et al., Generalized parton distributions and rapidity gap survival in exclusive diffractive pp scattering, Phys.Rev.D **75** (Mar. 2007).

[70] T. Ferbel, Experimental Techniques in High-energy Nuclear and Particle Physics, World Scientific, 1991, ISBN: 9789810208677,
URL: https://books.google.ca/books?id=ieMrqqJbaMsC.

[71] T. A. Collaboration, The ATLAS Experiment at the CERN Large Hadron Collider, Journal of Instrumentation **3** (2008) S08003,
URL: http://stacks.iop.org/1748-0221/3/i=08/a=S08003.

[72] L. Evans and P. Bryant, LHC Machine,
Journal of Instrumentation **3** (2008) S08001,
URL: http://stacks.iop.org/1748-0221/3/i=08/a=S08001.

[73] CERN, Design study of the large hadron collider (LHC):A Multiparticle collider in the LEP tunnel (1991).

[74] A. Blas et al.,
The PS complex as proton pre-injector for the LHC: Design and implementation report (2000), ed. by M. Benedikt.

[75] D. Boussard and T. Linnecar, The LHC Superconducting RF System,
Adv. Cryog. Eng. **45A** (2000) p. 835.

[76] F. Marcastel, CERN's Accelerator Complex. La chaîne des accélérateurs du CERN (2013), General Photo, URL: https://cds.cern.ch/record/1621583.

[77] ATLAS Luminosity Public Results,
URL: https://twiki.cern.ch/twiki/bin/view/AtlasPublic/LuminosityPublicResultsRun2#Luminosity_summary_plots_for_201.

[78] J. Rossbach and P. Schmueser, Basic course on accelerator optics,
Conf. Proc. **C9209071** (1992) p. 17.

[79] G Baud et al., Performance Assessment of Wire-Scanners at CERN (2013) 4 p,
URL: https://cds.cern.ch/record/1638354.

[80] M Capeans et al., ATLAS Insertable B-Layer Technical Design Report,
tech. rep. CERN-LHCC-2010-013. ATLAS-TDR-19, 2010,
URL: https://cds.cern.ch/record/1291633.

[81] C. Grupen and B. Shwartz, Particle Detectors,
Cambridge Monographs on Particle Physics, Nuclear Physics and Cosmology,
Cambridge University Press, 2008.

[82] ATLAS experiment website,
URL: http://atlasexperiment.org/photos/inner-detector-combined.html.

[83] M. Kayl, Tracking Performance of the ATLAS Inner Detector and Observation of Known Hadrons,
Hadron collider physics. Proceedings, 22nd Conference, HCP 2010, Toronto, Canada,
2010, arXiv: 1010.1091 [physics.ins-det],
URL: http://inspirehep.net/record/871877/files/arXiv:1010.1091.pdf.

[84] G. Aad et al., The ATLAS Inner Detector commissioning and calibration,
Eur. Phys. J. **C70** (2010) p. 787, arXiv: 1004.5293 [physics.ins-det].

[85] L Adamczyk et al.,
Technical Design Report for the ATLAS Forward Proton Detector,
tech. rep. CERN-LHCC-2015-009. ATLAS-TDR-024, 2015,
URL: https://cds.cern.ch/record/2017378.

[86] S Jakobsen, Technical and operational overview of ATLAS-ALFA,
tech. rep. ATL-COM-FWD-2013-004,
Invited technical talk for an ISOLDE seminar at CERN, October 2013
https://indico.cern.ch/conferenceDisplay.py?confId=273506: CERN, 2013,
URL: https://cds.cern.ch/record/1600829.

[87] R. Battiston et al., The Roman pot spectrometer and the vertex detector of experiment UA4 at the CERN SPS collider,
Nuclear Instruments and Methods in Physics Research A **238** (July 1985) p. 35.

[88] U. Amaldi et al., The real part of the forward proton proton scattering amplitude measured at the CERN intersecting storage rings,
Physics Letters B **66** (1977) p. 390 , ISSN: 0370-2693,
URL: http://www.sciencedirect.com/science/article/pii/0370269377900223.

[89] S Cavalier et al., Measurement of the total cross section in pp collisons at $\sqrt{(s)} = 7$ TeV from elastic scattering with the ATLAS detector,
tech. rep. ATL-COM-PHYS-2013-1357, CERN, 2013,
URL: https://cds.cern.ch/record/1602297.

[90] M Trzebinski, J. Chwastowski, and C. Royon,
Study of QCD and Diffraction with the ATLAS detector at the LHC,
Presented 20 Sep 2013, 2013, URL: https://cds.cern.ch/record/1616661.

[91] M Trzebinski and J Chwastowski,
Monte Carlo Studies for ALFA Runs at $\sqrt{s} = 8$ TeV: Some Aspects of Optics, Beam Profiles, Elastic and Diffractive Event Patterns and Rates,
tech. rep. ATL-COM-LUM-2012-012, CERN, 2012,
URL: https://cds.cern.ch/record/1472560.

[92] Forward Transport TWiki Page,
URL: https://twiki.cern.ch/twiki/bin/viewauth/Atlas/ForwardTransport.

[93] S. H. Stark, P. Hansen, and J. B. Hansen,
Study of forward elastic pp scattering at $\sqrt{s} = 8$ TeV with the ALFA detector,
Presented 24 Feb 2017, 2017, URL: https://cds.cern.ch/record/2283206.

[94] B. Giacobbe et al., Measurement of the total cross section from elastic scattering in pp collisions at $\sqrt{s} = 8$ TeV, tech. rep. ATL-COM-PHYS-2015-1371, CERN, 2015,
URL: https://cds.cern.ch/record/2067608.

[95] C. Da Via et al., 3D silicon sensors: Design, large area production and quality assurance for the ATLAS IBL pixel detector upgrade,
Nucl. Instrum. Meth. **A694** (2012) p. 321.

[96] M. Aaboud et al., Performance of the ATLAS Trigger System in 2015,
Eur. Phys. J. **C77** (2017) p. 317, arXiv: 1611.09661 [hep-ex].

[97] G. Aad et al.,
The performance of the jet trigger for the ATLAS detector during 2011 data taking,
Eur. Phys. J. **C76** (2016) p. 526, arXiv: 1606.07759 [hep-ex].

[98] ATLAS Luminosity Measurement Taskforce, URL: http://project-atlas-lucid.web.cern.ch/project-atlas-lucid/taskforce/main_10.html.

[99] J. Catmore et al., A new petabyte-scale data derivation framework for ATLAS,
Journal of Physics: Conference Series **664** (2015) p. 072007,
URL: http://stacks.iop.org/1742-6596/664/i=7/a=072007.

[100] S Albrand et al., ATLAS Dataset Nomenclature,
tech. rep. ATL-GEN-INT-2007-001. ATL-COM-GEN-2007-003, The scope of the document covers:- (1) Monte-Carlo datasets (2) Real Data Datasets. a. Primary b. Super datasets (including relational event collections) (3) User datasets (4) Group datasets (5) Conditions datasets (6) Application Internal datasets: CERN, 2007,
URL: https://cds.cern.ch/record/1070318.

[101] S. Agostinelli et al., Geant4—a simulation toolkit,
Nuclear Instruments and Methods in Physics Research Section A: Accelerators, Spectrometers, Detectors and Associated Equipment **506** (2003) p. 250 ,
ISSN: 0168-9002, URL:
http://www.sciencedirect.com/science/article/pii/S0168900203013688.

[102] Forward Transport TWiki,
URL: https://twiki.cern.ch/twiki/bin/viewauth/Atlas/ForwardTransport.

[103] G. Aad et al., Rapidity gap cross sections measured with the ATLAS detector in pp collisions at $\sqrt{s} = 7$ TeV, Eur. Phys. J. **C72** (2012) p. 1926,
arXiv: 1201.2808 [hep-ex].

[104] V. Khachatryan et al., Measurement of diffraction dissociation cross sections in pp collisions at $\sqrt{s} = 7$ TeV, Phys. Rev. **D92** (2015) p. 012003,
arXiv: 1503.08689 [hep-ex].

[105] Summary of ATLAS Pythia 8 tunes, tech. rep. ATL-PHYS-PUB-2012-003,
CERN, 2012, URL: https://cds.cern.ch/record/1474107.

[106] A study of the Pythia 8 description of ATLAS minimum bias measurements with the Donnachie-Landshoff diffractive model, tech. rep. ATL-PHYS-PUB-2016-017,
CERN, 2016, URL: https://cds.cern.ch/record/2206965.

[107] A. D. Martin et al., Parton distributions for the LHC,
Eur. Phys. J. **C63** (2009) p. 189, arXiv: 0901.0002 [hep-ph].

[108] R. D. Ball et al., Parton distributions with LHC data,
Nucl. Phys. **B867** (2013) p. 244, arXiv: 1207.1303 [hep-ph].

[109] P. Skands, S. Carrazza, and J. Rojo, Tuning PYTHIA 8.1: the Monash 2013 Tune,
Eur. Phys. J. C **74** (2014) 3024. 57 p, Comments: 57 pages,
URL: https://cds.cern.ch/record/1695787.

[110] W Bell et al., Offline Performance of the ATLAS Minimum Bias Trigger Scintillator Detector at $\sqrt{s} = 7$ TeV, tech. rep. ATL-COM-LUM-2010-033, CERN, 2010,
URL: https://cds.cern.ch/record/1309184.

[111] M. Aaboud et al., Measurement of the total cross section from elastic scattering in pp collisions at $\sqrt{s} = 8$ TeV with the ATLAS detector, Phys. Lett. **B761** (2016) p. 158, arXiv: 1607.06605 [hep-ex].

[112] A. Foster, personal communication, Feb. 2018.

[113] ATLAS Run Queries Website, URL: https://atlas-runquery.cern.ch/.

[114] H. Jeffreys, The Theory of Probability, Oxford Classic Texts in the Physical Sciences, OUP Oxford, 1998, ISBN: 9780191589676, URL: https://books.google.ca/books?id=vh9Act9rtzQC.

[115] G. D'Agostini, A multidimensional unfolding method based on Bayes' theorem, Nuclear Instruments and Methods in Physics Research Section A: Accelerators, Spectrometers, Detectors and Associated Equipment **362** (1995) p. 487 , ISSN: 0168-9002, URL: http://www.sciencedirect.com/science/article/pii/016890029500274X.

[116] T. Adye, Unfolding algorithms and tests using RooUnfold (2011) p. 313, Comments: 6 pages, 5 figures, presented at PHYSTAT 2011, CERN, Geneva, Switzerland, January 2011, to be published in a CERN Yellow Report, URL: https://cds.cern.ch/record/1349242.

[117] A. G. Foster et al., Measurement of the inclusive single diffractive dissociation cross section of pp collisions at $\sqrt{s}$= 8 TeV with the ATLAS detector using the ALFA forward detectors, tech. rep. ATL-COM-PHYS-2018-031, CERN, 2018, URL: https://cds.cern.ch/record/2300132.

[118] W. Lukas et al., Charged-particle multiplicities in pp interactions at $\sqrt{s} = 8$ TeV measured with the ATLAS detector at the LHC, tech. rep. ATL-COM-PHYS-2014-449, CERN, 2014, URL: https://cds.cern.ch/record/1700840.

[119] F. Abe et al., Measurement of $p\bar{p}$ single diffraction dissociation at $\sqrt{s}$ =546 and 1800 GeV, Phys. Rev. D **50** (9 1994) p. 5535, URL: https://link.aps.org/doi/10.1103/PhysRevD.50.5535.

[120] T. Affolder et al., Double diffraction dissociation at the Fermilab Tevatron collider, Phys. Rev. Lett. **87** (2001) p. 141802, arXiv: hep-ex/0107070 [hep-ex].

[121] D. Acosta et al., Inclusive double pomeron exchange at the Fermilab Tevatron $\bar{p}p$ collider, Phys. Rev. Lett. **93** (2004) p. 141601, arXiv: hep-ex/0311023 [hep-ex].

[122] C. O. Rasmussen and T. Sjöstrand, Hard diffraction with dynamic gap survival, Journal of High Energy Physics **2016** (2016) p. 142, ISSN: 1029-8479, URL: http://dx.doi.org/10.1007/JHEP02(2016)142.

[123] A. Chuinard, C. Royon, and R. Staszewski, Testing Pomeron flavour symmetry with diffractive W charge asymmetry, JHEP **04** (2016) p. 092, arXiv: 1510.04218 [hep-ph].

[124] F. Abe et al., The Charge asymmetry in W boson decays produced in $p\bar{p}$ collisions at $\sqrt{s} = 1.8$ TeV, Phys. Rev. Lett. **74** (1995) p. 850, arXiv: hep-ex/9501008 [hep-ex].

[125] V. M. Abazov et al., Search for Anomalous Wtb Couplings in Single Top Quark Production, Phys. Rev. Lett. **101** (22 2008) p. 221801, URL: https://link.aps.org/doi/10.1103/PhysRevLett.101.221801.

[126] T. Aaltonen et al., Direct Measurement of the W Production Charge Asymmetry in $p\bar{p}$ Collisions at $\sqrt{s} = 1.96$ TeV, Phys. Rev. Lett. **102** (18 2009) p. 181801, URL: https://link.aps.org/doi/10.1103/PhysRevLett.102.181801.

[127] K. Golec-Biernat et al., Electroweak vector boson production at the LHC as a probe of mechanisms of diffraction, Phys. Rev. **D84** (2011) p. 114006, arXiv: 1110.1825 [hep-ph].

[128] M. Boonekamp et al., FPMC: A Generator for forward physics (2011), arXiv: 1102.2531 [hep-ph].

[129] S. Fichet et al., Probing new physics in diphoton production with proton tagging at the Large Hadron Collider, Phys. Rev. **D89** (2014) p. 114004, arXiv: 1312.5153 [hep-ph].

[130] O. Kepka and C. Royon, Probing anomalous triple gauge boson vertex in photon induced processes using proton taggers, Nuclear Physics B - Proceedings Supplements **179-180** (2008) p. 265 , Proceedings of the International Workshop on High-Energy Photon Collisions at the LHC, ISSN: 0920-5632, URL: http://www.sciencedirect.com/science/article/pii/S0920563208000807.

[131] C. Baldenegro et al., Probing the anomalous $\gamma\gamma\gamma$Z coupling at the LHC with proton tagging, Journal of High Energy Physics **2017** (2017) p. 142, ISSN: 1029-8479, URL: https://doi.org/10.1007/JHEP06(2017)142.

[132] G. Aad et al.,
Readiness of the ATLAS Liquid Argon Calorimeter for LHC Collisions,
Eur. Phys. J. **C70** (2010) p. 723, arXiv: 0912.2642 [physics.ins-det].

[133] M. Aharrouche et al., Energy linearity and resolution of the ATLAS electromagnetic barrel calorimeter in an electron test-beam,
Nuclear Instruments and Methods in Physics Research Section A: Accelerators, Spectrometers, Detectors and Associated Equipment **568** (2006) p. 601 ,
ISSN: 0168-9002, URL:
http://www.sciencedirect.com/science/article/pii/S0168900206013222.

[134] P. Adragna et al.,
Testbeam studies of production modules of the ATLAS tile calorimeter,
Nucl. Instrum. Meth. **A606** (2009) p. 362.

[135] G. Cattani and the RPC group,
The Resistive Plate Chambers of the ATLAS experiment: performance studies,
Journal of Physics: Conference Series **280** (2011) p. 012001,
URL: http://stacks.iop.org/1742-6596/280/i=1/a=012001.

[136] K. Nagai, Thin gap chambers in ATLAS, Nuclear Instruments and Methods in Physics Research Section A: Accelerators, Spectrometers, Detectors and Associated Equipment **384** (1996) p. 219 , BEAUTY '96, ISSN: 0168-9002, URL:
http://www.sciencedirect.com/science/article/pii/S0168900296010650.

[137] ATLAS muon spectrometer: Technical design report (1997).

[138] K. H. Hiller et al., The ALFA Roman Pot Detectors of ATLAS,
tech. rep. ATL-COM-FWD-2016-014, CERN, 2016,
URL: https://cds.cern.ch/record/2162765.

[139] NNPDF Collaboration Website, URL: nnpdf.hepforge.org.

Acronyms

AFP ATLAS Forward Proton. 1, 8, 10, 32, 63, 73, 81, 82, 95–97, 99

ALFA A Luminosity For ATLAS. 1, 8, 10, 63, 73, 82, 83, 87, 89–95, 99, 100, 103, 104, 107–109, 112, 116–118, 120, 124–126, 131, 132, 135, 136, 139, 141, 142, 152, 154, 158, 159, 161

CD Central Diffraction. 1, 34, 35, 126, 127, 132, 133, 136, 152

D3PD Derived Physics Data. 1, 106

DD Double Diffraction. 1, 34, 35, 126, 127, 133, 136, 152

DDIS Diffractive Deep Inelatic Scattering. 1, 29

DGLAP Dokchizer, Gribov, Lipatov, Altarelli, Parisi. 1, 49, 50, 54

DIS Deep Inelatic Scattering. 1, 24, 29

DL Donnachie-Landshoff. 1, 48, 116

DPDF Diffractive PDF. 1, 30, 47–49, 54, 174, 175

EF Event Filter. 1, 102, 104

FPMC Forward Physics Monte Carlo. 1, 40, 48, 52

FSR Final-State Radiation. 1, 54

FTK Fast TracKer. 1, 102

IP Interaction Point. 1, 63, 66, 67, 71, 72, 75, 76, 81, 83, 90, 91, 93, 95, 96, 108

IS Ingelman and Schlein. 1, 29, 32, 33, 53, 186

ISR Initial State Radiation. 1, 28, 54

L1 Level 1. 1, 102–104

L2 Level 2. 1, 102, 103

LEP Large Electron-Position collider. 1, 64

LHC Large Hadron Collider. 1, 7, 9, 10, 32, 63–69, 71, 74, 75, 87, 91, 93, 96, 98–100, 105, 111, 116, 125, 126

LO Leading Order. 1, 49, 50

LUCID LUminosity measurement using Čerenkov Integrating Detector. 1, 82, 103, 141, 142

MAPMT Multi-Anode PhotoMultiplier Tubes. 1, 86

MBR Minimum Bias Rockefeller. 1, 42, 44, 48, 59

MBTS Minimum Bias Trigger Scintillators. 1, 103–105, 118, 120–122, 135, 137, 138, 140–142, 153, 158, 162

MCP-PMT Micro-Channel Plate PhotoMultipliers Tubes. 1, 98

MD Main ALFA Detector. 1, 85, 86

MPI Multi-Parton Interactions. 1, 46, 52, 53, 55, 60, 116

ND Non Diffractive. 1, 126, 127, 133, 135, 138, 152

NLO Next-to-Leading Order. 1, 49–51

OD ALFA Overlap Detector. 1, 85, 86, 94

PDF Parton Distribution Function. 1, 27–31, 46, 48–51, 54, 56, 60, 116, 155, 174, 175, 177, 178, 181

PMTs PhotoMultipliers Tubes. 1, 121

QCD Quantum Chromodynamics. 1, 8, 9, 26, 27, 29, 31, 34, 40, 50, 54, 55, 127, 132

QED Quantum Electrodynamics. 1, 24

QUARTIC Quartz Timing Čerenkov detector. 1, 98

RF Radio Frequency. 1, 65

RoI Region(s) of Interest. 1, 103

RP ALFA Roman Pot. 1, 84, 86, 87, 94–96, 99, 118, 132

Run I the first ATLAS run campaign. 1, 116

Run II the second ATLAS run campaign. 1, 101

SaS Schuler and Sjöstrand. 1, 42, 48, 116

SCI Soft Color Interaction. 1, 34

SCT Semi-Conductor Tracker. 1, 78, 79, 81

SD Single Diffraction. 1, 34, 35, 126, 127, 136, 137, 148, 152, 159, 162

SLAC Stanford Linear Accelerator. 1, 24, 27

ToF Time-of-Flight. 1, 95–99

TRT Transition Radiation Tracker. 1, 78, 81, 199

ZDC Zero Degree Calorimeter. 1, 82, 103, 142